frontiers | Research Topics

Multi-dimensional characterization of neuropsychiatric disorders

Edited by
Peng Wang, Jinglei Lv, Xiang Li and Shijie Zhao

Published in
Frontiers in Neuroscience

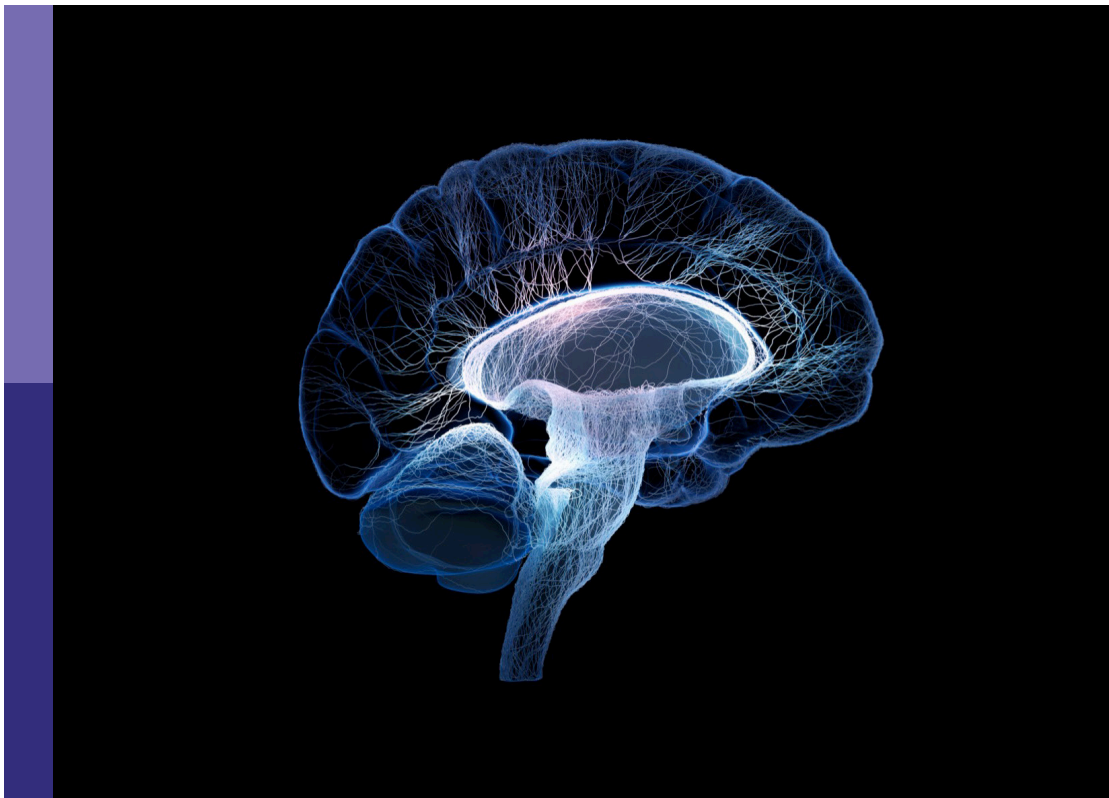

ISSN 1664-8714
ISBN 978-2-83251-059-9
DOI 10.3389/978-2-83251-059-9

About Frontiers

Frontiers is more than just an open access publisher of scholarly articles: it is a pioneering approach to the world of academia, radically improving the way scholarly research is managed. The grand vision of Frontiers is a world where all people have an equal opportunity to seek, share and generate knowledge. Frontiers provides immediate and permanent online open access to all its publications, but this alone is not enough to realize our grand goals.

Frontiers journal series

The Frontiers journal series is a multi-tier and interdisciplinary set of open-access, online journals, promising a paradigm shift from the current review, selection and dissemination processes in academic publishing. All Frontiers journals are driven by researchers for researchers; therefore, they constitute a service to the scholarly community. At the same time, the *Frontiers journal series* operates on a revolutionary invention, the tiered publishing system, initially addressing specific communities of scholars, and gradually climbing up to broader public understanding, thus serving the interests of the lay society, too.

Dedication to quality

Each Frontiers article is a landmark of the highest quality, thanks to genuinely collaborative interactions between authors and review editors, who include some of the world's best academicians. Research must be certified by peers before entering a stream of knowledge that may eventually reach the public - and shape society; therefore, Frontiers only applies the most rigorous and unbiased reviews. Frontiers revolutionizes research publishing by freely delivering the most outstanding research, evaluated with no bias from both the academic and social point of view. By applying the most advanced information technologies, Frontiers is catapulting scholarly publishing into a new generation.

What are Frontiers Research Topics?

Frontiers Research Topics are very popular trademarks of the *Frontiers journals series*: they are collections of at least ten articles, all centered on a particular subject. With their unique mix of varied contributions from Original Research to Review Articles, Frontiers Research Topics unify the most influential researchers, the latest key findings and historical advances in a hot research area.

Find out more on how to host your own Frontiers Research Topic or contribute to one as an author by contacting the Frontiers editorial office: frontiersin.org/about/contact

Multi-dimensional characterization of neuropsychiatric disorders

Topic editors

Peng Wang — Fuwai Hospital, Chinese Academy of Medical Sciences and Peking Union Medical College, China

Jinglei Lv — The University of Sydney, Australia

Xiang Li — Massachusetts General Hospital, Harvard Medical School, United States

Shijie Zhao — Northwestern Polytechnical University, China

Citation

Wang, P., Lv, J., Li, X., Zhao, S., eds. (2022). *Multi-dimensional characterization of neuropsychiatric disorders*. Lausanne: Frontiers Media SA.

doi: 10.3389/978-2-83251-059-9

Table of contents

frontiers | Frontiers in Neuroscience

TYPE Editorial
PUBLISHED 01 December 2022
DOI 10.3389/fnins.2022.1089886

OPEN ACCESS

EDITED AND REVIEWED BY
Vince D. Calhoun,
Georgia State University, United States

*CORRESPONDENCE
Xiang Li
xli60@mgh.harvard.edu
Jinglei Lv
jinglei.lv@sydney.edu.au

†These authors have contributed equally to this work

SPECIALTY SECTION
This article was submitted to Brain Imaging Methods, a section of the journal Frontiers in Neuroscience

RECEIVED 04 November 2022
ACCEPTED 09 November 2022
PUBLISHED 01 December 2022

CITATION
Wang P, Zhao S, Li X and Lv J (2022) Editorial: Multi-dimensional characterization of neuropsychiatric disorders.
Front. Neurosci. 16:1089886.
doi: 10.3389/fnins.2022.1089886

Editorial: Multi-dimensional characterization of neuropsychiatric disorders

Peng Wang[1†], Shijie Zhao[2,3†], Xiang Li[4*] and Jinglei Lv[5*]

[1]Fuwai Hospital, Chinese Academy of Medical Sciences and Peking Union Medical College, Beijing, China, [2]School of Automation, Northwestern Polytechnical University, Xi'an, China, [3]Research and Development Institute of Northwestern Polytechnical University in Shenzhen, Shenzhen, China, [4]Center for Advanced Medical Computing and Analysis (CAMCA), Department of Radiology, Massachusetts General Hospital and Harvard Medical School, Boston, MA, United States, [5]School of Biomedical Engineering and Brain and Mind Center, University of Sydney, Sydney, NSW, Australia

KEYWORDS

neuropsychiatric disorders (NPD), NeuroImage, electroencephalography, PET, MRI

Editorial on the Research Topic
Multi-dimensional characterization of neuropsychiatric disorders

Introduction

The human nervous system itself and its extensive connections with the human body form a complex system. The individual characteristics and abnormalities of the system can be observed on multiple dimensions, such as the brain functional, structural, molecular, genetic, and behavioral dimensions. Understanding the underlying multi-dimensional mechanisms and the corresponding biomarkers for neuropsychiatric disorders could be regarded as the highest-priority goal in neuroscience and a vital step for clinical practice (Li et al., 2019). In particular, brain disorders can be characterized on multiple dimensions, with reference either to the biomarkers of one modality or to those of multiple modalities. This multi-dimensional method of characterization provides a more objective and accurate identification of disorders; based on this level of precision, treatments can be developed to benefit patients in clinical practice.

This Research Topic assembles 10 articles on a broad spectrum of research in neuropsychiatric disorders. Authors from backgrounds in psychiatry, radiology, computer science, and engineering have all contributed to this Research Topic by conducting empirical studies, developing computational models, performing reviews, and introducing novel intervention techniques. In this Editorial, we provide an overview of these exciting and diverse articles, grouping them based on their conceptual design.

Computational modeling of multi-dimensional brain signals

The modeling scheme proposed by Lun et al. extracts features of motor imagery EEG signals separately for each hemisphere using a deep learning architecture and then combines the embeddings for classification. This research is helpful for the development of brain–machine interfaces for motor functional disability and spinal cord injury. The article by Peng et al. proposes to characterize the neural electrical signals captured by intracranial and scalp EEG on multiple temporal and frequency dimensions so that the rich information can be better utilized for seizure prediction in epilepsy. This is particularly important in surgery-planning for drug-resistant epilepsy. The model proposed by Liu K. et al. utilizes coupled integration for hierarchical feature representation of MCI and AD with structural MRI to enable improved discrimination of the different stages of AD. Also targeting AD diagnosis but using PET imaging, the article by Cui et al. proposes a region-by-region descriptor for FDG-PET. The collective descriptors are fed into a novel deep learning network (BMNet) featuring bilinear pooling and metric learning. It transpires that this method offers improved performance in the identification of EMCI and LMCI. This work is important for early diagnosis and intervention in AD.

Multi-dimensional data for treatment development

Sun, Guo et al. used an fMRI-derived measure of ALFF to identify potential age differences in the neuropathological mechanism of treatment-resistant depression. An investigation by Shadli et al. tested the possibility of using EEG as a biomarker for ketamine therapy in anxiety disorders. Among the signals from multiple electrodes and the frequency spectrum, the authors report right frontal theta power to be a possible biomarker. Wu et al. combined rs-fMRI, protein markers, and behavioral assessments to investigate the effect of rTMS on neural plasticity. Although this is a pre-clinical study, it provides evidence for cognitive enhancement that may have future human applications.

Identification and validation of imaging biomarkers of neuropsychiatric disorders

In a study of structural imaging biomarkers, Liu T. et al. investigated multiple variables relating to the structural connectome, measured with diffusion MRI. They found that local efficiency of the structural connectome is correlated with language function in infants, suggesting a relationship between language disorders and the early development of white matter in infancy. Functional brain signals also provide an effective approach to the characterization of brain alterations and treatment response. Under the approach proposed by Sun, Chen et al., the rich information obtained though rs-fMRI is modeled in the form of regional ReHo and ALFF, resulting in the discovery of functional alteration imaging biomarkers for first-episode and recurrent depression; this finding provides neuroimaging insights into the psychological mechanism of depression. Last but not least, the review article by Pan et al. revisits the efforts of the psychiatric and neuroimaging community over the course of 40 years to understand the neural substrates of post-stroke depression, covering regional lesion analysis and the study of brain networks, from structural to functional connectome. It is emphasized in this review that multivariate analysis has played an important role in the task, thereby further highlighting the importance of multi-dimensional characterization of the disorder.

In the current Research Topic, most of the articles have devoted efforts to the characterization of neuropsychiatric disorders within a single modality. We envision that, in the near future, it will be possible to measure many of these multi-dimensional modalities in a single patient, so that information across modalities can be integrated to provide a more comprehensive characterization of a particular disorder or spectrum of disorders. Such high-dimensional multi-modal characterization would provide higher discriminability and more accurate digital identification. High-dimensional characterization will become even more powerful if this method can be employed with a large-scale patient cohort, as the big data generated in this way can be fed into machine learning and artificial intelligence systems, enabling an improved understanding of the mechanisms of the disorder in question. As a consequence, we will be able to characterize patient subtypes more precisely and provide personalized diagnoses, resulting in improved treatment and early intervention for neuropsychiatric disorders.

Author contributions

PW: writing—original draft. SZ, XL, and JL: writing—review and editing. All authors contributed to the article and approved the submitted version.

Funding

This work was supported in part by the National Key R&D Program of China under Grant Number: 2020AAA0105702 and the National Natural Science Foundation of China

under Grant Numbers: 42271315, 61936007, 82060336, 62036011, and U1801265. Guangdong Basic and Applied Basic Research Foundation (2214050008706), Science and Technology Support Project of Guizhou Province under Grant Number: [2021]432, and Shenzhen Science and Technology Program (JCYJ20220530161409021).

Conflict of interest

The authors declare that the research was conducted in the absence of any commercial or financial relationships that could be construed as a potential conflict of interest.

Publisher's note

All claims expressed in this article are solely those of the authors and do not necessarily represent those of their affiliated organizations, or those of the publisher, the editors and the reviewers. Any product that may be evaluated in this article, or claim that may be made by its manufacturer, is not guaranteed or endorsed by the publisher.

References

Li, X., Guo, N., and Li, Q. (2019). Functional neuroimaging in the new era of big data. *Genom Proteom Bioinformat.* 17:393–401. doi: 10.1016/j.gpb.2018.11.005

frontiers in Neuroscience

ORIGINAL RESEARCH
published: 18 January 2022
doi: 10.3389/fnins.2021.825434

Seizure Prediction in EEG Signals Using STFT and Domain Adaptation

Peizhen Peng[1], *Yang Song*[2], *Lu Yang*[3] *and Haikun Wei*[1]*

[1] Key Laboratory of Measurement and Control of Control Science and Engineering (CSE), Ministry of Education, School of Automation, Southeast University, Nanjing, China, [2] State Grid Nanjing Power Supply Company, Nanjing, China, [3] Epilepsy Center, the Affiliated Brain Hospital of Nanjing Medical University, Nanjing, China

Epileptic seizure prediction is one of the most used therapeutic adjuvant strategies for drug-resistant epilepsy. Conventional approaches commonly collect training and testing samples from the same patient due to inter-individual variability. However, the challenging problem of domain shift between various subjects remains unsolved, resulting in a low conversion rate to the clinic. In this work, a domain adaptation (DA)-based model is proposed to circumvent this issue. The short-time Fourier transform (STFT) is employed to extract the time-frequency features from raw EEG data, and an autoencoder is developed to map these features into high-dimensional space. By minimizing the inter-domain distance in the embedding space, this model learns the domain-invariant information, such that the generalization ability is improved by distribution alignment. Besides, to increase the feasibility of its application, this work mimics the data distribution under the clinical sampling situation and tests the model under this condition, which is the first study that adopts the assessment strategy. Experimental results on both intracranial and scalp EEG databases demonstrate that this method can minimize the domain gap effectively compared with previous approaches.

Keywords: seizure prediction, feature extraction, neuropsychiatric disorders, domain adaptation, STFT, EEG

OPEN ACCESS

Edited by:
Shijie Zhao,
Northwestern Polytechnical University, China

Reviewed by:
Xingwu Wang,
North China Electric Power University, China
Zhaoyan Zhang,
Hebei University, China
Bin Chen,
Yangzhou University, China

***Correspondence:**
Haikun Wei
hkwei@seu.edu.cn

Specialty section:
This article was submitted to Brain Imaging Methods, a section of the journal Frontiers in Neuroscience

Received: *30 November 2021*
Accepted: *22 December 2021*
Published: *18 January 2022*

Citation:
Peng P, Song Y, Yang L and Wei H (2022) Seizure Prediction in EEG Signals Using STFT and Domain Adaptation. Front. Neurosci. 15:825434. doi: 10.3389/fnins.2021.825434

1. INTRODUCTION

1.1. Epilepsy Background

Epilepsy is a brain disorder characterized by the transient occurrence of unexpected seizures, which stems from excessive, or hypersynchronous neuronal activities (Fisher et al., 2005). It affects approximately 1.0% of the world's population (Banerjee et al., 2009), and around half of them experience severe seizures. Besides, although the anti-epileptic drug (AED) administration is applied to patients, about 30% of them suffer from drug-resistant epilepsy (Kwan et al., 2011; Lin et al., 2014). These individuals might have seizures at any moment, such that their daily lives are influenced by unexpected behavioral changes, loss of muscular control and sudden faint. As a result, a reliable seizure prediction device is becoming an emerging and significant demand to prevent the injury of epileptic coma, or even death. A successful seizure forecast commonly adopts data-driven techniques to monitor the electroencephalography (EEG) signals of the epileptic brain, since such data records rhythmic information induced by coordinated neuronal. The first-in-man study that proves the predictability of seizure has been reported in 2013 (Cook et al., 2013). Since then, many EEG-based studies regarding seizure prediction have been proposed.

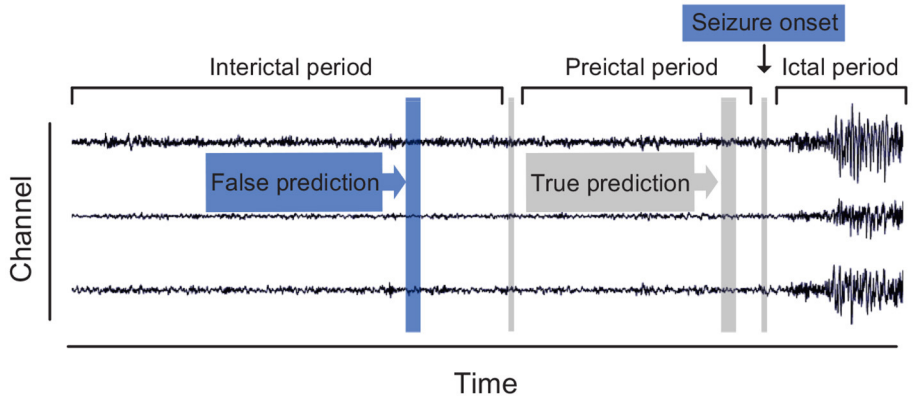

FIGURE 1 | Definition of three brain states in continuous epileptic EEG recordings.

1.2. Related Work

At present, there are two main streams for epileptic seizure prediction. The first stream is a binary classification framework trained to discriminate preictal samples from interictal samples. The ictal and postictal samples are deserted during the training procedure for the uselessness of their contribution to forecast. This stream is widely adopted among researchers in the area of seizure prediction. The second stream assumes that a specific index that fluctuates with changes of seizure stage exists in EEG recordings. These methods attempt to describe this index explicitly and monitor it with a threshold. For instance, spike rate (Li et al., 2013; Karoly et al., 2016; Guo et al., 2017), zero-crossing intervals (Zandi et al., 2013), and phase/amplitude locking value (Myers et al., 2016) have been reported as the indicators. Since a universal preictal biomarker has not been defined explicitly, we also follow the binary scheme of the first stream, which is depicted in **Figure 1**.

Studies adopting the binary classifier usually combine the features extraction algorithms with machine learning techniques. To be specific, the features extraction algorithms are commonly used in data preprocessing due to the complexity and diversity of EEG signals, and then the machine learning techniques can analyze these features and give their categories. Features extraction approaches like wavelet transform (Vahabi et al., 2015; Moctezuma and Molinas, 2020), Q-factor wavelet transform (Al Ghayab et al., 2019), Fourier neural network (Peng et al., 2021), and fractional Fourier transform (Fei et al., 2017), are employed to learn the high-dimensional representations of samples. Machine learning techniques like support vector machines (Mirowski et al., 2009; Direito et al., 2017; Sun et al., 2019), random forests (Brinkmann et al., 2016), *k*-nearest neighbor (Zhang et al., 2018), and ensemble learning (Peng et al., 2020) are utilized to learn the spatial and temporal representations of seizures. Besides, recently most authors apply deep learning frameworks for seizure prediction. Convolutional neural network (CNN) (Zhang et al., 2019; Lin et al., 2020; Liu et al., 2020), 3D CNN (Ozcan and Erturk, 2019), Long Short-Term Memory (LSTM) Network (Tsiouris et al., 2018; Daoud and Bayoumi, 2019; Li et al., 2020), and cascades of DNN (Özcan and Ertürk, 2017), are introduced to process continuously acquired EEG signals.

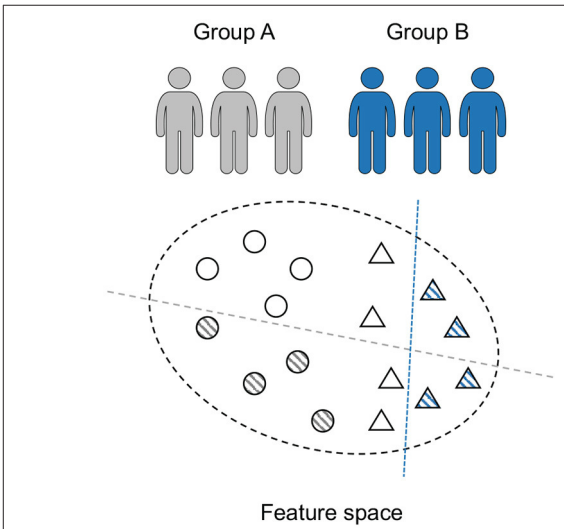

FIGURE 2 | Seizure prediction is a patient-specific problem. The discriminative models (dashed line) of various individuals (circle and triangle) differ significantly.

1.3. Significance

Although conventional studies report high precision (< 85% on average) for the epileptic seizure prediction task, their translation to the practical application is still a challenging issue. The major reason for this situation is that most of these studies only provide patient-specific results. For these patient-specific models, both training and testing sets are recorded from one subject, which leads to limited domain adaptability of previous approaches between different patients (each patient is considered as a domain). As shown in **Figure 2**, for the patients with epilepsy, the internal patterns vary significantly among various subjects

(Jirsa et al., 2017; Elger and Hoppe, 2018; Kuhlmann et al., 2018), which learn totally different discriminative hyperplanes. Therefore, these patient-specific models with good performance might obtain undesired results in real life, although they are significant to personalized medicine. It is obvious that how to develop a predictor that is universal to various patients is the key problem. However, this issue remains unsolved and thus the previous models are not yet in widespread use.

This work attempts to develop a seizure prediction model without the precondition of patient specificity. However, since the underlying patterns and dynamics of epilepsy are not well-understood in neuroscience, the complete desertion of the "target" samples (data of the patient to be tested) is impossible. The training set in existing studies is composed of the "target" data entirely. We attempt to reduce the reliance on the "target" data as much as possible until it reaches a clinically acceptable amount of EEG recordings. To be specific, due to the risk of infection in invasive surgery and the right of privacy, the training set in real life mainly consist of signals of previous patients. And only a small amount of "target" samples can be used for training. We try to simulate this sampling situation to train and test our model.

To achieve a higher generalizationa ability, this study introduces the strategy of domain adaptation (DA) methods for seizure prediction. It is a machine learning technique that can reduce the domain gap. In some successful DA models like maximum mean discrepancy-adversarial autoencoders (MMD-AAE) (Li et al., 2018) and cone manifold domain adaptation (CMDA) (Yair et al., 2019), to minimize the inter-domain distance in a high-dimensional space is the major optimization objective. Inspired by these researches, we hope to develop a generic seizure prediction model based on minimizing the inter-domain distance. To encode the raw EEG data into a high-dimensional space, we design a novel autoencoder using the short-time Fourier transform (STFT) (Cordes et al., 2021) and the MMD-AAE. The main contributions of this study are summarized as follow

- A general seizure prediction model for different patients is proposed based on the MMD-AAE model and STFT technique. It is tested under simulated clinical sampling conditions, making it feasible in practice.
- A domain adaptation framework is developed based on inter-domain distance. This algorithm can improve the generalization ability since it minimizes the domain gap between different patients.
- It is the first study to provide a comparison results of different domain adaptation algorithms on seizure forecast, which is important to follow-up researches.

Based on the MMD-AAE model and STFT technique, the proposed method obtains an above-par generalization ability. Experiments on two open datasets, the Freiburg Hospital EEG database and the CHB-MIT EEG database (Goldberger et al., 2000; Zhou et al., 2018), are conducted for model assessment. Compared with other methods, experimental results indicate that the proposed model achieves high robustness while preserving a decent precision.

2. DATA ACQUISITION AND PREPROCESSING

2.1. Patients

Two open EEG databases, the Freiburg Hospital intracranial EEG database (Zhou et al., 2018) and the CHB-MIT scalp EEG database (Goldberger et al., 2000), are selected to assess the model performance of our method.

The Freiburg Hospital database includes time series of 87 seizures of 21 subjects with medically intractable focal epilepsy, aged from 10 to 50 years old (8 males and 13 females). EEG signals are recorded invasively by 6 electrodes (3 near the epileptic focus and 3 away from the epileptogenic zone). The sampling rate is 256 Hz for all patients(data of Patient No.12 are sampled at 512 Hz but are down-sampled to 256 Hz).

The CHB-MIT database consists of scalp EEG sequences of 22 epileptic subjects, including 5 males aged from 3 to 22 years and 17 females aged from 1.5 to 19 years. The EEG signals are recorded at a 256 Hz sampling rate using 16-bit analog-to-digital converters. Most samples are collected from 23 channel surface electrodes following the 10-20 standard system for electrode placement (Rojas et al., 2018). Each individual has a subfolder that has 9 to 42 recordings.

2.2. Data Selection and Labeling

We use the power line noise removal to denoise the raw EEG recordings. In the intracranial EEG test set, the frequency bands of 47–53 and 97–103 Hz are deserted and in the scalp EEG test set, the frequency bands of 57–63 and 117–123 are discarded. This is because that the noise of the Freiburg database usually occurs at 50 Hz and noise of the CHB-MIT database occurs at 60 Hz. In addition, we perform a patient selection. Only patients who had at least 2 seizures but fewer than 15 per day are chosen, since less than 2 seizures would not be sufficient to support training, and more than 15 would render the prediction meaningless. The subjects chosen in this work are presented in **Tables 1**, **2**.

The seizure occurrence period (SPO) is set to 0. Only the seizure prediction horizon (SPH) is considered in this study. Thirty minutes before seizure occurrence is set as the SPH. This parameter is given by empirical evidence of comparison experiments applying multiple preictal lengths. If a seizure occurs within 30 min, the forecast model then returns a positive. The raw EEG recordings are split into continuous, non-overlapping segments over a 5-s time window. The sample number for each case is sufficient (> 38,400) to support training. In addition, to obtain equal amounts of preictal and interictal samples, a random subsample on the interictal data is implemented, which circumvents the imbalance of different kinds of training samples.

3. METHODS

To reduce the impact of inter-individual variability, we propose a generic seizure prediction model. The core idea of our method is to minimize the domain distance between different subjects in the high-dimensional space. Such that domain-invariant features can be extracted during domain distribution alignment. The maximum mean discrepancy (MMD) measure (Zhang

TABLE 1 | Details of the Freiburg Hospital test set.

Patient	Gender	Age	Seizure type	No. of seizures
Pt 1	F	15	SP	4
Pt 2	M	38	SP, CP, GTC	3
Pt 3	M	14	SP, CP	5
Pt 4	F	26	SP, CP, GTC	5
Pt 5	F	16	SP, CP, GTC	5
Pt 6	F	31	CP, GTC	3
Pt 8	F	32	SP, CP	2
Pt 9	M	44	CP, GTC	4
Pt 10	M	47	SP, CP, GTC	5
Pt 11	F	10	SP, CP, GTC	4
Pt 12	F	42	SP, CP, GTC	3
Pt 13	F	22	SP, CP, GTC	2
Pt 14	F	41	CP, GTC	4
Pt 15	M	31	SP, CP, GTC	4
Pt 16	F	50	SP, CP, GTC	5
Pt 17	M	28	SP, CP, GTC	5
Pt 18	F	25	SP, CP	5
Pt 19	F	28	SP, CP, GTC	4
Pt 20	M	33	SP, CP, GTC	5
Pt 21	M	13	SP, CP	5

F, Female; M, Male; SP, simple partial; CP, complex partial; GTC, generalized tonic-clonic.

TABLE 2 | Details of the CHB-MIT test set.

Patient	Gender	Age	Seizure type	No. of seizures
Pt 1	F	11	SP, CP	7
Pt 2	M	11	SP, CP, GTC	3
Pt 3	F	14	SP, CP	6
Pt 5	F	7	CP, GTC	5
Pt 6	F	2	CP, GTC	4
Pt 7	F	15	SP, CP, GTC	3
Pt 8	M	4	SP, CP, GTC	5
Pt 9	F	10	CP, GTC	4
Pt 10	M	3	SP, CP, GTC	6
Pt 13	F	3	SP, CP, GTC	5
Pt 14	F	9	CP, GTC	5
Pt 17	F	12	SP, CP, GTC	3
Pt 18	F	18	SP, CP	6
Pt 19	F	19	SP, CP, GTC	3
Pt 20	F	6	SP, CP, GTC	5
Pt 21	F	13	SP, CP	4

F, Female; M, Male; SP, simple partial; CP, complex partial; GTC, generalized tonic-clonic.

et al., 2020) is selected as the distance measure and the high-dimensional space is established by the adversarial autoencoders (AAE) (Makhzani et al., 2015).

3.1. Clinical Situation Simulation

The training set of conventional studies is not consistent with the sampling situation in real life. During clinical treatment, it is almost impossible to record a large number of EEG samples from a specific patient over a long period of time. Thus the traditional patient-specific learning strategy can not be performed because the data size is unable to support training. To tackle this issue, we propose a novel predictor that can use other patients' data for training.

To mimic the sampling situation in the clinic, we adopt a particular training and testing strategy, which is illustrated in **Figure 3**. To be specific, the training and validation set includes previous patient' data and one seizure from the "target" subject, while the remaining seizures of the "target" subject served as the test set. This strategy refers to the idea of the Leave-one-out cross-validation (LOOCV) approach (Peng et al., 2018). Moreover, the training and validation set are partitioned into 5-folds, and 80% of the data are assigned to the training set while the remaining 20% are assigned to the validation set to prevent overfitting.

3.2. Modal Transformation With STFT

Due to the low signal-to-noise ratio (SNR) of EEG recordings, we attempt to transform the input information from time domain into time-frequency domain. Two preprocessing techniques, wavelet and Fourier transforms (Muralidharan et al., 2011; Zhao et al., 2019), are commonly employed to convert EEG segments into image shapes. Here we adopt the short-time Fourier transform (STFT) to produce feature maps from raw EEG sequences. The conversion transforms the EEG time series into matrices, which can meet the input requirement of the two-dimensional MMD-AAE. This procedure can also extract the significant features for seizure prediction.

In the STFT module, the time-varying EEG fragment is converted to a two-dimensional matrix composed of frequency and time axes. Such that an insight in the time-evolution for each time window can be observed by the two-dimensional map. Suppose that there exist K domains (patient) in total. The input data from the K domains are denoted by $\bar{\boldsymbol{X}} = [\bar{\boldsymbol{x}}^{(1)}, \cdots, \bar{\boldsymbol{x}}^{(K)}]^T \in \mathbb{R}^{K\times d}$, where $\bar{\boldsymbol{x}} \in \mathbb{R}^{d\times 1}$. For an arbitrary domain, the segment with the time index t is given as $\bar{\boldsymbol{x}}(t)$. By performing the STFT procedure, we get the time-frequency feature map of $\bar{\boldsymbol{x}}(t)$, which is presented as:

$$\boldsymbol{x}(\omega, u) = \sum_t \bar{\boldsymbol{x}}(t) g(t-u) e^{j\omega t}, \tag{1}$$

where ω is the selected frequency band, $g(t-u)$ is the window function. For K domains, the STFT is implemented to each subject, and then the inputs are converts to $\boldsymbol{X} = [\boldsymbol{x}^{(1)}, \cdots, \boldsymbol{x}^{(K)}]^T \in \mathbb{R}^{K\times d}$. The samples of each case are represented by spectrograms. These time-frequency feature maps are then sent to the AAE for invariant feature extraction.

3.3. Construction of High-Dimensional Space

This module attempts to establish a high-dimensional space with an encoder and a decoder. The model is illustrated in **Figure 4**. By using an encoder, we can map the time-frequency images of raw EEG samples into an embedding subspace. And by using a decoder, these hidden layers are then mapped back

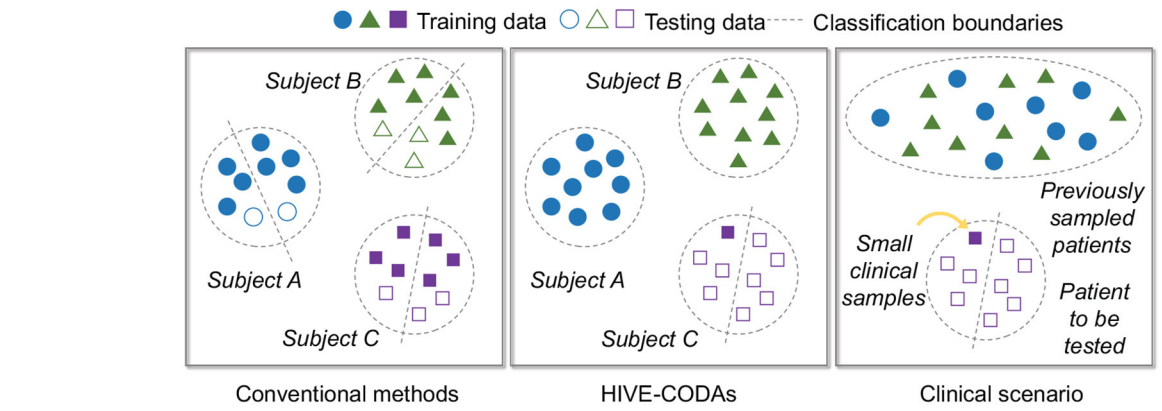

FIGURE 3 | Illustration of clinical situation simulation.

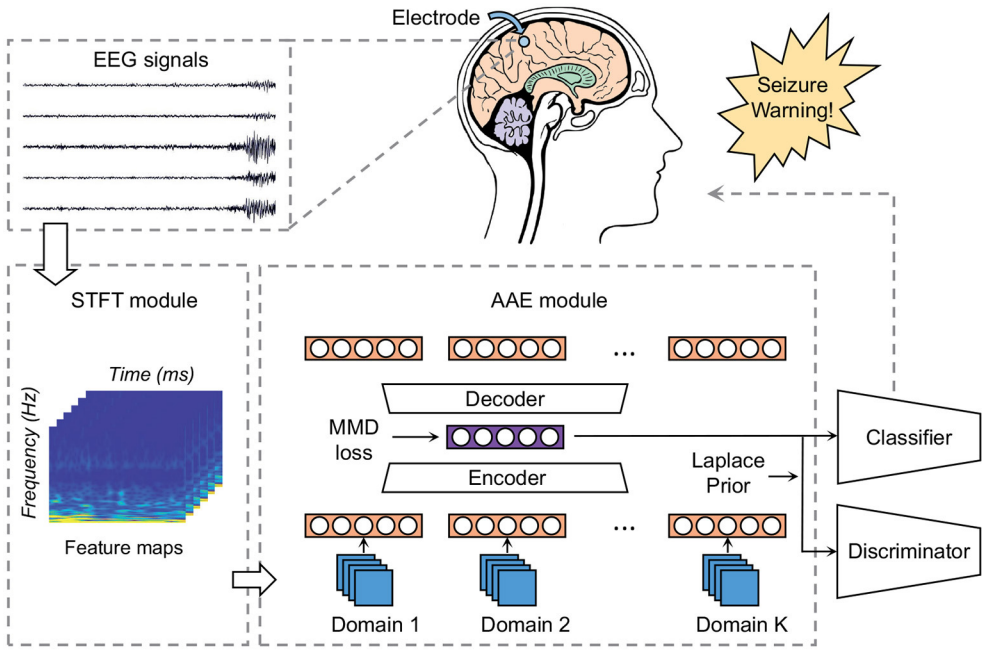

FIGURE 4 | Block diagram of our model: the STFT module converts raw EEG recordings into time-frequency images to meet the input requirement of the AAE module. The AAE module maps each domain's data into a high-dimensional space. MMD loss is employed as the measure to align distributions of different domains. The Laplace prior is exploited to optimize the hidden code z using adversarial learning.

to a "fake" input matrix. The hidden space is high-dimensional and therefore contains more information. The MMD measure is then utilized to align the distributions of high-dimensional feature vectors between different domains. Thus the optimized hidden code contains sharable information of various patients. We then extract these latent characteristics that are universal among patients for classification.

There are two procedures during the construction of embedding space: the reconstruction process and the distribution alignment process. In the reconstruction process, the autoencoder attempts to recover the time-frequency image from the high-dimensional vectors. The architecture of the autoencoder refers to the structure in MMD-AAE (Li et al., 2018). We set an optimization objective $\mathcal{L}_{rec}$ to guide the generated feature map $\tilde{\boldsymbol{x}}$ to match the input map $\boldsymbol{x}$. The loss function of the reconstruction procedure $\mathcal{L}_{rec}$ is defined as:

$$\mathcal{L}_{rec} = \left\| \tilde{\boldsymbol{x}} - \boldsymbol{x} \right\|_2^2. \tag{2}$$

Now, we specify the form of the inter-domain distance metric. The maximum mean discrepancy (MMD) measure (Jia et al., 2017) is exploited to align the distributions of different domains. Like the reconstruction process, we

also give a MMD-based regularization term to optimize the hyperparameters in the neural network (Li et al., 2018). Suppose that $\boldsymbol{Z} = [\boldsymbol{z}^{(1)}, \cdots, \boldsymbol{z}^{(K)}]^T \in \mathbb{R}^{K \times l}$ represents the learned high-dimensional features of K domains, where $\boldsymbol{z} \in \mathbb{R}^{l \times 1}$. For two arbitrary hidden vector $\boldsymbol{z}^{(i)}$ and $\boldsymbol{z}^{(j)}$, we assume that they belong to two unseen probability distribution $\mathbb{P}^{(i)}$ and $\mathbb{P}^{(j)}$, respectively. By adopting the kernel embedding technique (Smola et al., 2007), the instance is mapped to a reproducing kernel Hilbert space (RKHS) $\mathcal{H}$. The corresponding mean value in RKHS is given as:

$$\mu(\mathbb{P}) = \mathbb{E}_{\boldsymbol{z} \sim \mathbb{P}}[h(\boldsymbol{z}, \cdot)], \tag{3}$$

where is $\mu(\cdot)$ the mean map operation. $h(\boldsymbol{z}, \cdot)$ is the kernel function induced by the feature map in $\mathcal{H}$. In this work, we adopt the RBF kernel following the MMD-AAE model (Li et al., 2018). The inter-domain distance between the latent codes $\boldsymbol{z}^{(i)}$ and $\boldsymbol{z}^{(j)}$ can be described as:

$$dis(\boldsymbol{z}^{(i)}, \boldsymbol{z}^{(j)}) = \left\| \mu_{\mathbb{P}^{(i)}} - \mu_{\mathbb{P}^{(j)}} \right\|_{\mathcal{H}}. \tag{4}$$

Then, it is obvious that the regularization item of the entire latent space can be defined as:

$$\mathcal{R}_{dis}(\boldsymbol{z}^{(1)}, \cdots, \boldsymbol{z}^{(K)}) = \frac{1}{K^2} \sum_{1 \le i,j \le K} dis(\boldsymbol{z}^{(i)}, \boldsymbol{z}^{(j)}). \tag{5}$$

With the distance error above, the extracted high-dimensional features can generalize well across all the domains, since the neural network learns their common code by aligning their distributions.

3.4. Optimization Using Adversarial Learning

To further optimize the learned features in section 3.3, we introduce an adversarial learning-based module according to AAE (Makhzani et al., 2015). Adversarial learning is an emerging machine learning approach in recent years, which has been successfully applied in the area of epileptic EEG signal processing. It usually contains a generator network G with parameters Θ_G and a discriminator network D with parameters Θ_D. The generator network G will produce some fake version of the inputs. These fake data are sent to the discriminator network D together with the real input data. Then the discriminator network D will tell whether the input sample is artificially generated. During the training procedure, the neural network finds a Nash equilibrium between the generator and the discriminator, and the fake data are gradually approaching the real one. This "zero-sum game" can be described as:

$$\min_G \max_D \mathbb{E}_{\boldsymbol{x}_r \sim p_r} \left[\log D_{\Theta_D}(\boldsymbol{x}_r) \right] - \mathbb{E}_{\boldsymbol{x}_f \sim p_f} \left[\log D_{\Theta_D}(\boldsymbol{x}_f) \right], \tag{6}$$

where $\boldsymbol{x}_r$ and p_r are the real data and the corresponding distribution, $\boldsymbol{x}_f$ and p_f are the fake version. After the optimization with the loss $\mathcal{J}_{gan}$, the adversarial subnetwork can align p_f to the constant prior p_r.

We hope to utilize the aforementioned principle in the embedding space. Therefore, we assume that the "true" universal features among different patients comes from an arbitrary prior distribution $p(\boldsymbol{z})$. The adversarial module draws samples from the prior distribution $p(\boldsymbol{z})$ and considers these samples as the real data $\boldsymbol{z}_r$. Accordingly, the learned latent information $\boldsymbol{z}$ is considered as the fake data $\boldsymbol{z}_f$, where the autoencoder represents the generator G. A discriminator D is also implemented in the adversarial module, which distinguishes the produced vector $\boldsymbol{z}$ from the samples of the prior. In this study, the prior distribution is selected as the Laplace distribution $\boldsymbol{z} \sim Laplace(\eta)$, where η denotes the hyperparameter.

The training strategy of the adversarial module is a variational inference process. To be specific, first, the latent coding space has been established by the encoder explicitly. Then the distributions among different domains are aligned with the MMD regularization item to extract the domain-invariant feature vectors. These features are guided to approach a prior distribution $p(\boldsymbol{z})$. To match the hidden code with an arbitrary distribution can effectively alleviate the overfitting to a certain patient. After the optimization process, the aggregated posterior distribution $q(\boldsymbol{z})$ of the hidden layer is as follows:

$$q(\boldsymbol{z}) = \int_{\boldsymbol{x}} q(\boldsymbol{z} \mid \boldsymbol{x}) p_d(\boldsymbol{x}) \, d\boldsymbol{x}, \tag{7}$$

where $q(\boldsymbol{z} \mid \boldsymbol{x})$ is the encoding function of the autoencoder, $p_d(\boldsymbol{x})$ is the marginal distribution of data. During the training phase, the probabilistic autoencoder is regularized with an adversarial loss function $\mathcal{J}_{adv}$, which is described as:

$$\begin{aligned} \mathcal{J}_{adv} = {} & \mathbb{E}_{\boldsymbol{z} \sim p(\boldsymbol{z})} \left[\log D(\boldsymbol{z}) \right] \\ & + \mathbb{E}_{\boldsymbol{x} \sim p_d} \left[\log \left(1 - D(G(\boldsymbol{x})) \right) \right]. \end{aligned} \tag{8}$$

After training, a generative model is defined by imposing the prior $p(\boldsymbol{z})$ on the data distribution. A one-hot encoding vector $\boldsymbol{y}$ is used for supervised learning (Kumar et al., 2018; Saito et al., 2020). Then we use the learned domain-invariant features for seizure prediction. An SVM classifier is introduced to analyze the extracted features. The loss function of the classification procedure is denoted by $\mathcal{L}_{cla}$. The objective function of the entire model can be defined as:

$$\min_{G,C} \max_D \mathcal{L}_{cla} + \lambda_0 \mathcal{L}_{rec} + \lambda_1 \mathcal{J}_{adv} + \lambda_2 \mathcal{R}_{dis}, \tag{9}$$

where λ_0, λ_1 and λ_2 represent the trade-off positive parameters, and C is the classifier. Our model is optimized jointly with these modules. In general, the MMD-based regularization term is designed to align the distributions among different patients. The AAE architecture is used to construct the latent feature space. The adversarial module is developed to match the hidden code with a prior distribution. Thus this model can circumvent the overfitting to a certain patient.

4. RESULTS AND DISCUSSION

In this section, comparison experiments are conducted to verify the generalization ability and evaluate the forecast precision. Our model is tested on both intracranial and scalp EEG signals.

TABLE 3 | Results compared with conventional methods on the Freiburg Hospital database.

Source	Target	FT-CNN		PLV		SBP		Wav-CNN		Our model	
		S_n	FPR (/h)	S_n	FPR (/h)	S_n	FPR (/h)	S_n	FPR (/h)	S_n	FPR (/h)
S.C.	Pt 1	0.64	0.21	0.66	0.20	0.69	0.19	0.70	0.17	0.79	0.16
S.C.	Pt 2	0.63	0.3	0.65	0.28	0.66	0.26	0.67	0.24	0.82	0.12
S.C.	Pt 3	0.58	0.24	0.59	0.23	0.62	0.22	0.64	0.22	0.74	0.20
S.C.	Pt 4	0.64	0.25	0.65	0.24	0.66	0.22	0.69	0.20	0.83	0.16
S.C.	Pt 5	0.56	0.4	0.58	0.39	0.59	0.38	0.60	0.38	0.57	0.30
S.C.	Pt 6	0.64	0.27	0.64	0.26	0.67	0.26	0.69	0.26	0.73	0.18
S.C.*	Pt 8	0.54	0.33	0.55	0.33	0.57	0.32	0.57	0.31	0.68	0.29
S.C.	Pt 9	0.70	0.18	0.72	0.17	0.75	0.15	0.77	0.13	0.77	0.19
S.C.	Pt 10	0.52	0.34	0.53	0.33	0.55	0.32	0.58	0.30	0.81	0.16
S.C.	Pt 11	0.50	0.32	0.5	0.30	0.52	0.29	0.52	0.28	0.68	0.29
S.C.	Pt 12	0.72	0.15	0.74	0.13	0.75	0.12	0.77	0.13	0.82	0.09
S.C.*	Pt 13	0.55	0.27	0.56	0.25	0.59	0.24	0.60	0.23	0.66	0.29
S.C.	Pt 14	0.56	0.46	0.57	0.46	0.58	0.44	0.60	0.43	0.75	0.22
S.C.	Pt 15	0.66	0.17	0.66	0.16	0.69	0.15	0.69	0.13	0.83	0.12
S.C.	Pt 16	0.59	0.33	0.6	0.32	0.63	0.31	0.65	0.30	0.85	0.12
S.C.	Pt 17	0.59	0.34	0.62	0.33	0.63	0.31	0.65	0.30	0.77	0.21
S.C.	Pt 18	0.76	0.14	0.78	0.13	0.80	0.11	0.83	0.12	0.84	0.09
S.C.	Pt 19	0.48	0.29	0.48	0.28	0.48	0.27	0.5	0.26	0.73	0.23
S.C.	Pt 20	0.45	0.33	0.47	0.33	0.48	0.33	0.51	0.32	0.82	0.15
S.C.	Pt 21	0.60	0.28	0.62	0.27	0.62	0.25	0.65	0.24	0.66	0.31
Avg.		0.59	0.28	0.61	0.27	0.63	0.26	0.64	0.25	0.76	0.19

S.C., simulated clinical samples; S_n, sensitivity; FPR, false prediction rate; Avg., average result. S.C. uses NO samples of the predictor user.*

TABLE 4 | Results compared with conventional methods on the CHB-MIT database.

Source	Target	FT-CNN		PLV		SBP		Wav-CNN		Our model	
		S_n	FPR (/h)	S_n	FPR (/h)	S_n	FPR (/h)	S_n	FPR (/h)	S_n	FPR (/h)
S.C.	Pt 1	0.52	0.33	0.54	0.31	0.55	0.31	0.56	0.31	0.77	0.25
S.C.	Pt 2	0.46	0.37	0.47	0.37	0.48	0.34	0.49	0.32	0.56	0.32
S.C.	Pt 3	0.59	0.30	0.60	0.30	0.63	0.29	0.63	0.28	0.70	0.24
S.C.	Pt 5	0.48	0.39	0.48	0.37	0.49	0.35	0.51	0.34	0.74	0.23
S.C.	Pt 6	0.64	0.3	0.66	0.29	0.68	0.28	0.70	0.28	0.79	0.27
S.C.	Pt 7	0.53	0.21	0.56	0.21	0.56	0.29	0.57	0.26	0.71	0.15
S.C.	Pt 8	0.58	0.26	0.60	0.25	0.61	0.24	0.63	0.23	0.82	0.22
S.C.	Pt 9	0.51	0.34	0.54	0.33	0.55	0.33	0.56	0.32	0.78	0.20
S.C.	Pt 10	0.5	0.31	0.51	0.29	0.53	0.28	0.54	0.26	0.72	0.24
S.C.	Pt 13	0.46	0.21	0.47	0.20	0.50	0.28	0.50	0.27	0.54	0.37
S.C.	Pt 14	0.46	0.38	0.48	0.38	0.49	0.36	0.50	0.34	0.80	0.14
S.C.	Pt 17	0.42	0.37	0.43	0.35	0.44	0.35	0.44	0.35	0.75	0.3
S.C.	Pt 18	0.49	0.29	0.52	0.29	0.53	0.27	0.54	0.25	0.70	0.22
S.C.	Pt 19	0.56	0.28	0.58	0.27	0.60	0.25	0.63	0.23	0.73	0.19
S.C.	Pt 20	0.57	0.24	0.59	0.22	0.60	0.2	0.62	0.28	0.82	0.16
S.C.	Pt 21	0.63	0.25	0.66	0.24	0.67	0.22	0.70	0.20	0.68	0.28
Avg.		0.51	0.30	0.54	0.29	0.56	0.29	0.57	0.28	0.73	0.24

S.C., simulated clinical samples; S_n, sensitivity; FPR, false prediction rate; Avg., average result.

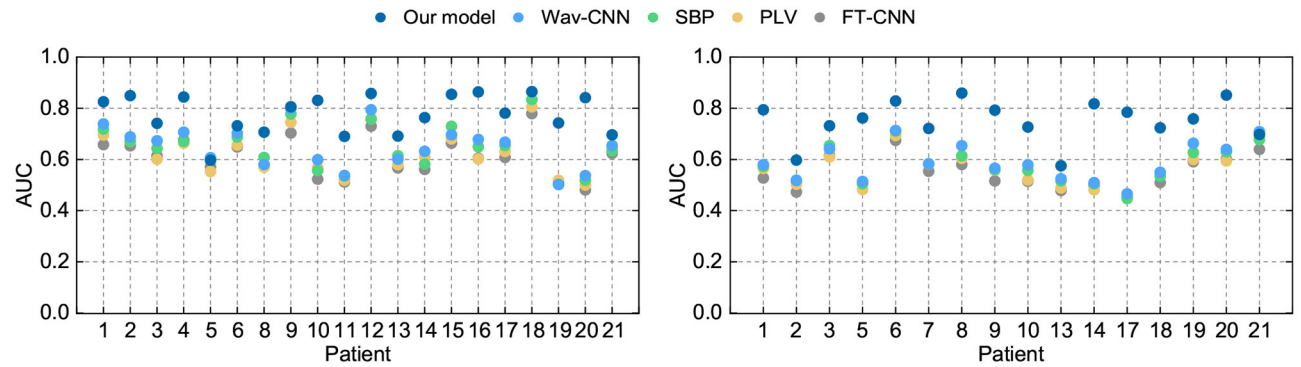

FIGURE 5 | AUC of different seizure prediction models on the Freiburg Hospital test set **(left)** and the CHB-MIT test set **(right)**.

Three commonly-used indicators about model performance are exploited in experiments: sensitivity, false alarm rate per hour (FPR), and area under the receiver operating characteristic curve (AUC). Noted that each EEG fragment represents an event so that the event-based indicators are used for evaluation (Temko et al., 2011).

4.1. Comparison With Conventional Methods

To demonstrate the advantages over conventional methods, we select four seizure prediction researches for comparison: FT-CNN (Truong et al., 2018), phase locking value (PLV) (Cho et al., 2016), spectral band power (SBP) (Ozcan and Erturk, 2019), and Wav-CNN (Khan et al., 2017). All these approaches have obtained good model performance when the training and testing processes are performed on the same subject. But data from previous cases are not used in their training phases. Here we train these models with EEG samples from multiple patients and test them with the "unseen" patient's data. The sensitivity and FPR are provided in **Tables 3**, **4**. The AUC value for each patient is illustrated in **Figure 5**.

The widely-used Freiburg Hospital database is employed in this work to evaluate our model on the intracranial EEG. **Table 3** illustrates that our model outperforms all the other conventional methods in a clear margin. It is reasonable since the prior studies adopt the patient-specific strategy and consider little about the domain adaptability. Conversely, our method exhibits obvious advantages in terms of generalization ability, which achieves a sensitivity of 76% and an FPR of 0.19/h on average. Although these results do not achieve the high accuracy of tests under the patient-specific conditions, such precision can still meet the daily needs of patients with epilepsy because they are similar to the warning frequency in the first-in-man trial (Cook et al., 2013).

Still, the simulated clinical sampling situation is "harsh" for the forecast task. It can be observed that the performances of all these models are not desired. Moreover, on several outliers like Pt 5, 11, and 21, the performance degradation is particularly noticeable. It might be caused by a more complex internal mode in the high-dimensional space. Note that even on these outliers, the sensitivity of our model is slightly higher than other methods, which demonstrates that our approach achieves better robustness.

As for the scalp EEG recordings, we test these methods using the public CHB-MIT database, produced by the Massachusetts Institute of Technology. As shown in **Table 4**, our algorithm achieves a sensitivity of 73% and an FPR of 0.24/h on average. The results of our model show a significant improvement compared with the conventional methods, which is consistent with the results on intracranial EEG. However, all the model performances drop to a varying degree compared with the precisions on the Freiburg test set. It might be caused by the low spatial resolution of the scalp EEG signals for they are more susceptible to being contaminated by noises (Ramantani et al., 2016; Usman et al., 2019). In other words, intracranial EEG recordings have the higher SNR and the artifacts are typically seen in scalp EEG.

There are also some outliers in the tests on the scalp EEG signal. On Pt 2, 13, and 21, all these models obtain a subpar performance. Larger domain gaps might exist in the sample space of these outliers, which makes the hyperplane difficult to capture. Even on these outliers, the precision of our model is slightly higher than the lower bound of a random binary classifier. It gives us confidence in applying DA techniques to epileptic seizure prediction.

4.2. Comparison With DA Methods

We further compare our model with domain adaptation (DA) methods in the existing literature. However, few applications regarding DA approaches have been reported in the area of epileptic seizure prediction. Thus we have to employ DA methods from other fields. The maximum independence domain adaptation (MIDA) (Yan et al., 2017), model-agnostic learning of semantic features (MASF), conditional deep convolutional generative adversarial networks (C-DCGANs) (Zhang et al., 2021) and subject-invariant domain adaption (SIDA) (Rayatdoost et al., 2021) are introduced to verify the advantage of our model. The sensitivity and FPR are provided in **Tables 5**, **6**. The AUC value for each patient is illustrated in **Figure 6**.

TABLE 5 | Results compared with DA methods on the Freiburg Hospital database.

Source	Target	MIDA		MASF		C-DCGANs		SIDA		Our model	
		S_n	FPR (/h)	S_n	FPR (/h)	S_n	FPR (/h)	S_n	FPR (/h)	S_n	FPR (/h)
S.C.	Pt 1	0.57	0.22	0.62	0.21	0.78	0.19	0.83	0.18	0.79	0.16
S.C.	Pt 2	0.56	0.28	0.60	0.26	0.73	0.26	0.82	0.25	0.82	0.12
S.C.	Pt 3	0.52	0.23	0.62	0.22	0.77	0.22	0.78	0.20	0.74	0.2
S.C.	Pt 4	0.49	0.23	0.60	0.23	0.61	0.21	0.62	0.20	0.83	0.16
S.C.	Pt 5	0.57	0.37	0.53	0.35	0.78	0.35	0.79	0.33	0.57	0.30
S.C.	Pt 6	0.53	0.23	0.60	0.23	0.63	0.23	0.70	0.23	0.73	0.18
S.C.*	Pt 8	0.45	0.33	0.51	0.33	0.53	0.33	0.55	0.30	0.68	0.29
S.C.	Pt 9	0.49	0.37	0.51	0.36	0.68	0.26	0.70	0.24	0.77	0.19
S.C.	Pt 10	0.52	0.33	0.54	0.32	0.62	0.32	0.64	0.31	0.81	0.16
S.C.	Pt 11	0.59	0.33	0.57	0.32	0.67	0.30	0.79	0.31	0.68	0.29
S.C.	Pt 12	0.59	0.36	0.63	0.34	0.73	0.24	0.75	0.22	0.82	0.09
S.C.*	Pt 13	0.45	0.29	0.56	0.29	0.69	0.27	0.69	0.26	0.66	0.29
S.C.	Pt 14	0.45	0.46	0.52	0.45	0.65	0.44	0.60	0.44	0.75	0.22
S.C.	Pt 15	0.56	0.16	0.67	0.16	0.52	0.36	0.74	0.16	0.83	0.12
S.C.	Pt 16	0.44	0.35	0.48	0.33	0.76	0.33	0.64	0.31	0.85	0.12
S.C.	Pt 17	0.44	0.36	0.47	0.35	0.53	0.32	0.52	0.32	0.77	0.21
S.C.	Pt 18	0.58	0.36	0.61	0.35	0.77	0.22	0.77	0.21	0.84	0.09
S.C.	Pt 19	0.45	0.29	0.47	0.28	0.53	0.27	0.58	0.26	0.73	0.23
S.C.	Pt 20	0.47	0.34	0.53	0.34	0.62	0.31	0.66	0.31	0.82	0.15
S.C.	Pt 21	0.52	0.30	0.54	0.29	0.52	0.27	0.66	0.26	0.66	0.31
Avg.		0.51	0.31	0.56	0.30	0.66	0.29	0.69	0.27	0.76	0.19

S.C., simulated clinical samples; S_n, sensitivity; FPR, false prediction rate; Avg., average result. S.C. uses NO samples of the predictor user.*

TABLE 6 | Results compared with DA methods on the CHB-MIT database.

Source	Target	MIDA		MASF		C-DCGANs		SIDA		Our model	
		S_n	FPR (/h)	S_n	FPR (/h)	S_n	FPR (/h)	S_n	FPR (/h)	S_n	FPR (/h)
S.C.	Pt 1	0.55	0.34	0.61	0.33	0.74	0.30	0.74	0.28	0.77	0.25
S.C.	Pt 2	0.43	0.38	0.49	0.38	0.66	0.37	0.64	0.35	0.56	0.32
S.C.	Pt 3	0.51	0.28	0.50	0.27	0.65	0.25	0.67	0.24	0.70	0.24
S.C.	Pt 5	0.48	0.42	0.51	0.40	0.69	0.37	0.69	0.36	0.74	0.23
S.C.	Pt 6	0.46	0.29	0.52	0.27	0.72	0.27	0.72	0.25	0.79	0.27
S.C.	Pt 7	0.54	0.25	0.56	0.24	0.73	0.21	0.73	0.19	0.71	0.15
S.C.	Pt 8	0.48	0.27	0.60	0.26	0.67	0.25	0.66	0.24	0.82	0.22
S.C.	Pt 9	0.46	0.31	0.51	0.29	0.58	0.27	0.57	0.25	0.78	0.20
S.C.	Pt 10	0.45	0.28	0.46	0.27	0.52	0.25	0.52	0.24	0.72	0.24
S.C.	Pt 13	0.48	0.21	0.51	0.39	0.61	0.38	0.62	0.26	0.54	0.37
S.C.	Pt 14	0.47	0.39	0.48	0.39	0.64	0.36	0.65	0.35	0.80	0.14
S.C.	Pt 17	0.49	0.38	0.50	0.37	0.61	0.37	0.59	0.35	0.75	0.30
S.C.	Pt 18	0.50	0.30	0.49	0.30	0.57	0.28	0.61	0.28	0.70	0.22
S.C.	Pt 19	0.51	0.39	0.51	0.36	0.62	0.34	0.62	0.24	0.73	0.19
S.C.	Pt 20	0.53	0.25	0.55	0.23	0.70	0.23	0.66	0.21	0.82	0.16
S.C.	Pt 21	0.50	0.27	0.52	0.26	0.63	0.24	0.68	0.22	0.68	0.28
Avg.		0.49	0.31	0.52	0.31	0.65	0.30	0.65	0.27	0.73	0.24

S.C., simulated clinical samples.

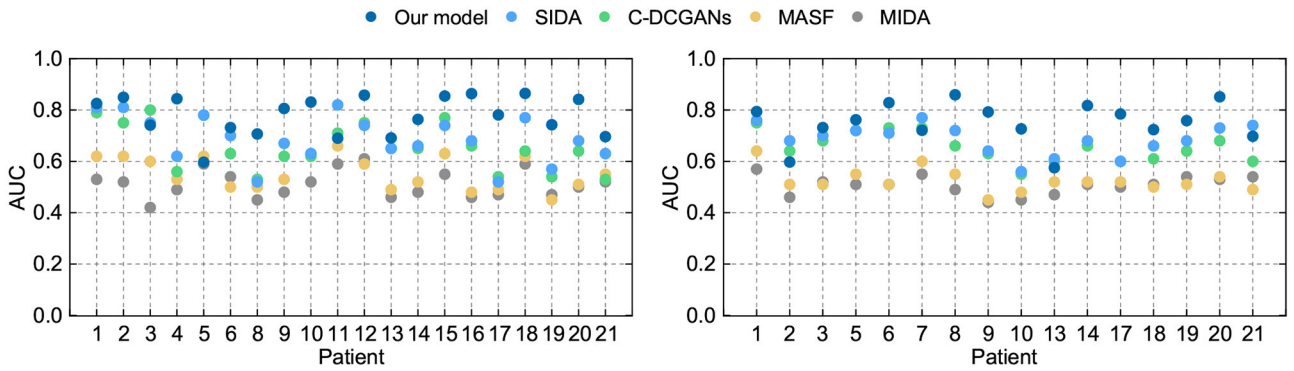

FIGURE 6 | AUC of different DA models on the Freiburg Hospital test set **(left)** and the CHB-MIT test set **(right)**.

For the intracranial EEG samples, we still exploit the Freiburg Hospital database as the test set. Evidently, compared with other DA methods, our model achieves the best performance with a sensitivity of 76% and an FPR of 0.19/h on average. Then the SIDA method exhibits a slight advantage over other methods. Comparing this model to SIDA, we see a benefit of approximately 7% is obtained. Comparing our method to C-DCGANs, we remark that a further 3% benefit is obtained. As for the MASF, a benefit of 20% is observed, for a total of 25% margin over MIDA.

In terms of the scalp EEG data, the open CHB-MIT dataset is applied in the experiment. The order of precision of these DA algorithms is consistent with the performance of the intracranial EEG data. Our model has obvious advantages over other approaches with a sensitivity of 73% and an FPR of 0.24/h on average. The high model performance of our model on both intracranial and scalp EEG testifies to the application potential on seizure forecast.

Evidently, SIDA achieves the best performance except for the proposed method. The reason for this superiority might credit the combination of CNN and generative adversarial network (GAN). SIDA is the deep neural network from the field of emotion recognition. Raw EEG data are converted to spectrum in EEG. By minimizing loss of emotion recognition and subject confusion, SIDA extracts the invariant features among different domains. We conjecture that the architecture of GAN in SIDA might have advantages in this task, which needs to be further proved.

The C-DCGANs makes a relatively larger contribution compared with other modules. An adversarial learning-based structure is also employed by C-DCGANs. It also uses the data augmentation technique, which generates EEG recordings artificially. By increasing the data diversity, C-DCGANs hopes to improve the domain shift robustness. Nevertheless, the man-made data may involve more artifacts (Fahimi et al., 2020) that contaminate EEG samples. Besides, C-DCGANs is a variation of deep learning-based frameworks. As such, it has uncertainties associated with DNN, in particular a lack of formal convergence guarantees.

Not surprisingly, the results of MASF and MIDA are not satisfactory. The core idea of MASF is to establish a model-agnostic learning paradigm using semantic features and gradient-based meta-learning. However, the discriminant hyperplane in the high-dimensional space might be too complex to be described with semantic features. MIDA reduces differences between distributions of domains by learning a subspace with background information. It is obvious that the background-specific features are not valid characteristics.

Based on the aforementioned observations, we conjecture that adversarial learning-based techniques are relatively superior for alleviating individual variability, since all the adversarial learning-based models achieve a decent model performance and generalization ability for seizure prediction. Experiments on both intracranial and scalp EEG datasets suggest that adversarial structure has potential in developing a generic seizure forecast model.

4.3. Impact on Different Components

In this section, we conduct experiments to understand the impact of different modules of the proposed model on the final forecast results. To calculate the contribution of each component quantitatively, we adjust the corresponding trade-off positive parameters and observe the variation tendency. The experiment results are listed in **Tables 7**, **8**. Here we discuss three components in this model: the reconstruction module with a loss $\mathcal{L}_{rec}$, the adversarial module with a loss $\mathcal{J}_{adv}$, and the inter-domain distance regularization term $\mathcal{R}_{dis}$.

As shown in **Tables 7**, **8**, we observe that removing the inter-domain distance regularization item, the adversarial subnetwork, or the classification component causes performance drop on both intracranial and scalp EEG databases. Such results indicate that these modules can effectively improve the model performance: (1) AAE is suitable for epileptic EEG signal processing, and the embedding space made by AAE is meaningful. (2) MMD is an appropriate distance measure to minimize the domain gaps in the seizure forecast task. (3) The reconstruction procedure can force the model to learn the significant features from the latent high-dimensional space.

TABLE 7 | Comparison results on the Freiburg Hospital database using various components.

Method	S_n	FPR (/h)	Acc	AUC
No $\mathcal{R}_{dis}$	0.60 ± 0.03	0.35 ± 0.03	0.63 ± 0.04	0.63 ± 0.03
No $\mathcal{J}_{adv}$	0.67 ± 0.03	0.31 ± 0.03	0.68 ± 0.03	0.69 ± 0.03
No $\mathcal{L}_{rec}$	0.71 ± 0.03	0.27 ± 0.03	0.72 ± 0.03	0.72 ± 0.03
Our model	0.76 ± 0.03	0.19 ± 0.03	0.78 ± 0.03	0.78 ± 0.03

S_n, sensitivity; FPR, false positive rate; Acc, accuracy.

TABLE 8 | Comparison results on the CHB-MIT database using various components.

Method	S_n	FPR (/h)	Acc	AUC
No $\mathcal{R}_{dis}$	0.57 ± 0.03	0.36 ± 0.03	0.59 ± 0.03	0.59 ± 0.03
No $\mathcal{J}_{adv}$	0.64 ± 0.04	0.33 ± 0.03	0.66 ± 0.04	0.66 ± 0.03
No $\mathcal{L}_{rec}$	0.68 ± 0.03	0.29 ± 0.03	0.69 ± 0.03	0.70 ± 0.03
Our model	0.73 ± 0.03	0.24 ± 0.03	0.75 ± 0.03	0.75 ± 0.03

S_n, sensitivity; FPR, false positive rate; Acc, accuracy.

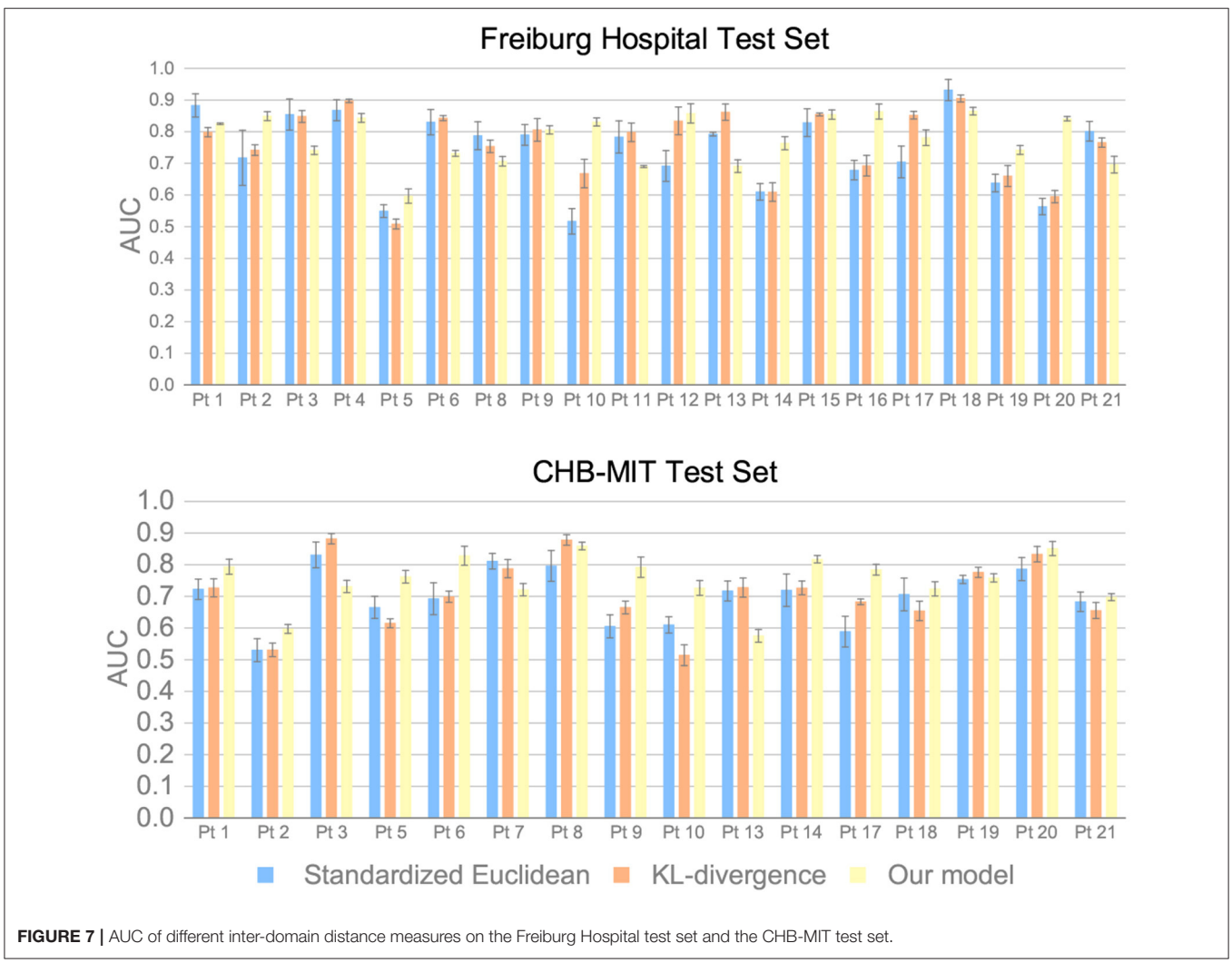

FIGURE 7 | AUC of different inter-domain distance measures on the Freiburg Hospital test set and the CHB-MIT test set.

By adjusting these trade-off items, a set of hyperparameters that are suitable for seizure prediction can be obtained. For the intracranial EEG data, the most appropriate trade-off parameters are set as $\lambda_0 = 1.05, \lambda_1 = 1.2e2, \lambda_2 = 0.7$. For the scalp EEG data, the most appropriate parameter are set as $\lambda_0 = 1, \lambda_1 = 1.1e2, \lambda_2 = 0.6$.

We also discuss the superiority of the MMD measure over other distance metrics. The standardized Euclidean distance and the KL-divergence are used for comparison. Experimental results are provided in **Figure 7**. The results suggest that the precision can increase by 3% for intracranial EEG and 4% for scalp EEG by applying the MMD measure, which demonstrates the advantage of MMD measure on the seizure prediction task.

5. CONCLUSION

This work proposes a generic seizure predictor to alleviate the impact of individual variability. By combining STFT with MMD-AAE, our model reduces the effects of epileptic domain variance and improves the generalization ability. Besides, a simulated clinical sampling scenario is used during training and testing periods, which is the first attempt to adopt this assessing strategy. Compared with the patient-specific strategy from previous researches, such a test approach is relatively challenging. Nonetheless, our method achieves high domain shift robustness and precision, which demonstrates its feasibility of real-world applications.

By analyzing the comparison results of DA methods, a conjecture about the effectiveness of adversarial learning in epileptic seizure prediction is obtained. The underlying causes of this phenomenon remain unclear because there is no definitive explanation of the dynamics of epilepsy in the existing literature. The search for more powerful DA algorithms and the underlying reasons will be considered as part of our future research.

DATA AVAILABILITY STATEMENT

The datasets presented in this study can be found in online repositories. The names of the repository/repositories and accession number(s) can be found in the article/supplementary material.

ETHICS STATEMENT

Ethical review and approval were not required for the current study in accordance with the local legislation and institutional requirements. Written informed consent was obtained from the individual(s), and minor(s)' legal guardian/next of kin, for the publication of any potentially identifiable images or data included in this article.

AUTHOR CONTRIBUTIONS

PP, LY, and HW designed the experiments. PP and HW analyzed the experimental results. All authors carried out the experiments, wrote the manuscript, contributed to the article, and approved the submitted version.

FUNDING

This work was supported in part by the National Natural Science Foundation of China (Grant Nos. 61802059 and 61773118), in part by the National Key R&D Program of China (Grant No. 2018YFB1500800), in part by the Science and Technology Project of State Grid Corporation of China, Intelligent operation and maintenance technology of distributed photovoltaic system (Grant No. SGTJDK00DYJS2000148), in part by the Natural Science Foundation of Jiangsu (Grant No. BK20180365), in part by Zhishan Young Scholar Program of Southeast University and the Fundamental Research Funds for the Central Universities (Grant No. 2242021R41118).

REFERENCES

Al Ghayab, H. R., Li, Y., Siuly, S., and Abdulla, S. (2019). A feature extraction technique based on tunable Q-factor wavelet transform for brain signal classification. *J. Neurosci. Methods* 312, 43–52. doi: 10.1016/j.jneumeth.2018.11.014

Banerjee, P. N., Filippi, D., and Hauser, W. A. (2009). The descriptive epidemiology of epilepsy–a review. *Epilepsy Res.* 85, 31–45. doi: 10.1016/j.eplepsyres.2009.03.003

Brinkmann, B. H., Wagenaar, J., Abbot, D., Adkins, P., Bosshard, S. C., Chen, M., et al. (2016). Crowdsourcing reproducible seizure forecasting in human and canine epilepsy. *Brain* 139, 1713–1722. doi: 10.1093/brain/aww045

Cho, D., Min, B., Kim, J., and Lee, B. (2016). EEG-based prediction of epileptic seizures using phase synchronization elicited from noise-assisted multivariate empirical mode decomposition. *IEEE Trans. Neural Syst. Rehabil. Eng.* 25, 1309–1318. doi: 10.1109/TNSRE.2016.2618937

Cook, M. J., O'Brien, T. J., Berkovic, S. F., Murphy, M., Morokoff, A., Fabinyi, G., et al. (2013). Prediction of seizure likelihood with a long-term, implanted seizure advisory system in patients with drug-resistant epilepsy: a first-in-man study. *Lancet Neurol.* 12, 563–571. doi: 10.1016/S1474-4422(13)70075-9

Cordes, D., Kaleem, M. F., Yang, Z., Zhuang, X., Curran, T., Sreenivasan, K. R., et al. (2021). Energy-period profiles of brain networks in group fMRI resting-state data: a comparison of empirical mode decomposition with the short-time Fourier transform and the discrete wavelet transform. *Front. Neurosci.* 15:663403. doi: 10.3389/fnins.2021.663403

Daoud, H., and Bayoumi, M. A. (2019). Efficient epileptic seizure prediction based on deep learning. *IEEE Trans. Biomed. Circ. Syst.* 13, 804–813. doi: 10.1109/TBCAS.2019.2929053

Direito, B., Teixeira, C. A., Sales, F., Castelo-Branco, M., and Dourado, A. (2017). A realistic seizure prediction study based on multiclass SVM. *Int. J. Neural Syst.* 27:1750006. doi: 10.1142/S012906571750006X

Elger, C. E., and Hoppe, C. (2018). Diagnostic challenges in epilepsy: seizure under-reporting and seizure detection. *Lancet Neurol.* 17, 279–288. doi: 10.1016/S1474-4422(18)30038-3

Fahimi, F., Dosen, S., Ang, K. K., Mrachacz-Kersting, N., and Guan, C. (2020). Generative adversarial networks-based data augmentation for brain-computer interface. *IEEE Trans. Neural Netw. Learn. Syst.* doi: 10.1109/TNNLS.2020.3016666

Fei, K., Wang, W., Yang, Q., and Tang, S. (2017). Chaos feature study in fractional Fourier domain for preictal prediction of epileptic seizure. *Neurocomputing* 249, 290–298. doi: 10.1016/j.neucom.2017.04.019

Fisher, R. S., Boas, W. V. E., Blume, W., Elger, C., Genton, P., Lee, P., et al. (2005). Epileptic seizures and epilepsy: definitions proposed by the International League Against Epilepsy (ILAE) and the International Bureau for Epilepsy (IBE). *Epilepsia* 46, 470–472. doi: 10.1111/j.0013-9580.2005.66104.x

Goldberger, A. L., Amaral, L. A., Glass, L., Hausdorff, J. M., Ivanov, P. C., Mark, R. G., et al. (2000). PhysioBank, PhysioToolkit, and PhysioNet: components of a new research resource for complex physiologic signals. *Circulation* 101, e215–e220. doi: 10.1161/01.CIR.101.23.e215

Guo, L., Wang, Z., Cabrerizo, M., and Adjouadi, M. (2017). A cross-correlated delay shift supervised learning method for spiking neurons with application to interictal spike detection in epilepsy. *Int. J. Neural Syst.* 27:1750002. doi: 10.1142/S0129065717500022

Jia, X., Zhao, M., Di, Y., Yang, Q., and Lee, J. (2017). Assessment of data suitability for machine prognosis using maximum mean discrepancy. *IEEE Trans. Indus. Electron.* 65, 5872–5881. doi: 10.1109/TIE.2017.2777383

Jirsa, V. K., Proix, T., Perdikis, D., Woodman, M. M., Wang, H., Gonzalez-Martinez, J., et al. (2017). The virtual epileptic patient: individualized whole-brain models of epilepsy spread. *Neuroimage* 145, 377–388. doi: 10.1016/j.neuroimage.2016.04.049

Karoly, P. J., Freestone, D. R., Boston, R., Grayden, D. B., Himes, D., Leyde, K., et al. (2016). Interictal spikes and epileptic seizures: their relationship and underlying rhythmicity. *Brain* 139, 1066–1078. doi: 10.1093/brain/aww019

Khan, H., Marcuse, L., Fields, M., Swann, K., and Yener, B. (2017). Focal onset seizure prediction using convolutional networks. *IEEE Trans. Biomed. Eng.* 65, 2109–2118. doi: 10.1109/TBME.2017.2785401

Kuhlmann, L., Lehnertz, K., Richardson, M. P., Schelter, B., and Zaveri, H. P. (2018). Seizure prediction-ready for a new era. *Nat. Rev. Neurol.* 14, 618–630. doi: 10.1038/s41582-018-0055-2

Kumar, A., Sattigeri, P., Wadhawan, K., Karlinsky, L., Feris, R., Freeman, W. T., et al. (2018). Co regularized alignment for unsupervised domain adaptation. *arXiv [Preprint]*.arXiv:1811.05443

Kwan, P., Schachter, S. C., and Brodie, M. J. (2011). Drug-resistant epilepsy. *N. Engl. J. Med.* 365, 919–926. doi: 10.1056/NEJMra1004418

Li, H., Pan, S. J., Wang, S., and Kot, A. C. (2018). "Domain generalization with adversarial feature learning," in *Proceedings of the IEEE Conference on Computer Vision and Pattern Recognition* (Salt Lake City, UT), 5400–5409. doi: 10.1109/CVPR.2018.00566

Li, S., Zhou, W., Yuan, Q., and Liu, Y. (2013). Seizure prediction using spike rate of intracranial EEG. *IEEE Trans. Neural Syst. Rehabil. Eng.* 21, 880–886. doi: 10.1109/TNSRE.2013.2282153

Li, Y., Yu, Z., Chen, Y., Yang, C., Li, B., Li, X. A., et al. (2020). Automatic seizure detection using fully convolutional nested LSTM. *Int. J. Neural Syst.* 30:2050019. doi: 10.1142/S0129065720500197

Lin, L.-C., Ouyang, C.-S., Chiang, C.-T., Yang, R.-C., Wu, R.-C., and Wu, H.-C. (2014). Early prediction of medication refractoriness in children with idiopathic epilepsy based on scalp EEG analysis. *Int. J. Neural Syst.* 24:1450023. doi: 10.1142/S0129065714500233

Lin, L.-C., Ouyang, C.-S., Wu, R.-C., Yang, R.-C., and Chiang, C.-T. (2020). Alternative diagnosis of epilepsy in children without epileptiform discharges using deep convolutional neural networks. *Int. J. Neural Syst.* 30:1850060. doi: 10.1142/S0129065718500600

Liu, G., Zhou, W., and Geng, M. (2020). Automatic seizure detection based on s-transform and deep convolutional neural network. *Int. J. Neural Syst.* 30:1950024. doi: 10.1142/S0129065719500242

Makhzani, A., Shlens, J., Jaitly, N., Goodfellow, I., and Frey, B. (2015). Adversarial autoen coders. *arXiv [Preprint]*. arXiv:1511.05644

Mirowski, P., Madhavan, D., LeCun, Y., and Kuzniecky, R. (2009). Classification of patterns of EEG synchronization for seizure prediction. *Clin. Neurophysiol.* 120, 1927–1940. doi: 10.1016/j.clinph.2009.09.002

Moctezuma, L. A., and Molinas, M. (2020). EEG channel-selection method for epileptic-seizure classification based on multi-objective optimization. *Front. Neurosci.* 14:593. doi: 10.3389/fnins.2020.00593

Muralidharan, A., Chae, J., and Taylor, D. (2011). Extracting attempted hand movements from EEGs in people with complete hand paralysis following stroke. *Front. Neurosci.* 5:39. doi: 10.3389/fnins.2011.00039

Myers, M. H., Padmanabha, A., Hossain, G., de Jongh Curry, A. L., and Blaha, C. D. (2016). Seizure prediction and detection via phase and amplitude lock values. *Front. Hum. Neurosci.* 10:80. doi: 10.3389/fnhum.2016.00080

Özcan, A. R., and Ertürk, S. (2017) "Epileptic seizure prediction with recurrent convolutional neural networks," in *Signal Processing and Communications Applications Conference* (Antalya), 1–4. doi: 10.1109/SIU.2017.7960594

Ozcan, A. R., and Erturk, S. (2019). Seizure prediction in scalp EEG using 3D convolutional neural networks with an image-based approach. *IEEE Trans. Neural Syst. Rehabil. Eng.* 27, 2284–2293. doi: 10.1109/TNSRE.2019.2943707

Peng, L.-H., Yin, J., Zhou, L., Liu, M.-X., and Zhao, Y. (2018). Human microbe-disease association prediction based on adaptive boosting. *Front. Microbiol.* 9:2440. doi: 10.3389/fmicb.2018.02440

Peng, P., Wei, H., Xie, L., and Song, Y. (2020). "Epileptic seizure prediction in scalp EEG using an improved HIVE-COTE model," in *Chinese Control Conference* (Shenyang: IEEE), 6450–6457. doi: 10.23919/CCC50068.2020.9188930

Peng, P., Xie, L., and Wei, H. (2021). A deep Fourier neural network for seizure prediction using convolutional neural network and ratios of spectral power. *Int. J. Neural Syst.* 31:2150022. doi: 10.1142/S0129065721500222

Ramantani, G., Maillard, L., and Koessler, L. (2016). Correlation of invasive EEG and scalp EEG. *Seizure* 41, 196–200. doi: 10.1016/j.seizure.2016.05.018

Rayatdoost, S., Yin, Y., Rudrauf, D., and Soleymani, M. (2021). "Subject-invariant EEG representation learning for emotion recognition," in *IEEE International Conference on Acoustics, Speech and Signal Processing* (Barcelona), 3955–3959. doi: 10.1109/ICASSP39728.2021.9414496

Rojas, G. M., Alvarez, C., Montoya, C. E., de la Iglesia-Vayá, M., Cisternas, J. E., and Gálvez, M. (2018). Study of resting-state functional connectivity networks using EEG electrodes position as seed. *Front. Neurosci.* 12:235. doi: 10.3389/fnins.2018.00235

Saito, K., Kim, D., Sclaroff, S., and Saenko, K. (2020). Universal Domai n Adaptation through Self Supervision. *arXiv [Preprint]*.arXiv:2002.07953

Smola, A., Gretton, A., Song, L., and Schölkopf, B. (2007). "A Hilbert space embedding for distributions," in *International Conference on Algorithmic Learning Theory* (Sendai: Springer), 13–31. doi: 10.1007/978-3-540-75225-7_5

Sun, C., Cui, H., Zhou, W., Nie, W., Wang, X., and Yuan, Q. (2019). Epileptic seizure detection with EEG textural features and imbalanced classification based on easyensemble learning. *Int. J. Neural Syst.* 29:1950021. doi: 10.1142/S0129065719500217

Temko, A., Thomas, E., Marnane, W., Lightbody, G., and Boylan, G. (2011). Performance assessment for EEG-based neonatal seizure detectors. *Clin. Neurophysiol.* 122, 474–482. doi: 10.1016/j.clinph.2010.06.035

Truong, N. D., Nguyen, A. D., Kuhlmann, L., Bonyadi, M. R., Yang, J., Ippolito, S., et al. (2018). Convolutional neural networks for seizure prediction using intracranial and scalp electroencephalogram. *Neural Netw.* 105, 104–111. doi: 10.1016/j.neunet.2018.04.018

Tsiouris, K. M., Pezoulas, V. C., Zervakis, M., Konitsiotis, S., Koutsouris, D. D., and Fotiadis, D. I. (2018). A long short-term memory deep learning network for the prediction of epileptic seizures using EEG signals. *Comput. Biol. Med.* 99, 24–37. doi: 10.1016/j.compbiomed.2018.05.019

Usman, S. M., Khalid, S., Akhtar, R., Bortolotto, Z., Bashir, Z., and Qiu, H. (2019). Using scalp EEG and intracranial EEG signals for predicting epileptic seizures: review of available methodologies. *Seizure* 71, 258–269. doi: 10.1016/j.seizure.2019.08.006

Vahabi, Z., Amirfattahi, R., Shayegh, F., and Ghassemi, F. (2015). Online epileptic seizure prediction using wavelet-based bi-phase correlation of electrical signals tomography. *Int. J. Neural Syst.* 25:1550028. doi: 10.1142/S0129065715500288

Yair, O., Ben-Chen, M., and Talmon, R. (2019). Parallel transport on the cone manifold of SPD matrices for domain adaptation. *IEEE Trans. Signal Process.* 67, 1797–1811. doi: 10.1109/TSP.2019.2894801

Yan, K., Kou, L., and Zhang, D. (2017). Learning domain-invariant subspace using domain features and independence maximization. *IEEE Trans. Cybernet.* 48, 288–299. doi: 10.1109/TCYB.2016.2633306

Zandi, A. S., Tafreshi, R., Javidan, M., and Dumont, G. A. (2013). Predicting epileptic seizures in scalp EEG based on a variational Bayesian Gaussian mixture model of zero-crossing intervals. *IEEE Trans. Biomed. Eng.* 60, 1401–1413. doi: 10.1109/TBME.2012.2237399

Zhang, T., Chen, W., and Li, M. (2018). Fuzzy distribution entropy and its application in automated seizure detection technique. *Biomed. Signal Process. Control* 39, 360–377. doi: 10.1016/j.bspc.2017.08.013

Zhang, W., Yan, F., Han, F., He, R., Li, E., Wu, Z., et al. (2021). Auto recognition of solar radio bursts using the C-DCGAN method. *Front. Phys*. 9:646556. doi: 10.3389/fphy.2021.646556

Zhang, Y., Guo, Y., Yang, P., Chen, W., and Lo, B. (2019). Epilepsy seizure prediction on EEG using common spatial pattern and convolutional neural network. *IEEE J. Biomed. Health Inform*. 24, 465–474. doi: 10.1109/JBHI.2019.2933046

Zhang, Y., Zhou, Z., Bai, H., Liu, W., and Wang, L. (2020). Seizure classification from EEG signals using an online selective transfer TSK fuzzy classifier with joint distribution adaption and manifold regularization. *Front. Neurosc*. 14:496. doi: 10.3389/fnins.2020.00496

Zhao, J., Lin, C.-M., and Chao, F. (2019). Wavelet fuzzy brain emotional learning control system design for MIMO uncertain nonlinear systems. *Front. Neurosci*. 12:918. doi: 10.3389/fnins.2018.00918

Zhou, M., Tian, C., Cao, R., Wang, B., Niu, Y., Hu, T., et al. (2018). Epileptic seizure detection based on EEG signals and CNN. *Front. Neuroinform*. 12:95. doi: 10.3389/fninf.2018.00095

Conflict of Interest: The authors declare that the research was conducted in the absence of any commercial or financial relationships that could be construed as a potential conflict of interest.

frontiers in Neuroscience

ORIGINAL RESEARCH
published: 24 February 2022
doi: 10.3389/fnins.2022.831533

BMNet: A New Region-Based Metric Learning Method for Early Alzheimer's Disease Identification With FDG-PET Images

Wenju Cui[1,2†], Caiying Yan[3†], Zhuangzhi Yan[1], Yunsong Peng[2,4], Yilin Leng[1,2], Chenlu Liu[3], Shuangqing Chen[3], Xi Jiang[5*], Jian Zheng[2] and Xiaodong Yang[2]*

[1] Institute of Biomedical Engineering, School of Communication and Information Engineering, Shanghai University, Shanghai, China, [2] Medical Imaging Department, Suzhou Institute of Biomedical Engineering and Technology, Chinese Academy of Sciences, Suzhou, China, [3] Department of Radiology, The Affiliated Suzhou Hospital of Nanjing Medical University, Suzhou, China, [4] School of Biomedical Engineering, Division of Life Sciences and Medicine, University of Science and Technology of China, Hefei, China, [5] School of Life Sciences and Technology, The University of Electronic Science and Technology of China, Chengdu, China

OPEN ACCESS

Edited by:
Xiang Li,
Massachusetts General Hospital and Harvard Medical School, United States

Reviewed by:
Lu Zhang,
University of Texas at Arlington, United States
Mingxia Liu,
University of North Carolina at Chapel Hill, United States

***Correspondence:**
Shuangqing Chen
sznaonao@163.com
Xi Jiang
xjiang@uestc.edu.cn

† These authors have contributed equally to this work

Specialty section:
This article was submitted to Brain Imaging Methods, a section of the journal Frontiers in Neuroscience

Received: *08 December 2021*
Accepted: *11 January 2022*
Published: *24 February 2022*

Citation:
Cui W, Yan C, Yan Z, Peng Y, Leng Y, Liu C, Chen S, Jiang X, Zheng J and Yang X (2022) BMNet: A New Region-Based Metric Learning Method for Early Alzheimer's Disease Identification With FDG-PET Images. Front. Neurosci. 16:831533. doi: 10.3389/fnins.2022.831533

18F-fluorodeoxyglucose (FDG)-positron emission tomography (PET) reveals altered brain metabolism in individuals with mild cognitive impairment (MCI) and Alzheimer's disease (AD). Some biomarkers derived from FDG-PET by computer-aided-diagnosis (CAD) technologies have been proved that they can accurately diagnosis normal control (NC), MCI, and AD. However, existing FDG-PET-based researches are still insufficient for the identification of early MCI (EMCI) and late MCI (LMCI). Compared with methods based other modalities, current methods with FDG-PET are also inadequate in using the inter-region-based features for the diagnosis of early AD. Moreover, considering the variability in different individuals, some hard samples which are very similar with both two classes limit the classification performance. To tackle these problems, in this paper, we propose a novel bilinear pooling and metric learning network (BMNet), which can extract the inter-region representation features and distinguish hard samples by constructing the embedding space. To validate the proposed method, we collect 898 FDG-PET images from Alzheimer's disease neuroimaging initiative (ADNI) including 263 normal control (NC) patients, 290 EMCI patients, 147 LMCI patients, and 198 AD patients. Following the common preprocessing steps, 90 features are extracted from each FDG-PET image according to the automatic anatomical landmark (AAL) template and then sent into the proposed network. Extensive fivefold cross-validation experiments are performed for multiple two-class classifications. Experiments show that most metrics are improved after adding the bilinear pooling module and metric losses to the Baseline model respectively. Specifically, in the classification task between EMCI and LMCI, the specificity improves 6.38% after adding the triple metric loss, and the negative predictive value (NPV) improves 3.45% after using the bilinear pooling module. In addition, the accuracy of classification between EMCI and LMCI achieves 79.64% using imbalanced FDG-PET images, which illustrates that the proposed method yields a state-of-the-art result of the classification accuracy between EMCI and LMCI based on PET images.

Keywords: early Alzheimer's disease, mild cognitive impairment, FDG-PET images, bilinear pooling, inter-region representation, metric learning, embedding space

INTRODUCTION

Alzheimer's disease (AD), a brain degenerative disorder, is harming the health of thousands of old people now, and its rate of prevalence is expected to increase rapidly in the coming decades (Wang et al., 2013; Alzheimer's Association, 2018, 2019). Mild cognitive impairment (MCI) is considered to be a preclinical precursor of AD, but it is difficult to predict whether it will convert to AD or not (Gauthier et al., 2006; Dubois et al., 2016; Hampel and Lista, 2016). Considering the unpredictable process of MCI, it is crucial to develop relevant methods for diagnosing the early MCI and AD.

18F-fluorodeoxyglucose (FDG)-positron emission tomography (PET) can reveal altered brain metabolism in individuals with MCI and AD (Sörensen et al., 2019; Zhou et al., 2019; Wang et al., 2020). Various recent studies have proved that biomarkers derived from FDG-PET by computer-aided-diagnosis (CAD) technologies of machine learning and deep learning can accurately diagnose NC, MCI, and AD (Pagani et al., 2017; Choi et al., 2018; Blazhenets et al., 2019). Liu et al. (2018) proposed a new classification framework for AD diagnosis with 3D PET images. They decomposed 3D images into 2D slices to learn the intra-slice and inter-slice features and achieved a promising classification performance of AUC of 83.9% for MCI vs. NC classification. Zhou et al. (2021) developed a new deep belief network model for AD diagnosis based on sparse-response theory, which identified a better classification result than that of other models. To solve the multimodal data missing problem, Dong et al. (2021) proposed a high-order Laplacian regularized low-rank representation method for the classification tasks of NC, MCI, and AD. Pan et al. (2021) developed a disease-image-specific deep learning (DSDL) framework which can achieve neuroimage synthesis and disease diagnosis simultaneously using incomplete multi-modality neuroimages.

Many studies have achieved good performance on the classification of NC, MCI, and AD based on FDG-PET images. However, when it comes to the more refined task like classification of early MCI (EMCI) and late MCI (LMCI), the studies with FDG-PET images are still insufficient. Hao et al. (2020) proposed a novel multi-modal neuroimaging feature selection method with consistent metric constraint (MFCC) and obtained an accuracy (ACC) of 73.87% for the classification between EMCI and LMCI based on MRI and FDG-PET but only 64.69% when just using FDG-PET. Singh et al. (2017) proposed a multilayer neural network involving probabilistic principal component analysis for binary classification and only achieved an F1 score of 68.44%. Nozadi et al. (2018) used learned features from semantically labeled PET images to perform group classification and got an ACC of 72.5%. Forouzannezhad et al. (2018, 2020) applied a novel deep neural network and a random forest model respectively, and both models got a moderate ACC. Fang et al. (2020) introduced a supervised Gaussian discriminative component analysis (GDCA) algorithm for the effective classification of early Alzheimer's disease with MRI and PET. Yang and Liu (2020) applied the Convolutional Architecture for Fast Feature Embedding (CAFFE) as the framework of the deep learning platform for early Alzheimer's disease diagnosis. By comparison, based on fMRI and DTI images, Lei et al. (2020) got an ACC of 78.05% for the classification between EMCI and LMCI *via* proposing a new joint multi-task learning method by combining low-rank self-calibrated functional and structural brain networks. Song et al. (2021) constructed a new graph convolution network (GCN) and got an ACC of 79.26% based on fMRI and 82.92% based on DTI for the same classification task. With MRI images, Lian et al. (2018) developed a hierarchical fully convolutional network that can achieve an ACC of 81% for the classification between progressive MCI (pMCI) and stable MCI (sMCI).

To sum up, the refined classification performance for early AD based on FDG-PET images still has some room for improvement. One of the reasons might be that existing classification methods based on FDG-PET have not fully explored the inter-region representation among different brain regions. For example, based on fMRI, there are many methods like Pearson's correlation and sparse representation for functional brain network (FBN) estimation (Huang J. et al., 2020). However, several studies have proved that brain metabolism connectivity has value in the diagnosis of early AD (Huang et al., 2010; Sanabria-Diaz et al., 2013; Titov et al., 2017), but few PET-based studies are using the inter-region features to improve classification performance. In addition, another reason might be that the number of PET images is generally much more than that of fMRI images in most researches. The bigger dataset might increase the variety of individuals and the probability of special samples which are hard to distinguish, thus causing complexity of the problem for classification tasks.

Considering these two limitations, we propose a novel bilinear pooling and metric learning network (BMNet) for early Alzheimer's disease identification with FDG-PET images, especially for the classification task between EMCI and LMCI. Our main contributions are as follows: (1) We propose a shallow convolutional neural network model to achieve the classification; (2) We introduce a bilinear pooling module into the model for exploring the inter-region representation features in the whole brain; (3) We introduce the deep metric learning to help model learn the hard samples in the embedding feature space; (4) We conduct our method on the dataset collected from the publicly released ADNI database and obtain a state-of-the-art result of the classification between EMCI and LMCI based on PET images.

The rest of this paper is organized as follows. In section "Materials and Methods," we present details of the materials and the proposed methods. Section "Results" presents the results of the experiments on the public ADNI database. Finally, we provide the discussions and conclusion of this paper in section "Discussion and Conclusion."

MATERIALS AND METHODS

Image Acquisition and Preprocessing

In this work, we use the data in the publicly released Alzheimer's Disease Neuroimaging Initiative (ADNI) database (Jack et al., 2008). We collect a cohort of subjects with FDG-PET images from the ADNI databases. The ADNI cohort includes FDG-PET

images from 898 subjects, including 263 NC, 290 EMCI, 147 LMCI, and 198 AD participants. **Table 1** lists the demographic characteristics of subjects.

We choose FDG-PET images which are in a state of rest with 30–35 min with 185 ± 18.5 MBq FDG, and details of acquisition can be obtained from the study protocols in the ADNI database. Firstly, we normalize the images based on the template of the Montreal Neurological Institute (MNI). Then, we perform the smoothing with a Gaussian filter of 8 mm fullwidth at half-maximum (FWHM) (Wang et al., 2020). Finally, to verify the effectiveness of the proposed method, we do the main experiments using two different brain atlas. Based on the automated anatomical labeling (AAL) (Ashburner and Friston, 2000) atlas, we extract features of 90 regions of interest (ROIs) from FDG-PET images with intensity normalized averagely. Similarly, based on the Schaefer et al. (2018) atlas (Schaefer et al., 2018), we extract features of 400 regions. We perform all preprocessing steps by Statistical Parametric Mapping software (SPM12) (Tzourio-Mazoyer et al., 2002) and Matlab (2020).

Methods

Overview of the Proposed Network

Figure 1 illustrates the method framework of this study. The left box is the preprocessing step of FDG-PET images, in which the left image is the raw PET image of the brain, and the right one is the AAL template. Then 90 features extracted based on the AAL template are input into the subsequent model. The model consists of two convolution layers, a bilinear pooling layer, and two fully connected layers.

After extracting the first-order features through two convolution layers, the bilinear pooling module is used to further extract the inter-region-based features. Finally, the metric learning loss is added to the classification loss to strengthen the ability to learn hard samples of the proposed model.

Baseline Model

We construct a shallow neural network as the Baseline model, including two convolution blocks and three fully connected layers. Each convolution block includes a convolution layer, a batch normalization layer, and a Rectified Linear Unit (ReLU) activation layer.

Given a set of nodes (regions) R = {r1, r2, r3}, and the features of each region is denoted as X_i. Each convolution block is defined as:

$$Y_i = \sigma[BN(f(X_i))] \tag{1}$$

TABLE 1 | Demographic characteristics of the subjects in the ADNI database.

Subjects	NC	EMCI	LMCI	AD
Number	263	290	147	198
Gender (M/F)	130/133	160/130	80/67	119/79
Age	75.49 ± 6.47	71.40 ± 7.33	72.16 ± 7.55	75.05 ± 7.60
MMSE	29.06 ± 1.13	28.32 ± 1.57	27.62 ± 1.84	23.20 ± 2.17

The values are presented as mean ± standard deviation.
MMSE, Mini-Mental State Examination.

Where the f represents the convolution process, BN represents the batch normalization process, σ represents the activation process.

Generating Inter-Region Representation *via* Bilinear Pooling Module

In this section, we propose to use a bilinear pooling module to further generate second-order features which may represent inter-region features among whole brain regions. Bilinear pooling is an effective feature fusion method, which has been widely used in various computer vision and machine learning tasks (Lin et al., 2015; Gao et al., 2020). Bilinear pooling captures the high-order statistical information of features by matrix operations and then generates an expressive global representation (Kim et al., 2016; Li et al., 2017; Gao et al., 2020). In the research of DTI and fMRI, this method is also used to extract connectivity-based features between brain regions (Huang F. et al., 2020). In theory, by using these features, the inter-region representation among the whole brain regions in FDG-PET images could be exploited to some extent, as the functional brain network of fMRI.

In this work, we introduce a new factorized bilinear pooling method (Gao et al., 2020) to capture inter-region features by fusing homogeneous features where the input features are from the same source. This new bilinear pooling method simplifies the complexity of calculation, reduces heavy computational redundancy issues. Based on factorized bilinear coding, it is proved that bilinear features are rank-one matrices whose rank is one. The bilinear features could be extracted by factorizing dictionary atoms into low-rank matrices and Hadamard product, instead of massive matrix operations, reducing the dimension of matrices and computational burden.

The main operations of bilinear features are as follows (Kim et al., 2016; Gao et al., 2020):

$$B = Y^T W Y = Y^T U V^T Y = P^T (U^T Y \circ V^T Y) \tag{2}$$

where B represents the bilinear features, and Y represents the input feature, U^T, V^T and P^T are learnable parameters of the dictionary, $\circ$ represents Hadamard product.

The low-rank matrix U and V are used to approximate W, and the operation is simplified. Matrix P is used to control the length of the output. In the network, three fully connected layers are used to learn U^T, V^T and P^T. Then, we use an average pooling layer to diminish the feature dimension and obtain the global information. Finally, the feature map is flattened to one-dimensional and a fully connected layer is used to diminish the feature dimension to facilitate subsequent learning processes.

We use this bilinear pooling method to capture inter-region representation with FDG-PET images. The homogeneous features achieve interaction of the whole brain by the bilinear pooling module, which needs complex and expensive computation before.

Distinguishing Hard Samples in Embedding Space by Metric Learning

In this section, we introduce the deep metric learning strategy into the classification of different stages of AD. Metric learning is widely utilized with deep neural networks in classification

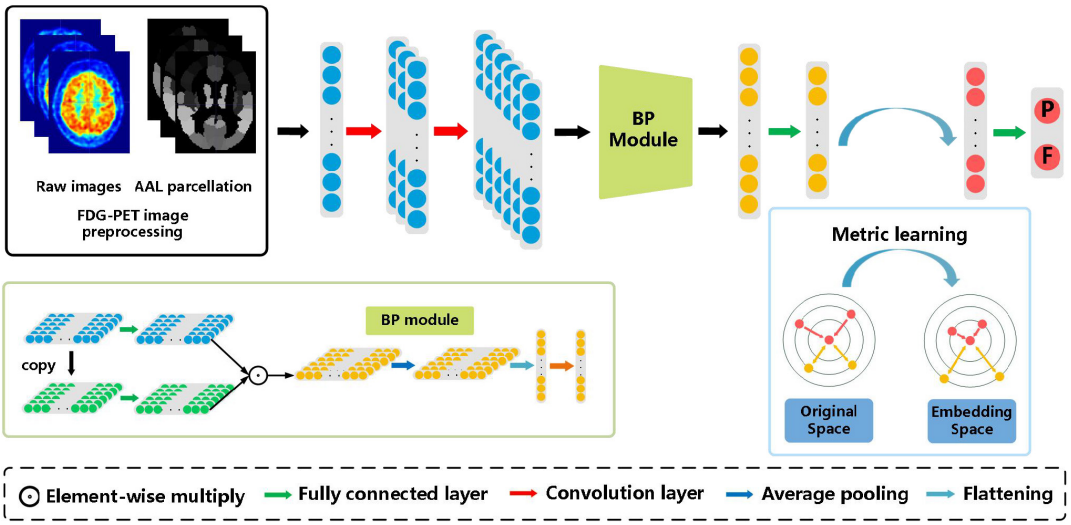

FIGURE 1 | The architecture of the proposed bilinear pooling and metric learning network (BMNet) for MCI diagnosis using PET images. There are four modules in our framework (i.e., images preprocessing module, convolutional feature-extraction module, bilinear pooling module, and the metric learning module).

tasks, especially in problems affected by large intra-class sample changes (Liu et al., 2017; Sundgaard et al., 2021). Deep metric learning loss maps features to the embedded space, which is conducive to learning difficult samples and can effectively deal with the imbalance of data (Sundgaard et al., 2021). Inspired by these, we argue that deep metric learning might be suitable for our classification task. Thus, in this paper, we employ deep metric learning for the diagnosis of AD to help distinguish hard samples in the embedding space.

In deep neural networks, the loss function is a manifestation of metric learning, and there are a variety of different metric learning loss functions. In this paper, we employ two deep metric learning loss functions for automatic diagnosis of early AD, including contrastive loss and triplet loss, which are widely used in recent studies (Cheng et al., 2016; He et al., 2021; Sundgaard et al., 2021). Contrastive loss employs a pair of positive and negative samples for each training iteration. The contrastive loss function is measured by the Euclidian distance between two vectors in embedding space. The contrastive loss function is given as (Hadsell et al., 2006):

$$L_c(b_{1,i}, b_{2,i}) = \sum_{i=1}^{N} [y_i d_{1,2}^2 + (1 - y_i)\{max(0,\ m - d_{1,2})\}^2] \quad (3)$$

$$d_{1,2} = ||f_{1,i} - f_{2,i}||_2^2 \quad (4)$$

where $y_i = 0$ for two positive vectors and $y_i = 1$ for negative pairs, $b_{1,i}$, $b_{2,i}$ is the training input from two classes, $f_{1,i}$, $f_{2,i}$ represents the embedding vector of each training input generated by the network, N is the number of input samples, and m is the margin, usually set to 1.0.

When the input is a positive sample pair, $d_{1,2}$ decreases gradually, and the same kind of samples will continue to form clusters in the feature space. On the contrary, when the network inputs a negative sample pair, $d_{1,2}$ will gradually rise until it reaches the set m. By minimizing the loss functions, the distance between positive sample pairs can be gradually reduced and the distance between negative sample pairs can be gradually increased, to meet the needs of the classification task.

Triplet loss is a widely used measure of metric learning loss, which is the basis of a large number of metric learning methods. Unlike contrastive loss, triplet loss requires three input samples including two positive samples and a negative sample. The three samples are named as fixed sample (anchor) b^a, positive sample (positive) b^p and negative sample (negative) b^n respectively. b^a and b^p form positive sample pairs, and b^a and b^n form negative sample pairs.

This triplet loss function simultaneously penalizes a short distance $d_{a,n}$ between an anchor and a negative sample and a long distance $d_{a,p}$ between an anchor and a positive sample, and is defined as (Schroff et al., 2015):

$$L_{triplet}(b_i^a, b_i^p, b_i^n) = \sum_{i=1}^{N} max(0, m + d_{a,p} - d_{a,n}) \quad (5)$$

where b_i^a, b_i^p, b_i^n is the input from two training groups, N represents the number of samples, and m is the margin, usually set to 1.0.

$$d_{a,p} = ||f_i^a - f_i^p||_2^2 \quad (6)$$

$$d_{a,n} = ||f_i^a - f_i^n||_2^2 \quad (7)$$

f_i^a, f_i^p, f_i^n represents the vector of training input in embedding space.

As shown in **Figure 1**, the triple loss can shorten the distance between positive sample pairs, while pushing away the distance between negative sample pairs. Finally, samples with the same class form feature clusters and embedding space to improve the performance of the classification tasks.

Loss Functions

In addition, we use cross-entropy loss L_C for the classification task. Therefore, the final loss function includes a joint loss function L_{total} that contains metric loss L_M for the embedding space and cross-entropy loss for the classification task.

$$L_{total} = \lambda L_M + L_C \tag{8}$$

$$L_C = \frac{1}{N}\sum_{i}^{N} - [y_i log(p_i) + (1 - y_i) log(1 - p_i)] \tag{9}$$

Where y_i represents the label of the sample i, where p_i represents the probability that the sample i is projected to be a positive class, λ represents the coefficient which we define as 0.05 by experience.

Performance Evaluation

We adopt six commonly used evaluation metrics to evaluate the performance of the models objectively, including accuracy (ACC), sensitivity (SEN), specificity (SPE), positive predictive value (PPV), negative predictive value (PPV), F1 score (F1), area under the receiver operating characteristic curve (AUC).

Implementation Details

We implement the proposed network based on the public platform PyTorch 1.8 and Intel Core i5-9400 CPU with 16 GB memory. Besides, we adapt stochastic gradient descent (SGD) to optimize the model, in which momentum and weight decay are set to 0.9 and 0.001 respectively.

Validation Strategies and Statistic Analysis Methods

To evaluate the effectiveness of the proposed model, we conduct a fivefold cross-validation strategy in all ablation and comparative experiments based on the AAL atlas. For each experiment, we divide data into five groups, and each group maintains the same proportion of two classes. In each fold experiment, four groups are used as train groups and another group is used as the test group. The detailed classification results on the ADNI database are summarized in section "Ablation Experiments."

In addition, we apply independent testing set strategy in the experiments based on Schaefer et al. (2018) atlas. We divide the collected dataset from the ADNI database into a training set (80%), validation set (10%), and testing set (10%). The corresponding detailed classification results are summarized in sections "Experiments on Different Atlases."

Similarly, to evaluate the effectiveness of the proposed model, we use two methods to validate the statistical significance including the *t*-test and DeLong test. In the experiments on the AAL atlas, we use the *t*-test. In the experiments on Schaefer et al. (2018) atlas, we use the DeLong test.

RESULTS

Ablation Experiments

To verify the effect of the bilinear pooling module and the metric learning loss on the performance of the proposed model, we remove the bilinear pooling module and the metric learning mechanism loss from the proposed BMNet, respectively. In the first experiment (i.e., our method without a bilinear pooling module), we directly use a fully connected layer to replace the bilinear pooling module. In the second experiment (i.e., our method without metric learning losses), we just use the cross-entropy loss function. The details are as follows and the results are shown in **Tables 2–5** and **Figure 2**.

TABLE 2 | Results of the ablation studies of BP module and metric learning losses for EMCI vs. LMCI classification (Mean ± Standard Deviation).

Method	ACC (%)	PPV (%)	NPV (%)	SEN (%)	SPE (%)	AUC	F1 (%)	p
Baseline	75.74 ± 2.96	83.79 ± 2.32	59.84 ± 13.06	80.79 ± 4.89	64.92 ± 2.09	0.7332 ± 0.0602	82.26 ± 1.53	–
Baseline + BP	78.48 ± 3.44	86.21 ± 4.22	63.29 ± 4.18	82.24 ± 2.03	70.29 ± 7.26	0.7629 ± 0.0719	84.17 ± 2.70	0.068
Tri-loss	77.35 ± 5.28	87.93 ± 5.72	56.34 ± 19.67	80.49 ± 6.45	71.3 ± 8.60	0.7415 ± 0.0963	84.05 ± 3.41	0.342
Tri-loss + BP	**79.64 ± 3.11**	**89.31 ± 2.56**	60.55 ± 9.54	81.84 ± 3.66	**74.29 ± 4.18**	0.7589 ± 0.0633	**85.41 ± 2.13**	**0.013***
Con-loss	77.81 ± 3.05	86.55 ± 3.57	59.17 ± 9.13	80.88 ± 3.37	70.53 ± 5.67	0.7387 ± 0.0801	83.94 ± 2.22	0.342
Con-loss + BP	79.40 ± 1.92	86.90 ± 6.41	**64.67 ± 10.58**	**83.22 ± 3.86**	72.43 ± 6.59	**0.7707 ± 0.0848**	85.01 ± 1.89	0.079

The bold values represent the highest number.
The asterisk represents the results have the statistical significance.

TABLE 3 | Results of the ablation studies of BP module and metric learning losses for NC VS. AD classification (Mean ± Standard Deviation).

Method	ACC (%)	PPV (%)	NPV (%)	SEN (%)	SPE (%)	AUC	F1 (%)	p
Baseline	85.25 ± 2.50	92.01 ± 2.82	76.33 ± 6.77	83.91 ± 3.96	87.99 ± 3.52	0.9074 ± 0.0215	87.77 ± 1.96	–
Baseline + BP	88.94 ± 1.20	93.52 ± 3.48	82.79 ± 3.50	87.92 ± 1.77	90.93 ± 4.33	0.9286 ± 0.0218	90.63 ± 1.22	0.051
Tri-loss	88.29 ± 0.86	93.54 ± 0.99	81.33 ± 2.04	86.92 ± 1.44	90.47 ± 1.31	0.9279 ± 0.0127	90.35 ± 0.74	0.059
Tri-loss + BP	**89.80 ± 0.62**	93.53 ± 3.70	**84.81 ± 4.88**	**89.28 ± 2.79**	91.20 ± 4.28	0.9281 ± 0.0192	91.11 ± 0.70	**0.032***
Con-loss	89.14 ± 1.75	93.53 ± 2.56	83.35 ± 2.78	88.02 ± 1.59	90.76 ± 3.54	0.9281 ± 0.0253	90.69 ± 1.48	0.088
Con-loss + BP	**89.80 ± 0.99**	**93.90 ± 2.44**	84.32 ± 3.40	88.91 ± 2.00	**91.40 ± 2.97**	**0.9334 ± 0.0141**	**91.35 ± 0.80**	**0.029***

The bold values represent the highest number.
The asterisk represents the results have the statistical significance.

TABLE 4 | Results of the ablation studies of BP module and metric learning loss for NC VS. LMCI classification (Mean ± Standard Deviation).

Method	ACC (%)	PPV (%)	NPV (%)	SEN (%)	SPE (%)	AUC	F1 (%)	p
Baseline	76.81 ± 4.27	78.86 ± 9.26	73.45 ± 10.68	84.50 ± 4.26	66.81 ± 6.33	0.7527 ± 0.0520	81.58 ± 4.79	–
Baseline + BP	80.00 ± 4.61	86.28 ± 6.49	68.71 ± 8.88	83.25 ± 3.83	74.45 ± 7.40	0.7871 ± 4.57	84.74 ± 4.03	**<0.001***
Tri-loss	80.49 ± 2.86	89.33 ± 4.01	64.60 ± 5.42	81.91 ± 2.04	77.68 ± 6.17	0.7702 ± 5.77	85.46 ± 2.34	**0.007***
Tri-loss + BP	**82.20 ± 4.36**	**89.36 ± 3.17**	69.42 ± 11.53	84.18 ± 5.23	**78.48 ± 5.76**	0.7985 ± 5.38	**86.69 ± 3.05**	**<0.001***
Con-loss	79.03 ± 4.83	83.22 ± 7.72	71.36 ± 13.62	84.31 ± 5.15	71.28 ± 6.79	0.7841 ± 4.18	83.76 ± 4.23	**0.016***
Con-loss + BP	81.46 ± 3.99	84.64 ± 6.62	**72.02 ± 9.80**	**84.96 ± 3.64**	76.05 ± 7.78	**0.8096 ± 4.22**	84.80 ± 4.35	**0.001***

The bold values represent the highest number.
The asterisk represents the results have the statistical significance.

TABLE 5 | Results of the ablation studies of BP module and metric learning loss for LMCI vs. AD classification (Mean ± Standard Deviation).

Method	ACC (%)	PPV (%)	NPV (%)	SEN (%)	SPE (%)	AUC	F1 (%)	p
Baseline	77.69 ± 2.67	74.16 ± 5.54	80.30 ± 6.73	74.57 ± 5.91	80.86 ± 2.54	0.7964 ± 0.0216	74.37 ± 2.67	–
Baseline + BP	80.06 ± 5.78	72.92 ± 11.12	**85.37 ± 4.11**	78.62 ± 5.95	81.29 ± 6.67	0.8108 ± 0.0581	75.66 ± 8.02	0.243
Tri-loss	80.60 ± 3.04	74.25 ± 9.76	85.31 ± 6.67	**79.77 ± 6.85**	82.23 ± 5.29	0.8040 ± 0.0422	76.91 ± 4.30	0.307
Tri-loss + BP	81.18 ± 2.72	**78.90 ± 7.80**	82.85 ± 4.39	77.53 ± 3.26	**84.41 ± 4.42**	0.8167 ± 0.0295	78.21 ± 3.97	**0.022***
Con-loss	79.71 ± 0.97	74.87 ± 7.56	83.31 ± 5.89	77.53 ± 5.36	82.00 ± 3.37	0.8018 ± 0.0332	76.18 ± 2.19	0.327
Con-loss + BP	**81.77 ± 4.50**	77.54 ± 8.19	84.91 ± 6.27	79.64 ± 6.88	83.84 ± 4.97	**0.8297 ± 0.0346**	**78.57 ± 5.53**	**0.028***

The bold values represent the highest number.
The asterisk represents the results have the statistical significance.

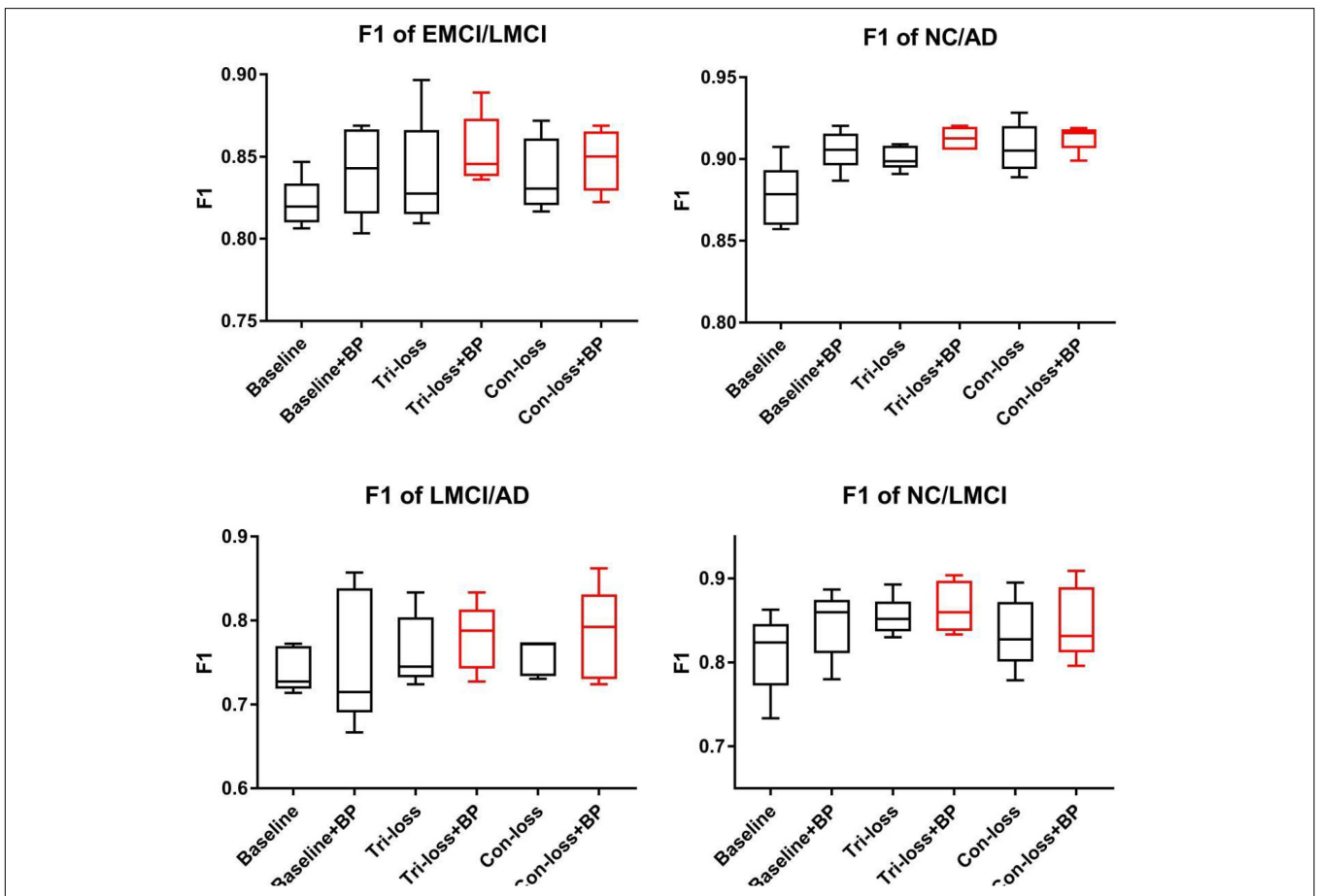

FIGURE 2 | The F1 scores of experiments for EMCI vs. LMCI classification, NC vs. LMCI classification, LMCI vs. AD classification and NC vs. AD classification.

TABLE 6 | Results of the main studies based on the Schaefer et al. (2018) atlas.

Class	Method	ACC	SEN	SPE	F1	AUC	*p*
EMCI-LMCI	Baseline	0.7500	0.7647	0.7000	0.8254	0.7379	**0.0358***
	Con-loss	0.7727	0.7714	0.7778	0.8438	0.7609	0.1090
	Baseline + BP	0.7955	0.8125	0.7500	0.8525	0.7425	0.0990
	Con-loss + BP	**0.8409**	**0.8235**	**0.9000**	**0.8889**	**0.8529**	–
NC-AD	Baseline	0.8298	0.8519	0.8000	0.8519	0.8796	**0.0395***
	Con-loss	0.8511	0.8571	0.8421	0.8727	0.9139	0.3212
	Baseline + BP	0.8511	0.8333	0.8824	0.8772	0.9259	0.3548
	Con-loss + BP	**0.8936**	**0.8929**	**0.8947**	**0.9091**	**0.9574**	–

The bold values represent the highest number.
The asterisk represents the results have the statistical significance.

The Ablation Experiments of the Bilinear Pooling Module

Firstly, we conduct the experiments based on the Baseline model. Then we conduct the experiments of adding a bilinear pooling (BP) module to the Baseline model. According to the results, after the BP module is added, the four groups of classification experimental results have been improved to a certain extent. Specifically, in classification experiments between EMCI and LMCI, ACC increases by 2.74%, and AUC increases by 2.97%. In classification experiments between NC and AD, the results are the best, where ACC increases by 3.69% and AUC increases by 2.12%. In addition, we also conduct experiments in the classification between NC and LMCI, LMCI, and AD. The results illustrate that the BP module has a good generalization ability in the different classification tasks.

Furthermore, we conduct comparative experiments to verify the effectiveness of the BP module based on metric learning loss. For example, in the classification experiments of EMCI and LMCI, after adding the BP model to the triplet loss (Tri-loss), ACC increases by 2.29%, and AUC increases by 1.74%.

The Ablation Experiments of Metric Learning Losses

In this sub-section, we perform comparative experiments in terms of metric learning losses, including the triplet loss (Tri-loss) and the contrastive loss (Con-loss). We use two kinds of metric learning losses respectively, and the results illustrate that the two metric learning losses are both effective in different experiments. Specifically, in the classification experiments between EMCI and LMCI, ACC increases by 2.07% after adding the contrastive loss, which is a little higher than that of triplet loss. Similarly, in the classification experiments between NC and AD, ACC increases by 3.89%. In the classification experiments between NC and LMCI, the results of triplet loss improve more than these of contrastive loss, and ACC reaches 0.8049. On the contrary, in the classification experiment between LMCI and AD, the results of contrastive loss are better, where ACC reaches 0.8177 and AUC reaches 0.8297.

Finally, we use the *t*-test to measure the statistical significance comparing AUCs and the results are shown as *p*-value in **Tables 2–5**. We can see that most results of the two final models (Con-loss + BP and Tri-loss + BP) are statistically significant. In addition, we can also see that most F1 scores of the two final models are higher than these of other models in **Figure 2**.

Experiments on Different Atlases

In this section, we evaluate the performance of our method (Con-loss + BP) based on the Schaefer et al. (2018) atlas. We conduct two groups of experiments for EMCI vs. LMCI classification and NC vs. AD classification and the results are shown in **Table 6** and **Figure 3**. As stated earlier, we apply independent testing set strategy in these experiments and use the DeLong test to validate the statistical significance.

The results illustrate that both BP module and contrastive loss are effective based on the Schaefer et al. (2018) atlas. In the experiments for EMCI vs. LMCI classification, ACC increases by 2.27% after adding the contrastive loss, which is a little

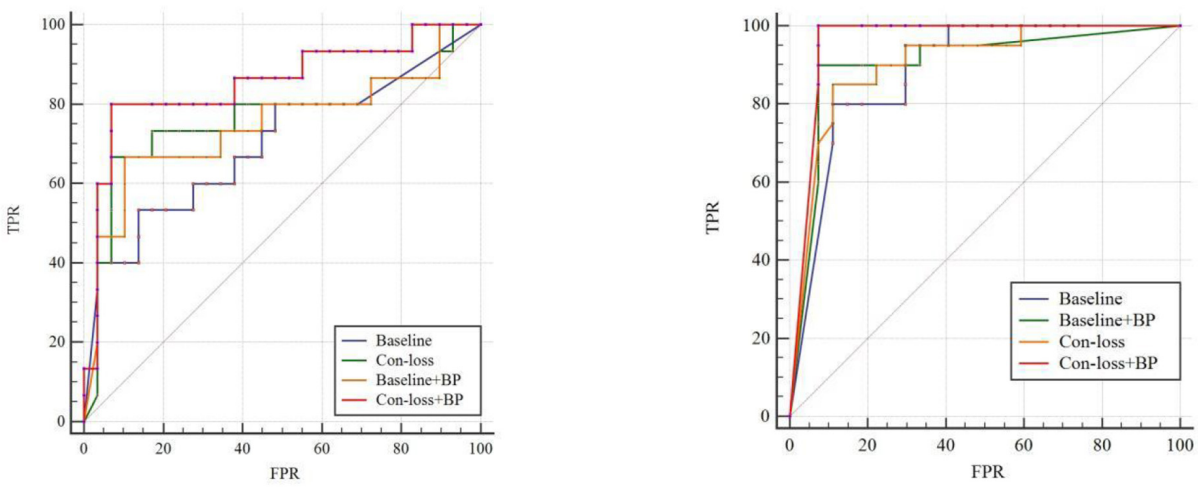

FIGURE 3 | Receiver operating characteristic (ROC) curves of experiments for EMCI vs. LMCI classification and the ROC of experiments for NC vs. AD classification based on the Schaefer et al. (2018) atlas. TPR, true positive rate; FPR, false-positive rate; AUC, area under the receiver operating characteristic curve. Please see the web version for the complete colorful picture.

TABLE 7 | Comparison of the performance of different model algorithms in experiments for EMCI vs. LMCI classification with the related works.

Method	Modality	DATA (EMCI/LMCI)	ACC	SEN	SPE	AUC	F1
SVM	PET	290/147	0.6620	0.7769	0.4653	0.6329	–
Singh et al., 2017	PET	178/158	–	0.6482	–	–	0.6844
Nozadi et al., 2018	PET	164/189	0.7250	0.7920	0.6990	0.790	–
Forouzannezhad et al., 2018	PET	296/193	0.6230	0.7820	0.4000	–	–
Forouzannezhad et al., 2020	PET	296/193	0.6280	0.6150	0.6430	–	–
Yang and Liu, 2020	PET	–	0.7219	0.7382	0.7305	–	–
Hao et al., 2020	PET	273/187	0.6469	0.7817	0.4444	0.6300	–
	PET+MRI		0.7387	0.9055	0.4952	0.7000	–
Fang et al., 2020	PET+MRI	297/196	0.8333	0.8235	0.8966	0.8947	
Lei et al., 2020	fMRI	44/38	0.7805	0.7368	0.8182	0.8571	–
	DTI		0.5366	0.5789	0.5000	0.5260	–
Song et al., 2021	fMRI	44/38	0.7926	0.8421	0.7500	0.9067	–
	DTI		**0.8292**	**0.9473**	0.7272	**0.9414**	–
Our method (Tri-loss+BP)	PET	290/147	0.7964	0.8184	0.7429	0.7589	**0.8541**
Our method(Con-loss+BP on Schaefer atlas)	PET	290/147	**0.8409**	**0.8235**	**0.9000**	**0.8889**	0.8529

The bold values represent the highest number.

lower than that of the BP module. Similarly, in the classification experiments between NC and AD, ACC increases by 2.13%. Finally, combining the BP module and contrastive loss, the final model (Con-loss + BP) achieves much improvement in both two classification experiments. Specifically, in the classification experiments for EMCI and LMCI, ACC, SEN, SPE, F1 and AUC achieve 84.09%, 82.35%, 90%, 88.89% and 0.8529 with an improvement of 9.09, 5.88, 20, 6.35, and 11.5% respectively, compared with Baseline model. In the NC vs. AD classification experiments, ACC, SEN, SPE, F1 and AUC increases by 6.38%, 4.1%, 9.47%, 5.72%, 7.78% and reach 89.36%, 89.29%, 89.47%, 90.91% and 0.9574.

Comparison With Other Methods

In this section, we compare the performance of our method (Tri-loss + BP) with that of several recent representative methods. In addition, we apply the least absolute shrinkage and selection operator (LASSO) feature selection method and support vector machine (SVM) method for the contrast experiments. From **Table 7**, we can find that our method gets the highest performance in classification experiments between EMCI and LMCI based on FDG-PET images. Specifically, the proposed

TABLE 8 | Comparison of the performance of different model algorithms in experiments for NC vs. AD classification with the related works.

Method	Modality	DATA (NC/AD)	ACC	SEN	SPE	AUC
SVM	**PET**	263/198	0.6213	0.8063	0.5547	0.8445
Hao et al., 2020	**PET**	211/160	0.8006	0.8602	0.7194	0.85
	MRI		0.8663	0.9028	0.8181	0.93
Lei et al., 2020	fMRI	44/38	0.7805	0.7368	0.8182	0.8571
	DTI		0.5366	0.5789	0.5000	0.5260
Song et al., 2021	fMRI	44/38	0.7926	0.8421	0.75	0.9067
	DTI		0.8292	0.9473	0.7272	0.9414
Lian et al., 2018	MRI	429/358	0.90	0.82	**0.97**	0.95
Dong et al., 2021	MRI+PET	440/367	**0.9305**	**0.9474**	**0.9091**	0.9732
Our method (Tri-loss+BP)	**PET**	263/198	**0.898**	0.8928	**0.912**	0.9281
Our method (Con-loss+BP on Schaefer atlas)	**PET**	263/198	0.8936	**0.8929**	0.8947	**0.9574**

The bold values represent the highest number.

TABLE 9 | Comparison of the performance of different model algorithms in experiments for NC vs. LMCI classification with the related works.

Method	Modality	DATA (NC/LMCI)	ACC	SEN	SPE	AUC
SVM	**PET**	263/147	0.6415	0.7446	0.5437	0.6724
Hao et al., 2020	**PET**	273/187	0.6677	0.7545	0.5594	0.68
	MRI		0.712	0.7801	0.6332	0.76
Lei et al., 2020	Fmri	44/38	0.7805	0.7368	**0.8182**	0.8571
	DTI		0.5366	0.5789	0.5000	0.5260
Song et al., 2021	fMRI	44/38	0.7926	0.8421	0.75	0.9067
	DTI		**0.8292**	**0.9473**	0.7272	**0.9414**
Our method (Tri-loss+BP)	**PET**	263/147	0.822	0.8418	0.7848	0.7985

The bold values represent the highest number.

TABLE 10 | Comparison of the performance of different model algorithms in experiments for LMCI vs. AD classification with the related works.

Method	Modality	DATA (LMCI/AD)	ACC	SEN	SPE	AUC
SVM	**PET**	147/198	0.5841	0.7834	0.5044	0.6908
Hao et al., 2020	**PET**	273/187	0.6677	0.7545	0.5594	0.68
	MRI		0.712	0.7801	0.6332	0.76
Lei et al., 2020	fMRI	44/38	0.7805	0.7368	0.8182	0.8571
	DTI		0.5366	0.5789	0.5000	0.5260
Song et al., 2021	fMRI	44/38	0.7926	0.8421	0.75	0.9067
	DTI		**0.8292**	**0.9473**	0.7272	**0.9414**
Our method (Tri-loss+BP)	**PET**	147/198	0.8118	0.7753	**0.8441**	0.8167

The bold values represent the highest number.

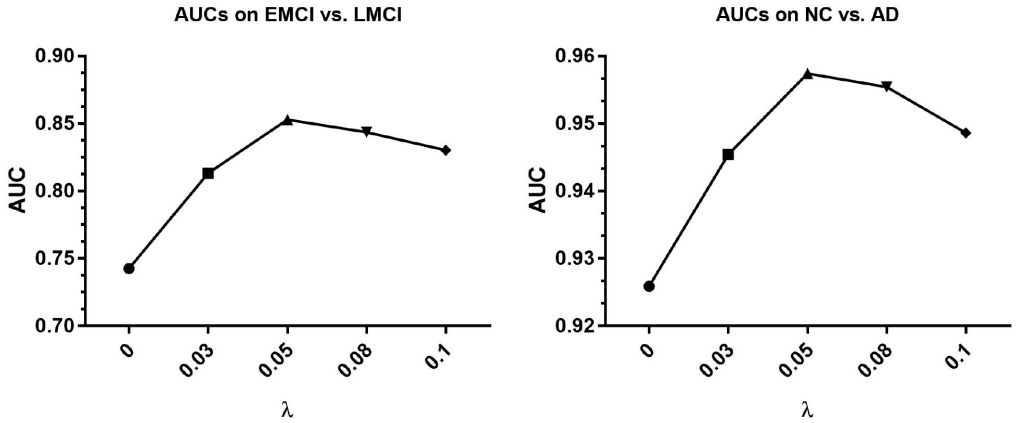

FIGURE 4 | The AUCs of ablation experiments loss functions for EMCI vs. LMCI classification and NC vs. AD classification based on the Schaefer et al. (2018) atlas. AUC, area under the receiver operating characteristic curve.

method yields big improvement than the results of Singh et al. (2017) and Nozadi et al. (2018), although the dataset in our experiments is highly unbalanced. Based on a similar dataset, the proposed method still has better performance than the methods proposed by Forouzannezhad et al. (2018, 2020). In addition, compared with the method proposed by Hao et al. (2020), our method achieves an overall huge improvement with 14.95% in ACC, 3.67% in SEN, 29.85% in SPE, and 12.89% in AUC, respectively. Compared to the results of the fusion of PET and MRI (Singh et al., 2017; Forouzannezhad et al., 2018, 2020; Nozadi et al., 2018; Fang et al., 2020; Hao et al., 2020), our method also achieves an improvement in most metrics. Besides, our method gets a comparable performance compared to the methods based on fMRI and DTI adapted by Lei et al. (2020) and by Song et al. (2021), but the subjects in our research are much more than those they use.

Similarly, from **Table 8**, we can find that our method gets the highest performance of classification experiments between NC and AD based on PET images too. Specifically, compared with the method proposed by Hao et al. (2020) based on PET images, our method achieves an overall huge improvement with 9.74% in ACC, 3.26% in SEN, 19.26% in SPE, and 7.81% in AUC, respectively. Besides, our method gets a comparable performance compared to the methods based on other modalities (Lian et al., 2018; Lei et al., 2020; Song et al., 2021). ACC, SEN, SPE, AUC of our method based on PET images improve 10.76%, 4.69%, 16.83%, and 2.82% than those of their method based on fMRI. While SEN and AUC are slightly lower, ACC and SPE based on PET images improve 7.1% and 19.11% than those based on DTI.

In addition, we conduct the classification experiments between NC and LMCI, LMCI and AD, and the results compared with other methods are shown in **Tables 9**, **10** respectively, to further validate the effectiveness of our method.

From those experiments above, we can see that our classification results between EMCI and LMCI have exceeded those of the existing methods overall based on FDG-PET images. In addition, our results are also comparable with those based on fMRI and DTI images.

DISCUSSION AND CONCLUSION

Comparison of Different Coefficients in Loss Functions

To select the proper coefficient of loss functions, we compare several numbers of coefficient λ in Equation 8, including 0, 0.03, 0.05, 0.08, and 0.1. We conduct the ablation experiments based on methods in section "Experiments on Different Atlases" and the corresponding AUCs are shown in **Figure 4**. It can be seen that the AUC turns out to be the highest when coefficient is around 0.05 and keep at a relatively high level in the range from 0.05 to 0.08. Therefore we set coefficient λ as 0.05 in most experiments.

Comparisons With Previous Researches

In general, there are three major advances between the proposed method and previous methods. Firstly, current PET-based methods are deficient in extracting representation features among different brain regions, incurring poor performance for the classification of early AD. The proposed BMNet introduces a bilinear pooling module into the model to explore the inter-region representation features and get a good classification performance. Secondly, there are few methods to study hard samples to improve the classification results in the brain disorder analysis. By comparison, we apply two metric learning losses to our model which has been proved useful for hard samples classification and they both get a good performance in the experiments. Thirdly, brain metabolism is very important for AD diagnosis and can only be obtained by PET images. Based on PET images, the proposed method could extract region-based features which represent the brain metabolic connectivity network, excavate the potential of PET images, and improve the diagnosis performance. This is the main superiority of inter-region-based methods with PET images compare with other modalities. In addition, the proposed PET-based method is comparable to other modalities in classification tasks between EMCI and LMCI.

Potential Applications in Other Modalities

Considering the good performance based on FDG-PET images, the proposed BMNet including the bilinear pooling module and the metric learning loss functions also has the potential capability of diagnosis for other neurological diseases with other kinds of brain images. Besides, the proposed method only requires features of each brain region as the input. This lightweight characteristic allows the model to be easily applied to fMR and DTI images. We will try to explore more applications of the proposed method in future work.

Limitations and Future Works

While the proposed BMNet achieves good results for the diagnosis of early AD, there are still some limitations. Firstly, considering the characteristics of the convolution neural network, the models and results are hard to be interpreted and the inter-region representation of the brain regions is hard to be visualized. Secondly, the proposed method focus on region-based features, which are lightweight but only utilize the metabolism of brain regions, limiting the ability of the network. In future work, we will try to integrate whole 3D PET images into the network to achieve joint feature extraction and classification. Finally, there is still some potential in exploiting methods that can extract brain inter-region representation features based on FDG-PET images. In the future, we will try to design methods that could extract inter-region representation features more effectively. In addition, the proposed method directly combined the contrastive loss and triplet loss with the entropy loss to better distinguish the hard samples. In the future, we will some novel designs of these losses based on domain knowledge.

Conclusion

We propose a novel neural network method for the diagnosis of early AD with FDG-PET. We firstly construct a shallow neural network as the Baseline model. Then we introduce a bilinear pooling module into the network to try to extract inter-region representation features among the whole brain. We also apply the deep metric learning losses into the final loss function to help distinguish hard samples in the embedding space. Finally, we conduct the BMNet on the ADNI database and the results show that our method yields comparable classification performance with several representative methods. Especially, we get a satisfying classification performance in the experiment between EMCI and LMCI, which is the state-of-the-art result with FDG-PET.

DATA AVAILABILITY STATEMENT

The original contributions presented in the study are included in the article/supplementary material, further inquiries can be directed to the corresponding author/s.

ETHICS STATEMENT

Written informed consent was obtained from the individual(s) for the publication of any potentially identifiable images or data included in this article.

AUTHOR CONTRIBUTIONS

WC contributed to idea conceptualization, experiments, and wrote the first draft of the manuscript. CY and CL collected data and organized the database. YP contributed to idea conceptualization. YL contributed to experiments. SC contributed to fund support and manuscript revising. XJ and JZ contributed to manuscript revising and idea conceptualization. ZY contributed to manuscript revising. XY contributed to fund support. WC, YP, JZ, XJ, and CY contributed to conception and design of the study. WC and YL performed the statistical analysis. XJ, SC, JZ, XY, and ZY wrote sections of the manuscript. All authors contributed to manuscript revision, read, and approved the submitted version.

FUNDING

This work is supported in part by the Key Project of Health Commission of Jiangsu Province (ZDB2020011), in part by the Technology Project of Diagnosis and treatment of key diseases in Suzhou (LCZX201909), and in part by the Suzhou Science and Technology Bureau (SJC2021023).

REFERENCES

Alzheimer's Association (2018). Alzheimer's disease facts and figures. *Alzheimer's Dementia* 14, 367–429.

Alzheimer's Association (2019). 2019 Alzheimer's disease facts and figures. *Alzheimer's Dementia* 15, 321–387.

Ashburner, J., and Friston, K. J. (2000). Voxel-based morphometry-the methods. *Neuroimage* 11, 805–821.

Blazhenets, G., Ma, Y., Sörensen, A., Rücker, G., Schiller, F., Eidelberg, D., et al. (2019). Principal components analysis of brain metabolism predicts development of Alzheimer dementia. *J. Nucl. Med.* 60, 837–843. doi: 10.2967/jnumed.118.219097

Cheng, D., Gong, Y., Zhou, S., Wang, J., and Zheng, N. (2016). "Person re-identification by multi-channel parts-based cnn with improved triplet loss function," in *Proceedings of the IEEE Conference on Computer Vision and Pattern Recognition* (Piscataway, NJ: IEEE), 1335–1344.

Choi, H., Jin, K. H., Alzheimer's Disease, and Neuroimaging Initiative (2018). Predicting cognitive decline with deep learning of brain metabolism and amyloid imaging. *Behav. Brain Res.* 344, 103–109. doi: 10.1016/j.bbr.2018.02.017

Dong, A., Li, Z., Wang, M., Shen, D., and Liu, M. (2021). High-Order laplacian regularized low-rank representation for multimodal dementia diagnosis. *Front. Neurosci.* 15:634124. doi: 10.3389/fnins.2021.634124

Dubois, B., Hampel, H., Feldman, H. H., Scheltens, P., Aisen, P., Andrieu, S., et al. (2016). Preclinical Alzheimer's disease: definition, natural history, and diagnostic criteria. *Alzheimer's Dementia* 12, 292–323. doi: 10.1016/j.jalz.2016.02.002

Fang, C., Li, C., Forouzannezhad, P., Cabrerizo, M., Curiel, R. E., Loewenstein, D., et al. (2020). Gaussian discriminative component analysis for early detection of Alzheimer's disease: a supervised dimensionality reduction algorithm. *J. Neurosci. Methods* 344:108856. doi: 10.1016/j.jneumeth.2020.108856

Forouzannezhad, P., Abbaspour, A., Li, C., Cabrerizo, M., and Adjouadi, M. (2018). "A deep neural network approach for early diagnosis of mild cognitive impairment using multiple features," in *Proceedings of the 2018 17th IEEE International Conference on Machine Learning and Applications (ICMLA)* (Piscataway, NJ: IEEE), 1341–1346.

Forouzannezhad, P., Abbaspour, A., Li, C., Fang, C., Williams, U., Cabrerizo, M., et al. (2020). A Gaussian-based model for early detection of mild cognitive impairment using multimodal neuroimaging. *J. Neurosci. Methods* 333:108544. doi: 10.1016/j.jneumeth.2019.108544

Gao, Z., Wu, Y., Zhang, X., Dai, J., Jia, Y., and Harandi, M. (2020). "Revisiting bilinear pooling: a coding perspective," in *Proceedings of the AAAI Conference on Artificial Intelligence*, Vol. 34 (New York, NY), 3954–3961. doi: 10.1609/aaai.v34i04.5811

Gauthier, S., Reisberg, B., Zaudig, M., Petersen, R. C., Ritchie, K., Broich, K., et al. (2006). Mild cognitive impairment. *Lancet* 367, 1262–1270.

Hadsell, R., Chopra, S., and LeCun, Y. (2006). *Dimensionality Reduction by Learning an Invariant Mapping*, Vol. 2. Piscataway, NJ: IEEE, 1735–1742.

Hampel, H., and Lista, S. (2016). The rising global tide of cognitive impairment. *Nat. Rev. Neurol.* 12, 131–132. doi: 10.1038/nrneurol.2015.250

Hao, X., Bao, Y., Guo, Y., Yu, M., Zhang, D., Risacher, S. L., et al. (2020). Multi-modal neuroimaging feature selection with consistent metric constraint for diagnosis of Alzheimer's disease. *Med. Image Anal.* 60:101625. doi: 10.1016/j.media.2019.101625

He, K., Lian, C., Adeli, E., Huo, J., Gao, Y., Zhang, B., et al. (2021). MetricUNet: synergistic image-and voxel-level learning for precise prostate segmentation via online sampling. *Med. Image Anal.* 71:102039. doi: 10.1016/j.media.2021.102039

Huang, F., Tan, E. L., Yang, P., Huang, S., Ou-Yang, L., Cao, J., et al. (2020). Self-weighted adaptive structure learning for ASD diagnosis via multi-template multi-center representation. *Med. Image Anal.* 63:101662. doi: 10.1016/j.media.2020.101662

Huang, J., Zhou, L., Wang, L., and Zhang, D. (2020). Attention-diffusion-bilinear neural network for brain network analysis. *IEEE Trans. Med. Imaging* 39, 2541–2552. doi: 10.1109/TMI.2020.2973650

Huang, S., Li, J., Sun, L., Ye, J., Fleisher, A., Wu, T., et al. (2010). Learning brain connectivity of Alzheimer's disease by sparse inverse covariance estimation. *NeuroImage* 50, 935–949. doi: 10.1016/j.neuroimage.2009.12.120

Jack, C. R. Jr., Bernstein, M. A., Fox, N. C., Thompson, P., Alexander, G., Harvey, D., et al. (2008). The Alzheimer's disease neuroimaging initiative (ADNI): MRI methods. *J. Magnetic Resonance Imag.* 27, 685–691. doi: 10.1002/jmri.21049

Kim, J. H., On, K. W., Lim, W., Kim, J., Ha, J. W., and Zhang, B. T. (2016). Hadamard product for low-rank bilinear pooling. *arXiv [preprint]*. Available online at: https://arxiv.org/abs/1610.04325 (accessed March 20, 2021).

Lei, B., Cheng, N., Frangi, A. F., Tan, E. L., Cao, J., Yang, P., et al. (2020). Self-calibrated brain network estimation and joint non-convex multi-task learning for identification of early Alzheimer's disease. *Med. Image Anal.* 61:101652. doi: 10.1016/j.media.2020.101652

Li, Y., Wang, N., Liu, J., and Hou, X. (2017). "Factorized bilinear models for image recognition," in *Proceedings of the IEEE International Conference on Computer Vision* (Piscataway, NJ.: IEEE), 2079–2087.

Lian, C., Liu, M., Zhang, J., and Shen, D. (2018). Hierarchical fully convolutional network for joint atrophy localization and Alzheimer's disease diagnosis using structural MRI. *IEEE Trans. Pattern Anal. Mach. Intell.* 42, 880–893. doi: 10.1109/TPAMI.2018.2889096

Lin, T. Y., RoyChowdhury, A., and Maji, S. (2015). "Bilinear cnn models for fine-grained visual recognition," in *Proceedings of the IEEE International Conference on Computer Vision* (Piscataway, NJ: IEEE), 1449–1457.

Liu, M., Cheng, D., Yan, W., Alzheimer's Disease, and Neuroimaging Initiative (2018). Classification of Alzheimer's disease by combination of convolutional and recurrent neural networks using FDG-PET images. *Front. Neuroinform.* 12:35. doi: 10.3389/fninf.2018.00035

Liu, W., Wen, Y., Yu, Z., Li, M., Raj, B., and Song, L. (2017). "Sphereface: deep hypersphere embedding for face recognition," in *Proceedings of the IEEE Conference on Computer Vision and Pattern Recognition* (Piscataway, NJ: IEEE), 212–220. doi: 10.1109/TPAMI.2019.2914680

Matlab (2020). *MATLAB 9.8*. MathWorks Inc. Available online at: https://ww2.mathworks.cn/products/matlab.html

Nozadi, S. H., Kadoury, S., Alzheimer's Disease, and Neuroimaging Initiative (2018). Classification of Alzheimer's and MCI patients from semantically parcelled PET images: a comparison between AV45 and FDG-PET. *Int. J. Biomed. Imag.* 2018:1247430. doi: 10.1155/2018/1247430

Pagani, M., Nobili, F., Morbelli, S., Arnaldi, D., Giuliani, A., Öberg, J., et al. (2017). Early identification of MCI converting to AD: a FDG PET study. *Eur. J. Nucl. Med. Mol. Imag.* 44, 2042–2052. doi: 10.1007/s00259-017-3761-x

Pan, Y., Liu, M., Xia, Y., and Shen, D. (2021). Disease-image-specific learning for diagnosis-oriented neuroimage synthesis with incomplete multi-modality data. *IEEE Trans. Pattern Anal. Mach. Intell.* Online ahead of print. doi: 10.1109/TPAMI.2021.3091214

Sanabria-Diaz, G., Martinez-Montes, E., Melie-Garcia, L., Alzheimer's Disease, and Neuroimaging Initiative (2013). Glucose metabolism during resting state reveals abnormal brain networks organization in the Alzheimer's disease and mild cognitive impairment. *PLoS One* 8:e68860. doi: 10.1371/journal.pone.0068860

Schaefer, A., Kong, R., Gordon, E. M., Laumann, T. O., Zuo, X. N., Holmes, A. J., et al. (2018). Local-global parcellation of the human cerebral cortex from intrinsic functional connectivity MRI. *Cereb. Cortex* 28, 3095–3114. doi: 10.1093/cercor/bhx179

Schroff, F., Kalenichenko, D., and Philbin, J. (2015). "Facenet: a unified embedding for face recognition and clustering," in *Proceedings of the IEEE Conference on Computer Vision and Pattern Recognition* (Piscataway, NJ: IEEE), 815–823.

Singh, S., Srivastava, A., Mi, L., Caselli, R. J., Chen, K., Goradia, D., et al. (2017). "Deep-learning-based classification of FDG-PET data for Alzheimer's disease categories," in *Proceedings of the 13th International Conference on Medical Information Processing and Analysis* (Bellingham, WA: International Society for Optics and Photonics). doi: 10.1117/12.2294537

Song, X., Zhou, F., Frangi, A. F., Cao, J., Xiao, X., Lei, Y., et al. (2021). Graph convolution network with similarity awareness and adaptive calibration for disease-induced deterioration prediction. *Med. Image Anal.* 69:101947. doi: 10.1016/j.media.2020.101947

Sörensen, A., Blazhenets, G., Rücker, G., Schiller, F., Meyer, P. T., Frings, L., et al. (2019). Prognosis of conversion of mild cognitive impairment to Alzheimer's dementia by voxel-wise Cox regression based on FDG PET data. *NeuroImage: Clin.* 21:101637. doi: 10.1016/j.nicl.2018.101637

Sundgaard, J. V., Harte, J., Bray, P., Laugesen, S., Kamide, Y., Tanaka, C., et al. (2021). Deep metric learning for otitis media classification. *Med. Image Anal.* 71:102034. doi: 10.1016/j.media.2021.102034

Titov, D., Diehl-Schmid, J., Shi, K., Perneczky, R., Zou, N., Grimmer, T., et al. (2017). Metabolic connectivity for differential diagnosis of dementing disorders. *J. Cereb. Blood Flow Metab.* 37, 252–262. doi: 10.1177/0271678X15622465

Tzourio-Mazoyer, N., Landeau, B., Papathanassiou, D., Crivello, F., Etard, O., Delcroix, N., et al. (2002). Automated anatomical labeling of activations in SPM using a macroscopic anatomical parcellation of the MNI MRI single-subject brain. *Neuroimage* 15, 273–289.

Wang, J., Zuo, X., Dai, Z., Xia, M., Zhao, Z., Zhao, X., et al. (2013). Disrupted functional brain connectome in individuals at risk for Alzheimer's disease. *Biol. Psychiatry* 73, 472–481. doi: 10.1016/j.biopsych.2012.03.026

Wang, M., Jiang, J., Yan, Z., Alberts, I., Ge, J., Zhang, H., et al. (2020). Individual brain metabolic connectome indicator based on Kullback-Leibler Divergence Similarity Estimation predicts progression from mild cognitive impairment to Alzheimer's dementia. *Eur. J. Nucl. Med. Mol. Imaging* 47, 2753–2764. doi: 10.1007/s00259-020-04814-x

Yang, Z., and Liu, Z. (2020). The risk prediction of Alzheimer's disease based on the deep learning model of brain 18F-FDG positron emission tomography. *Saudi J. Biol. Sci.* 27, 659–665. doi: 10.1016/j.sjbs.2019.12.004

Zhou, H., Jiang, J., Lu, J., Wang, M., Zhang, H., Zuo, C., et al. (2019). Dual-model radiomic biomarkers predict development of mild cognitive impairment progression to Alzheimer's disease. *Front. Neurosci.* 12:1045. doi: 10.3389/fnins.2018.01045

Zhou, P., Jiang, S., Yu, L., Feng, Y., Chen, C., Li, F., et al. (2021). Use of a sparse-response deep belief network and extreme learning machine to discriminate Alzheimer's disease, mild cognitive impairment, and normal controls based

on amyloid PET/MRI images. *Front. Med.* 7:621204. doi: 10.3389/fmed.2020.621204

Conflict of Interest: The authors declare that the research was conducted in the absence of any commercial or financial relationships that could be construed as a potential conflict of interest.

Publisher's Note: All claims expressed in this article are solely those of the authors and do not necessarily represent those of their affiliated organizations, or those of the publisher, the editors and the reviewers. Any product that may be evaluated in this article, or claim that may be made by its manufacturer, is not guaranteed or endorsed by the publisher.

frontiers | Frontiers in Neuroscience

REVIEW
published: 06 April 2022
doi: 10.3389/fnins.2022.812410

Neural Substrates of Poststroke Depression: Current Opinions and Methodology Trends

Chensheng Pan, Guo Li, Wenzhe Sun, Jinfeng Miao, Xiuli Qiu, Yan Lan, Yanyan Wang, He Wang, Zhou Zhu and Suiqiang Zhu**

Department of Neurology, Tongji Hospital, Tongji Medical College, Huazhong University of Science and Technology, Wuhan, China

Poststroke depression (PSD), affecting about one-third of stroke survivors, exerts significant impact on patients' functional outcome and mortality. Great efforts have been made since the 1970s to unravel the neuroanatomical substrate and the brain-behavior mechanism of PSD. Thanks to advances in neuroimaging and computational neuroscience in the past two decades, new techniques for uncovering the neural basis of symptoms or behavioral deficits caused by focal brain damage have been emerging. From the time of lesion analysis to the era of brain networks, our knowledge and understanding of the neural substrates for PSD are increasing. Pooled evidence from traditional lesion analysis, univariate or multivariate lesion-symptom mapping, regional structural and functional analyses, direct or indirect connectome analysis, and neuromodulation clinical trials for PSD, to some extent, echoes the frontal-limbic theory of depression. The neural substrates of PSD may be used for risk stratification and personalized therapeutic target identification in the future. In this review, we provide an update on the recent advances about the neural basis of PSD with the clinical implications and trends of methodology as the main features of interest.

Keywords: poststroke depression, neural substrate, lesion analysis, gray matter atrophy, regional brain activity, brain network, lesion-network mapping, disconnectome

OPEN ACCESS

Edited by:
Peng Wang,
Chinese Academy of Medical Sciences and Peking Union Medical College, China

Reviewed by:
Aaron Boes,
The University of Iowa, United States
Justin Reber,
University of Pennsylvania, United States

****Correspondence:***
Suiqiang Zhu
zhusuiqiang@163.com
Zhou Zhu
zhouzhu@hust.edu.cn

Specialty section:
This article was submitted to Brain Imaging Methods, a section of the journal Frontiers in Neuroscience

Received: *10 November 2021*
Accepted: *04 February 2022*
Published: *06 April 2022*

Citation:
Pan C, Li G, Sun W, Miao J, Qiu X, Lan Y, Wang Y, Wang H, Zhu Z and Zhu S (2022) Neural Substrates of Poststroke Depression: Current Opinions and Methodology Trends. Front. Neurosci. 16:812410. doi: 10.3389/fnins.2022.812410

INTRODUCTION

Poststroke depression (PSD) is a common complication of stroke, involving about 29% of patients at any time within 5 years poststroke (Ayerbe et al., 2013). PSD is associated with heavier healthcare burden, poorer functional outcome, and higher long-term mortality in stroke survivors (Robinson et al., 1986; Ghose et al., 2005; Jia et al., 2006; Ayerbe et al., 2013; Bartoli et al., 2013; Kutlubaev and Hackett, 2014). To aid in early prediction and effective intervention for PSD, its etiology and mechanisms need to be scrutinized. Based on accumulating evidence, it is generally believed that PSD has underlying neurobiological causes and is not only a psychosocial response to the new disability or stressful life event (Folstein et al., 1977; Towfighi et al., 2017; Mayman et al., 2021). The association between lesion location and PSD first reported in the 1970s (Robinson et al., 1975, 1983; Robinson and Price, 1982), although extensively investigated as a potential biological factor of PSD, is still of considerable debate (Nickel and Thomalla, 2017; Towfighi et al., 2017). Most of those studies were of traditional design with relatively low spatial accuracy for visual lesion localization (Nickel and Thomalla, 2017). Until 2003, a new technique called voxel-based lesion-symptom

mapping (VLSM) was developed to test the lesion–behavior correlation at the voxel level and has been widely used to identify the neural substrates of symptoms after focal brain damage such as PSD, poststroke cognitive impairment, poststroke dysphagia, and stroke-related myocardial injury (Bates et al., 2003; Ay et al., 2006; Kim et al., 2017; Hess et al., 2021; Weaver et al., 2021a). Moreover, there is a growing consensus that the rough lesion location used in traditional lesion analysis and the spatial topography information used in VLSM only represent the "tip of the iceberg": a surface-level depiction of the lesion largely blind to its impact on the underlying extensive brain networks (Catani et al., 2012; Fox, 2018). The brain network dysfunction caused by a given stroke lesion, instead of the lesion itself, might be the key neural substrate of poststroke symptoms especially when patients with the same symptom have lesions in various brain regions with little lesion overlap (Fox, 2018). Thanks to advances in neuroimaging techniques and statistical methodologies in the past two decades, lesion-symptom inference in high spatial resolution, with robust statistics and from the perspective of the human connectome, can be performed and new evidence for the neural substrates of PSD, beyond those findings from traditional studies, is emerging. In this review, we provide a brief summary of traditional studies and an update on the latest advances about the neural basis of PSD, which may shed light on the etiology, prediction, therapeutic target identification, and future research directions for PSD.

DEFINITION, DIAGNOSIS, AND MEASUREMENT OF POSTSTROKE DEPRESSION

The Diagnostic Statistical Manual of Mental Disorders-5 (DSM-5), as gold standard for PSD diagnosis, defines PSD as "depressive disorder due to another medical condition" with depressive features, major depressive-like episode, or mixed-mood features (American Psychiatric Association, 2013). Some aspects in DSM-5 criteria, such as "disturbance is the direct pathophysiological consequence of another medical condition," are almost impossible to prove in clinical practice (American Psychiatric Association, 2013). Therefore, the diagnosis of PSD relies on a thorough clinical interview with careful exploration of presenting symptoms and is commonly assisted by the use of screening tools (specifically the depression rating scales validated in PSD screening) (Chun et al., 2021). Although multiple depression scales have been applied and compared in previous studies, the optimal screening tool for PSD remains undetermined (Towfighi et al., 2017). One meta-analysis reported three scales as promising options with relatively high sensitivity and specificity in PSD screening: Center of Epidemiological Studies-Depression Scale (CESD), Hamilton Depression Rating Scale (HDRS), and Patient Health Questionnaire (PHQ)-9, compared with other scales including Geriatric Depression Scale (GDS), Hospital Anxiety and Depression Scale (HADS), and PHQ-2 (Meader et al., 2014). Another study found that HDRS, Beck Depression Inventory (BDI), and Clinical Global Impression (CGI) assessment by professionals showed similar performance in PSD screening (Berg et al., 2009). Of note, the optimal rating scale along with the optimal cutoff value for PSD diagnosis may vary across different stages after stroke (Berg et al., 2009), which warrants further investigation. The methods for PSD diagnosis or measurement in previous studies on the neural substrates of PSD are summarized in **Table 1**.

More recently, researchers on mental disorders tend to define depressive disorders as a complex symptom network. Both DSM-5 criteria and the sum score of a depression rating scale are based on the traditional "common cause" theory, assuming that depression as an entity causes various symptoms and these symptoms are interchangeable and diagnostically equivalent so that the number or severity of symptoms can be simply added up (Borsboom, 2008; Borsboom and Cramer, 2013; Fried and Cramer, 2017). The depressive symptoms, however, actually interact with each other in complex ways, which has long been common knowledge among clinicians (Borsboom, 2008; Borsboom and Cramer, 2013; Fried and Cramer, 2017). In the psychopathological network theory, mental disorders are conceptualized as dynamic and complex networks of symptoms influencing each other by creating causal pathways and feedback loops (e.g., depressed mood - > insomnia - > fatigue - > depressed mood, in depressive disorders) (Borsboom, 2008; Borsboom and Cramer, 2013; Fried and Cramer, 2017). Depressive symptom networks have been well established in neurologically healthy populations (van Borkulo et al., 2015; Belvederi Murri et al., 2020), and interactions among depressive symptoms may also exist in the stroke population (Ashaie et al., 2021). One recent study modeled poststroke depressive symptoms at three timepoints (discharge and 3 and 12 months after discharge) as networks in which depressed mood was consistently identified as a central symptom and might be responsible for triggering or sustaining the rest of symptoms *via* symptom–symptom interactions (Ashaie et al., 2021). Interestingly, the network structure and connectivity of poststroke depressive symptoms might vary across time after stroke (Ashaie et al., 2021). Accumulating evidence suggests that certain biological processes (e.g., inflammation and focal brain damage) may not be equally related to all depressive symptoms (Moriarity et al., 2022). Investigating risk factors and biomarkers for individual depressive symptoms has become a new research paradigm (Fried et al., 2014, 2020; Jokela et al., 2016; White et al., 2017; Triolo et al., 2021; Moriarity et al., 2022).

LESION LOCATION AND POSTSTROKE DEPRESSION

Traditional Lesion Analysis

The majority of the evidence about the association between lesion location and PSD is derived from traditional region-of-interest (ROI) analysis in which the lesion is assigned to overlap with a region or not by reviewing the scan without manual segmentation, followed by comparison for the prevalence of PSD in populations defined by the presence or absence of involvement of the ROI. The results from traditional studies before 2017 have been reviewed elsewhere and will not be redundantly

TABLE 1 | Study design and findings for studies on neural substrates of PSD.

Study	Imaging biomarker	Timing of behavioral assessment since lesion onset	Behavioral assessment method	Behavioral outcome	Regions or networks implicated	Results involving PFC
Traditional ROI analysis						
Nickel and Thomalla, 2017*	Lesion location	Varied*	Varied*	Varied*	Varied*	Yes, frontal lobe reported in 7/17 studies
Koenigs et al., 2008	Lesion location	More than 3 months	BDI-II, DSM-4, and NRS for one dataset; BDI-IA or BDI-II for another dataset	Ordinal (low, intermediate, or high severity)	Bilateral DLPFC	Yes
Lesion subtraction analysis						
Kim et al., 2017	Lesion location	Within 3 months	DSM-4 and GDS	Binary PSD diagnosis (DSM-4 met and GDS $>$ 16)	Inferior posterior lobe of the left cerebellar hemisphere	PFC not covered in study design
VLSM						
Gozzi et al., 2014	Lesion location	Within 12 days and at 1 month poststroke	DSM-4 and HADS	Binary PSD diagnosis (DSM-4 met and HADS $>$ 11)	Negative	No
Kim et al., 2017	Lesion location	Within 3 months	DSM-4 and GDS	Binary PSD diagnosis (DSM-4 met and GDS $>$ 16)	Posterior lobe of the left cerebellar hemisphere	PFC not covered in study design
Padmanabhan et al., 2019	Lesion location	Varied by five datasets with lesions of different etiologies including stroke; ranges from 28 days to 39 years	Varied by datasets: Neuro-QOL, GDSS, PHQ-9, HADS plus MINI, BDI-II	Binary PSD diagnosis (threshold varied by datasets: Neuro-QOL $\geq$ 59.9, GDSS $\geq$ 11, PHQ-9 $\geq$ 10, HADS $\geq$ 11 with DSM-4 net, BDI-II $\geq$ 20)	Negative	No
Multivariate LSM						
Grajny et al., 2016	Lesion location	At least 6 months	SADQ	Continuous sum score	Left DLPFC	Yes
Weaver et al., 2021b	Lesion location	Within 1 year, ranges from 1 to 361 days	GDS	Continuous sum score	Right amygdala and pallidum	No
VBM						
Shi et al., 2017	GMV	Ranges from 3 months to 1 year	DSM-4 and HDRS	Binary diagnosis (DSM-4 met and HDRS $>$ 17)	Bilateral PFC, limbic system and motor cortex	Yes
Hong et al., 2020	GMV	At least 6 months	DSM-4 and HDRS	Binary diagnosis (DSM-4 met and HDRS $>$ 7)	Left middle frontal gyrus	Yes
Regional functional activity						
Egorova et al., 2017	fALFF	3 months	PHQ-9	Both binary diagnosis (PHQ-9 $\geq$ 5) and continuous sum score	Left DLPFC and right precentral gyrus; left insula	Yes
Goodin et al., 2019	fALFF	3 months	MÅDRS	Binary (MÅDRS $>$ 8)	Frontostriatal, temporal, thalamic, and cerebellar regions	Yes
Direct connectome analysis						
Lassalle-Lagadec et al., 2012	rsFC	3 months	HDRS	Continuous sum score	Left middle temporal cortex and precuneus	No
Zhang P. et al., 2014	rsFC	Less than 2 weeks	DSM-4 and HDRS	Both binary diagnosis (HDRS $>$ 7) and continuous sum score	Increased rsFC between the left orbital part of the inferior frontal gyrus and ACC	Yes
Shi et al., 2017	rsFC	Ranges from 3 months to 1 year	DSM-4 and HDRS	Binary PSD diagnosis (DSM-4 met and HDRS $>$ 17)	Decreased rsFC of ACC with PFC, cingulate cortex, and motor cortex, but increased rsFC with the hippocampus, parahippocampal gyrus, insula, and amygdala	Yes
Vicentini et al., 2017	rsFC	Mean: 25 days	DSM-4 and BDI	Continuous BDI score	Left inferior parietal gyrus	No
Balaev et al., 2018	rsFC	7 $\pm$ 4 months	ADRS	Continuous sum score	Anterior DMN, salience network, left frontoparietal network	Yes

(Continued)

TABLE 1 | (Continued)

Study	Imaging biomarker	Timing of behavioral assessment since lesion onset	Behavioral assessment method	Behavioral outcome	Regions or networks implicated	Results involving PFC
Egorova et al., 2018	rsFC	3 months	PHQ-9	Both binary diagnosis (PHQ-9 $\geq$ 5) and continuous sum score	Decreased rsFC between left DLPFC and right supramarginal gyrus	Yes
Sun et al., 2018	rsFC	Mean: 3.6 months	HDRS	Ordinal (3 levels of severity: $\leq$5, 6–20, and >20)	Decreased rsFC between the parietal-occipital and the frontal areas	Yes
Zhang et al., 2018	rsFC	Mean: 10 days	DSM-4 and HDRS	Both binary diagnosis (HDRS > 7 with DSM-4 met) and continuous sum score	DMN, CCN, AN; left inferior parietal gyrus, the left orbital part of inferior frontal gyrus, and left angular gyrus	Yes
Zhang et al., 2019	rsFC	Less than 6 months	DSM-4 and HDRS	Both binary diagnosis (HDRS $\geq$ 17 with DSM-4 met) and continuous sum score	Altered rsFC of amygdala with the fronto-limbic-striatal circuit	Yes
Shi et al., 2019	Functional circuit	Ranges from 3 months to 1 year	DSM-4 and HDRS	Binary diagnosis (HDRS $\geq$ 17 with DSM-4 met)	Ventromedial PFC-ACC-amygdala-thalamus circuit	Yes
Liang et al., 2020	rsFC	3 months	GDS	Binary diagnosis (GDS $\geq$ 7)	DMN (inferior parietal lobule and dorsal prefrontal cortex)	Yes
Yang et al., 2015	FA; Structural network topology	Within 1 month	DSM-4 and HDRS	Ordinal: major, mild and non-PSD (HDRS $\geq$ 20, 10–19, <10, respectively)	Wide (including frontal) areas of white matter; a depression-related subnetwork composed of 17 brain regions (including frontal cortex)	Yes
Shen et al., 2019	FA, mean kurtosis	2 weeks	DSM-5 and HDRS	Binary PSD diagnosis based on DSM-5	Bilateral frontal and temporal lobes, genu of corpus callosum	Yes
Xu et al., 2019	Structural network topology	Within 2 weeks	DSM-4 and HDRS	Binary PSD diagnosis based on DSM-4 and HDRS $\geq$ 7	Disrupted global and local network topologies (involving ipsilesional superior frontal gyrus and middle frontal gyrus, etc.)	Yes
Oestreich et al., 2020	FA, structural network topology	27–82 days	GDS	Binary diagnosis (GDS $\geq$ 10)	Reward system (including PFC)	Yes
Indirect connectome analysis						
Padmanabhan et al., 2019	FDC	Varied by five datasets with lesions of different etiologies including stroke; ranges from 28 days to 39 years	Varied by datasets: Neuro-QOL, GDSS, PHQ-9, HADS plus MINI, BDI-II	Binary PSD diagnosis (threshold varied by datasets: Neuro-QOL $\geq$ 59.9, GDSS $\geq$ 11, PHQ-9 $\geq$ 10, HADS $\geq$ 11 with DSM-4 met, BDI-II $\geq$ 20)	A depression circuit centered on left DLPFC and spanning multiple regions (bilateral prefrontal, temporal and parietal)	Yes
Weaver et al., 2021b	SDC	Within 1 year, ranges from 1 to 361 days	GDS	Continuous sum score	Right parahippocampal white matter, right thalamus and pallidum, and right anterior thalamic radiation	Yes (anterior thalamic radiation originates from PFC)

ACC, anterior cingulate cortex; ADRS, aphasic depression rating scale; AN, affective network; BDI, Beck Depression Inventory; CCN, cognitive control network; DLPFC, dorsolateral prefrontal cortex; DMN, default mode network; DSM, Diagnostic Statistical Manual of Mental Disorders; fALFF, fractional amplitude of low frequency fluctuations; FA, fractional anisotropy; FDC, functional disconnection; GDS, Geriatric Depression Scale; GDSS, Geriatric Depression Score Short Form; GMV, gray matter volume; HADS, Hospital Anxiety and Depression Scale; HDRS, Hamilton Depression Rating Scale; LSM, lesion-symptom mapping; MÅDRS, Montgomery-Åsberg Depression Rating Scale; MINI, Mini-International Neuropsychiatric Interview; Neuro-QOL, Neuro-QOL Depression Scale; NRS, Neurobehavioral Rating Scale; PFC, prefrontal cortex; PHQ-9, Patient Health Questionnaire; PSD, poststroke depression; ROI, region of interest; rsFC, resting-state functional connectivity; SADQ; Stroke Aphasic Depression Questionnaire; SDC, structural disconnection; VBM, voxel-based morphometry; VLSM, voxel-based lesion-symptom mapping.
**The 17 traditional ROI studies reviewed by Nickel and Thomalla (2017) are not expanded in our table.*

described here (Nickel and Thomalla, 2017). In brief, the earliest notion that depression was more likely to be associated with left than with right hemispheric strokes and with lesions in the left anterior brain than with other regions (Robinson and Price, 1982; Starkstein et al., 1987) was not supported by other studies: some concluded with the association between PSD and right hemispheric strokes (MacHale et al., 1998; Wei et al., 2015), while others ended up with no association at all between lesion location and PSD (Carson et al., 2000; Kutlubaev and Hackett, 2014). No conclusion could be drawn regarding the role of lesion location (laterality, anterior–posterior gradient, within specific brain regions, etc.) in the etiology of PSD based on traditional evidence (Nickel and Thomalla, 2017). The traditional ROI approach has its intrinsic limitations. First, the association

between the ROI and PSD might be just a coincidence due to the coexisting involvement of other brain regions with common blood supply (so-called consistent error) (Ay et al., 2006; Mah et al., 2014). Second, the traditional approach dichotomizes the study sample with respect to involvement of a relatively large ROI, which precludes point localizations and may result in false negative results due to improper sampling or counterbalancing of effects among multiple small regions within a large ROI (Ay et al., 2006). Another traditional approach called lesion subtraction analysis is also used for lesion-symptom inference (Rorden and Karnath, 2004). Based on the hypothesis that the causative neural substrate is more frequently involved in patients with a specific symptom than in those without, the voxel-wise lesion incidence map of the non-PSD group is subtracted from that of the PSD group showing brain regions more frequently involved in PSD. One lesion subtraction study identified left cerebellar stroke to be correlated with PSD, which was consistent with the result of a subsequent VLSM analysis (Kim et al., 2017). However, the lesion subtraction plot alone may only provide a descriptive result of the possible neural substrate due to lack of statistical tests.

It is not surprising to get inconsistent results from traditional studies (and some other methods in the following text) given the heterogeneity in depression rating scales (**Table 1**), diverse timepoints of depression assessment since stroke onset (**Table 1**), small sample size, selection bias (e.g., exclusion for aphasia), different definitions of lesion location, inadequate imaging quality, combining lesions of various etiologies into a single analysis, and so on (Robinson and Jorge, 2016; Nickel and Thomalla, 2017; Towfighi et al., 2017). Of note, the interval between stroke onset and depression assessment might be an important factor exerting influence on the results of the traditional approach (and other methods as well). A longitudinal study focusing on depression at specific stages of stroke found that the association of PSD with left anterior lesions appeared to be a transient phenomenon restricted to the acute stage and the laterality tended to reverse to the right hemisphere in the long-term follow-up (Astrom et al., 1993). Another independent study also suggested that only in-hospital depression was associated with lesions in the left anterior hemisphere and depression at 1–2 years poststroke was associated with right-hemisphere lesion volume and lesion proximity to the occipital pole (Shimoda and Robinson, 1999). A meta-analysis with stratification by time of assessment showed that the association between right hemispheric stroke and PSD only existed at the subacute stage of stroke (Wei et al., 2015). It is conceivable that the neuroanatomic substrates of PSD might change over time or there might be distinct mechanisms for PSD at different stages of stroke (Astrom et al., 1993; Shimoda and Robinson, 1999). Therefore, studies mixing patients of various stages poststroke tend to produce inconsistent and unreliable results and performing PSD assessments at homogeneous stages after stroke might be helpful in future studies. Although inconclusive, some researchers still believe that there is an association between left frontal strokes and PSD within the first 2 months after stroke based on some converging evidence (Astrom et al., 1993; Shimoda and Robinson, 1999; Rajashekaran et al., 2013; Robinson and Jorge, 2016). The role of the left prefrontal cortex (PFC) in PSD was further supported by multiple clinical trials showing that repetitive transcranial magnetic stimulation (rTMS) targeted at the left dorsolateral PFC (DLPFC) can significantly alleviate the symptoms of PSD and vascular depression (Jorge et al., 2004; McIntyre et al., 2016; Gu and Chang, 2017; Shen et al., 2017; Frey et al., 2020).

Voxel-Based and Multivariate Lesion-Symptom Mapping

The general procedure of VLSM analysis involves lesion segmentation on computed tomography (CT) or magnetic resonance imaging (MRI) scans, spatial normalization of lesion masks, mass-univariate statistical tests voxel by voxel for the association between lesion status at a given voxel and presence or severity of the symptom of interest, correction for multiple comparisons to control false positive rates, and interpretation of the significant clusters. Three lesion-symptom mapping (LSM) studies on PSD before 2017 did not provide consistent results, as described in the previous review (Nickel and Thomalla, 2017). The first study showed negative results, and another two identified lesions in the left cerebellum and left DLPFC, respectively, as the neural substrates of PSD (Gozzi et al., 2014; Grajny et al., 2016; Kim et al., 2017). These are considered as pilot exploratory LSM studies with small sample size ($n < 100$) and therefore low statistical power (Nickel and Thomalla, 2017). Another study in 2019 which performed VLSM in five datasets (total $n = 461$) with focal brain damage of various etiologies (including stroke) failed to find any lesion location to be correlated with depression after brain damage (but did identify a functional depression circuit *via* connectome analysis) (Padmanabhan et al., 2019). Generally, only voxels with lesion incidence above a certain threshold (e.g., at least 10 patients or 5% of patients, indicating sufficient lesion affection) could be included in VLSM to ensure reasonable statistical power and anatomical validity (Medina et al., 2010; Sperber and Karnath, 2017). Small sample size tends to provide insufficient lesion coverage, leaving those infrequently involved brain regions with lower statistical power or being unexplored (Kimberg et al., 2007; Gozzi et al., 2014). Indeed, a large sample size will be required if we want to perform whole-brain VLSM analysis without predefined ROIs, considering the recent evidence that about 3,000 subjects were needed to achieve a lesion coverage of 86% of total brain voxels (Weaver et al., 2021a). The original VLSM approach with mass-univariate tests still suffers the aforementioned consistent error originating from collateral vasculature (Mah et al., 2014; Karnath et al., 2018). The latest machine learning-based multivariate LSM approaches, believed to be able to overcome this limitation, seem as promising alternatives in future studies (Mah et al., 2014; Karnath et al., 2018). One multivariate LSM study mentioned above applied support vector regression-based LSM (SVR-LSM) and found the association between lesions in the left DLPFC and severity of poststroke depressive symptoms (PSDS; Zhang Y. et al., 2014; Grajny et al., 2016). Another recent SVR-LSM study found that infarcts in the right amygdala, right pallidum, and right hippocampus

were associated with PSDS (Weaver et al., 2021b). External validation confirmed the association between infarcts in the right amygdala and pallidum, but not the right hippocampus, and PSDS (Weaver et al., 2021b). Another latest method named multivariate sparse canonical correlations technique (SCCAN), generally superior to the univariate approach at small sample sizes, may also be recommended in future studies (Pustina et al., 2018). Some neural substrates unlikely to be identified with the univariate approach may be unveiled with multivariate LSM which integrates lesion information from multiple voxels simultaneously in lesion-symptom inference (Karnath et al., 2018). Multivariate approaches are preferred if we have good reasons to assume that the symptom of interest is represented in an extensively distributed brain network, as in these cases the ability of the univariate approach to detect all of the network modules may be limited (Karnath et al., 2018; Xu et al., 2018). Based on current LSM studies showing non-convergent results, the role of lesion location in the etiology of PSD still warrants further investigation with large datasets and advanced methodologies.

REGIONAL STRUCTURAL AND FUNCTIONAL ABNORMALITIES AND POSTSTROKE DEPRESSION

Gray matter atrophy may serve as a transdiagnostic neural substrate for various mental illnesses (Goodkind et al., 2015). Voxel-based morphometry (VBM) is able to evaluate the intergroup difference of gray matter volume (GMV) at the voxel level using high-resolution structural MRI (sMRI; Ashburner and Friston, 2000). The procedure of VBM involves spatially normalizing and segmenting sMRI images into the same standard space (Ashburner and Friston, 2000). The gray matter segments are smoothed so that each voxel represents the average of itself and its neighbors (Ashburner and Friston, 2000). Parametric statistical tests are performed at the voxel level, followed by corrections for multiple comparisons with the theory of random fields (Ashburner and Friston, 2000). One study performed VBM analysis in 30 first-ever ischemic frontal stroke patients showing that decreased GMV in PSD was mainly observed in the prefrontal-limbic system and motor cortex compared with non-PSD patients (Shi et al., 2017). The involved limbic structures were mainly located in the right hemisphere, and the PFC showed a decreased GMV in both hemispheres (Shi et al., 2017). Recent evidence from another VBM study in 23 PSD and 33 non-PSD subcortical stroke patients suggested that the PSD group had significantly decreased GMV in the left middle frontal gyrus (MFG; Hong et al., 2020). Together with the clinical-demographic variables, the MFG's GMV prediction model was able to distinguish PSD from non-PSD with high sensitivity and specificity (Hong et al., 2020). The results from VBM studies are in accordance with the aforementioned role of the frontal cortex in PSD, as well as the frontal-limbic model which is well-recognized in depressive disorders such as major depressive disorder (MDD) and vascular depression (Taylor et al., 2013; Lai, 2021).

Resting-state functional MRI (rs-fMRI), reflecting brain activation *via* blood oxygenation level-dependent (BOLD) signal, has been widely used in research of neuropsychiatric disorders including stroke and depression (Ovadia-Caro et al., 2014; Oathes et al., 2015). Several measurements, such as amplitude of low-frequency fluctuations (ALFF) and fractional ALFF (fALFF), were developed to reflect the characteristics of spontaneous brain activity within a brain region (Zang et al., 2007; Zou et al., 2008). One rs-fMRI study performed in 64 participants at 3 months poststroke found significantly higher fALFF in PSD in the left DLPFC and the right precentral gyrus compared with non-PSD patients and a significant association between higher PSD severity and higher fALFF in the left insula (Egorova et al., 2017). The aberrant regional brain activity could be a more sensitive feature than lesion location and volume to characterize PSD in small samples (Egorova et al., 2017). Another rs-fMRI study identified a significant correlation between PSD severity and fALFF in frontostriatal, temporal, thalamic, and cerebellar regions (Goodin et al., 2019). These fMRI results also provided evidence for the role of the frontal-limbic system in PSD. However, functional neuroimaging is time-consuming and vulnerable to head motions which is difficult to control in stroke patients (Ovadia-Caro et al., 2014; Fox, 2018). Another major limitation of fMRI studies is that they can hardly be used for causal inference (Fox, 2018). Unlike visual or voxel-based lesion analyses which have a clear temporal order between lesion and PSD, fMRI analysis typically has neuroimaging performed at the time of or after PSD diagnosis for a case–control comparison. Therefore, whether this functional difference between PSD and non-PSD is causative, or whether it is a reactive or adaptive alteration to depression, remains elusive (Fox, 2018). The results from fMRI analyses should be regarded as correlation rather than causation (Fox, 2018). Future studies with longitudinal design might unravel the potential causal relationship between gray matter atrophy, regional functional abnormality, and development of PSD.

BRAIN NETWORK DISRUPTION AND POSTSTROKE DEPRESSION

Based on large amounts of lesion studies, the lesions of PSD patients fail to overlap in a single brain region. It has long been discovered that some neuropsychiatric symptoms can result from dysfunctions of anatomically intact brain regions which are distant but connected to the lesion ("diaschisis" phenomenon) (Carrera and Tononi, 2014). In the era of brain networks and human connectome, we have good reasons to assume that PSD might be a complex disconnection syndrome resulting from disruption of networks of interacting brain regions (Gong and He, 2015). There are two types of brain connectivity being explored. Functional connectivity (FC) is measured by the correlation of the fMRI BOLD time series between brain regions, and structural (or anatomical) connectivity (SC) can be derived from diffusion tensor imaging (DTI) in which water diffuses more freely along white matter fibers than across them (Fox and Raichle, 2007; Jbabdi et al., 2015). Brain networks can be analyzed at different levels: microscale (single neuron and synapses),

mesoscale (neuronal groups), and macroscale (brain regions and inter-region pathways) (Sporns et al., 2005). Quantitative analysis, especially graph theory analysis, can reveal important features of complex networks such as highly connected hubs, modularity, and small-world topology (Bullmore and Sporns, 2009; He and Evans, 2010). Importantly, these quantifiable network features were found to change in normal development, aging, and various neuropsychiatric disorders (He and Evans, 2010; Menon, 2011; Ovadia-Caro et al., 2014). With both FC and SC techniques, complex symptoms like PSD that transcend localization to single brain regions may be mapped to widely distributed brain networks.

Direct Connectome Analysis

Typically, the FC is directly derived from each patient's fMRI scans. One study in frontal stroke patients performed connectivity analysis with the anterior cingulate cortex (ACC) as the seed found decreased resting-state FC (rsFC) with the PFC, cingulate cortex, and motor cortex, but increased rsFC with the hippocampus, parahippocampal gyrus, insula, and amygdala, in the PSD group (Shi et al., 2017). Another study in temporal stroke patients found that the left amygdala had increased rsFC with the bilateral precuneus and right orbital frontal lobe but decreased rsFC with the right putamen in PSD compared with non-PSD patients (Zhang et al., 2019). The right amygdala had increased rsFC with the right temporal pole, right rectus gyrus, and left orbital frontal lobe but decreased rsFC with the right primary sensory area (S1) (Zhang et al., 2019). The amygdala's rsFCs with the right orbital frontal cortex, right insula, and right cingulate cortex were correlated with the HDRS score (Zhang et al., 2019). A multivariate Granger causality analysis in right frontal ischemic stroke patients found an emotional circuit (composed of ventromedial PFC, ACC, amygdala, and thalamus) to explain the network alterations in PSD (Shi et al., 2019). The DLPFC could predict the activity of the ACC *via* the temporal pole, and the activity of the insula could be regulated negatively by the thalamus *via* ACC (Shi et al., 2019). Altered rsFC of the default mode network (DMN), cognitive control network (CCN), and affective network (AN) was observed in PSD compared with non-PSD patients and normal comparisons (NC; Zhang et al., 2018). The left orbital part of the inferior frontal gyrus, the left inferior parietal gyrus, and the left angular gyrus (which indicated altered rsFCs) were significantly correlated with HDRS scores in PSD patients (Zhang et al., 2018). Dysfunction of the AN in PSD was also observed in another study which found that the rsFCs of the left inferior temporal gyrus, the left orbital part of the inferior frontal gyrus, and the right triangular part of the inferior frontal gyrus were increased with the ACC in PSD compared with non-PSD stroke patients (Zhang P. et al., 2014). Moreover, the rsFC between the left orbital part of the inferior frontal gyrus and ACC was positively correlated with PSD severity (Zhang P. et al., 2014). As for the CCN, PSD was associated with decreased rsFC between left DLPFC and right supramarginal gyrus (Egorova et al., 2018). Graph theory analysis found that the DMN configuration (especially at core hubs such as dorsal PFC and inferior parietal lobule) might be more essential in the pathogenesis of PSD than stroke lesions (Liang et al., 2020). RsFC between anterior DMN and salience network positively correlated with PSD severity, and rsFC between anterior DMN and left frontoparietal network decreased after treatment of PSD (Balaev et al., 2018). Earlier evidence suggested that DMN dysfunction soon after stroke was predictive of PSD severity at 3 months poststroke (Lassalle-Lagadec et al., 2012). Both PSD and poststroke anxiety was found to be associated with DMN disruption (Vicentini et al., 2017). Depression symptoms were found to be correlated with increased rsFC in the left inferior parietal gyrus (Vicentini et al., 2017). Other than fMRI, electroencephalography (EEG) can also be used for rsFC analysis. In one study using mutual information-based graph theory analysis on EEG data, stroke patients showed a decreasing trend in the rsFC between the parietal–occipital and the frontal areas as PSD severity increased (Sun et al., 2018). These functional studies provided promising evidence for the role of emotion- and cognition-related networks in PSD, of which the clinical applicability is yet to be determined considering the complexity of brain networks. Furthermore, most rs-fMRI studies lack the ability of causal inference but reveal a correlation instead as discussed in the previous section (Rorden and Karnath, 2004; Fox, 2018). A functional alteration may be the result of compensation for PSD rather than its cause, and treatment strategies suppressing the alteration could make the symptom worse (Fox, 2018). Targeting the region where brain activity is correlated with but not causally related to PSD may have no effect at all (Fox, 2018). These ambiguities, along with the susceptibility to motion artifacts, make it difficult to translate fMRI correlates directly with therapeutic targets (Rorden and Karnath, 2004; Ovadia-Caro et al., 2014; Fox, 2018).

Direct SC analysis is typically based on each patient's DTI scans. SC at the neuronal level is the densely distributed axonal streamlines within white matter to connect gray matter regions. Regions that are structurally connected tend to also be functionally connected; however, FC presents a different pattern than SC due to the impact of extensive polysynaptic connections (Fox and Raichle, 2007; Fornito et al., 2015). Recent evidence suggested that the functional brain network dysfunction after stroke can be explained by structural disconnection (SDC; Griffis et al., 2019, 2020). Therefore, SDC could be a more upstream neural substrate of PSD than functional network dysfunction. One study used fractional anisotropy (FA) to reflect white matter integrity and found that the mean FA of the intact areas of stroke-lesioned tracts was lower than that of completely intact fiber tracts (Yang et al., 2015). FA reductions were observed in wide areas of white matter in PSD compared with non-PSD (Yang et al., 2015). Graph theory analysis revealed that decreased local efficiency of a depression-related subnetwork was a significant risk factor for major depression poststroke (Yang et al., 2015). Another study suggested that aberrant global and local structural network topologies might contribute to the development and severity of PSD (Xu et al., 2019). Recent evidence showed that reduced FA, along with increased extracellular free water (a marker of neuroinflammation) and GMV loss, in the reward system was predictive of PSD (Oestreich et al., 2020). However, one major limitation of FA and tractography analysis lies in their susceptibility to complex brain architecture such as fiber crossing (Mori and van Zijl, 2002; Jeurissen et al., 2013). For example,

FA may be actually increased after microstructural disruption in regions of fiber crossing. The diffusion tensor model can account only for the Gaussian diffusion process which is not always the case in the human brain and the fiber crossing issue should not be overlooked in future DTI studies (Jeurissen et al., 2013). Diffusion kurtosis imaging (DKI), applying a more complex model than DTI to quantify non-Gaussian water diffusion and reveal complex microstructures, was also used to investigate the role of white matter integrity in PSD (Jensen et al., 2005). DKI may be useful for unveiling abnormalities in isotropic structures, such as fiber crossing and gray matter, where DTI is less applicable (Jensen et al., 2005). One DKI study found that the FA value of the left frontal lobe and the mean kurtosis (MK) value of the bilateral frontal and temporal lobes and genu of the corpus callosum were significantly decreased in PSD compared with non-PSD patients and NC (Shen et al., 2019). Concerning the relationship between the structural and functional networks in PSD, one study identified the SC-FC coupling as a potential biomarker of PSD (Zhang et al., 2021).

Indirect Atlas-Based Connectome Analysis

Thanks to great efforts such as the Human Connectome Project, connectome atlases of averaged FC and SC patterns from hundreds or thousands of normal populations are now readily available (Glasser et al., 2016). Beyond lesion analysis, we can now combine lesion data with connectome atlases to map the network substrates for PSD without specialized neuroimaging for each individual (Boes et al., 2015; Fox, 2018).

Lesion-network mapping (LNM), a technique to combine lesion with normative functional connectome, generally involves three steps: translating the three-dimensional lesion into the standard space; estimating FC of the lesion with the rest of the brain using normative functional connectome atlas; and overlapping or statistically comparing FC maps derived from patients with the same symptom to identify regions common to the syndrome of interest (Boes et al., 2015; Fox, 2018). LNM is becoming increasingly popular in recent years to map the strategic network substrates of various conditions such as PSD, poststroke behavioral deficits, and mania after brain damage (Padmanabhan et al., 2019; Cotovio et al., 2020; Salvalaggio et al., 2020). A recent LNM study suggested that the lesion locations associated with depression after focal brain damage could be mapped to a human depression circuit centered on left DLPFC (Padmanabhan et al., 2019). Three rTMS targets reported to be effective in treating PSD fell within this circuit (Padmanabhan et al., 2019). A similar method named "dys-connectome" or disconnectome has been used to map the structural network substrates for PSD, poststroke behavioral deficits, poststroke fatigue, and so on (Salvalaggio et al., 2020; Ulrichsen et al., 2021; Weaver et al., 2021b). Powerful tools, such as BCBtoolkit and Lesion Quantification Toolkit, allow researchers to indirectly estimate SDCs with the lesions embedded in the structural connectome atlas and then perform disconnection-symptom inference at tract or voxel levels (Foulon et al., 2018; Griffis et al., 2021). Recent evidence from a multivariate disconnection-symptom mapping study found that SDCs in the right parahippocampal white matter, right thalamus and pallidum, and right anterior thalamic radiation were significantly associated with PSDS (Weaver et al., 2021b).

The atlas-based approach, without need for specialized neuroimaging, may prove a broadly applicable and versatile way for understanding the neural basis of neuropsychiatric symptoms after focal brain damage (Boes et al., 2015; Fox, 2018). However, the atlas-based approach does not necessarily reveal the actual disconnection patterns (Weaver et al., 2021b). The connectome architecture has its intrinsic individual variability (Mueller et al., 2013). It should also be noted that concomitant conditions, other than the stroke lesion, may have impact on brain networks. For example, cerebral small vessel disease (CSVD) is common in elderly stroke patients and can increase the risk of PSD (Tang et al., 2010, 2014; Bae et al., 2019; Liang et al., 2019). Moreover, structural network disruption was observed in CSVD compared with NC (Xie et al., 2017; Lawrence et al., 2018). The impact on the brain network from concomitant factors with inter-person variability may only be taken into account by direct connectome analysis. In terms of causal inference, lesion network maps span several regions at all levels of the neuro-axis and the extent to which any of them are causal to the symptoms is unknown and would require other complementary approaches. The indirect nature of the atlas-based approach requires confirmation and complementation by other methods including direct mapping of residual structural and functional connections in the patients (Salvalaggio et al., 2020; Bobes et al., 2021; Boes, 2021).

DISCUSSION: FUTURE DIRECTIONS AND CLINICAL IMPLICATIONS

Studies reviewed in this work are summarized in **Table 1** regarding study design and findings. From the time of lesion analysis to the era of brain networks, our knowledge and understanding of the neural substrates for PSD are increasing. Pooled evidence (**Table 1**) from traditional lesion analysis, univariate or multivariate LSM, regional structural and functional analyses, and connectome analysis, to some extent, echoes the frontal-limbic theory described in multiple depressive disorders including MDD and vascular depression (Taylor et al., 2013; Robinson and Jorge, 2016; Lai, 2021). Despite differences in etiology and symptom profile (da Rocha e Silva et al., 2013; Albert, 2018), PSD and MDD may share the common neural basis. As shown in **Table 1**, the PFC as replicated across studies of various methodologies may be the structure most heavily implicated in the pathogenesis of PSD. The role of PFC in depressive disorders has been confirmed by multiple clinical trials, showing that rTMS targeted at the left DLPFC can significantly alleviate the symptoms of PSD, vascular depression, and MDD (Jorge et al., 2004; O'Reardon et al., 2007; George et al., 2010; McIntyre et al., 2016; Gu and Chang, 2017; Shen et al., 2017; Frey et al., 2020; Sackeim et al., 2020). We believe that the PFC is most promising as the avenue for future research or the target for treatment of PSD and other depressive disorders.

The distinct roles of subregions of the PFC in mood regulation (Koenigs et al., 2008) and the optimal stimulation target within PFC for neuromodulation therapy are yet to be scrutinized. To date, the definite neural substrates of PSD along with their clinical applications still entail further investigation. Patients with focal brain damage have long been proper study samples for understanding human brain-behavior mechanisms (Fox, 2018; Vaidya et al., 2019), and the findings from research on PSD may also be generalized to depressive disorders in neurologically healthy population.

To improve inter-study consistency and accumulate further evidence, we provide some suggestions for future studies in the field. First, in addition to DSM-5 criteria, researchers may apply a validated depression rating scale with a consistent cutoff value for PSD diagnosis (Berg et al., 2009). Scales that can be generalized to patients with aphasia may be recommended to reduce bias in patient selection (Cobley et al., 2012). Second, serial assessments of depression status (and neuroimaging if necessary) at acute, subacute, and chronic stages of stroke are performed to uncover the potentially dynamic neural substrates of PSD across various stages after stroke. Third, LSM and connectome studies in multicentric large datasets with cross or external validation are recommended to derive comprehensive maps for the strategic lesion locations and disconnection patterns for PSD. Fourth, the neural substrates of PSD at the individual symptom level are uncovered, rather than simply using a binary PSD diagnosis or a continuous sum score. Note that depressive symptoms may have different risk factors and biomarkers (Fried et al., 2014; Moriarity et al., 2022), and the neural substrates of PSD may also be symptom-specific. The symptom-specific anatomical correlates, as well as the complex and dynamic pattern of symptom-symptom interactions, may help us better understand the brain-behavior mechanisms of PSD. Fifth, preregistration of anatomical hypotheses may add rigor to this field. The anatomical hypothesis and analysis plan before observing the research outcomes are defined to prevent problematic research practices such as false positive results from p-hacking and publication bias (Nosek et al., 2018, 2019).

Understanding the neural substrates for PSD is of great predictive value. For example, the strategic lesion locations and disconnection patterns for PSD can be used to develop prediction models for risk stratification and early intervention (Munsch et al., 2016; Salvalaggio et al., 2020; Weaver et al., 2021a,b). Only a few PSD prediction models based on routine clinical-demographic data have been developed and validated (de Man-van Ginkel et al., 2013; Hirt et al., 2020). Stroke severity, physical disability, history of depression, and cognitive impairment have been the most well-recognized predictors of PSD (Towfighi et al., 2017). Sex, age, education level, social support, and personality traits (e.g., neuroticism) are also considered potential (although less clear) predictors of PSD (Towfighi et al., 2017; Chun et al., 2021). A previous study found that both functional dependence and neuroanatomical measures were correlated with more PSD symptoms (Singh et al., 2000). Although inferior frontal lesion location was a risk factor of PSD, the degree of functional dependence imparted the greatest risk (Singh et al., 2000). To date, no imaging predictor is found to outperform classic clinical-demographic variables in PSD prediction. Considering the biopsychosocial multifactorial nature of PSD, incorporating neural substrates into clinical-demographic predictors might be a good choice in PSD prediction (Munsch et al., 2016; Towfighi et al., 2017; Hong et al., 2020). Moreover, advances in methodology as detailed above may provide new promising imaging predictors for PSD in the future. The neural substrates of PSD also have significant preventive and therapeutic value. Many studies (**Table 1**) can provide convergent evidence for the role of PFC in PSD and therefore the effectiveness of rTMS targeted on left DLPFC. Future studies on brain networks might find personalized preventive or therapeutic targets for PSD based on human connectome (e.g., an emerging technique called connectomic neuromodulation) (Cocchi and Zalesky, 2018; Fox, 2018; Horn and Fox, 2020; Siddiqi et al., 2020). The optimal individualized stimulation site may provide enhanced response to neuromodulation therapy for depression (Cash et al., 2019, 2021). Of note, distinguishing adaptive brain alterations to PSD from causative neural substrates is of great importance in future studies because strategies to inhibit the adaptive changes may lead to exacerbation of PSD (Fox, 2018). Moreover, the techniques reviewed here for uncovering neural substrate can also be extended to clinical research for a broad range of disorders with focal brain damage.

AUTHOR CONTRIBUTIONS

SZ and ZZ led the study and reviewed and edited the final manuscript. GL, WS, JM, XQ, YL, YW, and HW searched and collected the literature. CP prepared the original draft. All authors contributed to the article and approved the submitted version.

FUNDING

This work was funded by the National Key R&D Program of China (grant number 2017YFC1310000), Hubei Technological Innovation Special Fund (grant number 2019ACA132), and National Natural Science Foundation of China (grant numbers 82101605 and 82171465).

REFERENCES

Albert, P. R. (2018). Is poststroke depression the same as major depression? *J. Psychiatry Neurosci.* 43, 76–78. doi: 10.1503/jpn.180015

American Psychiatric Association (2013). *Diagnostic and Statistical Manual of Mental Disorders*, 5th Edn. Washington, DC: American Psychiatric Association. doi: 10.1176/appi.books.9780890425596

Ashaie, S. A., Hung, J., Funkhouser, C. J., Shankman, S. A., and Cherney, L. R. (2021). Depression over time in persons with stroke: a network analysis approach. *J. Affect. Disord. Rep.* 4:100131. doi: 10.1016/j.jadr.2021.100131

Ashburner, J., and Friston, K. J. (2000). Voxel-based morphometry–the methods. *Neuroimage* 11(6 Pt. 1), 805–821. doi: 10.1006/nimg.2000.0582

Astrom, M., Adolfsson, R., and Asplund, K. (1993). Major depression in stroke patients. A 3-year longitudinal study. *Stroke* 24, 976–982. doi: 10.1161/01.str.24.7.976

Ay, H., Koroshetz, W. J., Benner, T., Vangel, M. G., Melinosky, C., Arsava, E. M., et al. (2006). Neuroanatomic correlates of stroke-related myocardial injury. *Neurology* 66, 1325–1329. doi: 10.1212/01.wnl.0000206077.13705.6d

Ayerbe, L., Ayis, S., Wolfe, C. D., and Rudd, A. G. (2013). Natural history, predictors and outcomes of depression after stroke: systematic review and meta-analysis. *Br. J. Psychiatry* 202, 14–21. doi: 10.1192/bjp.bp.111.107664

Bae, K. Y., Kang, H. J., Kim, J. W., Kim, S. W., Kim, J. T., Park, M. S., et al. (2019). Associations of white matter hyperintensities with poststroke depression: a 1-year longitudinal study. *Int. J. Geriatr. Psychiatry* 34, 162–168. doi: 10.1002/gps.5005

Balaev, V., Orlov, I., Petrushevsky, A., and Martynova, O. (2018). Functional connectivity between salience, default mode and frontoparietal networks in post-stroke depression. *J. Affect. Disord.* 227, 554–562. doi: 10.1016/j.jad.2017.11.044

Bartoli, F., Lillia, N., Lax, A., Crocamo, C., Mantero, V., Carra, G., et al. (2013). Depression after stroke and risk of mortality: a systematic review and meta-analysis. *Stroke Res. Treat.* 2013:862978. doi: 10.1155/2013/862978

Bates, E., Wilson, S. M., Saygin, A. P., Dick, F., Sereno, M. I., Knight, R. T., et al. (2003). Voxel-based lesion-symptom mapping. *Nat. Neurosci.* 6, 448–450. doi: 10.1038/nn1050

Belvederi Murri, M., Amore, M., Respino, M., and Alexopoulos, G. S. (2020). The symptom network structure of depressive symptoms in late-life: results from a European population study. *Mol. Psychiatry* 25, 1447–1456. doi: 10.1038/s41380-018-0232-0

Berg, A., Lonnqvist, J., Palomaki, H., and Kaste, M. (2009). Assessment of depression after stroke: a comparison of different screening instruments. *Stroke* 40, 523–529. doi: 10.1161/STROKEAHA.108.527705

Bobes, M. A., Van den Stock, J., Zhan, M., Valdes-Sosa, M., and de Gelder, B. (2021). Looking beyond indirect lesion network mapping of prosopagnosia: direct measures required. *Brain* 144:e75. doi: 10.1093/brain/awab276

Boes, A. D. (2021). Lesion network mapping: where do we go from here? *Brain* 144:e5. doi: 10.1093/brain/awaa350

Boes, A. D., Prasad, S., Liu, H., Liu, Q., Pascual-Leone, A., Caviness, V. S. Jr., et al. (2015). Network localization of neurological symptoms from focal brain lesions. *Brain* 138(Pt. 10), 3061–3075. doi: 10.1093/brain/awv228

Borsboom, D. (2008). Psychometric perspectives on diagnostic systems. *J. Clin. Psychol.* 64, 1089–1108. doi: 10.1002/jclp.20503

Borsboom, D., and Cramer, A. O. (2013). Network analysis: an integrative approach to the structure of psychopathology. *Annu. Rev. Clin. Psychol.* 9, 91–121. doi: 10.1146/annurev-clinpsy-050212-185608

Bullmore, E., and Sporns, O. (2009). Complex brain networks: graph theoretical analysis of structural and functional systems. *Nat. Rev. Neurosci.* 10, 186–198. doi: 10.1038/nrn2575

Carrera, E., and Tononi, G. (2014). Diaschisis: past, present, future. *Brain* 137(Pt. 9), 2408–2422. doi: 10.1093/brain/awu101

Carson, A. J., MacHale, S., Allen, K., Lawrie, S. M., Dennis, M., House, A., et al. (2000). Depression after stroke and lesion location: a systematic review. *Lancet* 356, 122–126. doi: 10.1016/S0140-6736(00)02448-X

Cash, R. F. H., Cocchi, L., Lv, J., Fitzgerald, P. B., and Zalesky, A. (2021). Functional magnetic resonance imaging-guided personalization of transcranial magnetic stimulation treatment for depression. *JAMA Psychiatry* 78, 337–339. doi: 10.1001/jamapsychiatry.2020.3794

Cash, R. F. H., Zalesky, A., Thomson, R. H., Tian, Y., Cocchi, L., and Fitzgerald, P. B. (2019). Subgenual functional connectivity predicts antidepressant treatment response to transcranial magnetic stimulation: independent validation and evaluation of personalization. *Biol. Psychiatry* 86, e5–e7. doi: 10.1016/j.biopsych.2018.12.002

Catani, M., Dell'acqua, F., Bizzi, A., Forkel, S. J., Williams, S. C., Simmons, A., et al. (2012). Beyond cortical localization in clinico-anatomical correlation. *Cortex* 48, 1262–1287. doi: 10.1016/j.cortex.2012.07.001

Chun, H. Y., Ford, A., Kutlubaev, M. A., Almeida, O. P., and Mead, G. E. (2021). Depression, anxiety, and suicide after stroke: a narrative review of the best available evidence. *Stroke* doi: 10.1161/STROKEAHA.121.035499 [Epub ahead of print].

Cobley, C. S., Thomas, S. A., Lincoln, N. B., and Walker, M. F. (2012). The assessment of low mood in stroke patients with aphasia: reliability and validity of the 10-item Hospital version of the Stroke Aphasic Depression Questionnaire (SADQH-10). *Clin. Rehabil.* 26, 372–381. doi: 10.1177/0269215511422388

Cocchi, L., and Zalesky, A. (2018). Personalized transcranial magnetic stimulation in psychiatry. *Biol. Psychiatry Cogn. Neurosci. Neuroimaging* 3, 731–741. doi: 10.1016/j.bpsc.2018.01.008

Cotovio, G., Talmasov, D., Barahona-Correa, J. B., Hsu, J., Senova, S., Ribeiro, R., et al. (2020). Mapping mania symptoms based on focal brain damage. *J. Clin. Invest.* 130, 5209–5222. doi: 10.1172/JCI136096

da Rocha e Silva, C. E., Alves Brasil, M. A., Matos do Nascimento, E., de Braganca Pereira, B., and Andre, C. (2013). Is poststroke depression a major depression? *Cerebrovasc. Dis.* 35, 385–391. doi: 10.1159/000348852

de Man-van Ginkel, J. M., Hafsteinsdottir, T. B., Lindeman, E., Ettema, R. G., Grobbee, D. E., and Schuurmans, M. J. (2013). In-hospital risk prediction for post-stroke depression: development and validation of the Post-stroke Depression Prediction Scale. *Stroke* 44, 2441–2445. doi: 10.1161/STROKEAHA.111.000304

Egorova, N., Cumming, T., Shirbin, C., Veldsman, M., Werden, E., and Brodtmann, A. (2018). Lower cognitive control network connectivity in stroke participants with depressive features. *Transl. Psychiatry* 7:4. doi: 10.1038/s41398-017-0038-x

Egorova, N., Veldsman, M., Cumming, T., and Brodtmann, A. (2017). Fractional amplitude of low-frequency fluctuations (fALFF) in post-stroke depression. *Neuroimage Clin.* 16, 116–124. doi: 10.1016/j.nicl.2017.07.014

Folstein, M. F., Maiberger, R., and McHugh, P. R. (1977). Mood disorder as a specific complication of stroke. *J. Neurol. Neurosurg. Psychiatry* 40, 1018–1020. doi: 10.1136/jnnp.40.10.1018

Fornito, A., Zalesky, A., and Breakspear, M. (2015). The connectomics of brain disorders. *Nat. Rev. Neurosci.* 16, 159–172. doi: 10.1038/nrn3901

Foulon, C., Cerliani, L., Kinkingnehun, S., Levy, R., Rosso, C., Urbanski, M., et al. (2018). Advanced lesion symptom mapping analyses and implementation as BCBtoolkit. *Gigascience* 7, 1–17. doi: 10.1093/gigascience/giy004

Fox, M. D. (2018). Mapping symptoms to brain networks with the human connectome. *N. Engl. J. Med.* 379, 2237–2245. doi: 10.1056/NEJMra1706158

Fox, M. D., and Raichle, M. E. (2007). Spontaneous fluctuations in brain activity observed with functional magnetic resonance imaging. *Nat. Rev. Neurosci.* 8, 700–711. doi: 10.1038/nrn2201

Frey, J., Najib, U., Lilly, C., and Adcock, A. (2020). Novel TMS for stroke and depression (NoTSAD): accelerated repetitive transcranial magnetic stimulation as a safe and effective treatment for post-stroke depression. *Front. Neurol.* 11:788. doi: 10.3389/fneur.2020.00788

Fried, E. I., and Cramer, A. O. J. (2017). Moving forward: challenges and directions for psychopathological network theory and methodology. *Perspect. Psychol. Sci.* 12, 999–1020. doi: 10.1177/1745691617705892

Fried, E. I., Nesse, R. M., Zivin, K., Guille, C., and Sen, S. (2014). Depression is more than the sum score of its parts: individual DSM symptoms have different risk factors. *Psychol. Med.* 44, 2067–2076. doi: 10.1017/S0033291713002900

Fried, E. I., von Stockert, S., Haslbeck, J. M. B., Lamers, F., Schoevers, R. A., and Penninx, B. (2020). Using network analysis to examine links between individual depressive symptoms, inflammatory markers, and covariates. *Psychol. Med.* 50, 2682–2690. doi: 10.1017/S0033291719002770

George, M. S., Lisanby, S. H., Avery, D., McDonald, W. M., Durkalski, V., Pavlicova, M., et al. (2010). Daily left prefrontal transcranial magnetic stimulation therapy for major depressive disorder: a sham-controlled randomized trial. *Arch. Gen. Psychiatry* 67, 507–516. doi: 10.1001/archgenpsychiatry.2010.46

Ghose, S. S., Williams, L. S., and Swindle, R. W. (2005). Depression and other mental health diagnoses after stroke increase inpatient and outpatient medical utilization three years poststroke. *Med. Care* 43, 1259–1264. doi: 10.1097/01.mlr.0000185711.50480.13

Glasser, M. F., Smith, S. M., Marcus, D. S., Andersson, J. L., Auerbach, E. J., Behrens, T. E., et al. (2016). The human connectome Project's neuroimaging approach. *Nat. Neurosci.* 19, 1175–1187. doi: 10.1038/nn.4361

Gong, Q., and He, Y. (2015). Depression, neuroimaging and connectomics: a selective overview. *Biol. Psychiatry* 77, 223–235. doi: 10.1016/j.biopsych.2014.08.009

Goodin, P., Lamp, G., Vidyasagar, R., Connelly, A., Rose, S., Campbell, B. C. V., et al. (2019). Correlated resting-state functional MRI activity of frontostriatal, thalamic, temporal, and cerebellar brain regions differentiates stroke survivors with high compared to low depressive symptom scores. *Neural Plast.* 2019:2357107. doi: 10.1155/2019/2357107

Goodkind, M., Eickhoff, S. B., Oathes, D. J., Jiang, Y., Chang, A., Jones-Hagata, L. B., et al. (2015). Identification of a common neurobiological substrate for mental illness. *JAMA Psychiatry* 72, 305–315. doi: 10.1001/jamapsychiatry.2014.2206

Gozzi, S. A., Wood, A. G., Chen, J., Vaddadi, K., and Phan, T. G. (2014). Imaging predictors of poststroke depression: methodological factors in voxel-based analysis. *BMJ Open* 4:e004948. doi: 10.1136/bmjopen-2014-004948

Grajny, K., Pyata, H., Spiegel, K., Lacey, E. H., Xing, S., Brophy, C., et al. (2016). Depression symptoms in chronic left hemisphere stroke are related to dorsolateral prefrontal cortex damage. *J Neuropsychiatry Clin. Neurosci.* 28, 292–298. doi: 10.1176/appi.neuropsych.16010004

Griffis, J. C., Metcalf, N. V., Corbetta, M., and Shulman, G. L. (2019). Structural disconnections explain brain network dysfunction after stroke. *Cell Rep.* 28, 2527–2540.e2529. doi: 10.1016/j.celrep.2019.07.100

Griffis, J. C., Metcalf, N. V., Corbetta, M., and Shulman, G. L. (2020). Damage to the shortest structural paths between brain regions is associated with disruptions of resting-state functional connectivity after stroke. *Neuroimage* 210:116589. doi: 10.1016/j.neuroimage.2020.116589

Griffis, J. C., Metcalf, N. V., Corbetta, M., and Shulman, G. L. (2021). Lesion quantification toolkit: a MATLAB software tool for estimating grey matter damage and white matter disconnections in patients with focal brain lesions. *Neuroimage Clin.* 30:102639. doi: 10.1016/j.nicl.2021.102639

Gu, S. Y., and Chang, M. C. (2017). The effects of 10-Hz repetitive transcranial magnetic stimulation on depression in chronic stroke patients. *Brain Stimul.* 10, 270–274. doi: 10.1016/j.brs.2016.10.010

He, Y., and Evans, A. (2010). Graph theoretical modeling of brain connectivity. *Curr. Opin. Neurol.* 23, 341–350. doi: 10.1097/WCO.0b013e32833aa567

Hess, F., Foerch, C., Keil, F., Seiler, A., and Lapa, S. (2021). Association of lesion pattern and dysphagia in acute intracerebral hemorrhage. *Stroke* 52, 2921–2929. doi: 10.1161/STROKEAHA.120.032615

Hirt, J., van Meijeren, L. C. J., Saal, S., Hafsteinsdottir, T. B., Hofmeijer, J., Kraft, A., et al. (2020). Predictive accuracy of the post-stroke depression prediction scale: a prospective binational observational study(). *J. Affect. Disord.* 265, 39–44. doi: 10.1016/j.jad.2020.01.019

Hong, W., Zhao, Z., Wang, D., Li, M., Tang, C., Li, Z., et al. (2020). Altered gray matter volumes in post-stroke depressive patients after subcortical stroke. *Neuroimage Clin.* 26:102224. doi: 10.1016/j.nicl.2020.102224

Horn, A., and Fox, M. D. (2020). Opportunities of connectomic neuromodulation. *Neuroimage* 221:117180. doi: 10.1016/j.neuroimage.2020.117180

Jbabdi, S., Sotiropoulos, S. N., Haber, S. N., Van Essen, D. C., and Behrens, T. E. (2015). Measuring macroscopic brain connections *in vivo*. *Nat. Neurosci.* 18, 1546–1555. doi: 10.1038/nn.4134

Jensen, J. H., Helpern, J. A., Ramani, A., Lu, H., and Kaczynski, K. (2005). Diffusional kurtosis imaging: the quantification of non-gaussian water diffusion by means of magnetic resonance imaging. *Magn. Reson. Med.* 53, 1432–1440. doi: 10.1002/mrm.20508

Jeurissen, B., Leemans, A., Tournier, J. D., Jones, D. K., and Sijbers, J. (2013). Investigating the prevalence of complex fiber configurations in white matter tissue with diffusion magnetic resonance imaging. *Hum. Brain Mapp.* 34, 2747–2766. doi: 10.1002/hbm.22099

Jia, H., Damush, T. M., Qin, H., Ried, L. D., Wang, X., Young, L. J., et al. (2006). The impact of poststroke depression on healthcare use by veterans with acute stroke. *Stroke* 37, 2796–2801. doi: 10.1161/01.STR.0000244783.53274.a4

Jokela, M., Virtanen, M., Batty, G. D., and Kivimaki, M. (2016). Inflammation and specific symptoms of depression. *JAMA Psychiatry* 73, 87–88. doi: 10.1001/jamapsychiatry.2015.1977

Jorge, R. E., Robinson, R. G., Tateno, A., Narushima, K., Acion, L., Moser, D., et al. (2004). Repetitive transcranial magnetic stimulation as treatment of poststroke depression: a preliminary study. *Biol. Psychiatry* 55, 398–405. doi: 10.1016/j.biopsych.2003.08.017

Karnath, H. O., Sperber, C., and Rorden, C. (2018). Mapping human brain lesions and their functional consequences. *Neuroimage* 165, 180–189. doi: 10.1016/j.neuroimage.2017.10.028

Kim, N. Y., Lee, S. C., Shin, J. C., Park, J. E., and Kim, Y. W. (2017). Voxel-based lesion symptom mapping analysis of depressive mood in patients with isolated cerebellar stroke: a pilot study. *Neuroimage Clin.* 13, 39–45. doi: 10.1016/j.nicl.2016.11.011

Kimberg, D. Y., Coslett, H. B., and Schwartz, M. F. (2007). Power in Voxel-based lesion-symptom mapping. *J. Cogn. Neurosci.* 19, 1067–1080. doi: 10.1162/jocn.2007.19.7.1067

Koenigs, M., Huey, E. D., Calamia, M., Raymont, V., Tranel, D., and Grafman, J. (2008). Distinct regions of prefrontal cortex mediate resistance and vulnerability to depression. *J. Neurosci.* 28, 12341–12348. doi: 10.1523/JNEUROSCI.2324-08.2008

Kutlubaev, M. A., and Hackett, M. L. (2014). Part II: predictors of depression after stroke and impact of depression on stroke outcome: an updated systematic review of observational studies. *Int. J. Stroke* 9, 1026–1036. doi: 10.1111/ijs.12356

Lai, C. H. (2021). Fronto-limbic neuroimaging biomarkers for diagnosis and prediction of treatment responses in major depressive disorder. *Prog. Neuropsychopharmacol. Biol. Psychiatry* 107:110234. doi: 10.1016/j.pnpbp.2020.110234

Lassalle-Lagadec, S., Sibon, I., Dilharreguy, B., Renou, P., Fleury, O., and Allard, M. (2012). Subacute default mode network dysfunction in the prediction of post-stroke depression severity. *Radiology* 264, 218–224. doi: 10.1148/radiol.12111718

Lawrence, A. J., Tozer, D. J., Stamatakis, E. A., and Markus, H. S. (2018). A comparison of functional and tractography based networks in cerebral small vessel disease. *Neuroimage Clin.* 18, 425–432. doi: 10.1016/j.nicl.2018.02.013

Liang, Y., Chen, Y. K., Liu, Y. L., Mok, V. C. T., Ungvari, G. S., Chu, W. C. W., et al. (2019). Exploring causal pathways linking cerebral small vessel diseases burden to poststroke depressive symptoms with structural equation model analysis. *J. Affect. Disord.* 253, 218–223. doi: 10.1016/j.jad.2019.04.092

Liang, Y., Yao, Y. C., Zhao, L., Shi, L., Chen, Y. K., Mok, V. C., et al. (2020). Topological reorganization of the default mode network in patients with poststroke depressive symptoms: a resting-state fMRI study. *J. Affect. Disord.* 260, 557–568. doi: 10.1016/j.jad.2019.09.051

MacHale, S. M., O'Rourke, S. J., Wardlaw, J. M., and Dennis, M. S. (1998). Depression and its relation to lesion location after stroke. *J. Neurol. Neurosurg. Psychiatry* 64, 371–374. doi: 10.1136/jnnp.64.3.371

Mah, Y. H., Husain, M., Rees, G., and Nachev, P. (2014). Human brain lesion-deficit inference remapped. *Brain* 137(Pt. 9), 2522–2531. doi: 10.1093/brain/awu164

Mayman, N., Stein, L. K., Erdman, J., Kornspun, A., Tuhrim, S., Jette, N., et al. (2021). Risk and predictors of depression following acute ischemic stroke in the elderly. *Neurology* 96, e2184–e2191. doi: 10.1212/WNL.0000000000011828

McIntyre, A., Thompson, S., Burhan, A., Mehta, S., and Teasell, R. (2016). Repetitive transcranial magnetic stimulation for depression due to cerebrovascular disease: a systematic review. *J. Stroke Cerebrovasc. Dis.* 25, 2792–2800. doi: 10.1016/j.jstrokecerebrovasdis.2016.08.043

Meader, N., Moe-Byrne, T., Llewellyn, A., and Mitchell, A. J. (2014). Screening for poststroke major depression: a meta-analysis of diagnostic validity studies. *J. Neurol. Neurosurg. Psychiatry* 85, 198–206. doi: 10.1136/jnnp-2012-304194

Medina, J., Kimberg, D. Y., Chatterjee, A., and Coslett, H. B. (2010). Inappropriate usage of the Brunner-Munzel test in recent voxel-based lesion-symptom mapping studies. *Neuropsychologia* 48, 341–343. doi: 10.1016/j.neuropsychologia.2009.09.016

Menon, V. (2011). Large-scale brain networks and psychopathology: a unifying triple network model. *Trends Cogn. Sci.* 15, 483–506. doi: 10.1016/j.tics.2011.08.003

Mori, S., and van Zijl, P. C. (2002). Fiber tracking: principles and strategies – a technical review. *NMR Biomed.* 15, 468–480. doi: 10.1002/nbm.781

Moriarity, D. P., Joyner, K. J., Slavich, G. M., and Alloy, L. B. (2022). Unconsidered issues of measurement noninvariance in biological psychiatry: a focus on biological phenotypes of psychopathology. *Mol. Psychiatry* doi: 10.1038/s41380-021-01414-5 [Epub ahead of print].

Mueller, S., Wang, D., Fox, M. D., Yeo, B. T., Sepulcre, J., Sabuncu, M. R., et al. (2013). Individual variability in functional connectivity architecture of the human brain. *Neuron* 77, 586–595. doi: 10.1016/j.neuron.2012.12.028

Munsch, F., Sagnier, S., Asselineau, J., Bigourdan, A., Guttmann, C. R., Debruxelles, S., et al. (2016). Stroke location is an independent predictor of cognitive outcome. *Stroke* 47, 66–73. doi: 10.1161/STROKEAHA.115.011242

Nickel, A., and Thomalla, G. (2017). Post-stroke depression: impact of lesion location and methodological limitations-a topical review. *Front. Neurol.* 8:498. doi: 10.3389/fneur.2017.00498

Nosek, B. A., Beck, E. D., Campbell, L., Flake, J. K., Hardwicke, T. E., Mellor, D. T., et al. (2019). Preregistration is hard, and worthwhile. *Trends Cogn. Sci.* 23, 815–818. doi: 10.1016/j.tics.2019.07.009

Nosek, B. A., Ebersole, C. R., DeHaven, A. C., and Mellor, D. T. (2018). The preregistration revolution. *Proc. Natl. Acad. Sci. U.S.A.* 115, 2600–2606. doi: 10.1073/pnas.1708274114

Oathes, D. J., Patenaude, B., Schatzberg, A. F., and Etkin, A. (2015). Neurobiological signatures of anxiety and depression in resting-state functional magnetic resonance imaging. *Biol. Psychiatry* 77, 385–393. doi: 10.1016/j.biopsych.2014.08.006

Oestreich, L. K. L., Wright, P., and O'Sullivan, M. J. (2020). Microstructural changes in the reward system are associated with post-stroke depression. *Neuroimage Clin.* 28:102360. doi: 10.1016/j.nicl.2020.102360

O'Reardon, J. P., Solvason, H. B., Janicak, P. G., Sampson, S., Isenberg, K. E., Nahas, Z., et al. (2007). Efficacy and safety of transcranial magnetic stimulation in the acute treatment of major depression: a multisite randomized controlled trial. *Biol. Psychiatry* 62, 1208–1216. doi: 10.1016/j.biopsych.2007.01.018

Ovadia-Caro, S., Margulies, D. S., and Villringer, A. (2014). The value of resting-state functional magnetic resonance imaging in stroke. *Stroke* 45, 2818–2824. doi: 10.1161/STROKEAHA.114.003689

Padmanabhan, J. L., Cooke, D., Joutsa, J., Siddiqi, S. H., Ferguson, M., Darby, R. R., et al. (2019). A human depression circuit derived from focal brain lesions. *Biol. Psychiatry* 86, 749–758. doi: 10.1016/j.biopsych.2019.07.023

Pustina, D., Avants, B., Faseyitan, O. K., Medaglia, J. D., and Coslett, H. B. (2018). Improved accuracy of lesion to symptom mapping with multivariate sparse canonical correlations. *Neuropsychologia* 115, 154–166. doi: 10.1016/j.neuropsychologia.2017.08.027

Rajashekaran, P., Pai, K., Thunga, R., and Unnikrishnan, B. (2013). Post-stroke depression and lesion location: a hospital based cross-sectional study. *Indian J. Psychiatry* 55, 343–348. doi: 10.4103/0019-5545.120546

Robinson, R. G., and Jorge, R. E. (2016). Post-stroke depression: a review. *Am. J. Psychiatry* 173, 221–231. doi: 10.1176/appi.ajp.2015.15030363

Robinson, R. G., and Price, T. R. (1982). Post-stroke depressive disorders: a follow-up study of 103 patients. *Stroke* 13, 635–641. doi: 10.1161/01.str.13.5.635

Robinson, R. G., Bolla-Wilson, K., Kaplan, E., Lipsey, J. R., and Price, T. R. (1986). Depression influences intellectual impairment in stroke patients. *Br. J. Psychiatry* 148, 541–547. doi: 10.1192/bjp.148.5.541

Robinson, R. G., Kubos, K. L., Starr, L. B., Rao, K., and Price, T. R. (1983). Mood changes in stroke patients: relationship to lesion location. *Compr. Psychiatry* 24, 555–566. doi: 10.1016/0010-440x(83)90024-x

Robinson, R. G., Shoemaker, W. J., Schlumpf, M., Valk, T., and Bloom, F. E. (1975). Effect of experimental cerebral infarction in rat brain on catecholamines and behaviour. *Nature* 255, 332–334. doi: 10.1038/255332a0

Rorden, C., and Karnath, H. O. (2004). Using human brain lesions to infer function: a relic from a past era in the fMRI age? *Nat. Rev. Neurosci.* 5, 813–819. doi: 10.1038/nrn1521

Sackeim, H. A., Aaronson, S. T., Carpenter, L. L., Hutton, T. M., Mina, M., Pages, K., et al. (2020). Clinical outcomes in a large registry of patients with major depressive disorder treated with Transcranial Magnetic Stimulation. *J. Affect. Disord.* 277, 65–74. doi: 10.1016/j.jad.2020.08.005

Salvalaggio, A., De Filippo De Grazia, M., Zorzi, M., Thiebaut de Schotten, M., and Corbetta, M. (2020). Post-stroke deficit prediction from lesion and indirect structural and functional disconnection. *Brain* 143, 2173–2188. doi: 10.1093/brain/awaa156

Shen, X. Y., Fan, Z. X., Wang, L., Cui, S., and Niu, J. L. (2019). Altered white matter microstructure in patients with post-stroke depression detected by diffusion kurtosis imaging. *Neurol. Sci.* 40, 2097–2103. doi: 10.1007/s10072-019-03947-8

Shen, X., Liu, M., Cheng, Y., Jia, C., Pan, X., Gou, Q., et al. (2017). Repetitive transcranial magnetic stimulation for the treatment of post-stroke depression: a systematic review and meta-analysis of randomized controlled clinical trials. *J. Affect. Disord.* 211, 65–74. doi: 10.1016/j.jad.2016.12.058

Shi, Y., Liu, W., Liu, R., Zeng, Y., Wu, L., Huang, S., et al. (2019). Investigation of the emotional network in depression after stroke: a study of multivariate Granger causality analysis of fMRI data. *J. Affect. Disord.* 249, 35–44. doi: 10.1016/j.jad.2019.02.020

Shi, Y., Zeng, Y., Wu, L., Liu, W., Liu, Z., Zhang, S., et al. (2017). A study of the brain abnormalities of post-stroke depression in frontal lobe lesion. *Sci. Rep.* 7:13203. doi: 10.1038/s41598-017-13681-w

Shimoda, K., and Robinson, R. G. (1999). The relationship between poststroke depression and lesion location in long-term follow-up. *Biol. Psychiatry* 45, 187–192. doi: 10.1016/s0006-3223(98)00178-4

Siddiqi, S. H., Taylor, S. F., Cooke, D., Pascual-Leone, A., George, M. S., and Fox, M. D. (2020). Distinct symptom-specific treatment targets for circuit-based neuromodulation. *Am. J. Psychiatry* 177, 435–446. doi: 10.1176/appi.ajp.2019.19090915

Singh, A., Black, S. E., Herrmann, N., Leibovitch, F. S., Ebert, P. L., Lawrence, J., et al. (2000). Functional and neuroanatomic correlations in poststroke depression: the Sunnybrook Stroke Study. *Stroke* 31, 637–644. doi: 10.1161/01.str.31.3.637

Sperber, C., and Karnath, H. O. (2017). Impact of correction factors in human brain lesion-behavior inference. *Hum. Brain Mapp.* 38, 1692–1701. doi: 10.1002/hbm.23490

Sporns, O., Tononi, G., and Kotter, R. (2005). The human connectome: a structural description of the human brain. *PLoS Comput. Biol.* 1:e42. doi: 10.1371/journal.pcbi.0010042

Starkstein, S. E., Robinson, R. G., and Price, T. R. (1987). Comparison of cortical and subcortical lesions in the production of poststroke mood disorders. *Brain* 110(Pt. 4), 1045–1059. doi: 10.1093/brain/110.4.1045

Sun, C., Yang, F., Wang, C., Wang, Z., Zhang, Y., Ming, D., et al. (2018). Mutual information-based brain network analysis in post-stroke patients with different levels of depression. *Front. Hum. Neurosci.* 12:285. doi: 10.3389/fnhum.2018.00285

Tang, W. K., Chen, Y. K., Lu, J. Y., Chu, W. C., Mok, V. C., Ungvari, G. S., et al. (2010). White matter hyperintensities in post-stroke depression: a case control study. *J. Neurol. Neurosurg. Psychiatry* 81, 1312–1315. doi: 10.1136/jnnp.2009.203141

Tang, W. K., Chen, Y., Liang, H., Chu, W. C., Mok, V. C., Ungvari, G. S., et al. (2014). Cerebral microbleeds as a predictor of 1-year outcome of poststroke depression. *Stroke* 45, 77–81. doi: 10.1161/STROKEAHA.113.002686

Taylor, W. D., Aizenstein, H. J., and Alexopoulos, G. S. (2013). The vascular depression hypothesis: mechanisms linking vascular disease with depression. *Mol. Psychiatry* 18, 963–974. doi: 10.1038/mp.2013.20

Towfighi, A., Ovbiagele, B., El Husseini, N., Hackett, M. L., Jorge, R. E., Kissela, B. M., et al. (2017). Poststroke depression: a scientific statement for healthcare professionals from the American heart association/American stroke association. *Stroke* 48, e30–e43. doi: 10.1161/STR.0000000000000113

Triolo, F., Belvederi Murri, M., Calderon-Larranaga, A., Vetrano, D. L., Sjoberg, L., Fratiglioni, L., et al. (2021). Bridging late-life depression and chronic somatic diseases: a network analysis. *Transl. Psychiatry* 11:557. doi: 10.1038/s41398-021-01686-z

Ulrichsen, K. M., Kolskar, K. K., Richard, G., Alnaes, D., Dorum, E. S., Sanders, A. M., et al. (2021). Structural brain disconnectivity mapping of post-stroke fatigue. *Neuroimage Clin.* 30:102635. doi: 10.1016/j.nicl.2021.102635

Vaidya, A. R., Pujara, M. S., Petrides, M., Murray, E. A., and Fellows, L. K. (2019). Lesion studies in contemporary neuroscience. *Trends Cogn. Sci.* 23, 653–671. doi: 10.1016/j.tics.2019.05.009

van Borkulo, C., Boschloo, L., Borsboom, D., Penninx, B. W., Waldorp, L. J., and Schoevers, R. A. (2015). Association of symptom network structure with the course of depression. *JAMA Psychiatry* 72, 1219–1226. doi: 10.1001/jamapsychiatry.2015.2079

Vicentini, J. E., Weiler, M., Almeida, S. R. M., de Campos, B. M., Valler, L., and Li, L. M. (2017). Depression and anxiety symptoms are associated to disruption of default mode network in subacute ischemic stroke. *Brain Imaging Behav.* 11, 1571–1580. doi: 10.1007/s11682-016-9605-7

Weaver, N. A., Kuijf, H. J., Aben, H. P., Abrigo, J., Bae, H. J., Barbay, M., et al. (2021a). Strategic infarct locations for post-stroke cognitive impairment: a pooled analysis of individual patient data from 12 acute ischaemic stroke cohorts. *Lancet Neurol.* 20, 448–459. doi: 10.1016/S1474-4422(21)00060-0

Weaver, N. A., Lim, J. S., Schilderinck, J., Biessels, G. J., Kang, Y., Kim, B. J., et al. (2021b). Strategic infarct locations for post-stroke depressive symptoms: a lesion- and disconnection-symptom mapping study. *Biol. Psychiatry Cogn. Neurosci. Neuroimaging* doi: 10.1016/j.bpsc.2021.09.002 [Epub ahead of print].

Wei, N., Yong, W., Li, X., Zhou, Y., Deng, M., Zhu, H., et al. (2015). Post-stroke depression and lesion location: a systematic review. *J. Neurol.* 262, 81–90. doi: 10.1007/s00415-014-7534-1

White, J., Kivimaki, M., Jokela, M., and Batty, G. D. (2017). Association of inflammation with specific symptoms of depression in a general population of older people: the English Longitudinal Study of Ageing. *Brain Behav. Immun.* 61, 27–30. doi: 10.1016/j.bbi.2016.08.012

Xie, X., Shi, Y., and Zhang, J. (2017). Structural network connectivity impairment and depressive symptoms in cerebral small vessel disease. *J. Affect. Disord.* 220, 8–14. doi: 10.1016/j.jad.2017.05.039

Xu, T., Jha, A., and Nachev, P. (2018). The dimensionalities of lesion-deficit mapping. *Neuropsychologia* 115, 134–141. doi: 10.1016/j.neuropsychologia.2017.09.007

Xu, X., Tang, R., Zhang, L., and Cao, Z. (2019). Altered topology of the structural brain network in patients with post-stroke depression. *Front. Neurosci.* 13:776. doi: 10.3389/fnins.2019.00776

Yang, S., Hua, P., Shang, X., Cui, Z., Zhong, S., Gong, G., et al. (2015). A significant risk factor for poststroke depression: the depression-related subnetwork. *J. Psychiatry Neurosci.* 40, 259–268. doi: 10.1503/jpn.140086

Zang, Y. F., He, Y., Zhu, C. Z., Cao, Q. J., Sui, M. Q., Liang, M., et al. (2007). Altered baseline brain activity in children with ADHD revealed by resting-state functional MRI. *Brain Dev.* 29, 83–91. doi: 10.1016/j.braindev.2006.07.002

Zhang, P., Wang, J., Xu, Q., Song, Z., Dai, J., and Wang, J. (2018). Altered functional connectivity in post-ischemic stroke depression: a resting-state functional magnetic resonance imaging study. *Eur. J. Radiol.* 100, 156–165. doi: 10.1016/j.ejrad.2018.01.003

Zhang, P., Xu, Q., Dai, J., Wang, J., Zhang, N., and Luo, Y. (2014). Dysfunction of affective network in post ischemic stroke depression: a resting-state functional magnetic resonance imaging study. *Biomed Res. Int.* 2014:846830. doi: 10.1155/2014/846830

Zhang, X. F., He, X., Wu, L., Liu, C. J., and Wu, W. (2019). Altered functional connectivity of amygdala with the fronto-limbic-striatal circuit in temporal lobe lesion as a proposed mechanism for poststroke depression. *Am. J. Phys. Med. Rehabil.* 98, 303–310. doi: 10.1097/PHM.0000000000001081

Zhang, X., Shi, Y., Fan, T., Wang, K., Zhan, H., and Wu, W. (2021). Analysis of correlation between white matter changes and functional responses in post-stroke depression. *Front. Aging Neurosci.* 13:728622. doi: 10.3389/fnagi.2021.728622

Zhang, Y., Kimberg, D. Y., Coslett, H. B., Schwartz, M. F., and Wang, Z. (2014). Multivariate lesion-symptom mapping using support vector regression. *Hum. Brain Mapp.* 35, 5861–5876. doi: 10.1002/hbm.22590

Zou, Q. H., Zhu, C. Z., Yang, Y., Zuo, X. N., Long, X. Y., Cao, Q. J., et al. (2008). An improved approach to detection of amplitude of low-frequency fluctuation (ALFF) for resting-state fMRI: fractional ALFF. *J. Neurosci. Methods* 172, 137–141. doi: 10.1016/j.jneumeth.2008.04.012

Conflict of Interest: The authors declare that the research was conducted in the absence of any commercial or financial relationships that could be construed as a potential conflict of interest.

Publisher's Note: All claims expressed in this article are solely those of the authors and do not necessarily represent those of their affiliated organizations, or those of the publisher, the editors and the reviewers. Any product that may be evaluated in this article, or claim that may be made by its manufacturer, is not guaranteed or endorsed by the publisher.

frontiers | Frontiers in Neuroscience

ORIGINAL RESEARCH
published: 25 April 2022
doi: 10.3389/fnins.2022.876121

Altered Brain Function in First-Episode and Recurrent Depression: A Resting-State Functional Magnetic Resonance Imaging Study

Jifei Sun[1,2†], Limei Chen[1,2†], Jiakai He[2,4], Zhongming Du[3], Yue Ma[1,2], Zhi Wang[1,2], Chunlei Guo[1,2], Yi Luo[1,2], Deqiang Gao[1], Yang Hong[1], Lei Zhang[1], Fengquan Xu[1], Jiudong Cao[1], Xiaobing Hou[5], Xue Xiao[5], Jing Tian[5], Jiliang Fang[1] and Xue Yu[5]**

[1] Guang'anmen Hospital, China Academy of Chinese Medical Sciences, Beijing, China, [2] Graduate School, China Academy of Chinese Medical Sciences, Beijing, China, [3] Dongzhimen Hospital, Beijing University of Chinese Medicine, Beijing, China, [4] Institute of Acupuncture and Moxibustion, China Academy of Chinese Medical Sciences, Beijing, China, [5] Beijing First Hospital of Integrated Chinese and Western Medicine, Beijing, China

OPEN ACCESS

Edited by:
Jinglei Lv,
The University of Sydney, Australia

Reviewed by:
Xiao Chen,
Institute of Psychology (CAS), China
Li Wang,
Beijing Institute of Technology, China

***Correspondence:**
Jiliang Fang
Fangmgh@163.com;
18211062986@163.com
Xue Yu
yuxue200704@126.com

† These authors have contributed equally to this work and share first authorship

Specialty section:
This article was submitted to Brain Imaging Methods, a section of the journal Frontiers in Neuroscience

Received: 15 February 2022
Accepted: 30 March 2022
Published: 25 April 2022

Citation:
Sun J, Chen L, He J, Du Z, Ma Y, Wang Z, Guo C, Luo Y, Gao D, Hong Y, Zhang L, Xu F, Cao J, Hou X, Xiao X, Tian J, Fang J and Yu X (2022) Altered Brain Function in First-Episode and Recurrent Depression: A Resting-State Functional Magnetic Resonance Imaging Study. Front. Neurosci. 16:876121. doi: 10.3389/fnins.2022.876121

Background: Studies on differences in brain function activity between the first depressive episode (FDE) and recurrent depressive episodes (RDE) are scarce. In this study, we used regional homogeneity (ReHo) and amplitude of low-frequency fluctuations (ALFF) as indices of abnormal brain function activity. We aimed to determine the differences in these indices between patients with FDE and those with RDE, and to investigate the correlation between areas of abnormal brain function and clinical symptoms.

Methods: A total of 29 patients with RDE, 28 patients with FDE, and 29 healthy controls (HCs) who underwent resting-state functional magnetic resonance imaging were included in this study. The ReHo and ALFF measurements were used for image analysis and further analysis of the correlation between different brain regions and clinical symptoms.

Results: Analysis of variance showed significant differences among the three groups in ReHo and ALFF in the frontal, parietal, temporal, and occipital lobes. ReHo was higher in the right inferior frontal triangular gyrus and lower in the left inferior temporal gyrus in the RDE group than in the FDE group. Meanwhile, ALFF was higher in the right inferior frontal triangular gyrus, left anterior cingulate gyrus, orbital part of the left middle frontal gyrus, orbital part of the left superior frontal gyrus, and right angular gyrus, but was lower in the right lingual gyrus in the RDE group than in the FDE group. ReHo and ALFF were lower in the left angular gyrus in the RDE and FDE groups than in the HC group. Pearson correlation analysis showed a positive correlation between the ReHo and ALFF values in these abnormal areas in the frontal lobe and the severity of depressive symptoms ($P < 0.05$). Abnormal areas in the temporal and occipital lobes were negatively correlated with the severity of depressive symptoms ($P < 0.05$).

Conclusion: The RDE and FDE groups had abnormal neural function activity in some of the same brain regions. ReHo and ALFF were more widely distributed in different brain regions and had more complex neuropathological mechanisms in the RDE group than in the FDE group, especially in the right inferior frontal triangular gyrus of the frontal lobe.

Keywords: first depressive episode, recurrent depressive episodes, magnetic resonance imaging, regional homogeneity, amplitude of low-frequency fluctuation

INTRODUCTION

Major depressive disorder (MDD) is a common clinical psychiatric disorder characterized by affective, cognitive, and somatic symptoms. Most of its clinical manifestations are common symptoms such as depressed mood, diminished interest, slowed thinking, loss of appetite, and insomnia (Wolfers et al., 2015). The World Health Organization reports that an estimated 350 million people worldwide have depression and that depression is the leading cause of suicide, with approximately 800,000 people dying by suicide each year (Zhang et al., 2018). By 2030, depression is expected to become the disease with the largest burden worldwide (Friedrich, 2017). Currently, the diagnosis of MDD relies on clinical scale assessment of the patient and the experience of the psychiatrist; however, knowledge about precise neurobiological biomarkers is lacking.

According to the classification criteria of the 10th revision of the International Statistical Classification of Diseases and Related Health Problems, MDD is classified into the first depressive episode (FDE) and recurrent depressive episodes (RDE) (Yuksel et al., 2018). Previous studies have demonstrated differences in depressive and somatic symptoms (Roca et al., 2011), cognitive functioning (Roca et al., 2015; Zu et al., 2021; Varghese et al., 2022), and quality of life (Zu et al., 2021) between patients with RDE and those with FDE. Epidemiological surveys have shown that depression has a high recurrence rate and that, once the first episode has occurred, it relapses within 5 years. In addition, approximately 80% of patients with depression have a history of two recurrences (Burcusa and Iacono, 2007). Moreover, the severity of MDD increases with the number of relapses (Harlev et al., 2021), and it is increasingly being recognized that the challenge in patients with depression is preventing relapse rather than promoting recovery (Fava et al., 2017). Therefore, the differences in pathogenesis between RDE and FDE need to be elucidated from a neuropathological perspective.

In recent years, with rapid developments in neuroimaging technology, resting-state functional magnetic resonance imaging (rs-fMRI) has gradually been applied to the study of insomnia (Marques et al., 2018), schizophrenia (Sheffield and Barch, 2016), autism (Bathelt and Geurts, 2021), and other psychiatric systemic disorders. It has also been applied to the study of MDD subtypes (Brown et al., 2019; Yue et al., 2020). rs-fMRI indirectly reflects neuronal spontaneous activity by measuring the blood oxygen level-dependent (BOLD) signal, which enables the investigation of brain function abnormalities in the early disease stage and has advantages of simplicity, non-invasiveness, and reproducibility (Lee et al., 2013). Regional homogeneity (ReHo) and amplitude of low-frequency fluctuations (ALFF) are two of the commonly used metrics in rs-fMRI analysis. ReHo mainly assesses the synchronous reflection of the sequence between a given voxel and its neighboring voxels, reflecting the temporal homogeneity of signals related to regional blood oxygen levels (Zang et al., 2004). ALFF is the sum of the spectral amplitude of each voxel signal in the low-frequency range (usually 0.01–0.08 Hz), reflecting the amplitude of low-frequency fluctuations caused by spontaneous neuronal activity (Zang et al., 2007). Combining the ReHo and ALFF methods can contribute to a better understanding of the abnormalities of brain function in patients with MDD (Ni et al., 2016).

However, the combination of ALFF and ReHo has been mainly applied in studies on mild cognitive impairment (Ni et al., 2016), schizophrenia (Zhao et al., 2018), and anxiety disorders (Shen et al., 2020), whereas the differences between FDE and RDE have not been investigated. A study in patients with FDE and remitting MDD (rMDD) showed differences in ALFF and ReHo in the temporal lobes, although patients with rMDD had been cured with antidepressant medication (Yang et al., 2018). Another study observed alterations in bilateral frontal BOLD signals in patients with FDE or RDE; however, the study used a task-state observation approach (Yuksel et al., 2018). The frontal lobe is an important brain region in the pathogenesis of MDD, and previous studies have also found differences in frontal lobe function between FDE and RDE (Talarowska et al., 2015).

In this study, we aimed to determine the differences in brain function activity among patients with FDE, patients with RDE, and healthy controls (HCs) by using the ReHo and ALFF methods based on rs-fMRI techniques. Further, we also aimed to analyze the correlation between different brain areas and clinical characteristics. We hypothesized that differences would be observed in the brain neural circuits of patients with FDE and those with RDE, especially in areas closely related to the frontal lobe. This study will provide a neuroimaging basis for the differences in neuropathological mechanisms between FDE and RDE and some insights for clinical research.

MATERIALS AND METHODS

Participants

A total of 59 outpatients with MDD from Guang'anmen Hospital, Chinese Academy of Traditional Chinese Medicine, Beijing First Hospital of Integrative Medicine, were recruited for this study. All patients met the Diagnostic and Statistical Manual of Mental Disorders Fifth Edition criteria for MDD.

We used the 17-item Hamilton Rating Scale for Depression (HAMD-17) (Hamilton, 1960) to assess the severity of depression in all patients and classified these patients into those with RDE [$n = 31$; mean frequency of recurrence, 2.27 (standard deviation = 0.79)] and those with FDE ($n = 28$, 0 recurrence). The inclusion criteria were (1) age 18–55 years; (2) HAMD-17 score > 17; and (3) The FDE group all had their FDE prior to enrollment and were not receiving any antidepressant medication. The RDE group had a previous history of depression, cured by antidepressant medication, now recurring and a history of antidepressant withdrawal for at least 4 weeks prior to enrollment. We also included 29 sex- and age-matched HCs (21 women and 8 men) who (1) were aged 18–55 years, (2) had a HAMD–17 score of < 7, (3) had right-handedness, and (4) had no history of any mental illness in first-degree relatives.

The exclusion criteria for patients and HCs were as follows: (1) serious mental illness and other diseases such as cardiovascular and cerebrovascular disorders; (2) history of drug and alcohol abuse; (3) any contraindications to MRI, such as presence of a heart pacemaker, metal fixed false teeth, or severe claustrophobia; (4) pregnant or lactating status; and (5) bipolar disorder or suicidal ideation.

All patients were required to sign an informed consent form before enrollment. This study was approved by the ethics committee of Guang'anmen Hospital, Chinese Academy of Traditional Chinese Medicine.

Scan Acquisition

All patients in this study underwent MRI using a Magnetom Skyra 3.0-T scanner (Siemens, Erlangen, Germany). Before the scanning procedure, the patients were instructed to remain awake and avoid active thinking. During the scanning process, the patients were required to wear earplugs and noise-canceling headphones, to use a hood to immobilize the head, and to lie flat on the examination bed. The scanning procedure involved a localizer scan, high-resolution three-dimensional T1-weighted imaging, and BOLD-fMRI.

The scanning parameters were as follows: for three-dimensional T1-weighted imaging, time repetition/time echo = 2,500/2.98 ms, flip angle = 7°, matrix = 64 × 64, field of view = 256 mm × 256 mm, slice thickness = 1 mm, slice number = 48, slices = 192, scanning time = 6 min 3 s; for BOLD-fMRI, time repetition/time echo = 2,000/30 ms, flip angle = 90°, matrix = 64 × 64, field of view = 240 mm × 240 mm, slice number = 43, slice thickness/spacing = 3.0/1.0 mm, number of obtained volumes = 200, and scanning time = 6 min 40 s.

Image Processing

Functional Magnetic Resonance Imaging Data Preprocessing

The rs-fMRI data were preprocessed using DPARSF (Data Processing Assistant for rs-fMRI) software (DPABI5.0)[1] (Yan and Zang, 2010) in MATLAB (Mathworks Inc., Natick, MA, United States), according to the following process: (1) conversion of DICOM raw data to NIFTI format; (2) removal of the first 10 time points to place the data in a stable state; (3) slice timing; (4) realignment of head motion (removal of patients with head movements > 2 mm in any direction and motor rotation > 2°); (5) regression of covariates, including brain white matter signal, cerebrospinal fluid signal, and head movement parameters; (6) spatial normalization (the functional images of all patients were converted to Montreal Neurological Institute standard space using the DARTEL method); and (7) linear detrending and filtering (0.01–0.08 Hz).

Regional Homogeneity Analysis

The DPARSF (Data Processing Assistant for Resting-State fMRI Advanced Edition_V5.1_201001, see text footnote 1) software was used to analyze the ReHo and ALFF of the pre-processed data. The similarity of the time series of each voxel to its neighboring voxels (26 neighboring voxels) was assessed using the Kendall's coefficient of concordance (KCC) (Kendall, 1990), i.e., ReHo values. The whole-brain ReHo images of the subjects were obtained by calculating the KCC values of the whole-brain voxels. To improve the signal-to-noise ratio, the Re Ho images were spatially smoothed using a 6 mm × 6 mm × 6 mm full-width half-height Gaussian kernel.

Amplitude of Low-Frequency Fluctuations Analysis

Data were spatially normalized and smoothed, and a fast Fourier transform was performed to switch the time series to the frequency domain to obtain the power spectrum. The square root of the power spectrum at each frequency was calculated to obtain the average square root of the ALFF measurement for each voxel in the range of 0.01–0.08 Hz. Finally, time bandpass filtering (0.01–0.08 Hz) was performed. To reduce the inter-individual variability, ALFF was transformed to zALFF using Fisher's z transformation before statistical analysis.

Statistical Analyses

Clinical Data Analysis

Clinical data were analyzed using the SPSS 23.0 statistical software (IBM Corporation, Somers, NY, United States). One-way analysis of variance was used to compare age and educational level among the three groups, and the chi-square test was used to compare sex differences. A two-sample t-test was used to compare the duration of disease, HAMD-17 scores, and frequency of recurrence between the two patient groups, with a threshold of $P < 0.05$ (two-tailed) set as statistically significant.

Functional Magnetic Resonance Imaging Data Analysis

Imaging data were analyzed using the DPARSF toolbox, and a voxel-based one-way analysis of variance was performed to compare the whole-brain ReHo/ALFF map among the three groups. Sex, age, educational level, and framewise displacement (a metric derived from Jenkinson's formula) were used as covariates, and brain areas with ReHo/ALFF differences among the three

[1] http://www.rfmri.org/DPARSF

groups were corrected for Gaussian random fields. The corrected cluster level was set at $P < 0.05$ (two-tailed), and threshold voxel levels of $P < 0.005$ were defined as statistically different. We performed *post-hoc t*-test analysis using DPARSF 5.1 software for two-by-two comparisons between groups, and Bonferroni correction was applied to the results, setting a threshold of $P < 0.016$ (0.05/3) for statistical significance. The threshold was set to clusters > 10 voxels.

To verify the relationship between ReHo/ALFF values and clinical symptoms, we extracted the mean ReHo/ALFF values of three different brain regions and performed Pearson correlation analysis of the clinical scale scores of each group. Significance was set at a statistical threshold of $P < 0.05$ (two-tailed).

RESULTS

Characteristics of Research Samples

Two patients with RDE were excluded because of excessive head movement displacement. Therefore, a total of 29 patients with RDE, 28 patients with FDE, and 29 HCs met the inclusion criteria. No statistical differences among the three groups were found in terms of sex, age, and years of education. The HAMD-17 scores

TABLE 1 | Demographic and clinical characteristics of the study participants.

Variable	RDE ($n = 29$)	FDE ($n = 28$)	HCs ($n = 29$)	$t(F)/\chi^2$	P -value
Sex (M/F)	8/21	8/20	8/21	0.043	0.958[a]
Age (years)	33.62 ± 10.28	32.85 ± 9.77	33.24 ± 9.42	0.018	0.982[b]
Education (years)	14.96 ± 2.44	14.28 ± 2.80	14.93 ± 3.05	0.538	0.586[b]
Duration of illness (months)	22.96 ± 11.49	2.28 ± 0.93	NA	9.487	<0.001[c]*
HAMD-17 score	23.31 ± 3.26	23.10 ± 3.16	NA	0.238	0.812[c]
Frequency of recurrence	2.34 ± 0.76	0	NA	16.133	<0.001[c]*

RDE, recurrent depressive episode; FDE, first depressive episode; HCs, healthy controls; HAMD-17, 17-item Hamilton Rating Scale for Depression; NA, not applicable.
[a]The P-values of sex distribution among the three groups were obtained using the chi-square test.
[b]P-value from one-way analysis of variance tests.
[c]P-value from a two-sample t-test.
**Significant difference.*

TABLE 2 | ReHo differences in RDE, FDE, and HCs.

Clusters	Brain regions	MNI peak			Cluster size	F/T-value (peak)
		X	*Y*	*Z*		
Differences among three groups						
1	Right inferior frontal triangular gyrus	33	30	30	27	17.934[a]
2	Left anterior cingulate cortex	−12	51	3	25	12.561[a]
3	Left middle temporal gyrus	−39	−54	18	34	15.505[a]
	Left angular gyrus					
4	Left superior temporal gyrus	−45	−30	15	29	13.698[a]
5	Left inferior temporal gyrus	−39	−57	−6	53	12.601[a]
	Left inferior occipital gyrus					
6	Right Rolandic operculum gyrus	42	−18	24	34	11.938[a]
RDE vs. FDE						
1	Right inferior frontal triangular gyrus	33	30	30	19	4.344[b]
2	Left inferior temporal gyrus	−42	−57	−6	35	−4.270[b]
RDE vs. HCs						
1	Right inferior frontal triangular gyrus	33	30	27	23	4.745[b]
2	Left anterior cingulate cortex	−12	51	3	25	4.272[b]
3	Left superior temporal gyrus	−45	−30	15	29	4.543[b]
4	Left angular gyrus	−39	−63	27	17	−2.881[b]
FDE vs. HCs						
1	Left inferior temporal gyrus	−44	−63	−9	25	2.905[b]
2	Left middle temporal gyrus	−39	−51	15	23	−2.816[b]
	Left angular gyrus					

MNI peak, coordinates of primary peak locations in the Montreal Neurological Institute space.
[a]F-value of the peak voxel showing gray matter volume differences among the three groups.
[b]T-value of the peak voxel showing gray matter volume differences among the three groups (post hoc two-group comparisons).

TABLE 3 | ALFF differences in RDE, FDE, and HCs.

Clusters	Brain regions	MNI Peak			Cluster size	*F/T*-value (peak)
		X	*Y*	*Z*		
Differences among three groups						
1	Right inferior frontal triangular gyrus	33	30	30	22	12.285[a]
2	Left anterior cingulate cortex Orbital part of the left middle frontal gyrus	−12	42	−18	109	11.440[a]
3	Left angular gyrus Left middle temporal gyrus	−39	−57	24	45	15.704[a]
4	Right angular gyrus	39	−63	36	36	14.556[a]
5	Left inferior temporal gyrus Left inferior occipital gyrus	−60	−63	−15	31	12.380[a]
6	Right lingual gyrus	21	−54	−6	70	13.548[a]
7	Vermis_3	6	−45	−21	51	12.253[a]
RDE vs. FDE						
1	Right inferior frontal triangular gyrus	34	18	25	14	4.222[b]
2	Left anterior cingulate cortex	−6	36	6	14	3.376[b]
3	Orbital part of the left middle frontal gyrus	−12	48	−3	17	3.942[b]
4	Orbital part of the left superior frontal gyrus	−12	42	18	42	4.445[b]
5	Right angular gyrus	39	−63	33	15	4.167[b]
6	Right lingual gyrus	15	−51	−9	65	−2.909[b]
RDE vs. HCs						
1	Left anterior cingulate cortex	−15	48	−3	24	3.641[b]
2	Left angular gyrus	−39	−60	21	18	−3.094[b]
3	Right angular gyrus	42	−63	36	26	4.097[b]
FDE vs. HCs						
1	Left middle temporal gyrus Left angular gyrus	−42	−51	12	36	−3.015[b]
2	Left inferior temporal gyrus	−60	−63	−15	26	4.055[b]
3	Vermis_3	6	−45	−21	15	3.830[b]

MNI peak, coordinates of primary peak locations in the Montreal Neurological Institute space.
[a] *F-value of the peak voxel showing gray matter volume differences among the three groups.*
[b] *T-value of the peak voxel showing gray matter volume differences among the three groups (post hoc two-group comparisons).*

were not statistically different between the RDE and FDE groups, whereas a statistical difference was observed in the duration of illness and frequency of recurrence (**Table 1**).

Differences in Regional Homogeneity/Amplitude of Low-Frequency Fluctuations Between the Recurrent Depressive Episodes, First Depressive Episode, and Healthy Controls

One-way analysis of variance showed significant differences in ReHo and ALFF among the three groups in the right inferior frontal triangular gyrus, left anterior cingulate cortex, left middle temporal gyrus/left angular gyrus, and left inferior temporal gyrus/left inferior occipital gyrus. Meanwhile, ReHo was significantly different in the left superior temporal gyrus and right Rolandic operculum gyrus. ALFF was also significantly different in the right angular gyrus, right lingual gyrus, and Vermis_3 (**Tables 2**, **3** and **Figures 1**, **2**).

Compared with the FDE group, the RDE group had elevated ReHo in the right inferior frontal triangular gyrus and decreased ReHo in the left inferior temporal gyrus. Meanwhile, the RDE group had elevated ALFF in the right inferior frontal triangular gyrus, left anterior cingulate gyrus, orbital part of the left middle frontal gyrus, orbital part of the left superior frontal gyrus, and right angular gyrus, but had decreased ALFF in the right lingual gyrus (**Tables 2**, **3** and **Figure 3**).

Compared with the HC group, the RDE group had elevated ReHo in the right inferior frontal triangular gyrus, left anterior cingulate gyrus, and left superior temporal gyrus, but had reduced ReHo in the left angular gyrus. Meanwhile, the RDE group had elevated ALFF in the left anterior cingulate gyrus and right angular gyrus, but had decreased ALFF in the left angular gyrus (**Tables 2**, **3** and **Figure 4**).

Compared with the HC group, the FDE group had elevated ReHo in the left inferior temporal gyrus and decreased ReHo in the left middle temporal gyrus/left angular gyrus. Meanwhile, the FDE group had elevated ALFF in the left inferior temporal gyrus and Vermis_3, but had decreased ALFF in the left middle temporal gyrus/left angular gyrus (**Tables 2**, **3** and **Figure 5**).

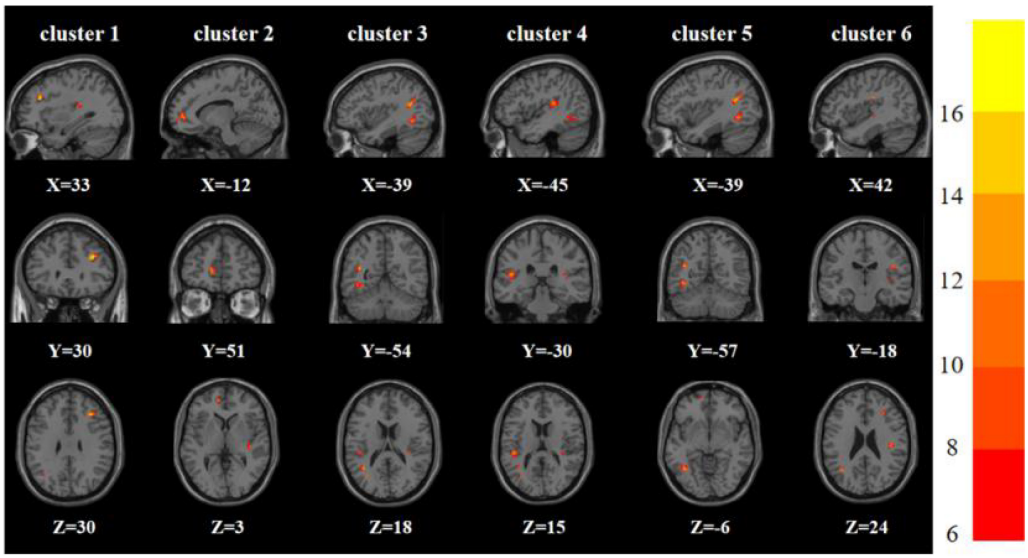

FIGURE 1 | Brain regions with abnormal ReHo among the three groups based on one-way analysis of variance. The color bars indicate the *F*-value.

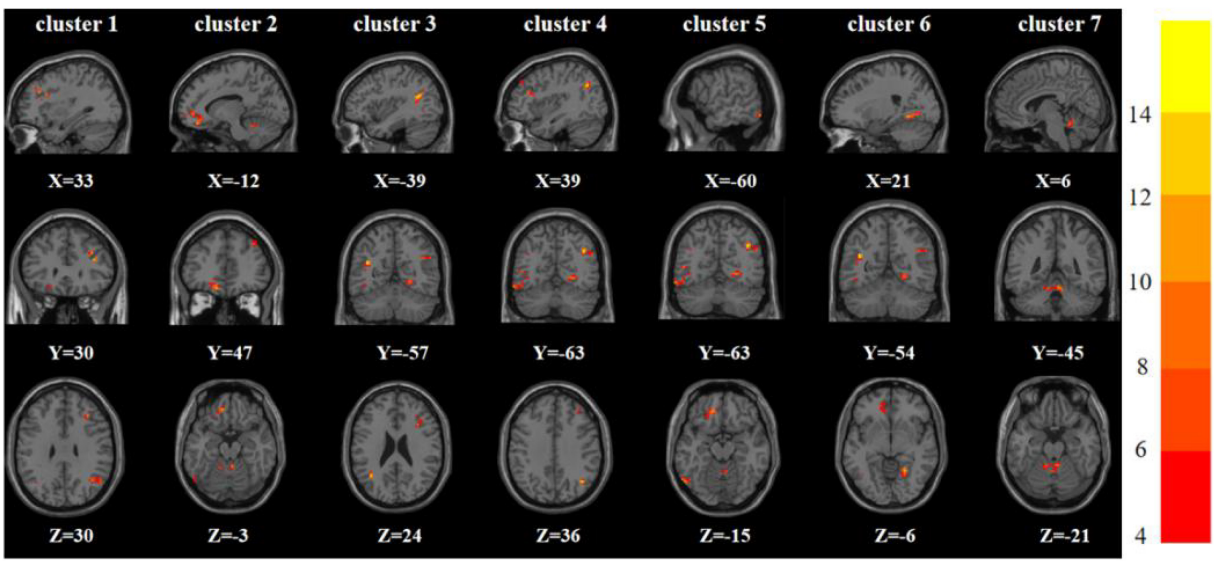

FIGURE 2 | Brain regions with abnormal ALFF among the three groups based on one-way analysis of variance. The color bars indicate the *F*-value.

Significant Correlation Between Functional Image and Clinical Feature

To test the correlation between areas of abnormal brain activity and the severity of clinical depressive symptoms, we further performed Pearson correlation analysis. We found a positive correlation between the ReHo/ALFF values of the right inferior frontal triangular gyrus and the HAMD-17 scores in the RDE group ($r = 0.436$, $P = 0.018$; $r = 0.394$, $P = 0.034$). Meanwhile, we observed a positive correlation between the ReHo values in the left anterior cingulate cortex/orbital part of the left middle frontal gyrus and the HAMD-17 scores in the FDE group ($r = 0.488$, $P = 0.008$). Furthermore, we found a negative correlation between the ReHo values in the left inferior temporal gyrus/left inferior occipital gyrus and right lingual gyrus and the HAMD-17 scores in the FDE group ($r = -0.412$, $P = 0.029$; $r = -0.408$, $P = 0.030$) (**Table 4** and **Figure 6**).

DISCUSSION

To our knowledge, this is the first study to investigate the changes in local brain function activity in patients with RDE or FDE using the ReHo and ALFF methods. The results of this study showed that the RDE and FDE groups had abnormal neural function

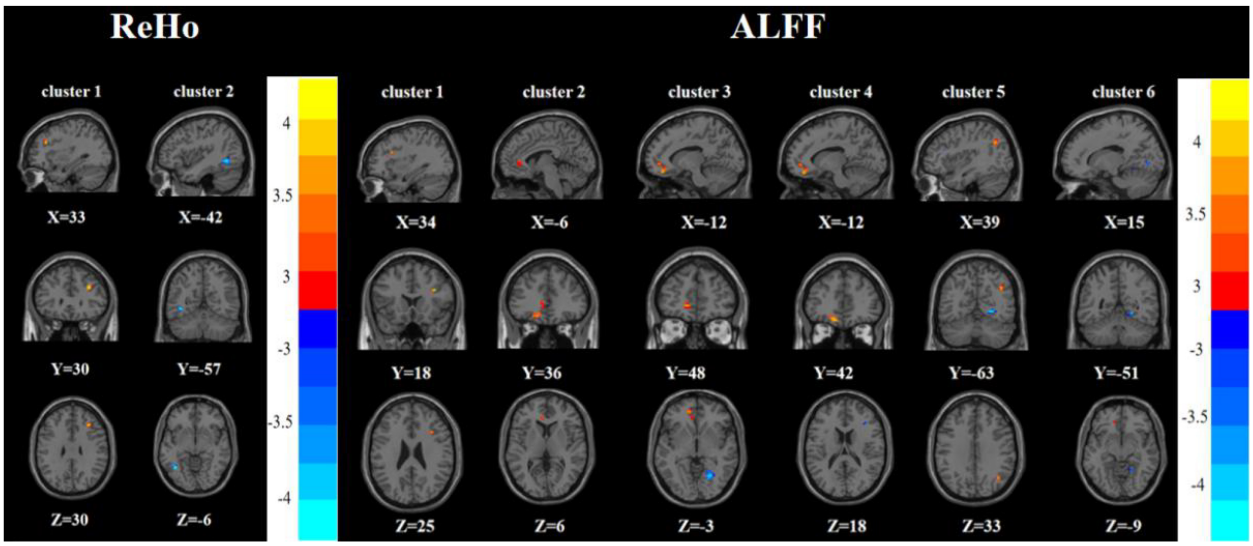

FIGURE 3 | Brain regions with abnormal ReHo **(left)** and ALFF **(right)** between the RDE group and the FDE group based on a *post hoc t*-test. The color bars indicate the *T*-value.

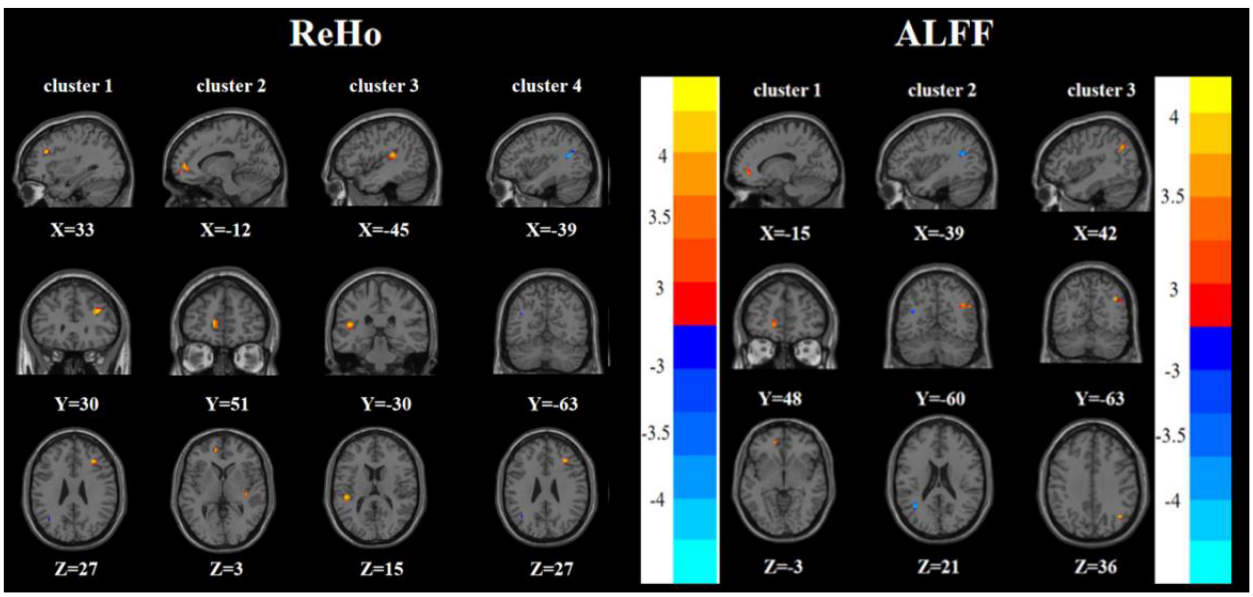

FIGURE 4 | Brain regions with abnormal ReHo **(left)** and ALFF **(right)** between the RDE group and the HC group based on a *post hoc t*-test. The color bars indicate the *T*-value.

activity in some of the same brain regions. ReHo and ALFF were more widely distributed in different brain regions and had more complex neuropathological mechanisms in the RDE group than in the FDE group. This study provides a reference for the differences in brain function activity between RDE and FDE.

We found increased ReHo and ALFF in the right inferior frontal triangular gyrus in the RDE group compared with the FDE group. The right inferior frontal triangular gyrus is located in the dorsolateral prefrontal cortex (DLPFC), an important component of executive function that is closely related to working memory, thought activity, and cognitive control (Wang et al., 2020; Brosch et al., 2021; Nejati et al., 2022). Previous studies have also shown that depressed mood and cognitive behavioral impairment in patients with depression are associated with abnormalities in executive function (Sun et al., 2018). Patients with mild impairment in the DLPFC often show symptoms of depression, such as loss of interest, poor memory, slow thinking, lack of motivation, and insomnia (Elliott, 2003; Li et al., 2021). Previous studies have found that the right inferior frontal triangle gyrus plays an important role in the

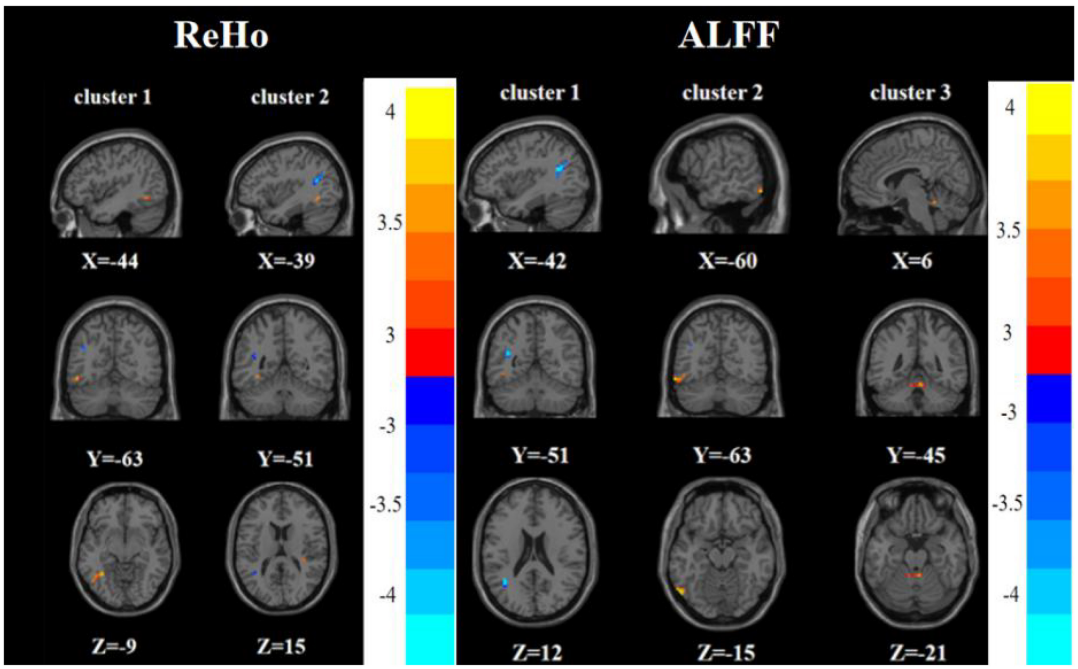

FIGURE 5 | Brain regions with abnormal ReHo **(left)** and ALFF **(right)** between the FDE group and the HC group based on a *post hoc t*-test. The color bars indicate the *T*-value.

early pathogenesis of MDD (Zhang et al., 2021) and that the gray matter volume of the DLPFC is reduced in patients with RDE after 6 weeks of antidepressant therapy (Li et al., 2010). Another study showed that stimulation of the right and left DLPFC with transcranial direct current stimulation was effective in reducing the risk of recurrence in patients with depression (Aparicio et al., 2019). The BOLD signals in the DLPFC have also been found to differ between RDE and FDE (Yuksel et al., 2018). This suggests that patients with RDE and those with FDE have differences in executive function. The correlation analysis in this study showed that the ReHo and ALFF values in the right inferior frontal triangular gyrus were positively correlated with the HAMD-17 scores in the RDE group, whereas no such correlation was found in the FDE group. These results suggest that the right inferior frontal triangular gyrus is an important neurobiological imaging marker for RDE and an important brain region for differentiating RDE from FDE.

We also found differences in ALFF in the left anterior cingulate gyrus and left orbitofrontal gyrus between the RDE and FDE groups. The anterior cingulate gyrus is an important component of the limbic system. It has extensive fibrous connections to many cortical and subcortical structures; is involved in the regulation of a wide range of functions, such as emotion, cognition, and motivation; and is closely associated with the onset of depression (Xiao and Zhang, 2018; Zheng et al., 2018; Rolls, 2019). Previous studies have found higher ALFF in the right ventral anterior cingulate gyrus in patients with anxious depression than in patients with rMDD and in HCs. In addition, abnormal activation of the anterior cingulate gyrus at rest in patients with MDD may be related to the failure of emotional control, which is a central factor in negative rumination and persistent self-focus in these patients (Amodio and Frith, 2006; Liu et al., 2015). Therefore, the results of this study suggest that patients with RDE show abnormal activation of the left side of the anterior cingulate gyrus. The orbitofrontal cortex is an important part of the reward network and is closely associated with emotional information and sensory stimuli (O'Doherty, 2004; Liu et al., 2017). A previous study found that patients with refractory depression, which is characterized by persistence and recurrence, had significantly higher ALFF in the orbitofrontal cortex than

TABLE 4 | Correlation of abnormal brain areas with clinical symptoms.

Variables	group	Brain regions	HAMD-17 score	
			Coefficient	*P*-value
ReHo	RDE	Right inferior frontal triangular gyrus	0.436	0.018[a,#]
	FDE	Left inferior temporal gyrus	−0.412	0.029[a,#]
		Left inferior occipital gyrus		
ALFF	RDE	Right inferior frontal triangular gyrus	0.394	0.034[a,#]
	FDE	Left anterior cingulate cortex	0.488	0.008[a,#]
		Orbital part of the left middle frontal gyrus		
	FDE	Right lingual gyrus	−0.408	0.030[a,#]

[a] *P-value from Pearson correlation (not corrected).*
[#] *Statistical significance.*

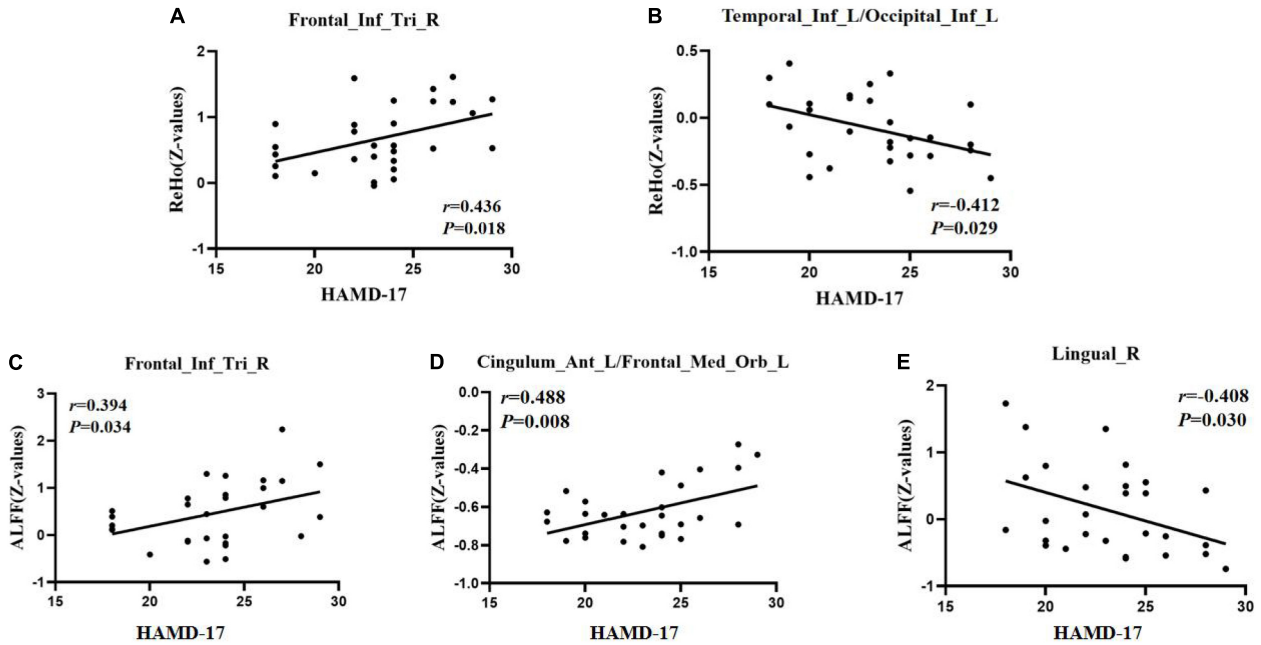

FIGURE 6 | Positive correlation between the ReHo/ALFF values of abnormal brain regions and the HAMD-17 scores. **(A)** ReHo values in the recurrent depressive episode (RDE) group. **(C)** ALFF values in the RDE group. **(D)** ALFF values in the first depressive episode (FDE) group. Negative correlation between the ReHo/ALFF values of abnormal brain regions and the HAMD-17 scores. **(B)** ReHo values in the FDE group. **(E)** ALFF values in the FDE group. Frontal_Inf_Tri_R, right inferior frontal triangular gyrus; Cingulum_Ant_L/Frontal_Med_Orb_L, left anterior cingulate cortex/orbital part of the left middle frontal gyrus; Temporal_Inf_L/Occipital_Inf_L, left inferior temporal gyrus/left inferior occipital gyrus; Lingual_R, right lingual gyrus; ReHo, regional homogeneity; ALFF, amplitude of low-frequency fluctuations; HAMD-17, 17-item Hamilton Rating Scale for Depression.

HCs (Liu et al., 2014). This suggests that abnormal activation of the orbitofrontal cortex is a cause of the complexity of RDE. Another study also showed that patients with FDE had reduced ALFF in the left and right orbitofrontal cortex compared with HCs, suggesting that patients with FDE have reduced regulation of the reward network (Zhang et al., 2014). Although these results were from different studies, they all support the involvement of the anterior cingulate gyrus and orbitofrontal cortex in regulating the pathophysiology of MDD. The correlation analysis in the current study showed that the ALFF values in the left anterior cingulate cortex/orbital part of the left middle frontal gyrus were positively correlated with the HAMD-17 scores in the FDE group, thus identifying an important brain region for differentiating between RDE and FDE.

In addition, we found that the RDE group had higher ALFF values in the right lingual gyrus than the FDE group. The lingual gyrus is part of the occipital lobe, and previous studies have shown that the lingual gyrus is also involved in activities related to visual memory processing and is closely associated with the development of MDD (Jung et al., 2014; Le et al., 2017; Palejwala et al., 2021). One study found that patients with rMDD had lower ALFF values in the right lingual gyrus than HCs, suggesting that reduced ALFF in the right lingual gyrus is a marker for the remission of depression (Yang et al., 2018). Another study also showed that patients with FDE had lower ALFF values in the right lingual gyrus than HCs (Wang et al., 2012). Our correlation analysis showed that the ALFF values in the right lingual gyrus were negatively correlated with the HAMD-17 scores in the FDE group. This suggests that the right lingual gyrus can be used as a status marker for FDE.

Meanwhile, we found that the ALFF in the right angular gyrus was higher in the RDE group than in the FDE group. A previous study reported that the right angular gyrus is associated with the self-localization function in humans and is potentially associated with psychiatric disorders, and that an abnormality in this function affects both sensory and perceptual functions, with a causal relationship between them (de Boer et al., 2020). This may also be informative in elucidating the differences in neuropathological mechanisms between RDE and FDE. The inferior temporal gyrus is involved in functions such as social cognition, emotional stimulus processing, self-referential processing, and semantic processing and is closely associated with MDD development (Chao et al., 1999; Cabeza and Nyberg, 2000; Herath et al., 2001; Hu et al., 2017; Kocsis et al., 2021). Previous studies have found that ReHo is significantly higher in the left middle temporal gyrus in patients with FDE than in those with rMDD, suggesting that enhanced metabolism in the left middle temporal gyrus may be one of the pathogenic mechanisms of FDE (Yang et al., 2018). Therefore, we suggest that differences exist between RDE and FDE in terms of abnormalities in the frontal, temporal, parietal, and occipital lobes, particularly in the right inferior frontal triangular gyrus of the frontal lobe.

Interestingly, we also found that the RDE and FDE groups had lower ReHo and ALFF in the left angular gyrus than the

HC group. The angular gyrus is located in the posterior part of the inferior parietal lobe and is mainly involved in human semantic and numerical processing, memory retrieval, spatial cognition, word reading and comprehension, reasoning, and social cognition, with the left angular gyrus playing a more important role in situational simulation and memory (Seghier, 2013; Thakral et al., 2017; Ramanan and Bellana, 2019). The angular gyrus is also an important part of the default mode network (Raichle et al., 2001; Raichle, 2015). Previous studies have found differences in BOLD signals in the angular gyrus between patients with RDE or FDE and HCs, consistent with the present study (Yuksel et al., 2018). Other studies have also reported that the ReHo and ALFF values in the left angular gyrus were lower in patients with MDD than in HCs (Wang et al., 2012; Liu et al., 2021). Abnormalities in angular gyrus function can lead to cognitive impairment, a common clinical manifestation of MDD (Lee et al., 2012). Therefore, this suggests that (1) both RDE and FDE are characterized by default mode network dysfunction and (2) ReHo and ALFF abnormalities in the left angular gyrus are important markers for differentiating patients with MDD from HCs.

Some limitations of this study should be considered. First, the patients with RDE enrolled in this study might have still been affected by an underlying antidepressant action despite having stopped medication for 4 weeks. Second, the number of recurrences in the RDE group was inconsistent, and a first-recurrence study of patients with RDE seem to have greater research value. Third, this study focused on only one scale (HAMD-17). To enhance the scientific value of this study, more scales need to be used in the future to focus on the detailed correlation of cognitive, somatic, anxiety, and insomnia symptoms with RDE and FDE. Finally, this study did not find a difference between RDE and FDE in depressive symptoms, which may be related to the specificity and small size of the study population. Further studies with a larger sample size are needed to confirm or refute the findings of this study.

CONCLUSION

This study used ReHo and ALFF, which are indices based on the rs-fMRI technique, to preliminarily analyze the differences between RDE and FDE in terms of neural activity in different brain regions. The RDE and FDE groups showed abnormal changes in neural function activity in some of the same brain regions, with ReHo and ALFF being more widely distributed in different brain regions and the neuropathological mechanisms being more complex in the RDE group than in the FDE group, particularly in the right inferior frontal triangular gyrus of the frontal lobe.

DATA AVAILABILITY STATEMENT

The raw data supporting the conclusions of this article will be made available by the authors, without undue reservation.

ETHICS STATEMENT

The experimental protocol was approved by the Ethics Committee of Guang'anmen Hospital, Chinese Academy of Traditional Chinese Medicine (No. 2017-021-SQ), Trial registration: China Clinical Trials Registry, chiCTR1800014277. The patients/participants provided their written informed consent to participate in this study.

AUTHOR CONTRIBUTIONS

JF conceived and designed this experiment. JS wrote and revised the manuscript and participated in the collection of cases and statistical analysis of the data. LC drew diagrams and made statistical analysis of data and revised the manuscript. ZD analyzed the data and revised the manuscript. JH, DG, YM, ZW, CG, and YL participated in data analysis, case collection, and manuscript writing. YH, LZ, and JC performed fMRI on the patient. FX, XH, XX, JT, and XY involved in case collection and symptom assessment of patients. All authors contributed to the article and approved the submitted version.

FUNDING

This research was supported by the Science and Technology Innovation Project of Chinese Academy of Traditional Chinese Medicine (CI2021A03301), the National Natural Science Foundation of China (82174282 and 81774433), and the National Key Research and Development Program of China (2018YFC1705800).

ACKNOWLEDGMENTS

We thank all the patients, healthy people who participated in the experiment for their support.

REFERENCES

Amodio, D. M., and Frith, C. D. (2006). Meeting of minds: the medial frontal cortex and social cognition. *Nat. Rev. Neurosci.* 7, 268–277. doi: 10.1038/nrn1884

Aparicio, L. V. M., Rosa, V., Razza, L. M., Sampaio-Junior, B., Borrione, L., Valiengo, L., et al. (2019). Transcranial direct current stimulation (tDCS) for preventing major depressive disorder relapse: Results of a 6-month follow-up. *Depress Anxiety* 36, 262–268. doi: 10.1002/da.22878

Bathelt, J., and Geurts, H. M. (2021). Difference in default mode network subsystems in autism across childhood and adolescence. *Autism* 25, 556–565. doi: 10.1177/1362361320969258

Brosch, K., Stein, F., Meller, T., Schmitt, S., Yuksel, D., Ringwald, K. G., et al. (2021). DLPFC volume is a neural correlate of resilience in healthy

high-risk individuals with both childhood maltreatment and familial risk for depression. *Psychol. Med.* 1–7. doi: 10.1017/S0033291721001094 [Epub online ahead of print].

Brown, E., Clark, D., Hassel, S., MacQueen, G., and Ramasubbu, R. J. N. d (2019). Intrinsic thalamocortical connectivity varies in the age of onset subtypes in major depressive disorder. *Neuropsychiatr. Dis. Treat.* 15, 75–82. doi: 10.2147/ndt.S184425

Burcusa, S. L., and Iacono, W. G. (2007). Risk for recurrence in depression. *Clin. Psychol. Rev.* 27, 959–985. doi: 10.1016/j.cpr.2007.02.005

Cabeza, R., and Nyberg, L. (2000). Imaging cognition II: An empirical review of 275 PET and fMRI studies. *J. Cogn. Neurosci.* 12, 1–47. doi: 10.1162/089892900511375851

Chao, L. L., Haxby, J. V., and Martin, A. (1999). Attribute-based neural substrates in temporal cortex for perceiving and knowing about objects. *Nat. Neurosci.* 2, 913–919. doi: 10.1038/13217

de Boer, D. M. L., Johnston, P. J., Kerr, G., Meinzer, M., and Cleeremans, A. (2020). A causal role for the right angular gyrus in self-location mediated perspective taking. *Sci. Rep.* 10:19229. doi: 10.1038/s41598-020-76235-7

Elliott, R. (2003). Executive functions and their disorders. *Br. Med. Bull.* 65, 49–59. doi: 10.1093/bmb/65.1.49

Fava, G. A., Cosci, F., Guidi, J., and Tomba, E. (2017). Well-being therapy in depression: New insights into the role of psychological well-being in the clinical process. *Depress Anxiety* 34, 801–808. doi: 10.1002/da.22629

Friedrich, M. J. (2017). Depression Is the Leading Cause of Disability Around the World. *JAMA* 317:1517. doi: 10.1001/jama.2017.3826

Hamilton, M. (1960). A rating scale for depression. *J. Neurol. Neurosurg. Psychiatr.* 23, 56–62. doi: 10.1136/jnnp.23.1.56

Harlev, D., Ravona-Springer, R., Nuriel, Y., and Fruchter, E. (2021). Sleep Monitoring Using WatchPAT Device to Predict Recurrence of Major Depression in Patients at High Risk for Major Depression Disorder Recurrence: A Case Report. *Front. Psychiatr.* 12:572660. doi: 10.3389/fpsyt.2021.572660

Herath, P., Kinomura, S., and Roland, P. E. (2001). Visual recognition: evidence for two distinctive mechanisms from a PET study. *Hum. Brain Mapp.* 12, 110–119. doi: 10.1002/1097-0193(200102)12:2<110::aid-hbm1008>3.0.co;2-0

Hu, B., Rao, J., Li, X., Cao, T., Li, J., Majoe, D., et al. (2017). Emotion Regulating Attentional Control Abnormalities In Major Depressive Disorder: An Event-Related Potential Study. *Sci. Rep.* 7:13530. doi: 10.1038/s41598-017-13626-3

Jung, J., Kang, J., Won, E., Nam, K., Lee, M. S., Tae, W. S., et al. (2014). Impact of lingual gyrus volume on antidepressant response and neurocognitive functions in Major Depressive Disorder: a voxel-based morphometry study. *J. Affect. Disord.* 169, 179–187. doi: 10.1016/j.jad.2014.08.018

Kendall, M. G. (1990). *Rank Correlation Methods* (5th ed ed.). Oxford: Oxford University Press.

Kocsis, K., Holczer, A., Kazinczi, C., Boross, K., Horvath, R., Nemeth, L. V., et al. (2021). Voxel-based asymmetry of the regional gray matter over the inferior temporal gyrus correlates with depressive symptoms in medicated patients with major depressive disorder. *Psychiatr. Res. Neuroimaging* 317:111378. doi: 10.1016/j.pscychresns.2021.111378

Le, T. M., Borghi, J. A., Kujawa, A. J., Klein, D. N., and Leung, H. C. (2017). Alterations in visual cortical activation and connectivity with prefrontal cortex during working memory updating in major depressive disorder. *Neuroimage Clin.* 14, 43–53. doi: 10.1016/j.nicl.2017.01.004

Lee, M. H., Smyser, C. D., and Shimony, J. S. (2013). Resting-state fMRI: a review of methods and clinical applications. *Am. J. Neuroradiol.* 34, 1866–1872. doi: 10.3174/ajnr.A3263

Lee, R. S., Hermens, D. F., Porter, M. A., and Redoblado-Hodge, M. A. (2012). A meta-analysis of cognitive deficits in first-episode Major Depressive Disorder. *J. Affect. Disord.* 140, 113–124. doi: 10.1016/j.jad.2011.10.023

Li, C. T., Lin, C. P., Chou, K. H., Chen, I. Y., Hsieh, J. C., Wu, C. L., et al. (2010). Structural and cognitive deficits in remitting and non-remitting recurrent depression: a voxel-based morphometric study. *Neuroimage* 50, 347–356. doi: 10.1016/j.neuroimage.2009.11.021

Li, D., Zhang, H., Liu, Y., Liang, X., Chen, Y., Zheng, Y., et al. (2021). Abnormal Functional Connectivity of Posterior Cingulate Cortex Correlates With Phonemic Verbal Fluency Deficits in Major Depressive Disorder. *Front. Neurol.* 12:724874. doi: 10.3389/fneur.2021.724874

Liu, C., Ma, X., Song, L., Fan, J., Wang, W., and Lv, X. (2015). Abnormal spontaneous neural activity in the anterior insular and anterior cingulate cortices in anxious depression. *Behav. Brain Res.* 281, 339–347. doi: 10.1016/j.bbr.2014.11.047

Liu, J., Ren, L., Womer, F. Y., Wang, J., Fan, G., Jiang, W., et al. (2014). Alterations in amplitude of low frequency fluctuation in treatment-naive major depressive disorder measured with resting-state fMRI. *Hum. Brain Mapp.* 35, 4979–4988. doi: 10.1002/hbm.22526

Liu, S., Ma, R., Luo, Y., Liu, P., Zhao, K., Guo, H., et al. (2021). Facial Expression Recognition and ReHo Analysis in Major Depressive Disorder. *Front. Psychol.* 12:688376. doi: 10.3389/fpsyg.2021.688376

Liu, Y., Zhao, X., Cheng, Z., Zhang, F., Chang, J., Wang, H., et al. (2017). Regional homogeneity associated with overgeneral autobiographical memory of first-episode treatment-naive patients with major depressive disorder in the orbitofrontal cortex: A resting-state fMRI study. *J. Affect. Disord.* 209, 163–168. doi: 10.1016/j.jad.2016.11.044

Marques, D. R., Gomes, A. A., Caetano, G., and Castelo-Branco, M. (2018). Insomnia Disorder and Brain's Default-Mode Network. *Curr. Neurol. Neurosci. Rep.* 18:45. doi: 10.1007/s11910-018-0861-3

Nejati, V., Majidinezhad, M., and Nitsche, M. (2022). The role of the dorsolateral and ventromedial prefrontal cortex in emotion regulation in females with major depressive disorder (MDD): A tDCS study. *J. Psychiatr. Res.* 148, 149–158. doi: 10.1016/j.jpsychires.2022.01.030

Ni, L., Liu, R., Yin, Z., Zhao, H., Nedelska, Z., Hort, J., et al. (2016). Aberrant Spontaneous Brain Activity in Patients with Mild Cognitive Impairment and concomitant Lacunar Infarction: A Resting-State Functional MRI Study. *J. Alzheimers. Dis.* 50, 1243–1254. doi: 10.3233/JAD-150622

O'Doherty, J. P. (2004). Reward representations and reward-related learning in the human brain: insights from neuroimaging. *Curr. Opin. Neurobiol.* 14, 769–776. doi: 10.1016/j.conb.2004.10.016

Palejwala, A. H., Dadario, N. B., Young, I. M., O'Connor, K., Briggs, R. G., Conner, A. K., et al. (2021). Anatomy and White Matter Connections of the Lingual Gyrus and Cuneus. *World Neurosurg.* 151, e426–e437. doi: 10.1016/j.wneu.2021.04.050

Raichle, M. E. (2015). The brain's default mode network. *Annu. Rev. Neurosci.* 38, 433–447. doi: 10.1146/annurev-neuro-071013-014030

Raichle, M. E., MacLeod, A. M., Snyder, A. Z., Powers, W. J., Gusnard, D. A., and Shulman, G. L. (2001). A default mode of brain function. *Proc. Natl. Acad. Sci. U S A* 98, 676–682. doi: 10.1073/pnas.98.2.676

Ramanan, S., and Bellana, B. (2019). A Domain-General Role for the Angular Gyrus in Retrieving Internal Representations of the External World. *J. Neurosci.* 39, 2978–2980. doi: 10.1523/JNEUROSCI.3231-18.2019

Roca, M., Armengol, S., Garcia-Garcia, M., Rodriguez-Bayon, A., Ballesta, I., Serrano, M. J., et al. (2011). Clinical differences between first and recurrent episodes in depressive patients. *Compr. Psychiatr.* 52, 26–32. doi: 10.1016/j.comppsych.2010.04.011

Roca, M., Lopez-Navarro, E., Monzon, S., Vives, M., Garcia-Toro, M., and Garcia-Campayo, J. (2015). Cognitive impairment in remitted and non-remitted depressive patients: A follow-up comparison between first and recurrent episodes. *Eur. Neuropsychopharmacol.* 25, 1991–1998. doi: 10.1016/j.euroneuro.2015.07.020

Rolls, E. T. (2019). The cingulate cortex and limbic systems for action, emotion, and memory. *Handb. Clin. Neurol.* 166, 23–37. doi: 10.1016/B978-0-444-64196-0.00002-9

Seghier, M. L. (2013). The angular gyrus: multiple functions and multiple subdivisions. *Neuroscientist* 19, 43–61. doi: 10.1177/1073858412440596

Sheffield, J. M., and Barch, D. M. (2016). Cognition and resting-state functional connectivity in schizophrenia. *Neurosci. Biobehav. Rev.* 61, 108–120. doi: 10.1016/j.neubiorev.2015.12.007

Shen, Z., Zhu, J., Ren, L., Qian, M., Shao, Y., Yuan, Y., et al. (2020). Aberrant amplitude low-frequency fluctuation (ALFF) and regional homogeneity (ReHo) in generalized anxiety disorder (GAD) and their roles in predicting treatment remission. *Ann. Transl. Med.* 8:1319. doi: 10.21037/atm-20-6448

Sun, H., Luo, L., Yuan, X., Zhang, L., He, Y., Yao, S., et al. (2018). Regional homogeneity and functional connectivity patterns in major depressive disorder, cognitive vulnerability to depression and healthy subjects. *J. Affect. Disord.* 235, 229–235. doi: 10.1016/j.jad.2018.04.061

Talarowska, M., Zajączkowska, M., and Gałecki, P. J. P. D. (2015). Cognitive functions in first-episode depression and recurrent depressive disorder. *Psychiatr. Danub.* 27, 38–43.

Thakral, P. P., Madore, K. P., and Schacter, D. L. (2017). A Role for the Left Angular Gyrus in Episodic Simulation and Memory. *J. Neurosci.* 37, 8142–8149. doi: 10.1523/JNEUROSCI.1319-17.2017

Varghese, S., Frey, B. N., Schneider, M. A., Kapczinski, F., and de Azevedo Cardoso, T. (2022). Functional and cognitive impairment in the first episode of depression: A systematic review. *Acta. Psychiatr. Scand.* 145, 156–185. doi: 10.1111/acps.13385

Wang, L., Dai, W., Su, Y., Wang, G., Tan, Y., Jin, Z., et al. (2012). Amplitude of low-frequency oscillations in first-episode, treatment-naive patients with major depressive disorder: a resting-state functional MRI study. *PLoS One* 7:e48658. doi: 10.1371/journal.pone.0048658

Wang, Y., Zhang, A., Yang, C., Li, G., Sun, N., Liu, P., et al. (2020). Enhanced Functional Connectivity Within Executive Function Network in Remitted or Partially Remitted MDD Patients. *Front. Psychiatr.* 11:538333. doi: 10.3389/fpsyt.2020.538333

Wolfers, T., Buitelaar, J. K., Beckmann, C. F., Franke, B., and Marquand, A. F. (2015). From estimating activation locality to predicting disorder: A review of pattern recognition for neuroimaging-based psychiatric diagnostics. *Neurosci. Biobehav. Rev.* 57, 328–349. doi: 10.1016/j.neubiorev.2015.08.001

Xiao, X., and Zhang, Y. Q. (2018). A new perspective on the anterior cingulate cortex and affective pain. *Neurosci. Biobehav. Rev.* 90, 200–211. doi: 10.1016/j.neubiorev.2018.03.022

Yan, C. G., and Zang, Y. F. (2010). DPARSF: A MATLAB Toolbox for "Pipeline" Data Analysis of Resting-State fMRI. *Front. Syst. Neurosci.* 4:13. doi: 10.3389/fnsys.2010.00013

Yang, C., Zhang, A., Jia, A., Ma, J. X., Sun, N., Wang, Y., et al. (2018). Identify abnormalities in resting-state brain function between first-episode, drug-naive major depressive disorder and remitted individuals: a 3-year retrospective study. *Neuroreport* 29, 907–916. doi: 10.1097/WNR.0000000000001054

Yue, Y., Jiang, Y., Shen, T., Pu, J., Lai, H., and Zhang, B. J. F. i. n (2020). ALFF and ReHo Mapping Reveals Different Functional Patterns in Early- and Late-Onset Parkinson's Disease. *Front. Neurosci.* 14:141. doi: 10.3389/fnins.2020.00141

Yuksel, D., Dietsche, B., Konrad, C., Dannlowski, U., Kircher, T., and Krug, A. (2018). Neural correlates of working memory in first episode and recurrent depression: An fMRI study. *Prog. Neuropsychopharmacol. Biol. Psychiatr.* 84, 39–49. doi: 10.1016/j.pnpbp.2018.02.003

Zang, Y., Jiang, T., Lu, Y., He, Y., and Tian, L. (2004). Regional homogeneity approach to fMRI data analysis. *Neuroimage.* 22, 394–400. doi: 10.1016/j.neuroimage.2003.12.030

Zang, Y. F., He, Y., Zhu, C. Z., Cao, Q. J., Sui, M. Q., Liang, M., et al. (2007). Altered baseline brain activity in children with ADHD revealed by resting-state functional MRI. *Brain Dev.* 29, 83–91. doi: 10.1016/j.braindev.2006.07.002

Zhang, F. F., Peng, W., Sweeney, J. A., Jia, Z. Y., and Gong, Q. Y. (2018). Brain structure alterations in depression: Psychoradiological evidence. *CNS Neurosci. Ther.* 24, 994–1003. doi: 10.1111/cns.12835

Zhang, X., Zhu, X., Wang, X., Zhu, X., Zhong, M., Yi, J., et al. (2014). First-episode medication-naive major depressive disorder is associated with altered resting brain function in the affective network. *PLoS One* 9:e85241. doi: 10.1371/journal.pone.0085241

Zhang, Z., Chen, Y., Wei, W., Yang, X., Meng, Y., Yu, H., et al. (2021). Changes in Regional Homogeneity of Medication-Free Major Depressive Disorder Patients With Different Onset Ages. *Front. Psychiatr.* 12:713614. doi: 10.3389/fpsyt.2021.713614

Zhao, C., Zhu, J., Liu, X., Pu, C., Lai, Y., Chen, L., et al. (2018). Structural and functional brain abnormalities in schizophrenia: A cross-sectional study at different stages of the disease. *Prog. Neuropsychopharmacol. Biol. Psychiatr.* 83, 27–32. doi: 10.1016/j.pnpbp.2017.12.017

Zheng, H., Li, F., Bo, Q., Li, X., Yao, L., Yao, Z., et al. (2018). The dynamic characteristics of the anterior cingulate cortex in resting-state fMRI of patients with depression. *J. Affect. Disord.* 227, 391–397. doi: 10.1016/j.jad.2017.11.026

Zu, S., Wang, D., Fang, J., Xiao, L., Zhu, X., Wu, W., et al. (2021). Comparison of Residual Depressive Symptoms. Functioning, and Quality of Life Between Patients with Recurrent Depression and First Episode Depression After Acute Treatment in China. *Neuropsychiatr Dis Treat* 17, 3039–3051. doi: 10.2147/NDT.S317770

Conflict of Interest: The authors declare that the research was conducted in the absence of any commercial or financial relationships that could be construed as a potential conflict of interest.

Publisher's Note: All claims expressed in this article are solely those of the authors and do not necessarily represent those of their affiliated organizations, or those of the publisher, the editors and the reviewers. Any product that may be evaluated in this article, or claim that may be made by its manufacturer, is not guaranteed or endorsed by the publisher.

frontiers | Frontiers in Neuroscience

ORIGINAL RESEARCH
published: 09 May 2022
doi: 10.3389/fnins.2022.865594

A Motor Imagery Signals Classification Method *via* the Difference of EEG Signals Between Left and Right Hemispheric Electrodes

Xiangmin Lun[1], *Jianwei Liu*[1], *Yifei Zhang*[1], *Ziqian Hao*[2] *and Yimin Hou*[1]*

[1] School of Automation Engineering, Northeast Electric Power University, Jilin, China, [2] School of Finance and Business, Jinan Vocational College, Jinan, China

Brain-computer interface (BCI) based on motor imagery (MI) can help patients with limb movement disorders in their normal life. In order to develop an efficient BCI system, it is necessary to decode high-accuracy motion intention by electroencephalogram (EEG) with low signal-to-noise ratio. In this article, a MI classification approach is proposed, combining the difference in EEG signals between the left and right hemispheric electrodes with a dual convolutional neural network (dual-CNN), which effectively improved the decoding performance of BCI. The positive and inverse problems of EEG were solved by the boundary element method (BEM) and weighted minimum norm estimation (WMNE), and then the scalp signals were mapped to the cortex layer. We created nine pairs of new electrodes on the cortex as the region of interest. The time series of the nine electrodes on the left and right hemispheric are respectively used as the input of the dual-CNN model to classify four MI tasks. The results show that this method has good results in both group-level subjects and individual subjects. On the Physionet database, the averaged accuracy on group-level can reach 96.36%, while the accuracies of four MI tasks reach 98.54, 95.02, 93.66, and 96.19%, respectively. As for the individual subject, the highest accuracy is 98.88%, and its four MI accuracies are 99.62, 99.68, 98.47, and 97.73%, respectively.

Keywords: brain-computer interface (BCI), electroencephalography (EEG), motor imagery (MI), convolutional neural network (CNN), weighted minimum norm estimation (WMNE)

OPEN ACCESS

Edited by:
Shijie Zhao,
Northwestern Polytechnical University, China

Reviewed by:
Weijie Ren,
Harbin Engineering University, China
Xi Jiang,
University of Electronic Science and Technology of China, China

***Correspondence:**
Yimin Hou
ymh7821@163.com

Specialty section:
This article was submitted to Brain Imaging Methods, a section of the journal Frontiers in Neuroscience

Received: *30 January 2022*
Accepted: *25 February 2022*
Published: *09 May 2022*

Citation:
Lun X, Liu J, Zhang Y, Hao Z and Hou Y (2022) A Motor Imagery Signals Classification Method via the Difference of EEG Signals Between Left and Right Hemispheric Electrodes. Front. Neurosci. 16:865594. doi: 10.3389/fnins.2022.865594

1. INTRODUCTION

The electroencephalogram (EEG) signal is the electrical activity of neurons in the brain recorded by EEG sensors. It has high temporal resolution and low spatial resolution (Nakamura et al., 2005). Currently, motor imagery EEG (MI-EEG) has received widespread attention because it can decode motion intention (Pfurtscheller et al., 2006). The brain-computer interface (BCI) can detect the intention of the MI-EEG signal and convert it into an executable output by the machine (Millan and Del, 2002). In other words, it can communicate with external devices by decoding MI tasks, so as to achieve two-way feedback between the user and the BCI system. The external device receives signals from the brain to control the device, and the device feeds back the control results to the brain for judgment (Jin et al., 2020). MI-BCI can help some disabled patients independently control external

devices such as wheelchairs (Wang and Bezerianos, 2017) and artificial limbs (Condori et al., 2016; Cho et al., 2019). Bhattacharyya et al. (2021) designed a real-time BCI neurofeedback system to reflect the expected tasks of hand movement and imagery.

Effective feature extraction can achieve high-precision decoding on MI-BCI. Entropy and sensor-imotor rhythm (SMR) are currently popular features in MI-BCI. In SMR-based BCI, He et al. (2015) reviewed the principles and approaches of developing an SMR EEG based BCI and found that the SMR based noninvasive BCI has the potential to provide communication and control capabilities. Yuan and He (2014) described the characteristic features of SMR from the human brain and discussed their underlying neural sources, also reviewed the functional components of SMR-based BCI, together with its current clinical applications. Serafeim et al. (2018) trained two severely impaired participants with chronic spinal cord injury (SCI) following mutual learning approach in a virtual BCI race game, it substantiates the effectiveness of this type of training. In entropy-based BCI, Stefano et al. (2019) proposed a novel approach based on the entropy of the EEG signals to provide a continuous identification of motion intention. The result shows that the proposed system can be used to predict motion in real-time at a frame rate of 8 Hz with 80 $\pm$ 5% of accuracy. Lei et al. (2012) extracted the sample entropy of the EEG and used support vector machines for pattern classification, it is found that sample entropy can effectively distinguish the characteristics of the brain in different states. Hsu (2015) extracted wavelet fuzzy approximate entropy and used SVM for classification, the results indicate that the proposed system including wavelet-based fuzzy approximate entropy (wfApEn) obtains better performance in average classification.

Recently, there have been many studies on the cortex. Hou et al. (2019) created ten regions of interest in the cortex and performed a time-frequency analysis on them. Edelman B. et al. (2015) explored the cortex dynamics during movements of an unaffected body part in tetraplegic subjects with chronic spinal cord injury. Kim and Kim (2018) analyzed the motor cortex of primates and provided an effective method to decode invasive BCI.

A convolutional neural network (CNN) is a practical tool in many fields, such as image classification (Krizhevsky et al., 2017), sentence classification (Kim, 2014), and EEG decoding (Schirrmeister et al., 2017). It reduces the data preprocessing steps and manual feature processing steps. Also, deep learning has made outstanding contributions to the improvement of MI-BCI (Li et al., 2018; Zhang et al., 2018; Cho et al., 2019; Robinson et al., 2019). Nakagome et al. (2020) used neural networks and machine learning algorithms to decode EEG. The results indicate that neural networks are of great significance in the decoding of EEG signals. Tortora et al. (2020) used a trained long short term memory deep neural network to decode EEG gait, and the proposed decoding method obtains more than 90% robust reconstruction. Al-Saegh et al. (2021) gathered 40 related articles on deep neural network architecture and MI-EEG tasks, and the results show that deep neural networks play a positive role in MI-EEG classification.

Brain-computer interface is a technology that reads EEG signals, records and decodes brain activities, manipulates the activities of specific brain regions, and affects its functions. Based on this, accurate decoding of EEG signals is very important for BCI systems. Since EEG signal is dynamic time series data with a low signal-to-noise ratio, the decoding accuracy of EEG signals has always been a challenge. Although many scholars have made remarkable achievements in this field, there is still a gap between the BCI system and practical application standards, and there is still much room for improvement in the classification method and accuracy of EEG signals.

The contributions of this article are summarized as follows: In this article, we proposed a MI signals classification method *via* the difference of EEG signals between left and right hemispheric electrodes. Based on the Physionet database, the EEG signal on the scalp layer is inversely mapped to the cortex of the brain, and then 9 pairs of new electrode pairs are created, which contain higher SNR information. The time-frequency analysis method is used to extract feature information from the time and frequency series of cortical electrodes. The dual-CNN model proposed in this article has the same settings, including 4 layers of CNN for learning EEG features, 4 layers of max pooling for dimension reduction, a Flatten operation for converting multidimensional data into one-dimensional data, and 1-layer fully connected (FC) layer for classification. This method combines the electrode channel information of the symmetrical regions of interest on the left and right hemispheres of the cortex with the CNN, which realizes the high-precision classification task and provides a new idea for simplifying the design of the BCI system.

The remainder of this article is organized as follows: Section 2 is the Materials and Methods. Section 3 is the Classification Accuracies of the Subjects. Section 4 is a Discussion. Finally, Section 5 is the Conclusion of this article.

2. MATERIALS AND METHODS

2.1. The Framework

The overall block diagram is shown in **Figure 1**. In this study, we first preprocessed the EEG on the scalp layer and then preprocessed it on the cortex layer. The noise covariance matrix of each subject was calculated in the cortex preprocessing, and the real head model was constructed with the help of the colin27 template and BEM algorithm. We used distributed current model (DCD) and WMNE algorithm to build a source model and then limited the source to the cortex layer. Then, manually created nine pairs of new electrodes on the left and right hemispheric of the cortex. Finally, the time series carried by the nine pairs of electrodes on the left and right hemispheric were used as the input of the dual-CNN classification model. The preprocessing process and the CNN model structure will be introduced in detail in the following Sections 2.3 and 2.4.2.

2.2. Dataset

The dataset we used was created by the developers of BCI2000 at a sampling frequency of 160Hz in a standard environment (Schalk et al., 2004). It is obtained through the corresponding

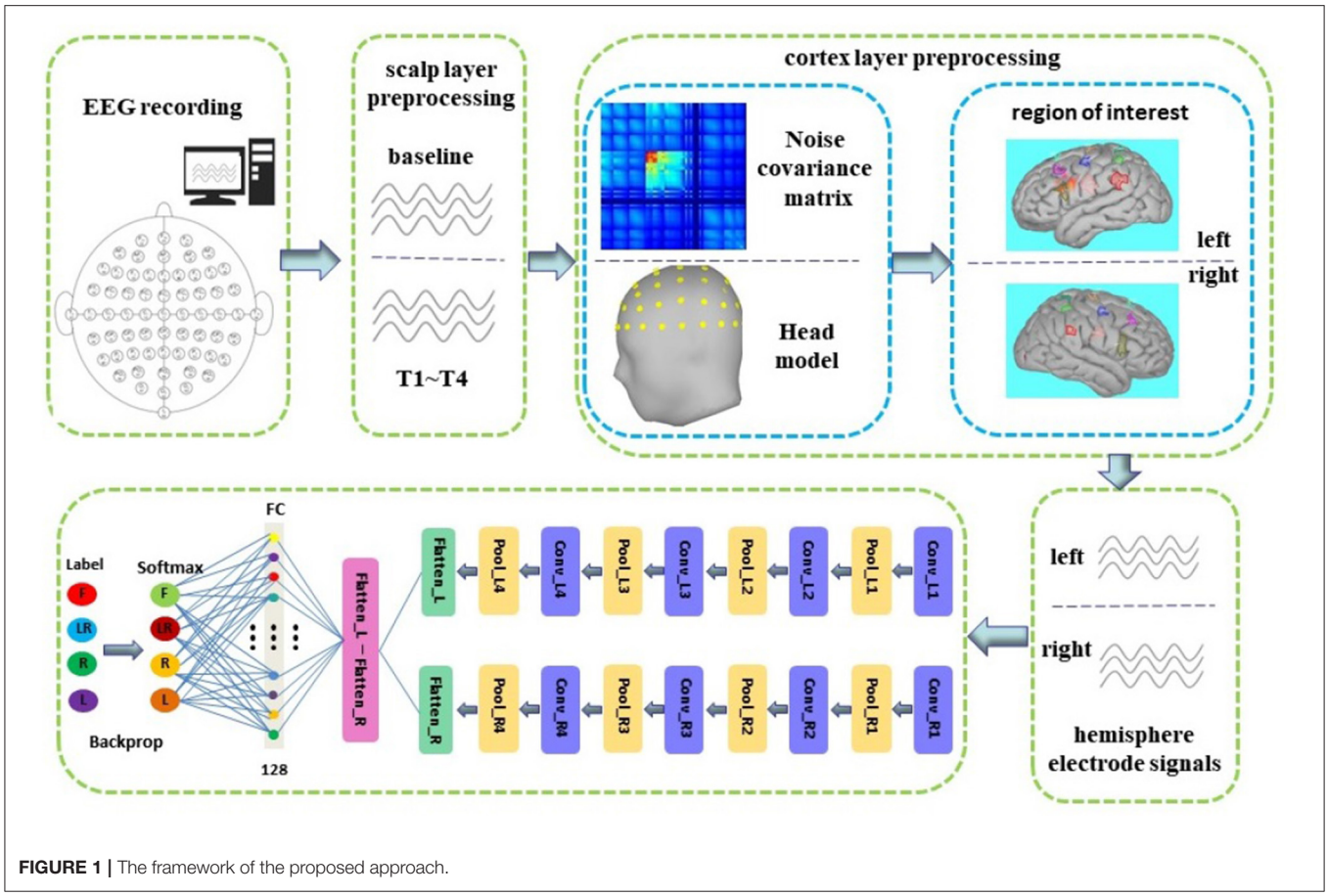

FIGURE 1 | The framework of the proposed approach.

10-10 system 64-channel EEG (excluding electrodes Nz, F9, F10, FT9, FT10, A1, A2, TP9, TP10, P9, and P10). The dataset records 4 MI tasks (left fist, right fist, both fists, and both feet) of 109 subjects. Each subject consists of 84 trails with 21 trails per class, each trail takes 1–2 min, and the duration of each MI task is slightly more than 4 s. The four tasks are as follows:

(1) A target appears on the left side of the screen. The subject imagines opening and closing the left fist until the target disappears. Then the subject relaxes.
(2) A target appears on the right side of the screen. The subject imagines opening and closing the right fist until the target disappears. Then the subject relaxes.
(3) A target appears on the top of the screen. The subject imagines opening and closing both fists until the target disappears. Then the subject relaxes.
(4) A target appears on the bottom of the screen. The subject imagines opening and closing either both feet until the target disappears. Then the subject relaxes. Detailed data description is given at https://archive.physionet.org/pn4/eegmmidb/.

2.3. Data Preprocessing

Data preprocessing is divided into two parts: scalp layer preprocessing and cortex layer preprocessing. In the scalp layer preprocessing, we marked 4 MI tasks (left fist, right fist, both fists, and both feet) of each subject as T1, T2, T3, and T4, respectively. Since each MI task is slightly more than 4 s, we used a time window of 4s to unify the size of 4 MI tasks, and then performed 8–30 Hz band-pass filter processing for each MI task.

The positive problem of EEG is the use of EEG sensors to collect electrical signals generated by a large number of neurons in the brain (Wheless and Castillo, 2004). However, the signals transmitted from the brain to the scalp are already very weak and cannot accurately represent the activities inside the brain. Therefore, inverting EEG into the brain will improve the quality of EEG and also help improve its decoding intention. The process of using EEG to acquire signals inside the brain is an inverse problem (Becker, 2015). Solving the positive problem of EEG is the basis for solving its inverse problem.

The positive problem of EEG is also called the forward model of EEG, which can be described as follows (Baillet and Garnero, 1997; Engemann and Gramfort, 2015):

$$y = b + \varepsilon = Lx + \varepsilon \tag{1}$$

Where n represents the number of sensors of EEG, p represents the number of dipoles in source space, $L \in R^{n \times p}$ is gain matrix or leadfield, and ε is noise.

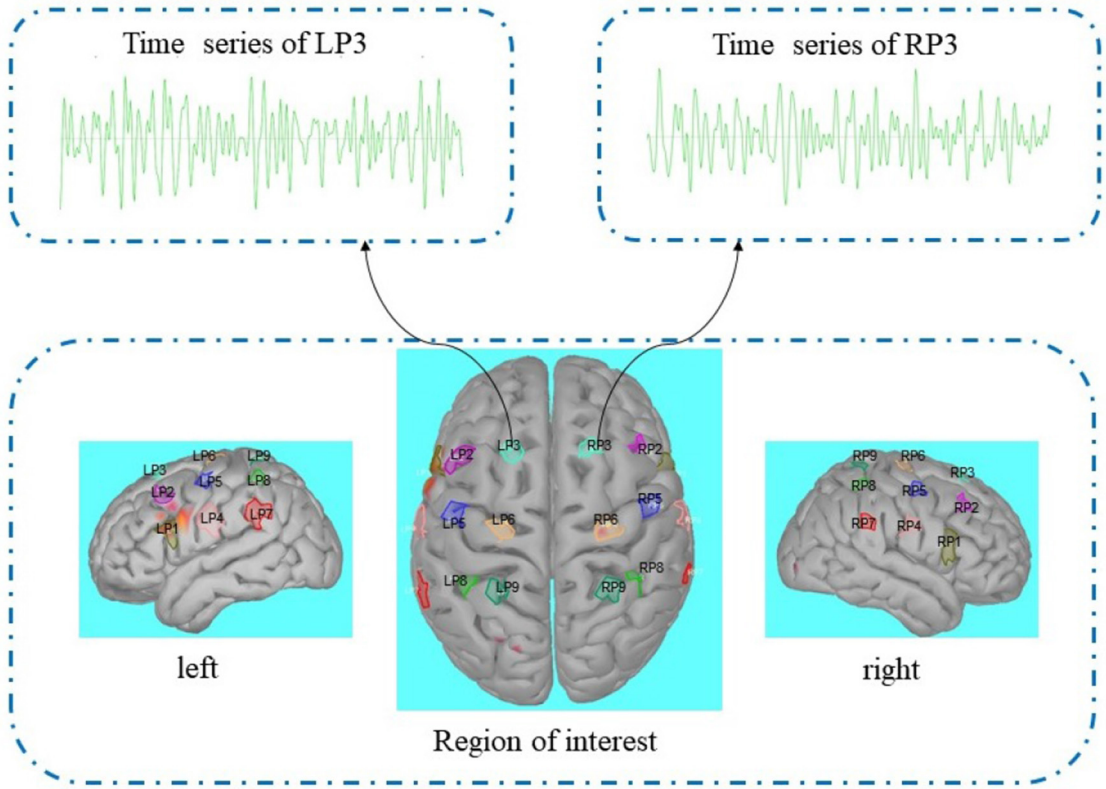

FIGURE 2 | Cortex preprocessing.

According to Maxwell equations (Noraini et al., 2013), the electromagnetic field R^n in Formula (1) is the linear combination of the fields generated by all sources $x \in R^p : b = Lx$. Solving the L matrix in Equation (1), finding sources that can best explain the value of EEG, and tracing the neurons in the brain is called the inverse problem of EEG (Janati et al., 2020).

The solution of the EEG forward problem consists of two parts: the head model and the algorithm. The head model is obtained by magnetic resonance imaging (MRI) of each subject. Since there is no permission to access the MRI of each subject, we used the high-precision colin27 template to build the head model (Collins et al., 1998).

In this part, we first completed the calibration of MRI and EEG and then calculated the noise covariance matrix according to baseline data for each subject to solve the problem of noise differences between different subjects. Then we used the BEM (Mosher et al., 1999; Gramfort, 2010) to solve the EEG positive problem and built a three-layer (cortex, skull, and scalp) head volume conduction model, also L was solved in the Equation (1).

Since the number of sources in the brain is far greater than the number of EEG sensors on the scalp, the result of the EEG inverse problem is not unique. It requires us to limit the source to a certain range. There are many cells on the cortex layer, they are close to the scalp, and the direction is basically perpendicular to the scalp, which is the main source of EEG (Okada, 1993). According to this, we used the DCD model to limit the source to the cortex layer of the brain. DCD model divides the entire cortex into discrete fixed sub-regions, each sub-region is placed with a current dipole perpendicular to the cortex, and this dipole is the source.

We used WMNE to solve the EEG inverse problem, as shown below (Phillips et al., 2002; Wu et al., 2003; Hassan et al., 2014):

$$I = L^T(LL^T + \lambda\omega)^{-1}R \tag{2}$$

Then we got a source model, the preprocessing of the cortex layer on the source model is shown in **Figure 2**. Similar to the research method of EEG source imaging, the region of interest can be selected by identifying particular gyral landmarks on the subject special cortex model (Edelman B. J. et al., 2015). According to Lun et al. (2020) we selected 18 scouts on the motor cortex as the region of interest. Nine sources on the left hemispheric are termed FC5, FC3, FC1, C5, C3, C1, CP5, CP3, CP1, and nine sources on the right hemispheric are termed FC6, FC4, FC2, C6, C4, C2, CP6, CP4, CP2. Each of the scouts was extended to 20 vertices, each vertex with one source (dipole) in constrained dipoles orientations. While the positions of the 18 sources are the projection on the cortex of nine pairs of electrodes (FC5, FC3, FC1, C5, C3, C1, CP5, CP3, CP1; FC6, FC4, FC2, C6, C4, C2, CP6, CP4, CP2), we marked these 18 sources as nine pairs of new

TABLE 1 | Proposed CNN architecture.

	Layer	Input size	Map	Convolution kernel size	Pooling size	Output size
L1	Input	1,280×9	1	-	-	640×9,640×9
L2	Conv_L1,Conv_R1	640×9	25	11×9×25	-	630×1×25
L3	Pool_L1, Pool_R1	630×1×25	25	-	3×1	210×1×25
L4	Conv_L2,Conv_R2	210×1×25	50	11×1×50	-	200××50
L5	Pool_L2, Pool_R2	200×1×50	50	-	3×1	66×1×50
L6	Conv_L3,Conv_R3	66×1×50	100	11×1×100	-	56×1×100
L7	Pool_L3, Pool_R3	56×1×100	100	-	3×1	18×1×100
L8	Conv_L4,Conv_R4	18×1×100	200	11×1×200	-	8×1×200
L9	Pool_L4, Pool_R4	8×1×200	200	-	2×1	4×1×200
L10	Flatten_L,Flatten_R	4×1×200	1	-	-	800
L11	Flatten_L-Flatten_R	800	1	-	-	800
L12	FC	800	1	-	-	128
L13	Softmax	128	1	-	-	4

electrodes on the left and right hemispheric. The time series of nine pairs of new electrodes on the left and right hemispheric were extracted by brainstorming in MATLAB (Tadel et al., 2011).

2.4. CNN Theory and CNN Structure

2.4.1. CNN Theory

Convolutional neural network is generally composed of a convolution layer, pooling layer, and fully connected layer to complete feature extraction and classification (Schirrmeister et al., 2017; Kaldera et al., 2019). When the convolution operation is performed layer by layer, CNN can not only automatically extract rich features but also convey depth information. The initial layer of convolution is used to extract local features, and the end layer is used to extract global features. Among them, the convolutional layer contains multiple filters to extract features that are useful for classification (Liu and Liu, 2017). It uses the output of the previous layer as the input of the next layer to extract features, as follows (Ji et al., 2013):

$$x_j^l = f\left(\sum_{i \in M_j} x_i^{l-1} * k_{ij}^l + b_j^l\right) \tag{3}$$

Where x_j^l is the output of the jth channel of the l layer in the convolutional layer, $f(\cdot)$ is the activation function, M_j is the set of selection inputs, and x_i^{l-1} is the output of the ith channel of $l-1$ layer in the convolutional layer, $*$ represents convolution operation, k_{ij}^l is convolution kernel matrix, and b_j^l is offset value.

The pooling layer is generally used after the convolutional layer to reduce the number of parameters. It mainly includes average pool and max pool, which can be described as follows:

$$x_j^l = f\left(\beta_j^l down(x_j^{l-1}) + b_j^l\right) \tag{4}$$

Where $f(\cdot)$ is the activation function, $down(\cdot)$ is the down-sampling function, β_j^l is the weight coefficient of the jth channel of the lth layer in the pooling layer, and b_j^l is bias (Zang et al., 2020).

Rectified linear unit (ReLU) is a commonly used activation function in convolution and pooling layers, which plays an important role in simulating biological neurons (Nair and Hinton, 2010; Karthik et al., 2020).

After multiple convolutional layers and pooling layers, the data will enter a fully connected layer. First, the data is processed by weighted summation, then processed by the activation function, and finally, the output of the fully connected network is obtained, as follows:

$$x^l = f(\omega^l x^{l-1} + b^l) \tag{5}$$

Among them, $\omega^l x^{l-1} + b^l$ is the net activation of layer l in a fully connected layer. ω^l is the weight coefficient, and b^l is bias.

Since the training is for subjects, the output of each category label will be converted into conditional probability by the softmax function as follows (Amin et al., 2019):

$$p(l_k | f(X^j; \theta)) = \frac{exp f_k(X^j; \theta)}{\sum_{k=1}^{K} exp(f_k(X^j; \theta))} \tag{6}$$

Where l_k is the given label, X^j is input, θ is parameter including weight and bias, and K is the category.

2.4.2. CNN Structure

The network structure and parameters of CNN are determined by the experimental method, as shown in **Table 1**. We proposed a novel dual-CNN model for MI classification, which can process the time series of nine hemispheric electrodes on the cortex layer, and the structure is shown in **Figure 1**. The specific process description is as follows:

(1) We used 4s MI data as the input of the neural network. At a sampling frequency of 160Hz, its data dimension is 640, and the dimension remains unchanged after cortex layer processing. First, connect the time series of the left and right hemispheric symmetrical electrodes horizontally, and then connect the data of the nine pairs of electrodes vertically,

TABLE 2 | The classification accuracy of individual subject.

Subject	Accuracy (%)	T1 accuracy (%)	T2 accuracy (%)	T3 accuracy (%)	T4 accuracy (%)
S1	97.77	99.67	97.14	96.08	98.18
S2	97.30	99.59	96.00	96.45	97.17
S3	96.35	99.73	96.90	95.89	92.86
S4	98.88	99.62	99.68	98.47	97.73
S5	97.14	99.56	98.15	91.49	99.34
S6	97.61	98.93	97.56	95.91	98.04
S7	96.23	99.14	93.18	96.45	96.15
S8	96.33	99.92	99.37	90.91	95.12
S9	97.34	99.81	97.44	95.83	96.27
S10	98.81	99.74	97.56	99.56	98.36

so that the data format that enters the neural network is $1,280 \times 9$. The first layer of the network separates the nine electrodes of the left and right brains through the reshape operation to form two data with a size of 640×9, representing the time series of the nine electrodes of the left and right brains, respectively.

(2) We used two CNN structures with exactly the same parameters to form a dual-CNN model. Each CNN structure contains 4-layer CNN for learning features, 4-layer max pooling for dimensionality reduction, and 1 FC layer that converts multi-dimensional data into one dimension.

(3) The one-dimensional data output by the left and right CNN model are subtracted, then the signal differences of the symmetrical electrode are entered into the FC layer, and the softmax function is used to predict the attribution of the test data.

In addition, based on 4-layer CNN and 4-layer max pooling, we try to add more CNN layers and max pooling layers. It is found that 4-layer dual-CNN performs best in the experiment, and the accuracy is not significantly improved after the number of convolutional layers exceeds 4-layer.We used spatial dropout and batch normalization (BN) techniques to prevent overfitting. In Section 3.5, our proposed model is compared with other models, and a better classification evaluation effect is obtained.

3. RESULTS

3.1. Classification Accuracy of Individual Subject

In order to obtain effective results, events T1-T4 in each subject are randomly intermingled and separated into 90% as the training set, and the remaining 10% as the test set. We conducted trial-based accuracy experiments for each subject (S1-S10) on the Physionet database. **Table 2** lists the accuracy of each subject and its four MI tasks (T1, T2, T3, T4). In **Table 2**, the highest accuracy is 98.88% (S4), and its four MI accuracies are 99.62, 99.68, 98.47, and 97.73%, respectively. The lowest accuracy is 96.23% (S7), and its four MI accuracies are 99.14, 93.18, 96.45, and 96.15%, respectively. The average accuracies of the four MI tasks for ten subjects are 99.57% (T1), 97.30% (T2), 95.70% (T3), and 96.92% (T4), respectively. T1 has the highest accuracy, it is indicative that the classification effect of the left fist is the best. The accuracy of T3 is the lowest, it indicates that the classification effect of both fists is the worst. The highest accuracy on T1 is 99.92% (S8), while the lowest is 98.93% (S6). The highest accuracy on T2 is 99.68% (S4) and the lowest is 93.18% (S7). The highest accuracy on T3 is 99.56% (S10), while the lowest is 90.91% (S8). The highest accuracy on T4 is 99.34% (S5), while the lowest is 92.86% (S3). According to the above results, it can be found that our proposed method achieves higher accuracy on S1-S10 and its four MI tasks.

During the CNN training iteration process, the accuracy curves of the ten subjects are shown in **Figure 3A**. The accuracy of an individual subject increases rapidly during the first 200 iterations and slows down during the 200–600 iterations. After 600 iterations, the accuracy can reach a stable state. The accuracy curve of the whole iterative process is relatively smooth with less burr. It shows that as the number of iterations increases, our proposed dual-CNN can achieve high classification accuracy and high stability.

The receiver operating characteristic (ROC) curves of 10 subjects are shown in **Figure 3B**, which is used to evaluate the classification model. The area under the ROC curve is represented by AUC, and the value range is between 0.5 and 1. The closer the AUC is to 1.0, the better the classification effect is. Among the 10 subjects, the best classification model is S4, with an AUC value of 0.999, and the worst classification model has an AUC value of 0.995 (S7). It can be seen the proposed method has achieved better generalization performance and higher classification effect in different subjects.

3.2. Classification Accuracy of Group-Level Subjects

We also conducted a group-level experiment of 10 subjects to obtain the classification performance. In this part, first, we divided the data of each subject into two groups: the training set and the test set. T1-T4 of each subject are randomly divided into 10 equal parts, 9 parts are mixed uniformly to become the training set, and the remaining part is randomly shuffled into the test set. The training set of each subject is mixed to form the final training set, and the test set of each subject is mixed to form the final test set. Then we used five index evaluations to

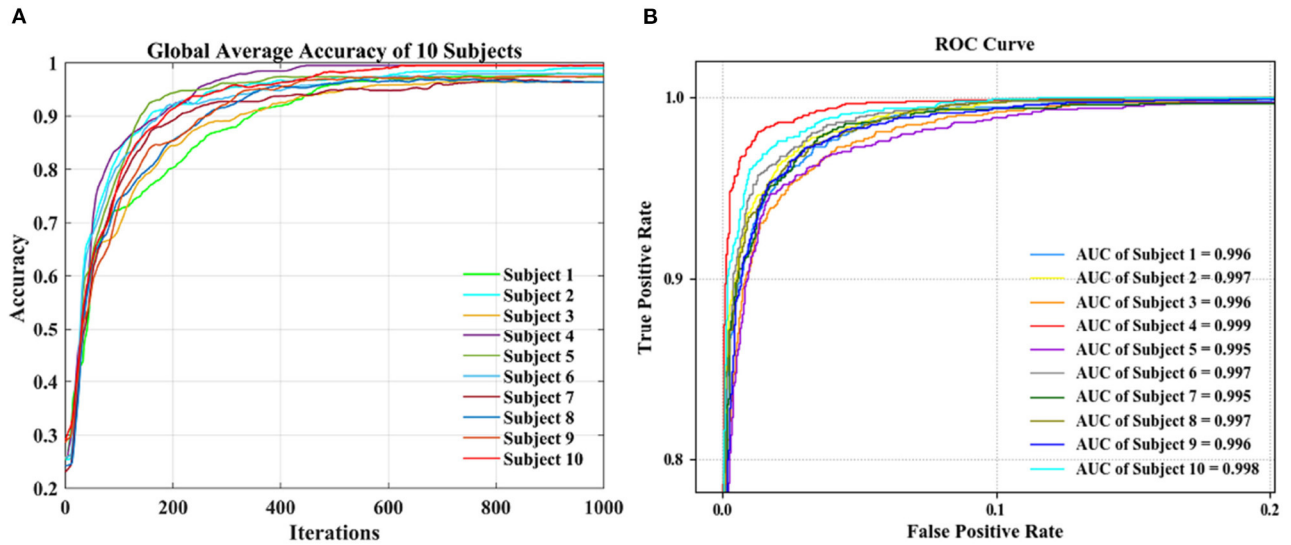

FIGURE 3 | Performance comparison of 10 subjects. **(A)** Accuracy comparison. **(B)** Receiver operating characteristic (ROC) curve comparison.

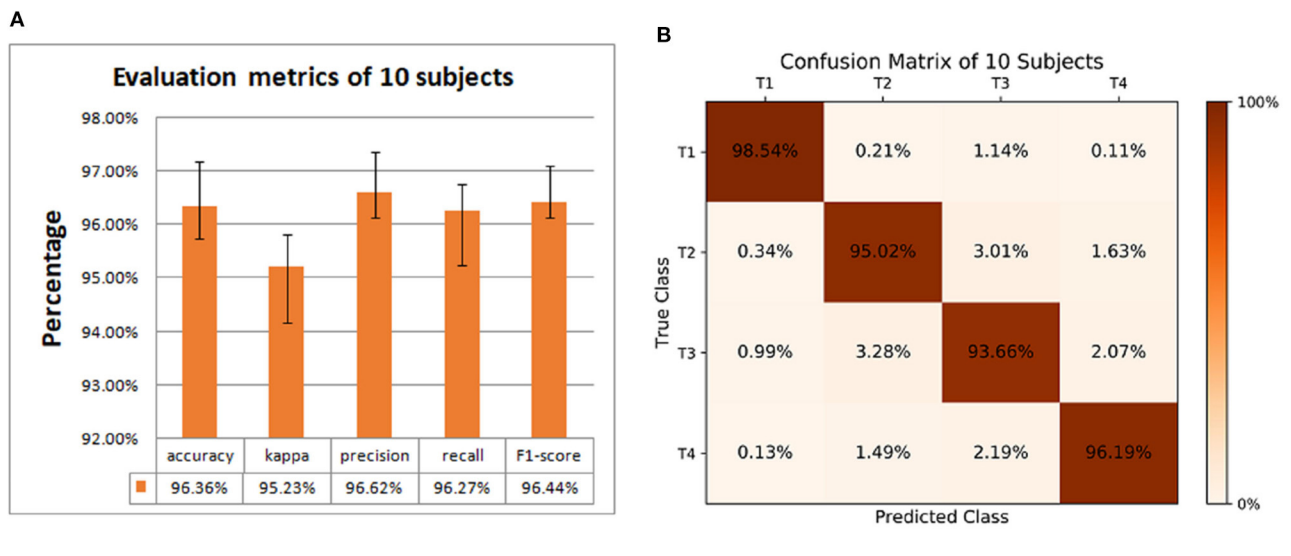

FIGURE 4 | Classification performance of 10 subjects. **(A)** Evaluation metrics. **(B)** Confusion matrix for the accuracy of 4 motor imagery (MI) tasks.

measure the effectiveness of classification, as shown in **Figure 4A**, accuracy, kappa, precision, recall, and F1-score are 96.36, 95.23, 96.62, 96.27, and 96.44%, respectively.

The confusion matrix in **Figure 4B** shows the accuracy of the 4 MI tasks at the group-level. The values on the diagonal of the confusion matrix are the correct classification, and the other values are the wrong classification. The accuracies of 4 MI tasks are 98.54 (T1), 95.02 (T2), 93.66 (T3), and 96.19% (T4), respectively. It can be seen the proposed method can also achieve good performance in group-level classification.

3.3. Comparison of Classification Models

In order to solve the problem of overfitting, spatial dropout and BN were used in our proposed model. Dropout refers to the random "temporary dropping" of a part of neuron nodes with a certain probability in training. Different neurons are then combined with each other for optimization during each training process. This process weakens the joint adaptability of all neurons and reduces the risk of overfitting. BN enhances the generalization ability of the model by imposing additional constraints on the distribution of data.

TABLE 3 | Performance comparison of different convolutional neural network (CNN) models.

Model	Accuracy (%)	kappa (%)	Precision (%)	Recall (%)	F1-score (%)
Proposed model	96.36	95.23	96.62	96.27	96.44
Model without dropout	94.06	90.74	94.32	93.82	94.07
Model without BN	90.77	89.02	90.51	91.20	90.85
Model without dropout & BN	86.39	82.24	86.77	86.13	86.45

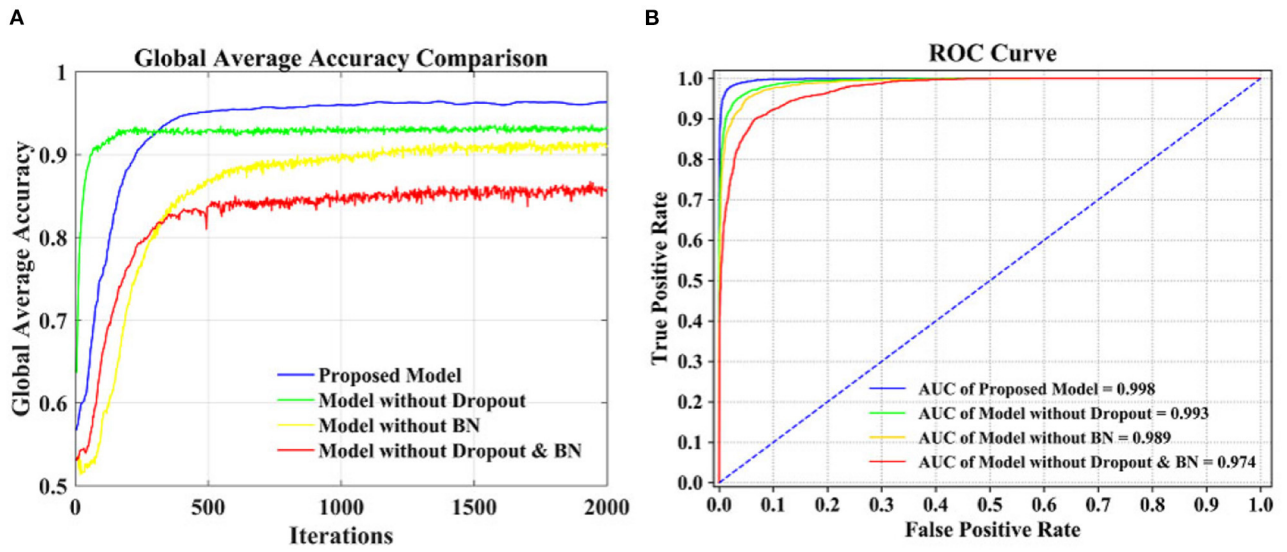

FIGURE 5 | Performance comparison of different models. **(A)** Accuracy comparison. **(B)** ROC curve comparison.

In this article, we compared the performance of our proposed models with three different models based on the data set of 10 subjects at group-level. **Table 3** compared the performance of the four models with five evaluation indicators. The accuracy, kappa, precision, recall, and F1-Score of our proposed model are 96.36, 95.23, 96.62, 96.27, and 96.44%, respectively, which are higher than other models, so its performance is better than other models.

Figure 5A is a comparison of the global average accuracy of the four models. It can be seen that all models can reach a stable state after iteration. Currently, the proposed model has the highest accuracy of 96.36%, followed by 94.06% for the model without dropout, 90.77% for the model without BN, and 86.39% for the model without dropout and BN. **Figure 5B** is the ROC curve and AUC curve of the four models. The model proposed in this paper has the largest AUC value, 0.996, which is the closest to 1, and the classification effect is the best. The accuracy curve and ROC curve of the CNN model we proposed to solve the overfitting problem are the smoothest and with the smallest burr. In addition, the values of various evaluation metrics are the highest, and the AUC value is also the highest when reaching the stable state after iterations. When the iteration reaches a stable state, the five evaluation indicators of accuracy, kappa, precision, recall, and F1-score are all the highest, and the AUC value is the largest. The performance of our proposed model is the most stable, and it does improve the classification effect.

3.4. Comparison of Loss on Test Data

Figure 6A shows the loss function curve of ten individual subjects on the test set, whose loss values decrease with the increase of iteration times. When the number of iterations is about 600, the loss values remain basically stable. Thus, the optimal testing effect can be obtained, and it can be seen that our model is convergent during testing. **Figure 6B** shows a comparison of the loss function curve of different classification models on the test set of group-level subjects. The loss values of the four curves decrease with the increase of iteration times and can reach equilibrium after 500 iterations. The blue curve is the test loss function curve of the proposed model. Compared with the other three models, it has the smoothest curve, the smallest burr, and the smallest loss when it reaches the stable state. In general, the proposed model has a good convergence effect on the test set of the individual subject and group-level subjects.

3.5. Comparison With Other Works

Electroencephalogram signal has low amplitude and contains a lot of noise, and there are differences between different subjects. This article compared and analyzed our study with Handiru and Prasad (2016), Azimirad et al. (2017), Dose et al. (2018), Athif and Ren (2019), and Hou et al. (2019) in **Table 4** under the same database and the same MI task. The results show that our method achieved the best results on both group-level subjects and

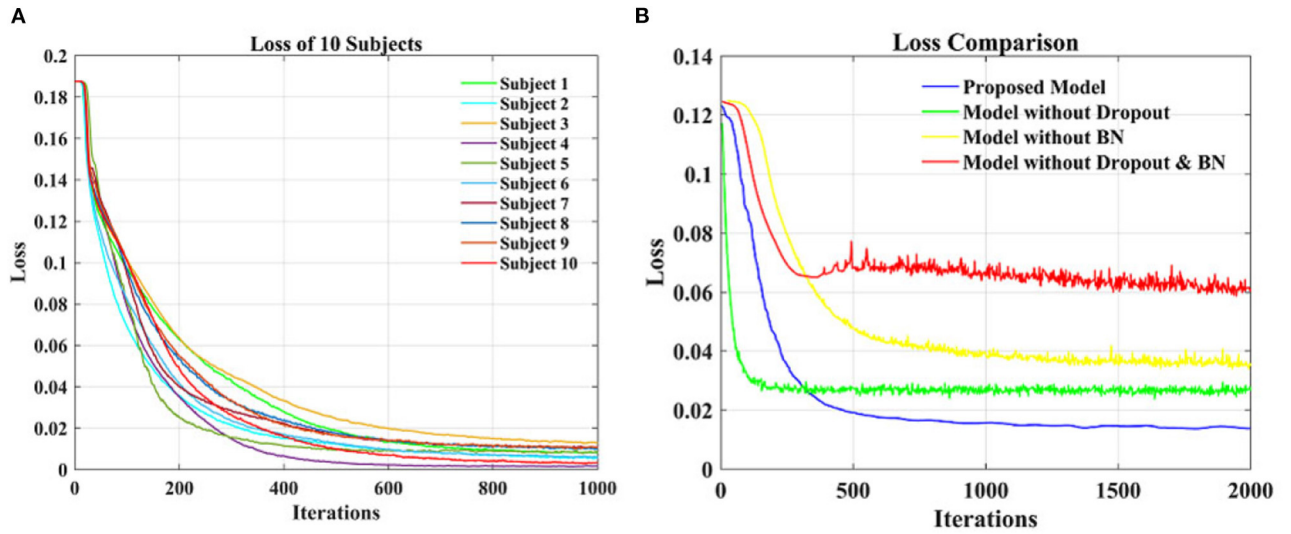

FIGURE 6 | The loss function curve on test data. **(A)** Loss function comparisons of 10 individual subjects. **(B)** Loss function comparisons of different classification models.

TABLE 4 | Performance comparison with other studies.

Work	Training	Accuracy (%)	Methods
Azimirad et al. (2017)	Global	81.00	SVM
Dose et al. (2018)	Global	80.38	CNN
	Subject	86.49	
Athif and Ren (2019)	Global	64.00	CSP
Hou et al. (2019)	Global	94.54	ESI + CNN
	Subject	94.50	
Handiru and Prasad (2016)	Global	61.01	SVM
This work	Global	96.38	CNN
	Subject	98.88	

individual subjects, which indicates that the difference between the left and right hemispheric on the cortex contains more information related to MI tasks and that our CNN structure is very helpful in improving the generalization performance of the model.

In particular, the subjects used in the Hou et al. (2019) partially overlap with the subjects used in our article, which are S5-S10. When the single subject is tested, the highest accuracies in Y.Hou et al. are 94.6%(S5), 94.1%(S6), 95.0%(S7), 93.2%(S8), 95.5%(S9), and 93.1%(S10). Then the accuracies of the method proposed in this article are 97.14%(S5), 97.61%(S6), 96.23%(S7), 96.33%(S8), 97.34%(S9), and 98.81%(S10), which are higher than Hou et al. In terms of real-time performance comparison, none of the articles achieved real-time control.

4. DISCUSSION

4.1. Data Analysis

From **Table 2** it can be found that the average accuracy of a single subject in this article is up to 98.88%, which is an improvement of 12 and 4% respectively compared with Dose et al. (2018) and Hou et al. (2019). This proves the effectiveness of this method. Specifically, Dose et al. only processes raw EEG signal, while this article processes the region of interest on the cortex layer, which shows that the preprocessing operation in this article is effective. Hou et al. used single layer CNN to classify data, which illustrates the feasibility and reliability of our proposed dual-CNN. **Figure 4** shows that the highest global accuracy rate of this article is 96.38%, which is also higher than Dose et al. and the Hou et al. In addition, our group-level accuracy is also higher than other articles in **Table 4**, which proves that the dual-CNN proposed in this paper has a significant effect on MI-BCI classification.

4.2. Limitations of the Proposed Method

The time spent on data processing and classification using neural networks is related to the amount of data, the complexity of the network structure, and the performance of computer equipment. When using CNN to process MI data, each learning iteration during the CNN training will take some time. At present, this paper cannot detect and classify MI tasks in real-time. Therefore, **Figure 3** still uses learning iterations during CNN training, instead of using time as the abscissa axis. But it is meaningful that the number of iterations is also another manifestation of time, which means that as time increases, our classification accuracy will continue to increase and eventually reach a stable state. With the improvement of computer performance, it will take less and less time for us to reach a stable state. Therefore, in the classification of non-real-time MI-BCI, it is also a good way to display the performance of the method with the number of iterations. There is still scope for simplifying the network structure, which will be investigated in the future. Also, it would be interesting in

the future to employ the current method for real-time online BCI experiments.

5. CONCLUSION

The key objective of the study presented in this article is to investigate the method of high classification accuracy on MI-EEG signals. This article proposed a new MI classification method that combines the difference between the left and right hemispheric electrodes on the cortex and dual-CNN. Using the Physionet database as the data source, restored the raw EEG signal from the low-density EEG scalp measurement, mapped nine pairs of electrodes from the scalp layer to the cortex layer as the region of interest, and extracted the time series of nine pairs of electrodes signals as the input of the proposed dual-CNN classification model. The results demonstrated that these MI tasks can be classified with high accuracy by the difference between the signals left and right hemispheric electrodes, and CNN plays an important role in improving generalization performance. The BCI system of MI based on left and right hemispheric electrodes and CNN can be applied in the daily life of all subjects. The results suggested that the classification accuracy of the proposed method is substantially higher than all other methods used in this study.

DATA AVAILABILITY STATEMENT

Publicly available datasets were analyzed in this study. This data can be found at: https://physionet.org/content/eegmmidb/1.0.0/.

AUTHOR CONTRIBUTIONS

XL: method design of the article. JL: programming and software design. YZ: data collection and pre-processing. ZH: experimental improvement and paper revise. YH: result analysis, method improvement, and manuscript calibration. All authors contributed to the article and approved the submitted version.

ACKNOWLEDGMENTS

The authors would like to thank PhysioNet for providing EEG Motor Movement/Imagery Dataset.

REFERENCES

Al-Saegh, A., Dawwd, S. A., and Abdul-Jabbar, J. M. (2021). Deep learning for motor imagery eeg-based classification: a review sciencedirect. *Biomed. Signal Process. Control*. 63, 102172. doi: 10.1016/j.bspc.2020.102172

Amin, S. U., Alsulaiman, M., Muhammad, G., Amine, M. A. M., and Hossain, M. S. (2019). Deep learning for eeg motor imagery classification based on multi-layer cnns feature fusion. *Future Generat. Comput. Syst*. 101, 542–554. doi: 10.1016/j.future.2019.06.027

Athif, M., and Ren, H. (2019). Wavecsp: a robust motor imagery classifier for consumer eeg devices. *Austral. Phys. Eng. Med*. 42, 159–168. doi: 10.1007/s13246-019-00721-0

Azimirad, V., Hajibabzadeh, M., and Shahabi, P. (2017). "A new brain-robot interface system based on svm-pso classifier," in *2017 Artificial Intelligence and Signal Processing Conference (AISP)* (Shiraz: IEEE), 124–128.

Baillet, S., and Garnero, L. (1997). A bayesian approach to introducing anatomo-functional priors in the eeg/meg inverse problem. *Biomed. Eng. IEEE Trans*. 44, 374–385. doi: 10.1109/10.568913

Becker, H., Albera, L., Comon, P., Gribonval, R., Wendling, F., and Merlet, I. (2015). Brain source imaging: from sparse to tensor models. *IEEE Signal. Process*. 32, 100–112. doi: 10.1109/MSP.2015.2413711

Bhattacharyya, S., Das, S., and Das, A. (2021). Neuro-feedback system for real-time bci decision prediction. *Microsyst. Technol*. 127, 104079. doi: 10.1007/s00542-020-05146-4

Cho, J. H., Jeong, J. H., Shim, K. H., Kim, D. J., and Lee, S. W. (2019). "Classification of hand motions within eeg signals for non-invasive bci-based robot hand control," in *2018 IEEE International Conference on Systems, Man, and Cybernetics (SMC)* (Miyazaki: IEEE), 515–518.

Collins, D. L., Zijdenbos, A. P., Kollokian, V., Sled, J. G., Kabani, N. J., Holmes, C. J., et al. (1998). Design and construction of a realistic digital brain phantom. *IEEE Trans. Med. Imaging* 17, 463–468. doi: 10.1109/42.712135

Condori, K. A., Urquizo, E. C., and Diaz, D. A. (2016). "Embedded brain machine interface based on motor imagery paradigm to control prosthetic hand," in *2016 IEEE ANDESCON* (Arequipa: IEEE).

Dose, H., Moller, J. S., Iversen, H. K., and Puthusserypady, S. (2018). An end-to-end deep learning approach to mi-eeg signal classification for bcis. *Expert. Syst. Appl*. 114, 532–542. doi: 10.1016/j.eswa.2018.08.031

Edelman, B., Baxter, B., and He, B. (2015). "Decoding and mapping of right hand motor imagery tasks using eeg source imaging," in *2015 7th International IEEE/EMBS Conference on Neural Engineering (NER)* (Montpellier: IEEE), 194–197.

Edelman, B. J., Baxter, B., and He, B. (2015). Eeg source imaging enhances the decoding of complex right hand motor imagery tasks. *IEEE Trans. Biomed. Eng*. 63, 4–14. doi: 10.1109/TBME.2015.2467312

Engemann, D. A., and Gramfort, A. (2015). Automated model selection in covariance estimation and spatial whitening of meg and eeg signals. *Neuroimage* 108, 328–342. doi: 10.1016/j.neuroimage.2014.12.040

Gramfort, A., Papadopoulo, T., Olivi, E., and Clerc, M. (2010). Openmeeg: opensource software for quasistatic bioelectromagnetics. *Biomed. Eng. Online* 9, 45. doi: 10.1186/1475-925X-9-45

Handiru, V. S., and Prasad, V. A. (2016). Optimized bi-objective eeg channel selection and cross subject generalization with brain computer interfaces. *IEEE Trans. Hum. Mach. Syst*. 46, 777–786. doi: 10.1109/THMS.2016.2573827

Hassan, M., Dufor, O., Merlet, I., Berrou, C., and Wendling, F. (2014). Eeg source connectivity analysis: from dense array recordings to brain networks. *PLoS ONE* 9, e105041. doi: 10.1371/journal.pone.0105041

He, B., Baxter, B., Edelman, B. J., Cline, C. C., and Ye, W. W. (2015). Noninvasive brain-computer interfaces based on sensorimotor rhythms. *Proc. IEEE* 103, 907–925. doi: 10.1109/JPROC.2015.2407272

Hou, Y., Zhou, L., Jia, S., and Lun, X. (2019). A novel approach of decoding eeg four-class motor imagery tasks via scout esi and CNN. *J. Neural Eng*. 17, 016048. doi: 10.1088/1741-2552/ab4af6

Hsu, W. Y. (2015). Assembling a multi-feature eeg classifier for left-right motor imagery data using wavelet-based fuzzy approximate entropy for improved accuracy. *Int. J. Neural Syst*. 25, 1550037. doi: 10.1142/S0129065715500379

Janati, H., Bazeille, T., Thirion, B., Cuturi, M., and Gramfort, A. (2020). Multi-subject meg/eeg source imaging with sparse multi-task regression. *Neuroimage* 220, 116847. doi: 10.1016/j.neuroimage.2020.116847

Ji, S., Xu, W., Yang, M., and Yu, K. (2013). 3d convolutional neural networks for human action recognition. *IEEE Trans. Pattern Anal. Mach. Intell*. 35, 221–231. doi: 10.1109/TPAMI.2012.59

Jin, W. C., Huh, S., and Jo, S. (2020). Improving performance in motor imagery bci-based control applications via virtually embodied feedback. *Comput. Biol. Med*. 127, 104079. doi: 10.1016/j.compbiomed.2020.104079

Kaldera, H. N. T. K., Gunasekara, S. R., and Dissanayake, M. B. (2019). "Brain tumor classification and segmentation using faster r-cnn," in *2019 Advances in Science and Engineering Technology International Conferences (ASET)* (Dubai).

Karthik, R., Hariharan, M., Anand, S., Mathikshara, P., Johnson, A., and Menaka, R. (2020). Attention embedded residual cnn for disease detection in tomato leaves. *Appl. Soft. Comput*. 86, 105933. doi: 10.1016/j.asoc.2019.105933

Kim, M. K., and Kim, S. P. (2018). "Decoding movement information from cortical activity for invasive bmis," in *International Conference on Brain-Computer Interface* (GangWon).

Kim, Y. (2014). Convolutional neural networks for sentence classification. *Eprint Arxiv*. doi: 10.3115/v1/D14-1181

Krizhevsky, A., Sutskever, I., and Hinton, G. E. (2017). Imagenet classification with deep convolutional neural networks. *Commun. ACM* 60, 84–90. doi: 10.1145/3065386

Lei, W., Xu, G., Yang, S., Guo, M., and Jiang, W. (2012). "Motor imagery BCI research based on sample entropy and SVM," in *Sixth International Conference on Electromagnetic Field Problems and Applications*.

Li, Y., Lei, M., Zhang, X., Cui, W., Guo, Y., Huang, T. W., et al. (2018). Boosted convolutional neural networks for motor imagery EEG decoding with multiwavelet-based time-frequency conditional granger causality analysis. doi: 10.48550/arXiv.1810.10353

Liu, Y., and Liu, Q. (2017). "Convolutional neural networks with large-margin softmax loss function for cognitive load recognition," in *2017 36th Chinese Control Conference (CCC)*.

Lun, X., Yu, Z., Wang, F., Chen, T., and Hou, Y. (2020). A novel approach of cnn for human motor imagery recognition using the virtual electrode pairs. *J. Intell. Fuzzy Syst*. 40, 5275–5288. doi: 10.3233/JIFS-202046

Millan, J., and Del, R. X. (2002). "Brain-computer interfaces," in *Handbook of Brain Theory and Neural Networks* (Bradford), 178–181.

Mosher, J. C., Leahy, R. M., and Lewis, P. S. (1999). Eeg and meg: forward solutions for inverse methods. *IEEE Trans. Biomed. Eng*. 46, 245–259. doi: 10.1109/10.748978

Nair, V., and Hinton, G. (2010). "Rectified linear units improve restricted boltzmann machines vinod nair," in *International Conference on International Conference on Machine Learning, Vol. 27*, 807–814.

Nakagome, S., Luu, T. P., He, Y., Ravindran, A. S., and Contreras-Vidal, J. L. (2020). An empirical comparison of neural networks and machine learning algorithms for eeg gait decoding. *Sci. Rep*. 10, 4372. doi: 10.1038/s41598-020-60932-4

Nakamura, M., Qian, C., Sugi, T., Ikeda, A., and Shibasaki, H. (2005). Technical quality evaluation of eeg recording based on electroencephalographers' knowledge. *Med. Eng. Phys*. 27, 93–100. doi: 10.1016/j.medengphy.2004.09.001

Noraini, I., Norma, A., Tahir, A., and Leila, S. (2013). Relationship between maxwell's equations and einstein field equation base on eeg source localization in the brain. *Res. J. Appl. Sci. Eng. Technol*. 6, 1582–1587. doi: 10.19026/rjaset.6.3873

Okada, Y. (1993). Empirical bases for constraints in current-imaging algorithms. *Brain Topogr*. 5, 373–377. doi: 10.1007/BF01128693

Pfurtscheller, G., Brunner, C., SchlGl, A., and Silva, F. (2006). Mu rhythm (de)synchronization and eeg single-trial classification of different motor imagery tasks. *Neuroimage* 31, 153–159. doi: 10.1016/j.neuroimage.2005.12.003

Phillips, C., Rugg, M. D., and Friston, K. J. (2002). Systematic regularization of linear inverse solutions of the eeg source localization problem. *Neuroimage* 17, 287–301. doi: 10.1006/nimg.2002.1175

Robinson, N., Lee, S. W., and Guan, C. (2019). "EEG representation in deep convolutional neural networks for classification of motor imagery," in *2019 IEEE International Conference on Systems, Man and Cybernetics (SMC)* (Bari: IEEE).

Schalk, G., McFarland, D. J., Hinterberger, T., Birbaumer, N., and Wolpaw, J. R. (2004). Bci2000: a general-purpose brain-computer interface (BCI) system. *IEEE Trans. Biomed. Eng*. 51, 1034–1043. doi: 10.1109/TBME.2004.827072

Schirrmeister, R. T., Springenberg, J. T., Fiederer, L. D. J., Glasstetter, M., Eggensperger, K., Tangermann, M., et al. (2017). Deep learning with convolutional neural networks for EEG decoding and visualization. *Hum. Brain Mapp*. 38, 5391–5420. doi: 10.1002/hbm.23730

Serafeim, P., Luca, T., Sareh, S., and Christoph, S. (2018). The cybathlon bci race Successful longitudinal mutual learning with two tetraplegic users. *PLoS Biol*. 16, e2003787. doi: 10.1371/journal.pbio.2003787

Stefano, T., Gloria, B., Luca, T., and Emanuele, M. (2019). "Entropy-based motion intention identification for brain-computer interface," in *2019 IEEE International Conference on Systems, Man and Cybernetics (SMC)* (Bari).

Tadel, F., Baillet, S., Mosher, J. C., Pantazis, D., and Leahy, R. M. (2011). Brainstorm: a user-friendly application for MEG/EEG analysis. *Comput. Intell. Neurosci*. 2011, 879716. doi: 10.1155/2011/879716

Tortora, S., Ghidoni, S., Chisari, C., Micera, S., and Artoni, F. (2020). Deep learning-based bci for gait decoding from eeg with lstm recurrent neural network. *J. Neural Eng*. 17, 046011. doi: 10.1088/1741-2552/ab9842

Wang, H., and Bezerianos, A. (2017). Brain-controlled wheelchair controlled by sustained and brief motor imagery bcis. *Electron. Lett*. 53, 1178–1180. doi: 10.1049/el.2017.1637

Wheless, J. W., and Castillo, E. M. V. (2004). Magnetoencephalography (MEG) and magnetic source imaging (MSI). *Neurologist* 10, 138. doi: 10.1097/01.nrl.0000126589.21840.a1

Wu, Q., Yan, W., Shen, X., Li, Y., He, S., and Xu, G. (2003). Eeg source reconstruction based on the boundary-element method and weighted minimum norm approaches. *IEEE Trans. Magn*. 39, 1547–1550. doi: 10.1109/TMAG.2003.810528

Yuan, H., and He, B. (2014). Brain-computer interfaces using sensorimotor rhythms: current state and future perspectives. *IEEE Trans. Biomed. Eng*. 61, 1425–1435. doi: 10.1109/TBME.2014.2312397

Zang, H., Liu, L., Sun, L., Cheng, L., and Sun, G. (2020). Short-term global horizontal irradiance forecasting based on a hybrid cnn-lstm model with spatiotemporal correlations. *Renew. Energy* 160, 26–41. doi: 10.1016/j.renene.2020.05.150

Zhang, X. R., Lei, M. Y., and Li, Y. (2018). "An amplitudes-perturbation data augmentation method in convolutional neural networks for EEG decoding," in *2018 5th International Conference on Information, Cybernetics, and Computational Social Systems (ICCSS)* (Hangzhou: IEEE).

Conflict of Interest: The authors declare that the research was conducted in the absence of any commercial or financial relationships that could be construed as a potential conflict of interest.

frontiers | Frontiers in Neuroscience

ORIGINAL RESEARCH
published: 03 June 2022
doi: 10.3389/fnins.2022.902528

The Coupled Representation of Hierarchical Features for Mild Cognitive Impairment and Alzheimer's Disease Classification

Ke Liu [1,2], Qing Li [1,3], Li Yao [1,2] and Xiaojuan Guo [1,2,4] for the Alzheimer's Disease Neuroimaging Initiative[*]*

[1] School of Artificial Intelligence, Beijing Normal University, Beijing, China, [2] Engineering Research Center of Intelligent Technology and Educational Application, Beijing Normal University, Beijing, China, [3] State Key Laboratory of Cognitive Neuroscience and Learning, Beijing Normal University, Beijing, China, [4] Beijing Key Laboratory of Brain Imaging and Connectomics, Beijing Normal University, Beijing, China

Structural magnetic resonance imaging (MRI) features have played an increasingly crucial role in discriminating patients with Alzheimer's disease (AD) and mild cognitive impairment (MCI) from normal controls (NC). However, the large number of structural MRI studies only extracted low-level neuroimaging features or simply concatenated multitudinous features while ignoring the interregional covariate information. The appropriate representation and integration of multilevel features will be preferable for the precise discrimination in the progression of AD. In this study, we proposed a novel inter-coupled feature representation method and built an integration model considering the two-level (the regions of interest (ROI) level and the network level) coupled features based on structural MRI data. For the intra-coupled interactions about the network-level features, we performed the ROI-level (intra- and inter-) coupled interaction within each network by feature expansion and coupling learning. For the inter-coupled interaction of the network-level features, we measured the coupled relationships among different networks *via* Canonical correlation analysis. We evaluated the classification performance using coupled feature representations on the Alzheimer's Disease Neuroimaging Initiative (ADNI) database. Results showed that the coupled integration model with hierarchical features achieved the optimal classification performance with an accuracy of 90.44% for AD and NC groups, with an accuracy of 87.72% for the MCI converter (MCI-c) and MCI non-converter (MCI-nc) groups. These findings suggested that our two-level coupled interaction representation of hierarchical features has been the effective means for the precise discrimination of MCI-c from MCI-nc groups and, therefore, helpful in the characterization of different AD courses.

Keywords: coupled interaction representation, hierarchical features, classification, mild cognitive impairment, Alzheimer's disease, structural MRI

Edited by:
Shijie Zhao, Northwestern Polytechnical University, China

Reviewed by:
Xi Jiang, University of Electronic Science and Technology of China, China
Qi Zhang, University of Technology Sydney, Australia

***Correspondence:**
Xiaojuan Guo
gxj@bnu.edu.cn

Data used in preparation of this article were obtained from the Alzheimer's Disease Neuroimaging Initiative (ADNI) database (adni.loni.usc.edu). As such, the investigators within the ADNI contributed to the design and implementation of ADNI and/or provided data but did not participate in analysis or writing of this report. A complete listing of ADNI investigators can be found at: http://adni.loni.usc.edu/wp-content/uploads/how_to_apply/ADNI_Acknowledgement_List.pdf.

Specialty section:
This article was submitted to Brain Imaging Methods, a section of the journal Frontiers in Neuroscience

Received: *23 March 2022*
Accepted: *25 April 2022*
Published: *03 June 2022*

Citation:
Liu K, Li Q, Yao L and Guo X (2022) The Coupled Representation of Hierarchical Features for Mild Cognitive Impairment and Alzheimer's Disease Classification. Front. Neurosci. 16:902528. doi: 10.3389/fnins.2022.902528

INTRODUCTION

Alzheimer's disease (AD) is one of the most severe neurodegenerative dementias in the elderly, and mild cognitive impairment (MCI) is a prodromal stage with a higher risk of progression to AD in patients with MCI than normal controls (NC) (Dona et al., 2016; Arbabshirani et al., 2017; Zhang et al., 2021a). Neuroimaging techniques provide objective and effective tools to study the human brain and have been widely used in the diagnosis of AD or MCI from NC. Neuroimaging studies have shown remarkable structural and functional alterations in the human brain during the course of AD (Vemuri and Jack, 2010; Rathore et al., 2017; Leandrou et al., 2018). Structural magnetic resonance imaging (MRI) studies have extracted hierarchical features [the voxel level, the regions of interest (ROI) level, or the network level] as explicit variables to discriminate AD and MCI from NC. However, a large number of structural MRI studies only extracted low-level features, or simply concatenated multitudinous features, while ignoring the interregional covariate information among features (Anstey and Maller, 2003; Yang et al., 2011; Moradi et al., 2015; Hu et al., 2016; Rathore et al., 2017; Rondina et al., 2018), so they cannot fully exploit the latent and complex information integrated with hierarchical features. The effective feature representations help to enhance the performance of classification. Therefore, the appropriate representation and integration of multilevel features will be preferable for the precise discrimination of AD, MCI, and NC.

Based on structural MRI data, researchers extracted hierarchical imaging features, such as the gray matter (GM) density as the voxel-level features (Moradi et al., 2015; Zeifman et al., 2015), the average gray matter volume (GMV) of brain regions as the ROI-level features (Shi et al., 2014; Hu et al., 2016), or the independent components (ICs) from independent component analysis (ICA) as brain network-level features (Yang et al., 2011). Moradi et al. considered the smoothed GM density from structural MRI data as voxel-level features for AD conversion prediction in subjects with MCI (Moradi et al., 2015). In comparison with the voxel-level features with redundant information but expensive computation, ROI-level features significantly reduce the dimensionality of brain imaging data by uniting the structural adjacent voxels. The GMV from different ROIs has been applied as an independent variable to investigate the predictive power for distinguishing AD with MCI (Zhang et al., 2011) and classifying AD from NC (Rondina et al., 2018). ICA is a data-driven approach that decomposes the whole-brain voxel-vise information into a few maximally independent components based on inter-regional covariance relationships. The brain GM networks obtained from ICA have been considered as brain network-level features to differentiate individuals with AD and NCs, thus providing new avenues for the network-level features in AD classification (Yang et al., 2011; Wei et al., 2016). However, it has been noted that ROI-level features in the same network exhibited more complicated regional dependencies than those in different brain networks (Liu et al., 2017a; Rathore et al., 2017; Filippi et al., 2020; Feng et al., 2021). Nevertheless, the aforementioned studies mostly constructed classification models using the single level of features separately while neglecting the complex interaction relationships among multilevel features.

There were explicit and hidden coupled interactions, much more abundant than simple linear correlation among attributes or features of objects in many domains, like the recommender systems (Wang and Cao, 2020; Zhang et al., 2021b), outlier detection (Pang et al., 2016), and pieces of neuroscience research (Shi et al., 2014, 2015, 2020). Many coupled analysis models were proposed to analyze the explicit and hidden couplings and revealed the non-independent and identical distribution (non-IIDness) characteristics for different data types (Wang et al., 2013, 2015a,b). For numerical data, Wang et al. detailed the intra-coupled interaction to capture the correlations between a feature and its own expanded powers and the inter-coupled interaction to quantify the interactive relationships among each feature and the expanded powers of the other features (Wang et al., 2013). A few imaging studies investigated AD classification with the coupling characteristics of the ROI-level features (Shi et al., 2014, 2020). Although such studies demonstrated high accuracy for AD, MCI, and NC classifications with coupled feature analysis, they still weakened or overlooked the coupled relationship at network-level features. The ROI-level features within the same network strongly interacted with each other (Brickman et al., 2007). Different brain networks collaborated with each other and carried explicit or implicit relationships (Betzel et al., 2014; Zuo et al., 2017). Consequently, greater effort should be focused on designing an appropriate coupled interaction model to integrate the ROI-level and network-level coupling relationships.

To integrate the intrinsic coupling relationships of the ROI-level and network-level features from structural MRI data, we proposed a novel inter-coupled feature representation method for the network-level features and built a two-level (the ROI level and the network level) coupled feature integration model for AD, MCI, and NC classification. For the intra-coupled interactions about the network-level features, we performed the ROI-level (intra- and inter-) coupled interaction within each network by feature expansion and coupling learning. For the inter-coupled interaction of the network-level features, we introduced the measurement of the coupled relationships among different networks *via* Canonical correlation analysis (CCA). We compared the identification performances in AD, MCI, and NC classification with different feature representation models. We hypothesized that two-level (the ROI level and the network level) coupled feature integration models would achieve better or comparable AD classification performance.

MATERIALS AND METHODS

Participants

This study included 121 patients with AD and 120 NC subjects, and 126 MCI converters (MCI-c) and 108 MCI non-converters (MCI-nc), with baseline structural MRI data from the Alzheimer's Disease Neuroimaging Initiative (ADNI) database (adni.loni.usc.edu). The up-to-date information on ADNI's general inclusion criteria is described at www.adni-info.org.

TABLE 1 | The characteristics of participants with AD, NC, MCI-c, and MCI-nc.

	AD ($n = 121$)	NC ($n = 120$)	MCI-c ($n = 126$)	MCI-nc ($n = 108$)
Age (years)	74.87 ± 8.07	75.26 ± 6.52	73.47 ± 7.23	73.33 ± 7.73
Gender (M/F)	70/51	58/62	77/49	69/39
Education (years)	15.72 ± 2.61	16.43 ± 2.74	16.09 ± 2.64	15.89 ± 2.63
MMSE score	21.71 ± 3.94	29.18 ± 0.98	26.88 ± 1.76	28.06 ± 1.75
APOE ε4 (NC/HT/HM)	41/80/0	79/33/8	37/65/24	67/35/6
ADAS-cog score	21.52 ± 7.96	5.76 ± 3.02	13.60 ± 4.64	8.03 ± 3.47
Conversion time (years)	–	–	1.48 ± 0.69	–

AD, Alzheimer's disease; NC, normal control; MCI, mild cognitive impairment; MCI-c, MCI converter; MCI-nc, MCI non-converter; M/F, male/female; MMSE, Mini-Mental State Examination; APOE, apolipoprotein E; NC, non-carrier; HT, heterozygote; HM, homozygote; ADAS-cog, Alzheimer's Disease Assessment Scale-Cognitive Subscale.

Briefly, the subjects were between 55 and 90 years of age. General group inclusion/exclusion criteria were as follows: (1) NC subjects: Mini-Mental State Examination (MMSE) scores between 26 and 30, a Clinical Dementia Rating (CDR) score of 0, non-depressed, non-MCI, and non-demented; (2) AD subjects: MMSE scores <26, a CDR score of 0.5 or 1, and met the National Institute of Neurological and Communicative Disorders and Stroke and the Alzheimer's Disease and Related Disorders Association (NINCDS/ADRDA) criteria for probable AD diagnosis; and (3) MCI subjects who had a CDR score of 0.5, MMSE scores between 21 and 30, and memory complaints and abnormal memory function according to the Logical Memory II subscale (Delayed Paragraph Recall but an absence of dementia. The patients with MCI who converted to AD within 3-year follow-up were classified into the MCI-c group; otherwise, they were classified into the MCI-nc group. With respect to the gender ratio and age, the AD group did not significantly differ from the NC group ($p = 0.14$ in the gender ratio and $p = 0.68$ in age), and the MCI-c did not significantly differ from the MCI-nc group ($p = 0.66$ in the gender ratio and $p = 0.20$ in age). However, the AD group exhibited significantly lower MMSE scores ($p = 1.25\ E - 42$) than the NC group. **Table 1** lists the demographics of all these subjects.

Structural MRI Data Acquisition

Structural MRI images were acquired from multiple sites and platforms with different acquisition parameters, which can be found at http://adni.loni.usc.edu/methods/documents/mriprotocols/. The T1-weighted magnetization prepared rapid gradient echo (MPRAGE) images of all these subjects were obtained from 1.5T or 3T scanners. For intensity non-uniformity and gradient nonlinearity correction, the grad warp, B1 calibration, and N3 correction were implemented on each structural MRI image. The processed NIFTI images were downloaded for this study. Details of the protocols of MRI image correction can be found at http://adni.loni.usc.edu/methods/mri-analysis/mri-pre-processing/.

Image Preprocessing

All of the spatial preprocessing of structural MRI images was performed *via* Statistical Parametric Mapping (SPM8) software (https://www.fil.ion.ucl.ac.uk/spm/software/spm8/) in MATLAB. The Voxel-Based Morphometry (VBM) Toolbox (http://dbm.neuro.uni-jena.de/wordpress/vbm/download/) was used for the automated segmentation and normalization of structural MRI images. First, each image was segmented into three parts: GM, white matter, and cerebrospinal fluid (CSF) (Rajapakse et al., 1997; Manjón et al., 2010). A de-noising filter and a classical Markov random field (MRF) approach were implemented to further improve the segmentation effect (Ashburner, 2007). Then, GM images were normalized by the Diffeomorphic Anatomical Registration using Exponential Lie Algebra (DARTEL) protocol and transformed into the Montreal Neurological Institute (MNI) space (Ashburner, 2007). Finally, all the subjects' GM images were smoothed with a kernel of 8-mm full width at half maximum (FWHM).

Feature Extraction

In this study, the brain network-level features were extracted *via* ICA using the Fusion ICA toolbox (FIT) (https://trendscenter.org/software/fit/). The GM images of the AD and NC groups were decomposed into a mixing coefficient matrix and a source matrix with the Minimum Description Length (MDL) criteria to estimate the optimal number of ICs. Each row of the source matrix represents an IC, and each column of the mixing coefficient matrix represents the contribution of each subject to the corresponding IC. A two-sample *t*-test was performed on the mixing coefficient of each IC, and then these IC maps with significant between-group differences were converted to a z-score brain map and reshaped to a binarization mask with a threshold $Z \geq 3$. For each IC, the main brain clusters were reported based on the Anatomical Automatic Labeling (AAL) atlas. For each subject in the AD, MCI-c, MCI-nc, and NC groups, only the top 3 ROIs ranked by the cluster size were selected as the ROI-level features within each network. The average GMV of each ROI falling into the brain network template was regarded as the ROI-level original feature value. The average GMV of voxels within each binarization network template was calculated as the value of network-level original features.

Two-Level Coupled Feature Representation

We took the AD and NC groups as an example to illustrate the implementation of coupled feature representation at the ROI level and the network level. The two-level coupled feature representations of the MCI-c and MCI-nc groups were generated using the same method as the AD and NC groups.

Suppose that there are m_1 samples in the AD group and m_2 samples in the NC group ($M = m_1 + m_2$), we assume that there are N ROI-level original features and L brain network-level original features for each subject. For the l_{th} brain network, if there are n ROI-level original features ($n \times L = N$), and the numerical value of the k_{th} ROI-level features of the i_{th} subject is denoted as $z_{i,k}^{(l)}$, then the ROI-level original feature vector can be represented as $\mathbf{z}_i^{(l)} \in \mathbb{R}^n = \left[z_{i,1}^{(l)}, z_{i,2}^{(l)}, \cdots, z_{i,n}^{(l)}\right]$. The whole

ROI-level original feature vector for the i_{th} subject is $\mathbf{z}_i \in \mathbb{R}^N = \left[\mathbf{z}_i^{(1)}, \mathbf{z}_i^{(2)}, \cdots, \mathbf{z}_i^{(L)}\right]$. For the i_{th} subject, the brain network-level original feature vector is $\mathbf{v}_i \in \mathbb{R}^L = \left[v_{i,1}, v_{i,2}, \cdots, v_{i,L}\right]$, and the numerical value of the j_{th} network-level features is denoted as $v_{i,j}$. The superscript $\top$ represents a transpose operator of a vector or a matrix. In particular, we considered two levels of feature representation with the **O**riginal **F**eatures **M**atrix (OFM): $\mathbf{Z}_{\mathrm{OFM}} = [\mathbf{z}_1, \cdots, \mathbf{z}_M]^\top \in \mathbb{R}^{M\times N}$ and $\mathbf{V}_{\mathrm{OFM}} = [\mathbf{v}_1, \cdots, \mathbf{v}_M]^\top \in \mathbb{R}^{M\times L}$ as follows:

$$\mathbf{Z}_{\mathrm{OFM}} = \begin{pmatrix} z_{1,1}^{(1)}, z_{1,2}^{(1)}, \cdots, z_{1,n}^{(1)}, \cdots, z_{1,1}^{(l)}, z_{1,2}^{(l)}, \cdots, z_{1,n}^{(l)}, \cdots, z_{1,1}^{(L)}, z_{1,2}^{(L)}, \cdots, z_{1,n}^{(L)} \\ \vdots \quad \vdots \quad \ddots \quad \vdots \\ z_{i,1}^{(1)}, z_{i,2}^{(1)}, \cdots, z_{i,n}^{(1)}, \cdots, z_{i,1}^{(l)}, z_{i,2}^{(l)}, \cdots, z_{i,n}^{(l)}, \cdots, z_{i,1}^{(L)}, z_{i,2}^{(L)}, \cdots, z_{i,n}^{(L)} \\ \vdots \quad \vdots \quad \ddots \quad \vdots \\ z_{M,1}^{(1)}, z_{M,2}^{(1)}, \cdots, z_{M,n}^{(1)}, \cdots, z_{M,1}^{(l)}, z_{M,2}^{(l)}, \cdots, z_{M,n}^{(l)}, \cdots, z_{M,1}^{(L)}, z_{M,2}^{(L)}, \cdots, z_{M,n}^{(L)} \end{pmatrix},$$

$$\text{and } \mathbf{V}_{\mathrm{OFM}} = \begin{pmatrix} v_{1,1}, & v_{1,2}, & \cdots, & v_{1,L} \\ \vdots & \vdots & \ddots & \vdots \\ v_{i,1}, & v_{i,2}, & \cdots, & v_{i,L} \\ \vdots & \vdots & \ddots & \vdots \\ v_{M,1}, & v_{M,2}, & \cdots, & v_{M,L} \end{pmatrix}.$$

Compared with the prior ROI-level coupled feature representation method (Shi et al., 2014), the present study proposed a novel two-level coupled feature representation method that attempted to investigate the complex coupling relationship of both the network-level feature matrix $\mathbf{V}_{\mathrm{OFM}}$ and the ROI-level feature matrix $\mathbf{Z}_{\mathrm{OFM}}$ for the identification of NC and AD using structural MRI data. We illustrated and schematized our framework in **Figure 1** compared with the previous ROI-level coupled interaction representation method (Shi et al., 2014).

The Network-Level Intra-coupled Interactions

We illustrated the method of performing the network-level intra-coupled feature representation by the ROI-level feature matrix of the l_{th} brain network as an example.

Referring to previous study about the coupled attribute analysis on numerical data (Wang et al., 2013), the ROI-level feature vector of each brain network, $\mathbf{z}_i^{(l)}$, was mapped into the expanded feature space, employing a matrix expansion with E_1 power as follows:

$$\left[\left\langle z_{i,1}^{(l)}\right\rangle^1, \left\langle z_{i,1}^{(l)}\right\rangle^2, \cdots, \left\langle z_{i,1}^{(l)}\right\rangle^{E_1}, \left\langle z_{i,2}^{(l)}\right\rangle^1, \left\langle z_{i,2}^{(l)}\right\rangle^2, \cdots, \left\langle z_{i,2}^{(l)}\right\rangle^{E_1}, \cdots \left\langle z_{i,n}^{(l)}\right\rangle^1, \left\langle z_{i,n}^{(l)}\right\rangle^2, \cdots, \left\langle z_{i,n}^{(l)}\right\rangle^{E_1}\right],$$

and we can represent the ROI-level **E**xtended **F**eatures **M**atrix (EFM) of this brain network as follows:

$$\mathbf{Z}_{\mathrm{EFM}} \in \mathbb{R}^{M\times(n\times E_1)} = \begin{pmatrix} \left\langle z_{1,1}^{(l)}\right\rangle^1, \left\langle z_{1,1}^{(l)}\right\rangle^2, \cdots, \left\langle z_{1,1}^{(l)}\right\rangle^{E_1}, \left\langle z_{1,2}^{(l)}\right\rangle^1, \left\langle z_{1,2}^{(l)}\right\rangle^2, \cdots, \left\langle z_{1,2}^{(l)}\right\rangle^{E_1}, \cdots \left\langle z_{1,n}^{(l)}\right\rangle^1, \left\langle z_{1,n}^{(l)}\right\rangle^2, \cdots, \left\langle z_{1,n}^{(l)}\right\rangle^{E_1} \\ \vdots \quad \vdots \quad \ddots \quad \vdots \\ \left\langle z_{i,1}^{(l)}\right\rangle^1, \left\langle z_{i,1}^{(l)}\right\rangle^2, \cdots, \left\langle z_{i,1}^{(l)}\right\rangle^{E_1}, \left\langle z_{i,2}^{(l)}\right\rangle^1, \left\langle z_{i,2}^{(l)}\right\rangle^2, \cdots, \left\langle z_{i,2}^{(l)}\right\rangle^{E_1}, \cdots \left\langle z_{i,n}^{(l)}\right\rangle^1, \left\langle z_{i,n}^{(l)}\right\rangle^2, \cdots, \left\langle z_{i,n}^{(l)}\right\rangle^{E_1} \\ \vdots \quad \vdots \quad \ddots \quad \vdots \\ \left\langle z_{M,1}^{(l)}\right\rangle^1, \left\langle z_{M,1}^{(l)}\right\rangle^2, \cdots, \left\langle z_{M,1}^{(l)}\right\rangle^{E_1}, \left\langle z_{M,2}^{(l)}\right\rangle^1, \left\langle z_{M,2}^{(l)}\right\rangle^2, \cdots, \left\langle z_{M,2}^{(l)}\right\rangle^{E_1}, \cdots \left\langle z_{M,n}^{(l)}\right\rangle^1, \left\langle z_{M,n}^{(l)}\right\rangle^2, \cdots, \left\langle z_{M,n}^{(l)}\right\rangle^{E_1} \end{pmatrix}.$$

Next, the Pearson's correlation coefficient, R, between each pair of the ROI-level features of $\mathbf{Z}_{\mathrm{EFM}}$, was calculated as the network-level intra-coupled weight matrix to reflect the ROI-level (intra- and inter-) coupled interactions within each brain network from both the linear and non-linear aspects. If the p-value of R was >0.05, the correlation coefficient was revised to 0. In this way, $\mathbf{R}^{\mathrm{intra}}$ describes the correlation between the k_{th} ROI-level original feature and its own expanded powers, and $\mathbf{R}^{\mathrm{inter}}$ describes the pairwise correlation between the k_{th} ROI-level feature and all the expanded powers of the others, as follows:

$$\mathbf{R}^{\mathrm{intra}}(k) \in \mathbb{R}^{E_1\times E_1} = \begin{pmatrix} \gamma_{11}, \gamma_{12}, \cdots, \gamma_{1E_1} \\ \gamma_{21}, \gamma_{22}, \cdots, \gamma_{2E_1} \\ \vdots \quad \ddots \quad \vdots \\ \gamma_{E_1 1}, \gamma_{E_1 2}, \cdots, \gamma_{E_1 E_1} \end{pmatrix}$$

$$\text{and } \mathbf{R}^{\mathrm{inter}}(\mathrm{k}) \in \mathbb{R}^{\mathrm{E_1}\times(\mathrm{E_1}\times(\mathrm{n}-1))} = \begin{pmatrix} \cdots, \delta_{12}^{k,\tau}, \cdots, \delta_{1E_1}^{k,\tau}, \cdots \\ \cdots \delta_{21}^{k,\tau} \cdots \delta_{2E_1}^{k,\tau} \cdots \\ \vdots \quad \vdots \quad \vdots \\ \cdots \delta_{E_1 1}^{k,\tau} \cdots \delta_{E_1 E_1}^{k,\tau} \cdots \end{pmatrix},$$

where γ_{pq} is the revised Pearson's correlation coefficient between the p_{th} and q_{th} power of the k_{th} ROI-level original feature, $\left\langle z_{:,k}^{(l)}\right\rangle^p$ and $\left\langle z_{:,k}^{(l)}\right\rangle^q$, respectively, and $\delta_{pq}^{k,\tau}$ is the revised Pearson's correlation coefficient between $\left\langle z_{:,k}^{(l)}\right\rangle^p$ and $\left\langle z_{:,\tau}^{(l)}\right\rangle^q$ $(k \neq \tau)$.

For the l_{th} brain network from the i_{th} subject, the network-level intra-coupled feature vector can be represented as $\mathbf{u}_i^{(l)} \in \mathbb{R}^{(n\times E_1)}$. The expanded vector of the k_{th} ROI-level feature is $\mathbf{z}_{\mathrm{EFM}}^{\mathrm{intra}}(i) = \left[\left\langle z_{i,k}^{(l)}\right\rangle^1, \left\langle z_{i,k}^{(l)}\right\rangle^2, \cdots, \left\langle z_{i,k}^{(l)}\right\rangle^{E_1}\right]$, and the expanded

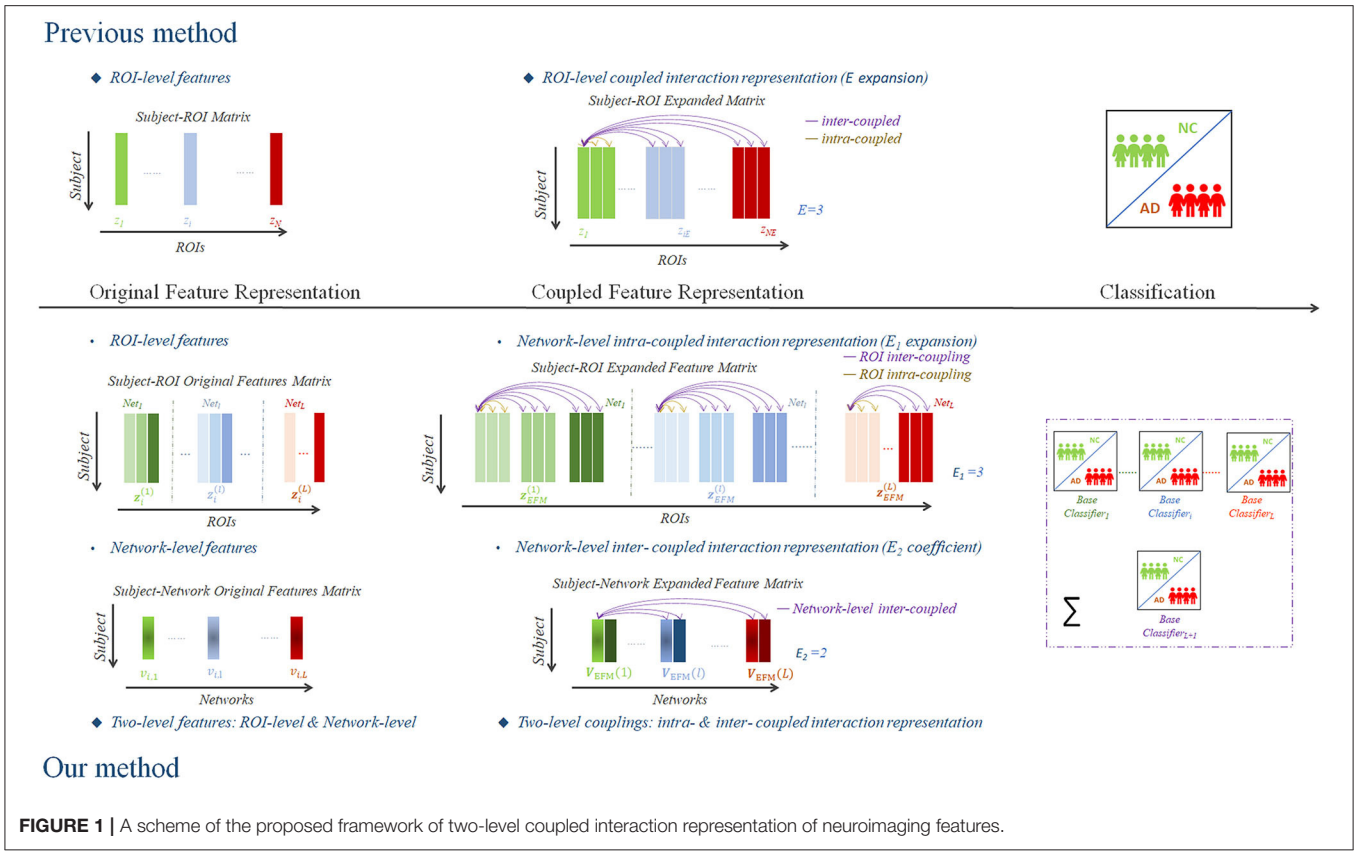

FIGURE 1 | A scheme of the proposed framework of two-level coupled interaction representation of neuroimaging features.

vector of other features is

$$\mathbf{z}_{\mathrm{EFM}}^{\mathrm{inter}}(i)=\left[\left\langle z_{i,1}^{(l)}\right\rangle^{1},\left\langle z_{i,1}^{(l)}\right\rangle^{2},\cdots,\left\langle z_{i,1}^{(l)}\right\rangle^{E_1},\cdots\langle z_{i,\tau}\rangle^{1},\left\langle z_{i,\tau}^{(l)}\right\rangle^{E_1},\right.$$
$$\left.\cdots,\left\langle z_{i,\tau}^{(l)}\right\rangle^{E_1},\cdots\left\langle z_{i,n}^{(l)}\right\rangle^{1},\left\langle z_{i,n}^{(l)}\right\rangle^{2},\cdots,\left\langle z_{i,n}^{(l)}\right\rangle^{E_1}\right],\ (k\neq\tau).$$

Finally, the k_{th} ROI-level coupled feature vector of the i_{th} subject for the l_{th} brain network is denoted as follows:

$$\mathbf{u}_i^{(l)}(k)=\mathbf{z}_{\mathrm{EFM}}^{\mathrm{intra}}(i)\odot\omega\otimes\left[R^{\mathrm{intra}}(k)\right]^{T}$$
$$+\mathbf{z}_{\mathrm{EFM}}^{\mathrm{inter}}(i)\odot\overbrace{[\omega,\omega.\ldots,\omega]}^{n-1}\otimes\left[R^{\mathrm{inter}}(k)\right]^{T},$$

where $\omega=\left[\frac{1}{1!},\frac{1}{2!},\cdots,\frac{1}{E_1!}\right]$,

Then, the network-level intra-coupled feature matrix (CFM) of the l_{th} brain network for the i_{th} subject is:

$$\mathbf{u}_i^{(l)}=\left[\mathbf{u}_i^{(l)}(1),\mathbf{u}_i^{(l)}(2),\ldots,\mathbf{u}_i^{(l)}(n)\right]\in\mathbb{R}^{(n\times E_1)}.$$

The network-level intra-coupled feature vector of the i_{th} subject is the concatenation of all networks' coupled features vectors, as follows:

$$\mathbf{U}_i=\left[\mathbf{u}_i^{(1)},\mathbf{u}_i^{(2)}\ldots\ldots,\mathbf{u}_i^{(L)}\right]\in\mathbb{R}^{(N\times E_1)}.$$

Note that the interactions on ROIs belonging to different networks are not included.

The Network-Level Inter-Coupled Interactions

For the network-level inter-coupled representation, we can represent the CFM as $\mathbf{F}\in\mathbb{R}^{M\times L}$ with the first E_2 coefficients from CCA. In contrast to the network-level intra-coupled feature representation used with the revised Pearson's correlation coefficient, we chose the CCA coefficients as the coupling weights matrix for the network-level coupled feature representation. CCA is a way of inferring information from cross-covariance matrices of different network-level features. The canonical correlation for the canonical variate pairs from any two network-level $\mathbf{Z}_{\mathrm{OFM}}{}^{(l)}$ is as follows: $\mathbf{w}_{l_1l_2}=R_{CCA}\left(\mathbf{Z}_{\mathrm{OFM}}{}^{(l_1)},\mathbf{Z}_{\mathrm{OFM}}{}^{(l_2)}\right)$, $(l_1\neq l_2)$, which can represent the inter-coupled interactions of different network-level features. The top E_2 canonical correlations are used for inter-coupled interactions description rather than simply involving the whole $\mathbf{w}_l$, revised as $\tilde{\mathbf{w}}_l=\tilde{R}_{CCA}\left(\mathbf{Z}_{\mathrm{OFM}}{}^{(l_1)},\mathbf{Z}_{\mathrm{OFM}}{}^{(l_2)}\right)$. For the whole brain, the network-level inter-coupled feature vector of the i_{th} subject is denoted as follows:

$$\mathbf{f}_i(w)=\mathbf{V}_{\mathrm{EFM}}(W_l)\odot\overbrace{[\omega,\omega.\ldots,\omega]}^{L-1}\otimes\tilde{w}_l,$$

where $\omega=\left[\frac{1}{1!},\frac{1}{2!},\cdots,\frac{1}{E_2!}\right]$ and $\mathbf{f}_i=[\mathbf{f}_i(1),\mathbf{f}_i(2),\cdots,\mathbf{f}_i(L)]\in\mathbb{R}^{L}$.

To obtain the coupled feature representation at two levels, the final $\mathbf{CFM}_{network}$ for the i_{th} subject can be represented as follows: $[\mathbf{U}_i, \mathbf{f}_i] \in \mathbb{R}^{(N\times E_1+L)}$.

Classification With Coupled Features

Boosting is a machine learning approach based on the idea of improving the accuracy of a decision by combining many relatively weak base learners (Schapire, 2013). The AdaBoost algorithm works by updating parameters of feature distribution in weak learners over training samples after each iteration sequentially and adaptively (Freund and Schapire, 1997; Collins et al., 2002). In this study, the two-level coupled feature matrix was represented for the following classification analysis. We chose an SVM classifier with a linear kernel function as the base learner. In total, $L + 1$ base learners were trained, of which the L base learners were trained for different brain network-level intra-coupled features, and one was trained for the brain network-level inter-coupled matrix.

We carried out separate analyses on two tasks: AD vs. NC and MCI-c vs. MCI-nc classification. First, the boosting models were constructed on the two-level **C**oupled **F**eatures **M**atrix, denoted as $\mathbf{CFM}_{\text{network}}$ for AD vs. NC, and MCI-c vs. MCI-nc classification. The 10-fold cross-validation was applied to evaluate the performance, and the average results were reported. In our two-level coupled feature representation and classification scheme, several parameters need to be set, including E_1 for the parameter of network-level intra-coupled expansion and E_2 for network-level inter-coupled coefficient selection. Here, the optimal values of E_1 and E_2 were searched from a small set of {2, 3, 4} and {1, 2, 3, 4, 5}, respectively.

We also constructed three other kinds of feature matrices separately: (1) The ROI-level **O**riginal **F**eatures **M**atrix only, denoted as OFM_{ROI}; (2) the ROI-level **C**oupled **F**eatures **M**atrix across the whole brain without the network-level information, denoted as $\mathbf{CFM}_{\text{ROI}}$; and 3) the network-level **O**riginal **F**eatures **M**atrix without coupling interaction information, denoted as $\mathbf{OFM}_{\text{network}}$. To validate the advantage of the two-level coupled feature representation, we compared the classification performances with these three different brain features.

RESULTS

The number of estimated ICs was 49 for the AD and NC groups with the structural MRI data, and 21 ICs showed significant between-group differences with Bonferroni correction. The results of our two-level coupled feature representation and the classification model showed that the best prediction accuracy is 90.44%, sensitivity is 88.5%, and specificity is 93.67% for AD and NC groups and the best prediction accuracy is 87.72%, sensitivity is 84.16%, and specificity is 91.64% for the MCI-c and MCI-nc groups.

Based on the two-level coupled feature representation, **Tables 2**, **3** show the classification results and give the detailed results of the best parameters of E_1 and E_2 as references for future studies. When E_1 and E_2 were set as 3 and 2, the two-level coupled feature representation achieved the best performance for AD vs. NC classification. The same parameter selection is applicable to the MCI-c vs. MCI-nc distinction.

The results of the comparison for four different brain feature representations for AD and NC classification are shown in **Table 2**. The best classification accuracies for different features are 69.21% for OFM_{ROI}, 73.51% for CFM_{ROI}, 71.29% for $\text{OFM}_{\text{network}}$, and 90.44% for $\text{CFM}_{\text{network}}$. **Table 3** shows the results of the classification performances for the four kinds of feature matrices for the MCI-c and MCI-nc classification. The best classification accuracies for different features are 64.15% for OFM_{ROI}, 75.10% for CFM_{ROI}, 68.62% for $\text{OFM}_{\text{network}}$, and 87.72% for $\text{CFM}_{\text{network}}$.

DISCUSSION

The current study proposed a novel network-level inter-coupled representation approach, integrated the intrinsic coupled relationships of both the ROI-level and the brain network-level features, and then applied them to the classification of subjects with AD, MCI-c, and MCI-nc from the normal elderly individuals based on structural MRI data. By integrating the intra- and inter-coupled interactions among the ROI-level and network-level features, we obtained the innovative coupled neuroimaging features, $\mathbf{CFM}_{\text{network}}$ and achieved the optimal classification accuracy for both AD vs. NC and MCI-nc vs. MCI-c classification compared with the OFM_{ROI}, $\mathbf{CFM}_{\text{ROI}}$, and $\mathbf{OFM}_{\text{network}}$. These results indicated the effectiveness of the coupled interaction representation among different levels of neuroimaging features. Furthermore, the best-coupled expansion parameter E_1 was 3 for the network-level intra-coupled interaction, and the best-coupled coefficient selection E_2 was 2 for the network-level inter-coupled interaction.

Two-Level Coupled Feature Representation for AD and NC Classification

In the current study, we explored the coupled interaction representation of two-level (the ROI -level and the network-level) neuroimaging features on structural MRI data. For AD and NC classification, the $\mathbf{OFM}_{\text{network}}$ representation obtained slightly better performance (accuracy = 71.29%) than the OFM_{ROI} representation (accuracy = 69.21%), and the $\mathbf{CFM}_{\text{network}}$ representation achieved much greater accuracy (accuracy = 90.44%) than the $\mathbf{CFM}_{\text{ROI}}$ representation (accuracy = 73.51%). Overall, the network-level feature representations showed preferable results to the ROI-level features, which suggested the advantages of the network-level features in the AD classification task. A number of studies built classification models to distinguish patients with AD from NCs based on the single-level features from brain neuroimaging data, such as the ROI-level features (Zhang et al., 2011; Zhan et al., 2015; Rondina et al., 2018) or the network-level features (Yang et al., 2011). For example, to identify the conversion from normal elderly cognition to AD, Zhan et al. defined 90 ROIs and computed the mean GMV as the ROI-level feature matrix and achieved an accuracy of 83.83% (Zhan et al., 2015). The ROI-level features computed by the ratio of increased GMV have also been extracted

TABLE 2 | Classification results for AD vs. NC with different kinds of feature representations.

Feature representation	OFM_{ROI}	$OFM_{network}$	CFM_{ROI}			$CFM_{network}$														
Parameters setting			$E_1 = 2$	$E_1 = 3$	$E_1 = 4$	$E_1 = 2$					$E_1 = 3$					$E_1 = 4$				
						$E_2 = 1$	$E_2 = 2$	$E_2 = 3$	$E_2 = 4$	$E_2 = 5$	$E_2 = 1$	$E_2 = 2$	$E_2 = 3$	$E_2 = 4$	$E_2 = 5$	$E_2 = 1$	$E_2 = 2$	$E_2 = 3$	$E_2 = 4$	$E_2 = 5$
ACC (%)	69.21	71.29	**73.51**	71.77	68.27	71.2	76.84	81.72	76.09	70.85	85.02	**90.44**	83.3	77.94	72.47	77.47	87.32	81.13	75.19	70.2
SEN (%)	67.29	67.72	**69.32**	69.57	64.03	68.67	74.12	76.75	72.41	68.29	82.28	**88.5**	81.08	74.04	68.01	79.4	85.72	77.42	71.01	67.18
SPE (%)	71.60	73.20	**75.42**	74.02	70.57	73.9	79.61	83.57	80.62	73.16	87.75	**93.67**	86.1	80.07	74.51	81.13	90.04	84.91	77.38	72.55

OFM_{ROI}, the original ROI-level feature representation; $OFM_{network}$, the original network-level feature representation; CFM_{ROI}, the coupled ROI-level feature representation; $CFM_{network}$, the two-level feature representation; Acc, accuracy; Sen, sensitivity; Spe, specificity. The values with the highest accuracy are highlighted in boldface. The shadow of gray color is used to visually differentiate columns of the table.

TABLE 3 | Classification results for MCI-c vs. MCI-nc with different kinds of feature representations.

Feature representation	OFM_{ROI}	$OFM_{network}$	CFM_{ROI}			$CFM_{network}$														
Parameters setting			$E_1 = 2$	$E_1 = 3$	$E_1 = 4$	$E_1 = 2$					$E_1 = 3$					$E_1 = 4$				
						$E_2 = 1$	$E_2 = 2$	$E_2 = 3$	$E_2 = 4$	$E_2 = 5$	$E_2 = 1$	$E_2 = 2$	$E_2 = 3$	$E_2 = 4$	$E_2 = 5$	$E_2 = 1$	$E_2 = 2$	$E_2 = 3$	$E_2 = 4$	$E_2 = 5$
ACC (%)	64.15	68.62	**75.10**	73.81	71.31	70.24	72.38	78.92	76.07	73.25	80.75	**87.72**	82.31	74.59	71.76	71.22	78.63	79.41	75.71	70.65
SEN (%)	62.30	66.44	**72.23**	70.54	67.90	66.21	69.70	75.92	73.82	70.61	78.42	**84.16**	78.73	72.16	69.02	68.78	76.23	77.20	71.02	68.99
SPE (%)	66.74	71.46	**79.42**	76.42	73.54	72.44	76.07	81.13	79.16	77.25	84.57	**91.64**	84.79	79.85	75.59	75.28	81.78	82.18	78.29	73.06

OFM_{ROI}, the original ROI-level feature representation; $OFM_{network}$, the original network-level feature representation; CFM_{ROI}, the coupled ROI-level feature representation; $CFM_{network}$, the two-level feature representation; Acc, accuracy; Sen, sensitivity; Spe, specificity. The values with the highest accuracy are highlighted in boldface. The shadow of gray color is used to visually differentiate columns of the table.

from structural MRI data, and they obtained a classification accuracy of 76.11% between AD and NC (Rondina et al., 2018). Different from them, Wang et al. considered the corresponding coefficients of ICs decomposed using the ICA algorithm as the network-level features and got 80.7% accuracy with the SVM classifier for the diagnosis of individuals with AD and HC (Yang et al., 2011). In this study, we not only extracted the ROI-level features but also obtained the network-level features and integrated them. Although the measurements or definitions of original features in our study were different from those in the prior studies, our study attempted to integrate hierarchical features from sMRI for the classification of AD and NC.

Compared with the original features (OFM_{ROI} and $OFM_{network}$), the coupled features ($\mathbf{CFM}_{ROI}$ and $\mathbf{CFM}_{network}$) helped improve the classification results in this study. Among the four kinds of feature representations, the $\mathbf{CFM}_{network}$ obtained the best classification performance of AD and NC (accuracy = 90.44%), which demonstrated the strengths of the integration of multilevel (the ROI level and the network level) coupled interaction representation of hierarchical features. It has been demonstrated that there were strong couplings, including the relations that exist explicitly or implicitly between source and destination entities, among values, attributes, and objects for numerical data (Wang et al., 2013; Cao, 2015). Wang et al. introduced the framework to quantify and integrate the intra-coupled and inter-coupled interactions with the original information from numerical data (Wang et al., 2013). Many studies indicated that the original neuroimaging features exhibited complex regional dependencies, and the features in different brain networks changed diversely along with the progression of MCI and AD (Liu et al., 2017c; Zheng et al., 2019; Lee et al., 2020). Inspired by these pieces of research, we quantitatively measured the network-level intra-coupled relationships and proposed the network-level inter-coupled interaction feature representation. Recently, several studies focusing on the coupled interactions for ROI-level features have been reported, in which they analyzed the ROI-level coupled relationships and appealed to the coupling analysis for numerical data (Shi et al., 2014, 2020). By hypothesizing that the ROI-level features (the average GMV) were related to each other in some ways, Shi et al. introduced the coupled interaction representation for the ROI-level features and adopted the coupled boosting algorithm to analyze the pairwise coupled-diversity correlation between modalities with the best performance of 86.% for AD and NC classification (Shi et al., 2014). Our model achieved higher accuracy of 90.44%, which illustrated the advantages of our two-level coupled interactions representation.

Two-Level Coupled Interaction Representation for MCI-C and MCI-Nc Classification

MCI is an intermediate stage in the trajectory from normal cognition to AD and is important for the early diagnosis of AD (Ahmed et al., 2017; Arbabshirani et al., 2017; Thung et al., 2018). To classify MCI-c and MCI-nc, we integrated the intra-coupled and inter-coupled interactions among the ROI-level and network-level features with the best accuracy of 87.72% compared with other feature representations. Considering the GM density from structural MRI data as the voxel-level features, Wang et al. obtained an accuracy of 69.77% for MCI-c vs. MCI-nc based on informed Partial Least Square models (Wang et al., 2016). Based on 38 subcortical volumes as ROI-level features, Aleksandra et al. classified MCI vs. NC with the Random Forest model (Lebedeva et al., 2017). Apart from the slight differences in classifiers, a common practice in former studies was the straight concatenation of all ROI-level features as independent variables into the input feature matrix. However, these schemes lost sight of the complicated dependencies among ROI-level features (Guo et al., 2015) and the diversified and heterogenous changes for different structural networks (Sui et al., 2014; Liu et al., 2017b). Compared with the abovementioned studies, we believe that the proposed two-level coupled interaction integration method which was validated could be more powerful for the diagnosis of MCI conversion to AD with promising results.

Methodological Considerations

ICA is a popular data-driven method to study brain functional networks (Damoiseaux et al., 2012) and structural networks (Guo et al., 2015; Liu et al., 2017c). The network-level features extracted by ICA could effectively reduce the data dimensions and depend entirely on brain neuroimaging data themselves without prior knowledge. It has been confirmed that ROIs in the same brain network carried similar and interregional covariate information and exhibited more complicated regional dependencies than those in different brain networks (Liu et al., 2017a; Filippi et al., 2020; Wang et al., 2022). Thus, we performed ICA to identify brain structural networks from AD and NC groups and defined the representation of the network-level and ROI-level neuroimaging features.

Then, we designed the two-level coupled interaction integration of hierarchical features to evaluate the network-level intra-coupled and inter-coupled effects in AD and MCI classification. More specifically, we innovatively considered both the network-level intra-coupled interaction for every network individually, quantified by the intra-coupled and inter-coupled interactions among the ROI-level features within this network but not ROIs across the whole brain; and the network-level inter-coupled interaction among different network-level features was captured by the coupled coefficients between the ROI-level feature set of this network and the ROI-level features set of others. Besides, CCA can maximize the correlation between a linear combination of the variables in two datasets and has been applied to identify the relationship between brain networks (Sui et al., 2012; Ouyang et al., 2015; Taquet et al., 2021). In this study, CCA was performed on the ROI-level feature sets of any two brain networks and obtained the inter-coupled coefficients of network-level features to avoid reusing the ROI-level features information for network-level coupled interaction representation.

In the current study, $E_1$was denoted as the maximal power for the expansion of the ROI-level features in the network-level intra-coupled interaction representation and E_2 as the number of the CCA coefficients selected to express the information for the

network-level inter-coupled interaction representation. In this way, we integrated the two-level coupled interactions, including both the intra-coupled and inter-coupled interactions for both the network-level and the ROI-level features. We set the range of E_1, from 2 to 4, and E_2, from 1 to 5, respectively. When the value of E_1 increases, the value of $E_1!$ will grow correspondingly so will $E_2!$. The coupled interactions for feature values are quantified by a Taylor-like expansion, $\omega = \left[\frac{1}{1!}, \frac{1}{2!}, \cdots, \frac{1}{E_1!}\right]$. Along with the increase of E_1 and E_2, the reciprocals, $\frac{1}{E_1!}$ and $\frac{1}{E_2!}$, decreased accordingly and caused the corresponding weight value of the expanded items to be too small to capture the interactions among different features. Furthermore, the greater E_1 or E_2 may have less significant effects on the classification performance. Then, the appropriate E_1 or E_2 helps to fully exploit the information of coupled interactions within hierarchical features. As our results indicated, the classification performance changed with the variation of the two coupled interaction parameters. When $E_1 = 3$ and $E_2 = 2$, the best result was obtained in this tudy, which implied that the information of coupled interactions within hierarchical features has been fully exploited. When $E_1 = 1$, the number of the ROI-level features was still invariant, which meant that the ROI-level coupled feature matrix was the original ROI-level feature matrix without coupled interaction analysis. When E_1 increased, the number of ROI features increased with E_1-fold accordingly. When E_1 was equal to 3, each ROI-level feature was expanded three times in numerical space than the original feature. The inter-coupled interaction parameter for brain network-level features indicated that the first E_2 pairs of canonical variables *via* CCA were maximally adequate to express the information among brain network-level features. When E_2 was equal to 2, the top two coefficients of CCA were selected for the network-level inter-coupled interaction representation. With regard to the ROI-level and network-level coupled interactions of parameters setting, we recommend $E_1 = 3$ and $E_2 = 2$ for similar analysis in the future.

Limitations and Future Work

The current study focused on constructing a novel coupled relationship representation to combine the ROI-level and network-level features, and then, we only adopted the numerical features from the structural MRI data. As different neuroimaging modality features provide complementary information, the coupled interactions of different modalities are heterogeneous (Zhang et al., 2011; Rathore et al., 2017). The coupled interactions based on multi-modality features are a novel issue that needs more exploration. The representation and integration of the intra-coupled interaction and inter-coupled interaction at multilevels, including the modality level, the network level, and the ROI level, will be investigated in future studies.

CONCLUSION

In the current study, we proposed a network-level inter-coupled interaction representation approach with the independent components from ICA as the network-level features and the CCA weights for network-level inter-coupled characteristics. Then, we integrated the ROI-level and network-level coupled interactions based on structural MRI data to classify subjects with AD, MCI-c, MCI-nc, and NC. Our results demonstrated that the two-level coupled interaction feature representation outperformed the original feature representation and the single-level coupled representation and provided a perspective based on the coupled interaction integration of hierarchical neuroimaging features.

DATA AVAILABILITY STATEMENT

Publicly available datasets were analyzed in this study. This data can be found at: adni.loni.usc.edu.

ETHICS STATEMENT

The ADNI study was approved by the Institutional Review Boards/Research Ethics Boards of each participating site. All participants provided their written informed consent in this study. The ethics committees/institutional review boards providing the approval for the ADNI study are: Albany Medical Center Committee on Research Involving Human Subjects Institutional Review Board, Boston University Medical Campus and Boston Medical Center Institutional Review Board, Butler Hospital Institutional Review Board, Cleveland Clinic Institutional Review Board, Columbia University Medical Center Institutional Review Board, Duke University Health System Institutional Review Board, Emory Institutional Review Board, Georgetown University Institutional Review Board, Health Sciences Institutional Review Board, Houston Methodist Institutional Review Board, Howard University Office of Regulatory Research Compliance, Icahn School of Medicine at Mount Sinai Program for the Protection of Human Subjects, Indiana University Institutional Review Board, Institutional Review Board of Baylor College of Medicine, Jewish General Hospital Research Ethics Board, Johns Hopkins Medicine Institutional Review Board, Lifespan – Rhode Island Hospital Institutional Review Board, Mayo Clinic Institutional Review Board, Mount Sinai Medical Center Institutional Review Board, Nathan Kline Institute for Psychiatric Research & Rockland Psychiatric Center Institutional Review Board, New York University Langone Medical Center School of Medicine Institutional Review Board, Northwestern University Institutional Review Board, Oregon Health and Science University Institutional Review Board, Partners Human Research Committee Research Ethics, Board Sunnybrook Health Sciences Centre, Roper St. Francis Healthcare Institutional Review Board, Rush University Medical Center Institutional Review Board, St. Joseph's Phoenix Institutional Review Board, Stanford Institutional Review Board, The Ohio State University Institutional Review Board, University Hospitals Cleveland Medical Center Institutional Review Board, University of Alabama Office of the IRB, University of British Columbia Research Ethics Board, University of California Davis Institutional Review Board Administration, University of California Los Angeles Office of the Human Research Protection Program, University of California San Diego Human

Research Protections Program, University of California San Francisco Human Research Protection Program, University of Iowa Institutional Review Board, University of Kansas Medical Center Human Subjects Committee, University of Kentucky Medical Institutional Review Board, University of Michigan Medical School Institutional Review Board, University of Pennsylvania Institutional Review Board, University of Pittsburgh Institutional Review Board, University of Rochester Research Subjects Review Board, University of South Florida Institutional Review Board, University of Southern, California Institutional Review Board, UT Southwestern Institution Review Board, VA Long Beach Healthcare System Institutional Review Board, Vanderbilt University Medical Center Institutional Review Board, Wake Forest School of Medicine Institutional Review Board, Washington University School of Medicine Institutional Review Board, Western Institutional Review Board, Western University Health Sciences Research Ethics Board, and Yale University Institutional Review Board.

AUTHOR CONTRIBUTIONS

KL, QL, LY, and XG conceived, designed the experiments, and drafted the manuscript. KL and QL analyzed the data. All authors contributed to the article and approved the submitted version.

FUNDING

This work was supported by the National Natural Science Foundation of China (Grant Nos. 62071051 and 61671066) and the Key Program of the National Natural Science Foundation of China (Grant No. 61731003).

ACKNOWLEDGMENTS

Data collection and sharing for this project were funded by the Alzheimer's Disease Neuroimaging Initiative (ADNI) (National Institutes of Health Grant U01 AG024904) and DOD ADNI (Department of Defense Award No. W81XWH-12-2-0012). ADNI was funded by the National Institute on Aging, the National Institute of Biomedical Imaging and Bioengineering, and through generous contributions from the following: AbbVie, Alzheimer's Association; Alzheimer's Drug Discovery Foundation; Araclon Biotech; BioClinica, Inc.; Biogen; Bristol-Myers Squibb Company; CereSpir, Inc.; Cogstate; Eisai Inc.; Elan Pharmaceuticals, Inc.; Eli Lilly and Company; EuroImmun; F. Hoffmann-La Roche Ltd. and its affiliated company Genentech, Inc.; Fujirebio; GE Healthcare; IXICO Ltd.; Janssen Alzheimer Immunotherapy Research & Development, LLC.; Johnson & Johnson Pharmaceutical Research & Development LLC.; Lumosity; Lundbeck; Merck & Co., Inc.; Meso Scale Diagnostics, LLC.; NeuroRx Research; Neurotrack Technologies; Novartis Pharmaceuticals Corporation; Pfizer Inc.; Piramal Imaging; Servier; Takeda Pharmaceutical Company; and Transition Therapeutics. The Canadian Institutes of Health Research was providing funds to support ADNI clinical sites in Canada. Private sector contributions are facilitated by the Foundation for the National Institutes of Health (www.fnih.org). The grantee organization is the Northern California Institute for Research and Education, and the study was coordinated by the Alzheimer's Therapeutic Research Institute at the University of Southern California. ADNI data are disseminated by the Laboratory for Neuro Imaging at the University of Southern California.

REFERENCES

Ahmed, O. B., Benois-Pineau, J., Allard, M., Catheline, G., and Amar, C. B. (2017). Recognition of Alzheimer's disease and mild cognitive impairment with multimodal image-derived biomarkers and multiple kernel learning. *Neurocomputing* 220, 98–110. doi: 10.1016/j.neucom.2016.08.041

Anstey, K. J., and Maller, J. J. (2003). The role of volumetric MRI in understanding mild cognitive impairment and similar classifications. *Aging Ment. Health* 7, 238–250. doi: 10.1080/1360786031000120732

Arbabshirani, M. R., Plis, S., Sui, J., and Calhoun, V. D. (2017). Single subject prediction of brain disorders in neuroimaging: promises and pitfalls. *Neuroimage* 145, 137–165. doi: 10.1016/j.neuroimage.2016.02.079

Ashburner, J. (2007). A fast diffeomorphic image registration algorithm. *Neuroimage* 38, 95–113. doi: 10.1016/j.neuroimage.2007.07.007

Betzel, R. F., Byrge, L., He, Y., Goñi, J., Zuo, X.-N., and Sporns, O. (2014). Changes in structural and functional connectivity among resting-state networks across the human lifespan. *Neuroimage* 102, 345–357. doi: 10.1016/j.neuroimage.2014.07.067

Brickman, A. M., Habeck, C., Zarahn, E., Flynn, J., and Stern, Y. (2007). Structural MRI covariance patterns associated with normal aging and neuropsychological functioning. *Neurobiol. Aging* 28, 284–295. doi: 10.1016/j.neurobiolaging.2005.12.016

Cao, L. (2015). Coupling learning of complex interactions. *Inf. Process. Manag.* 51, 167–186. doi: 10.1016/j.ipm.2014.08.007

Collins, M., Schapire, R. E., and Singer, Y. (2002). Logistic regression, AdaBoost and bregman distances. *Mach. Learn.* 48, 253–285. doi: 10.1023/A:1013912006537

Damoiseaux, J. S., Prater, K. E., Miller, B. L., and Greicius, M. D. (2012). Functional connectivity tracks clinical deterioration in Alzheimer's disease. *Neurobiol. Aging* 33, 828.e19–e30. doi: 10.1016/j.neurobiolaging.2011.06.024

Dona, O., Thompson, J., and Druchok, C. (2016). Comprehensive review on magnetic resonance imaging in Alzheimer's disease. *Crit. Rev. Biomed. Eng.* 44, 213–225. doi: 10.1615/CritRevBiomedEng.2016019544

Feng, J., Zhang, S.-W., Chen, L., and Xia, J. (2021). Alzheimer's disease classification using features extracted from nonsubsampled contourlet subband-based individual networks. *Neurocomputing* 421, 260–272. doi: 10.1016/j.neucom.2020.09.012

Filippi, M., Basaia, S., Canu, E., Imperiale, F., Magnani, G., Falautano, M., et al. (2020). Changes in functional and structural brain connectome along the Alzheimer's disease continuum. *Mol. Psychiatry* 25, 230–239. doi: 10.1038/s41380-018-0067-8

Freund, Y., and Schapire, R. E. (1997). A decision-theoretic generalization of on-line learning and an application to boosting. *J. Comput. Syst. Sci.* 55, 119–139. doi: 10.1006/jcss.1997.1504

Guo, X., Wang, Y., Guo, T., Chen, K., Zhang, J., Li, K., et al. (2015). Structural covariance networks across healthy young adults and their consistency. *J. Magn. Reson. Imaging* 42, 261–268. doi: 10.1002/jmri.24780

Hu, K., Wang, Y., Chen, K., Hou, L., and Zhang, X. (2016). Multi-scale features extraction from baseline structure MRI for MCI patient classification and AD early diagnosis. *Neurocomputing* 175, 132–145. doi: 10.1016/j.neucom.2015.10.043

Leandrou, S., Petroudi, S., Kyriacou, P. A., Reyes-Aldasoro, C. C., and Pattichis, C. S. (2018). Quantitative MRI brain studies in mild cognitive impairment and Alzheimer's disease: a methodological review. *IEEE Rev. Biomed. Eng.* 11, 97–111. doi: 10.1109/RBME.2018.2796598

Lebedeva, A. K., Westman, E., Borza, T., Beyer, M. K., Engedal, K., Aarsland, D., et al. (2017). MRI-based classification models in prediction of mild cognitive

impairment and dementia in late-life depression. *Front. Aging Neurosci.* 9, 13. doi: 10.3389/fnagi.2017.00013

Lee, P.-L., Chou, K.-H., Chung, C.-P., Lai, T.-H., Zhou, J. H., Wang, P.-N., et al. (2020). Posterior cingulate cortex network predicts Alzheimer's disease progression. *Front. Aging Neurosci.* 12, 608667. doi: 10.3389/fnagi.2020.608667

Liu, J., Li, M., Pan, Y., Lan, W., Zheng, R., Wu, F.-X., et al. (2017a). Complex brain network analysis and its applications to brain disorders: a survey. *Complexity* 2017, 1–27. doi: 10.1155/2017/8362741

Liu, K., Chen, K., Yao, L., and Guo, X. (2017b). Prediction of mild cognitive impairment conversion using a combination of independent component analysis and the cox model. *Front. Hum. Neurosci.* 11, 33. doi: 10.3389/fnhum.2017.00033

Liu, K., Yao, S., Chen, K., Zhang, J., Yao, L., Li, K., et al. (2017c). Structural brain network changes across the adult lifespan. *Front. Aging Neurosci.* 9, 275. doi: 10.3389/fnagi.2017.00275

Manjón, J. V., Coupé, P., Martí-Bonmatí, L., Collins, D. L., and Robles, M. (2010). Adaptive non-local means denoising of MR images with spatially varying noise levels. *J. Magn. Reson. Imaging* 31, 192–203. doi: 10.1002/jmri.22003

Moradi, E., Pepe, A., Gaser, C., Huttunen, H., and Tohka, J. (2015). Machine learning framework for early MRI-based Alzheimer's conversion prediction in MCI subjects. *Neuroimage* 104, 398–412. doi: 10.1016/j.neuroimage.2014.10.002

Ouyang, X., Chen, K., Yao, L., Hu, B., Wu, X., Ye, Q., et al. (2015). Simultaneous changes in gray matter volume and white matter fractional anisotropy in Alzheimer's disease revealed by multimodal CCA and joint ICA. *Neuroscience* 301, 553–562. doi: 10.1016/j.neuroscience.2015.06.031

Pang, G., Cao, L., Chen, L., and Liu, H. (2016). "Unsupervised feature selection for outlier detection by modelling hierarchical value-feature couplings," in *2016 IEEE 16th International Conference on Data Mining (ICDM)* (Barcelona: IEEE), 410–419. doi: 10.1109/ICDM.2016.0052

Rajapakse, J. C., Giedd, J. N., and Rapoport, J. L. (1997). Statistical approach to segmentation of single-channel cerebral MR images. *IEEE Trans. Med. Imaging* 16, 176–186. doi: 10.1109/42.563663

Rathore, S., Habes, M., Iftikhar, M. A., Shacklett, A., and Davatzikos, C. (2017). A review on neuroimaging-based classification studies and associated feature extraction methods for Alzheimer's disease and its prodromal stages. *Neuroimage* 155, 530–548. doi: 10.1016/j.neuroimage.2017.03.057

Rondina, J. M., Ferreira, L. K., de Souza Duran, F. L., Kubo, R., Ono, C. R., Leite, C. C., et al. (2018). Selecting the most relevant brain regions to discriminate Alzheimer's disease patients from healthy controls using multiple kernel learning: a comparison across functional and structural imaging modalities and atlases. *NeuroImage Clin.* 17, 628–641. doi: 10.1016/j.nicl.2017.10.026

Schapire, R. E. (2013). Boosting: foundations and algorithms. *Kybernetes* 42, 164–166. doi: 10.1108/03684921311295547

Shi, Y., Gao, Y., Liao, S., Zhang, D., Gao, Y., and Shen, D. (2015). Semi-Automatic segmentation of prostate in CT images via coupled feature representation and spatial-constrained transductive lasso. *IEEE Trans. Pattern Anal. Mach. Intell.* 37, 2286–2303. doi: 10.1109/TPAMI.2015.2424869

Shi, Y., Suk, H.-I., Gao, Y., Lee, S.-W., and Shen, D. (2020). Leveraging coupled interaction for multimodal Alzheimer's disease diagnosis. *IEEE Trans. Neural Networks Learn. Syst.* 31, 186–200. doi: 10.1109/TNNLS.2019.2900077

Shi, Y., Suk, H.-I., Gao, Y., and Shen, D. (2014). "Joint coupled-feature representation and coupled boosting for AD diagnosis," in *2014 IEEE Conference on Computer Vision and Pattern Recognition* (Columbus: IEEE), 2721–2728. doi: 10.1109/CVPR.2014.354

Sui, J., Adali, T., Yu, Q., Chen, J., and Calhoun, V. D. (2012). A review of multivariate methods for multimodal fusion of brain imaging data. *J. Neurosci. Methods* 204, 68–81. doi: 10.1016/j.jneumeth.2011.10.031

Sui, J., Huster, R., Yu, Q., Segall, J. M., and Calhoun, V. D. (2014). Function-structure associations of the brain: evidence from multimodal connectivity and covariance studies. *Neuroimage* 102, 11–23. doi: 10.1016/j.neuroimage.2013.09.044

Taquet, M., Smith, S. M., Prohl, A. K., Peters, J. M., Warfield, S. K., Scherrer, B., et al. (2021). A structural brain network of genetic vulnerability to psychiatric illness. *Mol. Psychiatry* 26, 2089–2100. doi: 10.1038/s41380-020-0723-7

Thung, K.-H., Yap, P.-T., Adeli, E., Lee, S.-W., and Shen, D. (2018). Conversion and time-to-conversion predictions of mild cognitive impairment using low-rank affinity pursuit denoising and matrix completion. *Med. Image Anal.* 45, 68–82. doi: 10.1016/j.media.2018.01.002

Vemuri, P., and Jack, C. R. (2010). Role of structural MRI in Alzheimer's disease. *Alzheimers Res. Ther.* 2, 23. doi: 10.1186/alzrt47

Wang, C., Chi, C. H., Zhou, W., and Wong, R. (2015a). Coupled interdependent attribute analysis on mixed data. *Proc. Natl. Conf. Artif. Intell.* 3, 1861–1867. Available online at: https://dl.acm.org/doi/10.5555/2886521.2886579

Wang, C., Dong, X., Zhou, F., Cao, L., and Chi, C. H. (2015b). Coupled attribute similarity learning on categorical data. *IEEE Trans. Neur. Netw. Learn. Syst.* 26, 781–797. doi: 10.1109/TNNLS.2014.2325872

Wang, C., She, Z., and Cao, L. (2013). "Coupled attribute analysis on numerical data," in *IJCAI International Joint Conference on Artificial Intelligence* (Beijing), 1736–1742.

Wang, P., Chen, K., Yao, L., Hu, B., Wu, X., Zhang, J., et al. (2016). Multimodal classification of mild cognitive impairment based on partial least squares. *J. Alzheimers Dis.* 54, 359–371. doi: 10.3233/JAD-160102

Wang, Q., Zhao, S., He, Z., Zhang, S., Jiang, X., Zhang, T., et al. (2022). Modeling functional difference between gyri and sulci within intrinsic connectivity networks. *Cereb. Cortex*. bhac111. doi: 10.1093/cercor/bhac111

Wang, S., and Cao, L. (2020). Inferring implicit rules by learning explicit and hidden item dependency. *IEEE Trans. Syst. Man Cybern. Syst.* 50, 935–946. doi: 10.1109/TSMC.2017.2768547

Wei, R., Li, C., Fogelson, N., and Li, L. (2016). Prediction of conversion from mild cognitive impairment to Alzheimer's disease using MRI and structural network features. *Front. Aging Neurosci.* 8, 76. doi: 10.3389/fnagi.2016.00076

Yang, W., Lui, R. L. M., Gao, J.-H., Chan, T. F., Yau, S.-T., Sperling, R. A., et al. (2011). Independent component analysis-based classification of Alzheimer's disease MRI data. *J. Alzheimers Dis.* 24, 775–783. doi: 10.3233/JAD-2011-101371

Zeifman, L. E., Eddy, W. F., Lopez, O. L., Kuller, L. H., Raji, C., Thompson, P. M., et al. (2015). Voxel level survival analysis of grey matter volume and incident mild cognitive impairment or Alzheimer's disease. *J. Alzheimers Dis.* 46, 167–178. doi: 10.3233/JAD-150047

Zhan, Y., Chen, K., Wu, X., Zhang, D., Zhang, J., Yao, L., et al. (2015). Identification of conversion from normal elderly cognition to Alzheimer's disease using multimodal support vector machine. *J. Alzheimers Dis.* 47, 1057–1067. doi: 10.3233/JAD-142820

Zhang, B., Lin, L., and Wu, S. (2021a). A review of brain atrophy subtypes definition and analysis for Alzheimer's disease heterogeneity studies. *J. Alzheimers Dis.* 80, 1339–1352. doi: 10.3233/JAD-201274

Zhang, D., Wang, Y., Zhou, L., Yuan, H., and Shen, D. (2011). Multimodal classification of Alzheimer's disease and mild cognitive impairment. *Neuroimage* 55, 856–867. doi: 10.1016/j.neuroimage.2011.01.008

Zhang, Q., Cao, L., Shi, C., and Niu, Z. (2021b). "Neural time-aware sequential recommendation by jointly modeling preference dynamics and explicit feature couplings," in *IEEE Transactions on Neural Networks and Learning Systems,* 1–13. doi: 10.1109/TNNLS.2021.3069058

Zheng, W., Yao, Z., Li, Y., Zhang, Y., Hu, B., and Wu, D. (2019). Brain connectivity based prediction of Alzheimer's disease in patients with mild cognitive impairment based on multi-modal images. *Front. Hum. Neurosci.* 13, 399. doi: 10.3389/fnhum.2019.00399

Zuo, X. N., He, Y., Betzel, R. F., Colcombe, S., Sporns, O., and Milham, M. P. (2017). Human connectomics across the life span. *Trends Cogn. Sci.* 21, 32–45. doi: 10.1016/j.tics.2016.10.005

Conflict of Interest: The authors declare that the research was conducted in the absence of any commercial or financial relationships that could be construed as a potential conflict of interest.

frontiers | Frontiers in Neuroscience

ORIGINAL RESEARCH
published: 04 July 2022
doi: 10.3389/fnins.2022.900105

Right Frontal Theta: Is It a Response Biomarker for Ketamine's Therapeutic Action in Anxiety Disorders?

Shabah M. Shadli[1†‡], Robert G. Delany[1], Paul Glue[2†] and Neil McNaughton[1†]*

[1] Department of Psychology, University of Otago, Dunedin, New Zealand, [2] Department of Psychological Medicine, University of Otago, Dunedin, New Zealand

OPEN ACCESS

Edited by:
Jinglei Lv,
The University of Sydney, Australia

Reviewed by:
Bin Zhang,
Guangzhou Medical University, China
Sara De La Salle,
University of Ottawa, Canada

***Correspondence:**
Shabah M. Shadli
shabah.shadli@otago.ac.nz

†ORCID:
Shabah M. Shadli
orcid.org/0000-0002-3607-3469
Paul Glue
orcid.org/0000-0002-7305-2800
Neil McNaughton
orcid.org/0000-0003-4348-8221

‡Present address:
Shabah M. Shadli,
Brain-Behaviour Research Group,
School of Science and Technology,
University of New England, Armidale,
NSW, Australia

Specialty section:
This article was submitted to Brain Imaging Methods, a section of the journal Frontiers in Neuroscience

Received: 20 March 2022
Accepted: 15 June 2022
Published: 04 July 2022

Citation:
Shadli SM, Delany RG, Glue P and McNaughton N (2022) Right Frontal Theta: Is It a Response Biomarker for Ketamine's Therapeutic Action in Anxiety Disorders? Front. Neurosci. 16:900105. doi: 10.3389/fnins.2022.900105

Anxiety disorders are the most prevalent mental disorders in the world, creating huge economic burdens on health systems and impairing the quality of life for those affected. Recently, ketamine has emerged as an effective anxiolytic even in cases resistant to conventional treatments (TR); but its therapeutic mechanism is unknown. Previous data suggest that ketamine anxiety therapy is mediated by reduced right frontal electroencephalogram (EEG) theta power measured during relaxation. Here we test for a similar theta reduction between population-sample, presumed treatment-sensitive, (TS) anxiety patients and healthy controls. Patients with TS DSM-5 anxiety disorder and healthy controls provided EEG during 10 min of relaxation and completed anxiety-related questionnaires. Frontal delta, theta, alpha1, alpha2, beta, and gamma power, Higuchi's fractal dimension (HFD) and frontal alpha asymmetry (FAA) values were extracted to match ketamine testing; and we predicted that the controls would have less theta power at F4, relative to the TS anxious patients, and no differences in HFD or FAA. We provide graphical comparisons of our frontal band power patient-control differences with previously published post-pre ketamine TR differences. As predicted, theta power at F4 was significantly lower in controls than patients and FAA was not significantly different. However, HFD was unexpectedly reduced at lateral sites. Gamma power did not increase between controls and patients suggesting that the increased gamma produced by ketamine relates to dissociation rather than therapy. Although preliminary, and indirect, our results suggest that the anxiolytic action of ketamine is mediated through reduced right frontal theta power.

Keywords: anxiety disorders, ketamine, electroencephalography (EEG), theta frequency, response biomarker

INTRODUCTION

Anxiety disorders are the most prevalent psychiatric diseases in Europe and the United States (Kessler et al., 2005, 2012), the sixth highest in terms of disability (Baxter et al., 2014), and account for about 1/10 suicides (Baxter et al., 2014). They are a grave and ever-increasing burden on healthcare resources (Kessler, 2007; Cryan and Sweeney, 2011; Maron and Nutt, 2017). Most strikingly, anxiety disorders tend to start early in life (Cryan and Sweeney, 2011; Maron and Nutt, 2017) and often result in chronic impairment (Meyer, 2017). In Europe, work days lost because of anxiety are higher than somatic disorders like diabetes (Bandelow and Michaelis, 2015). Across 36 large countries, anxiety and depression are expected to cost 12 billion days every year in lost

productivity equivalent to a loss of US$925B (Chisholm et al., 2016). A 1996 survey estimated the cost of anxiety disorders at US$47B in the USA (DuPont et al., 1996; Kessler and Greenberg, 2002). But costs increase every year and, in 2004, the cost for anxiety disorder in Europe was estimated at €41B (Bandelow and Michaelis, 2015) while in 2010, the estimated cost jumped nearly 5-fold to €200B (Olesen et al., 2012; Kalisch et al., 2017). The COVID-19 pandemic significantly increased the number of people diagnosed with anxiety disorders, with recent statistics showing ∼35% of the total population in western societies currently affected (Kowalczyk et al., 2021).

Key problems are that first-line conventional anti-anxiety drugs (which are often also antidepressant) take a long time to act on both anxiety (Bystritsky, 2006; Bandelow et al., 2008) and depression (Muller et al., 2016), improve symptoms for only an unpredictable subset of patients, and fail completely for both anxiety and depression in about 1/3rd of patients (Nemeroff, 2007; Muller et al., 2016). Only some patients respond to the first drug they try, and some do not show any improvement even after trials with multiple drugs (Bystritsky, 2006; Aan Het Rot et al., 2012). First line anxiolytic treatments produce remission in 25–35% and response in 50–60% (Roy-Byrne, 2015), so treatment resistance (TR) is common (Roy-Byrne, 2015; Van Ameringen et al., 2017) and "30–60% of patients have substantial and impairing remaining symptoms" (Bokma et al., 2019). Benzodiazepines are more specific to anxiety (Roy-Byrne, 2015) but have similar TR problems (Cryan and Sweeney, 2011).

Hope is raised by ketamine. A single sub-anesthetic dose of ketamine produces a clear therapeutic response in TR depression within a few hours of administration, which lasts for about a week (Aan Het Rot et al., 2012; Lai et al., 2014; Duman, 2018)—improving mood (Zarate C. A. et al., 2013), reducing suicidal ideation (Duman, 2018), and preventing loss of life (DiazGranados et al., 2010). Previously, we reported that low dose ketamine is also effective in TR anxiety disorder—both generalized (GAD) and social (SAD) (Glue et al., 2017). Ketamine is also effective in OCD (Rodriguez et al., 2013), and PTSD (Feder et al., 2014). Thus, most TR neurotic disorders may respond to ketamine (McNaughton and Glue, 2020).

Unfortunately, we do not know the neural basis for the therapeutic effects of ketamine. Ketamine is most obviously a high potency N-methyl-D-aspartate non-competitive glutamatergic antagonist (Zarate et al., 2006; Aan Het Rot et al., 2012; Murrough et al., 2015; Duman, 2018); but, other NMDA antagonists have not achieved: (1) rapid antidepressant onset; (2) robust efficacy; (3) and sustained efficacy with a single administration (Zarate and Machado-Vieira, 2017). We also recently found no relation between the improvement of anxiety symptoms in TR GAD/SAD and the levels of the ketamine and its metabolites norketmaine (Glue et al., 2019).

However, there are other clues to the basis of ketamine's therapeutic action. We recently (Shadli et al., 2018) reported effects on relaxation EEG in patients with TR GAD/SAD during ketamine therapy. Ketamine increased high frequency EEG power, and decreased low frequency power. Interestingly, *only the decrease in theta frequency band power at the right frontal site F4* significantly correlated with the rapid changes in anxiety measured by the Fear Questionnaire. These new patient findings appear to fit with earlier preclinical and human data that link anxiolytic action (Shadli et al., 2015) and anxiety disorder (Shadli et al., 2021) to changes in *task-elicited* (as opposed to relaxation) right-frontal theta-band EEG.

The aim of the present study was to assess whether the reported *relaxation* EEG effects of ketamine (Shadli et al., 2018) that correlated with its alleviation of anxiety disorder, match relaxation EEG differences between non-anxious participants and conventional anxiety disorder patients. Shadli et al. (2018), used a variety of other EEG measures to analyze ketamine's effects. These measures were chosen by them because "in depressed patients, ketamine specifically increases slow wave activity during sleep, especially in those with low baseline slow waves, and this may mediate its antidepressant effects (see Duncan and Zarate, 2013). In healthy participants, it can reduce delta (1–3 Hz), theta (4–7 Hz) and alpha (8–15 Hz) band power, while increasing gamma (> 32 Hz) band power (Hong et al., 2010; de la Salle et al., 2016). But it can also increase theta power while decreasing alpha power (Domino et al., 1965; Schűttler et al., 1987; Kochs et al., 1996), particularly at frontal sites (Muthukumaraswamy et al., 2015); *so changes in bands can be interleaved*, with decreased delta, alpha and beta (16–31 Hz) mixed with increased theta and gamma (Muthukumaraswamy et al., 2015; Rivolta et al., 2015). . . . [So] we assessed EEG by quantitation of power in specific frequency bands and by measures that show depression-related changes: frontal alpha asymmetry (FAA; Allen et al., 2004; Stewart et al., 2014; Mennella et al., 2017) and increased Higuchi's fractal dimension (HFD; Higuchi, 1988; Bachmann et al., 2013; Akar et al., 2015)."

Shadli et al. (2018) found no relation between therapeutic action and other power measures, FAA or HFD (Higuchi, 1988). Only F4 theta changes were related to therapeutic effect. Here, we hypothesized that healthy controls will have lower power in the theta band at the F4 channel than the anxiety disorder patients (but did not exclude other power changes). We also hypothesized that anxiety disorder patients and controls would not differ on FAA or HFD scores.

MATERIALS AND METHODS

There were 34 (26 female, 8 male) healthy and 47 (39 female, 8 male) patient participants recruited through online advertisements on a local newspaper site, Facebook, and advertisements in supermarkets. Healthy participants reported no major illness in the past month, were not prescribed any psychoactive medication in the previous 6 months, and had not consumed alcohol in the 24 h prior to participating in the study. The patient group consisted of individuals who reported experiencing chronic symptoms of anxiety or fear, but were not receiving any pharmacological treatments at the time of recruitment. Participants were also excluded from this study if they had any history of substance abuse or other neurological disorders. All patients (29 GAD, 10 SAD, and 8 PTSD) went through the Mini International Neuropsychiatric Interview (MINI) diagnostic examination by a clinical psychologist in

a separate session before having their electroencephalogram (EEG) recorded. Similar to the control group, these participants were otherwise healthy. They reported no significant illness in the past month, no use of psychoactive medications in the previous 6 months, and no consumption of alcohol in the 24 h before the experiment. All participants received petrol vouchers ($30) in compensation for their time and travel costs. The study was approved by the University of Otago Ethics Committee (Health: H15/005), and all participants provided written informed consent.

Questionnaires and Demographics

To avoid questionnaire fatigue, the questionnaires were administered in two sets. The first set of questionnaires was administered before EEG recording: the Spielberger State-Trait Anxiety Inventory form-Y (Spielberger et al., 1983); the Eysenck Personality Questionnaire-Revised (EPQ-R; Eysenck and Eysenck, 1991); and the BIS scale items from the Behavioral Activation System/Behavioral Inhibition System questionnaire (Carver and White, 1994). The second set was administered after the EEG recording, and contained a subset of scales from the Personality Inventory of the DSM-5 (PID-5) (Anderson et al., 2013). **Table 1** represents the demographic details of patients and healthy volunteers.

Electroencephalogram Recording

EEG data were recorded using a 32-channel Waveguard EEG cap (ANT Neurotechnology, Netherlands). The electrodes on the cap were arranged in accordance with to the 10–20 electrode placement system. EEG was recorded, sampled at 512 Hz, from 32 channels: Fp1, Fpz, Fp2, F7, F3, Fz, F4, F8, FC5, FC1, FC2, FC6, T7, C3, Cz, C4, T8, CP5, CP1, CP6, CP2, P7, P3, Pz, P4, P8, POz, Oz, O1, O2, M1 and M2 with CPz used as recording reference. Only the frontal electrodes F7, F3, Fz, F4, and F8 were analyzed to compare with our previous ketamine findings. The EEG was re-referenced to the average of M1 + M2 for analysis. Electro-gel (Electro Cap International, United States) was injected into all electrodes using a 3 ml syringe and a Precision Glide 16-gauge blunt needle (Becton, Dickenson & Co., New Jersey, United States). Impedance was brought down to below 20 KΩ for every electrode. 10 min of Resting EEG data were recorded in 1-min blocks of eyes open (EO) or eyes closed (EC) in the following sequence: EO, EC, EO, EC, EO, EC, EO, EC, EO, EC.

Data Processing and Analysis

Primary Pre-processing

We used the same EEG post-processing as our previous experiment (Shadli et al., 2018). EEG data and associated event markers were imported to the EEGLAB toolbox for MATLAB. Raw data were first down sampled to 128 Hz then a 1–63 Hz bandpass filter was applied. 50 Hz noise was removed using Cleanline (Bigdely-Shamlo et al., 2015). Data sets were epoched as 1 s (128 samples) non-overlapping epochs for automatic artifact rejection. Epoched data sets were visually inspected for gross artifacts and removed from the dataset and boundary markers were inserted to mark their previous locations. Independent component analysis (ICA) was subsequently applied to the remaining epoched data. ADJUST 1.1 (Mognon et al., 2011) was used to analyze the ICA results and remove artifact components to leave "clean" EEG. Artifact-free datasets were subsequently converted from epoched to continuous. Similar to our previous experiment (Shadli et al., 2018), we analyzed FAA and HFD.

Spectral Analysis

Artifact free datasets were re-epoched to 2 s, 50% overlapping, epochs with a Hanning window. A fast Fourier transform was applied, and the power spectrum was $\log_{10}$ transformed to normalize error variance. The resultant epochs were averaged to provide a single power spectrum for each participant, at each channel, and frequency values were averaged in bands defined as delta (1–3 Hz), theta (4–6 Hz), alpha1 (7–9 Hz), alpha2 (10–12 Hz), beta (25–34 Hz), and gamma (41–53 Hz) as previously (Shadli et al., 2018). FAA was calculated for 7–12 Hz by subtracting logarithmic power at left electrodes from their right-most counterparts [(ln (R)–ln (L)] for each of F8:F7 and F4:F3. This was for the purpose of directly comparing to the FAA results of Shadli et al. (2018).

"Fractal dimension was calculated using Higuchi's algorithm with a kmax of 8 (Higuchi, 1988). After the eye-blink removal stage, the data were subjected to an additional 2–36-Hz bandpass filter, and sections with artefacts were manually removed. The continuous data were then split into 2-s (256 sample) epochs with 50% overlap. Higuchi's algorithm creates kmax number of new time series (with k running from 1 to kmax), each obtained by taking every kth sample of the original epoch. The length of the curve of each series is calculated and plotted against k on a double logarithmic graph. If the length of the curve and k are proportional, then the plotted data will fall on a straight line. The slope of this line is the fractal dimension." (Shadli et al., 2018, p. 719).

Statistical Analysis

Statistical analysis was carried out with IBM SPSS (version 24). Mixed measures ANOVAs with group (patients, controls) as a between-subjects factor were carried out on each of band power, FAA, and HFD. For band power, channel (F7, F3, Fz, F4, and F8), and band (delta, theta, alpha1, alpha1, beta and gamma) were repeated measures with orthogonal polynomial components of channel and band automatically extracted by SPSS. For each band, log power values at each frequency were averaged to a single value prior to ANOVA. HFD was analyzed similarly except for there being no band factor. For FAA, asymmetry was calculated separately for the F7:F8 pair and the F3:F4 pair, and the two values treated as levels of a repeated measures factor "electrode pair." Significant effects were further explored where necessary with *post-hoc t*-tests.

RESULTS

Patient vs. Control Overview

Figure 1A displays the separate patient group and control group band power values across frontal channels (F7, F3, Fz, F4, and F8). Patients had largely similar power across channels. As band

frequency increased, power decreased, with delta expressing the highest power and gamma the lowest. Theta, alpha1 and alpha2 power were all approximately equal across all channels. Control band frequency is also inversely proportional to power, with higher frequency bands displaying lower power values. However, controls displayed an inverted-U distribution of power across channels, with power in the central channel (Fz) lower than in lateral channels (F7, F8).

Anxiety Effect

To allow a clearer picture of the role of anxiety, the patient-control *difference* is plotted in **Figure 1B** and shows the 3D relationship between frontal channel position and band frequency. The same data are plotted, overlayed, in **Figure 1C** to allow direct numerical comparison of the power bands and shows that in anxiety patients power increased at the midline (Fz), relative to control patients across *all* frequency bands. In the lateral channels (F7, F8), the difference between control and anxiety patient power was minimal and usually a decrease. Thus, the effect of anxiety on band power produced an inverted U-shape curve that varied in size, systematically (**Figures 1C,D**). This change was largely a progressive decrease from delta through gamma [group × band[***lin***] × left-right[quad], $F(1, 79) = 10.021$, $p = 0.002$] but with a marginal inflection with lower values either side of alpha [group × band[***quad***] × left-right[quad], $F(1, 79) = 3.573$, $p = 0.062$]. The linear and quadratic frequency trends of the inverted-U variation in the anxiety effect can be seen in a simplified form by plotting

TABLE 1 | shows the mean and *SD* for age, STAI-T (T), EPQ Neuroticism (N), PID-5 anxiety (Ax), anhedonia (Ah), and depression (D) scores for each of patients and healthy controls.

	Age		T		N		Ax		Ah		D	
Patients	33.3	*10.5*	53.1	*10.6*	14.5	*5.5*	28.4	*5.7*	17.1	*4.7*	29.6	*9.1*
Controls	31.0	*6.4*	36.3	*4.7*	4.6	*5.8*	16.6	*8.4*	12.8	*5.6*	20.5	*9.4*

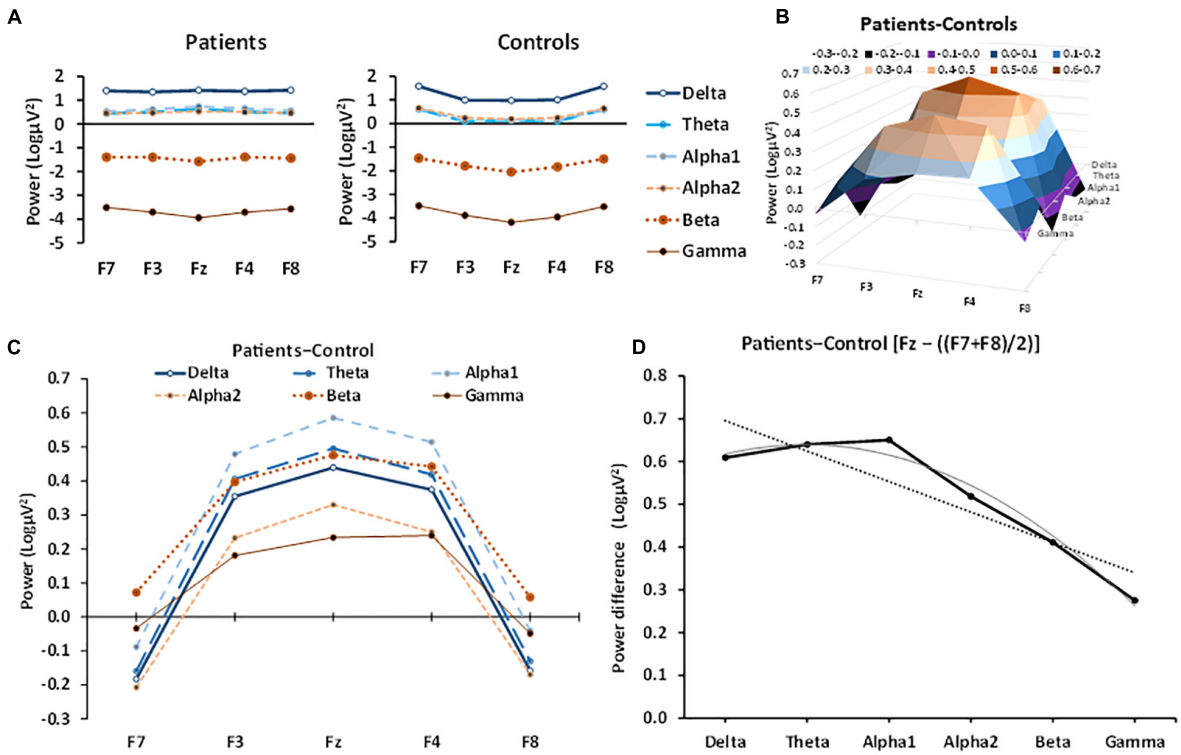

FIGURE 1 | Patient and control EEG power in the different bands across frontal channels. **(A)** Patient power curves are relatively flat across each channel for most bands with the possible exception of gamma, while control power curves generally have an inverted U-shape. **(B)** 3D representation of the effect of anxiety (patient-control power difference) in different bands at frontal-central electrodes, showing the systematic left-right channel × band frequency variation, detected statistically by a significant channel[quadratic] × frequency[linear] interaction. **(C)** The same data as in **B** but with different bands plotted against channel as overlapping curves to allow numerical comparison (frequency of the band is coded by line thickness). The anxiety effect for each band was an inverted-U function of channel; that is, the strongest difference in power was in the central channel, with minimal anxiety effects in the lateral channels. **(D)** Linear trend and quadratic trend of band frequency fitted to power values for Fz minus the average of F7 + F8 (which approximates the quadratic trend across channel). There is a significant decrease in this component from delta to gamma (the dotted line shows the significant linear trend). There appears to be some non-linearity, with an apparent peak at alpha1. The curved line shows the combination of the linear trend with the apparent slight, non-significant ($p = 6\%$), quadratic trend.

power for Fz minus the average power of F7 and F8 as a proxy for the quadratic trend of channel (**Figure 1D**). There is a predominantly linear fall off with frequency in the average anxiety effect (dotted straight line) except that the effect for delta is below what would be expected for a purely linear effect (solid gray linear + quadratic curve).

Frontal Band Power—Qualitative Comparison With Ketamine

Figure 2 compares the current "anxiolytic" effects on frontal channel band power (**Figure 2A**) with those obtained with various doses of ketamine (**Figure 2B**, adapted from Shadli et al., 2018). Patient power values were subtracted from control power values to mimic ketamine's anxiolytic effect (i.e., the opposite of the subtraction in **Figure 1**) matching the post–pre subtraction used by Shadli et al. (2018).

Figure 2A shows that control—anxiety patient power differences were distributed from F7 to F8 in a U-shaped curve, with the effect at lateral channels being close to zero. However, non-anxious power at more central channels was reduced compared to anxious patients. Across the central channels, alpha1 power showed the largest decrease and gamma expressed the highest increase.

Figure 2B shows the published effects of varying doses of post-ketamine administration relative to pre-ketamine administration (post-pre difference) in power across frontal channels. The post—pre effects increased steadily with dose across all channels: unlike **Figure 2A**, high frequency power increased (with beta and, particularly, gamma); while, like **Figure 2A**, low frequency power decreased (delta, theta, alpha1 and alpha2). So, in general, the effects of ketamine are opposite to the control-patient difference at high frequencies but similar at low frequencies.

Higuchi's Fractal Dimension and Frontal Alpha Asymmetry Comparison

Figure 3A displays the anxiety *reduction* effect (controls–patients) on HFD and compares this to the post-pre ketamine HFD scores of Shadli et al. (2018). There was a clear inverted-U difference between controls and patients with the lateral channels showing larger negative values [group × channel[quad], $F(1, 79) = 6.680$, $p = 0.012$]. There was little difference in HFD at Fz [$t(79) = 0.534$, NS]. There were no significant differences in HFD reported by Shadli et al. (2018). Further, K0.50 produced the highest decrease in Fear Questionnaire scores but minimal change in HFD. The non-significant quadratic trends with K0.25 and K1.00 are in the opposite direction to the current results.

FAA, averaged across electrode pair and group, was not significantly different from zero [intercept, $F(1, 79) = 1.181$, $p = 0.281$]. **Figure 3B** shows the FAA control-patient differences. FAA, averaged across electrode pair, did not differ between

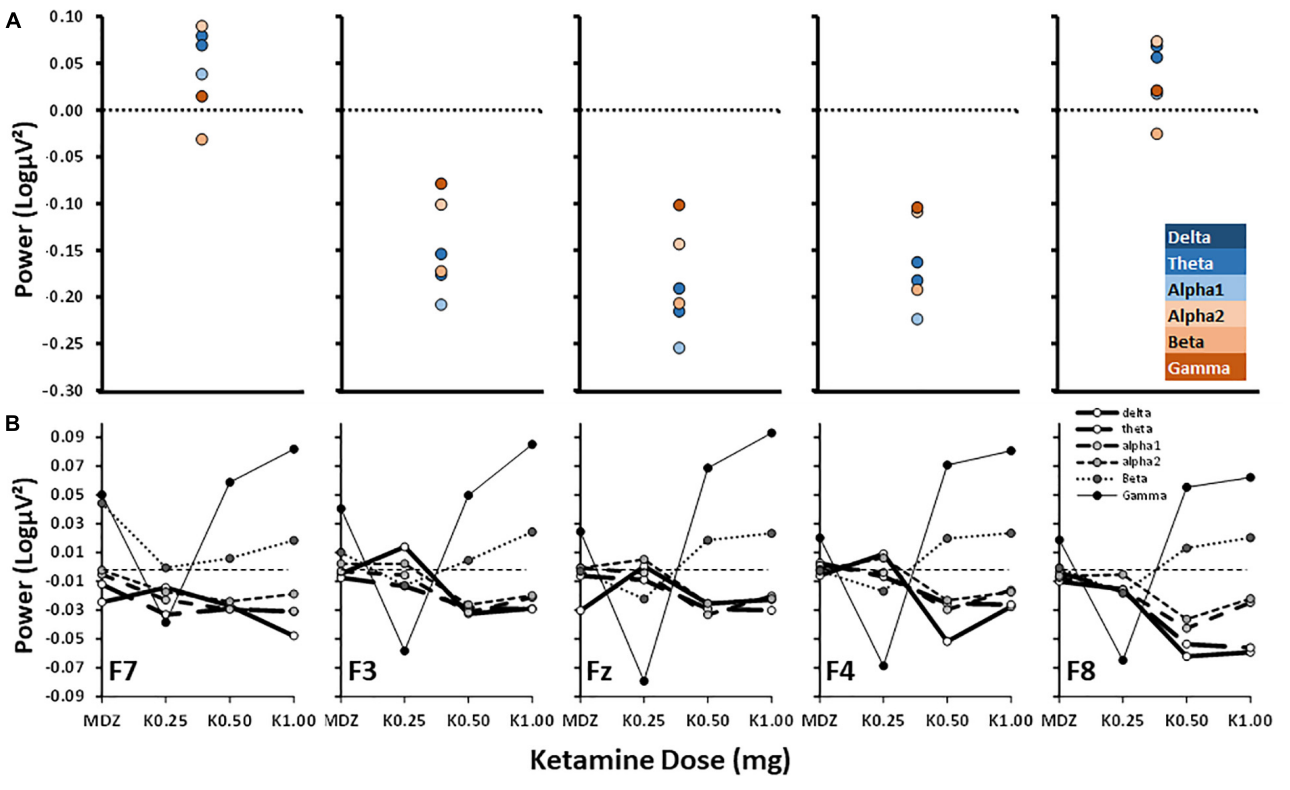

FIGURE 2 | Power difference scores for control–patient and post–pre ketamine across bands and frontal channels. **(A)** Control–patient power is as in **Figure 1C** but with the direction of subtraction reversed and graphs plotted to match the published results shown below in **(B)**. **(B)** Post–pre dose effect of ketamine from Shadli et al. (2018) with permission of the authors. MDZ = midazolam (active control); K0.25, etc., doses of ketamine in mg. Note power scale differences.

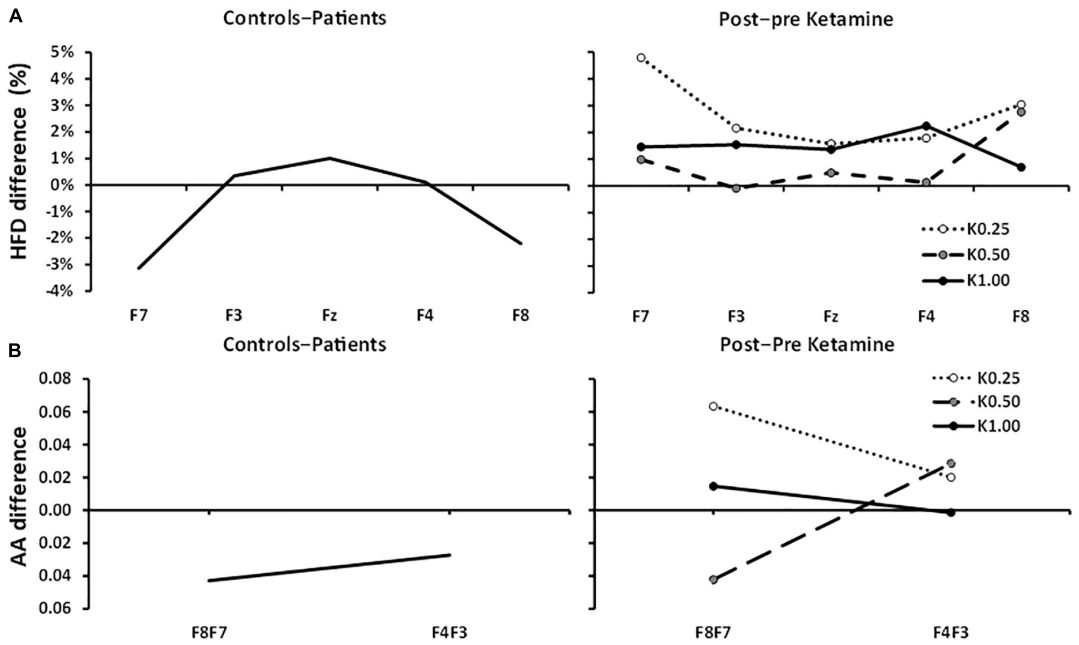

FIGURE 3 | Controls–patients and post–pre ketamine HFD and AA differences across frontal channels. **(A)** HFD: Controls–patients displays a significant U-shaped relationship between HFD change and frontal channels. 0.25, 0.5, and 1.0 mg/kg of ketamine produced no significant HFD effects and any trend is in the opposite direction. **(B)** Controls–Patients FAA differences were not significant at F8:F7 and F4:F3 pairs. Post–pre ketamine FAA was not significantly different across 0.25, 0.50, and 1.00 mg/kg doses at F8:F7 and F4:F3 pairs.

controls and patients [group, $F(1, 79) = 1.682$, $p = 0.198$] and showed no differences between the electrode pairs in the control-patient differences [electrode pair × group, $F(1, 79) = 0.150$, $p = 0.700$].

DISCUSSION

Overview of Findings

Our primary finding, *using identical procedures to our previous work with ketamine*, was that patients diagnosed with GAD, SAD, SP, and PTSD showed increases in frontal relaxation EEG rhythmicity compared to the controls. There was no anxiety effect at the lateral channels but anxiety was associated with significantly higher power centrally, across all frequency bands. These data are consistent with earlier findings with panic disorder patients compared to healthy controls (Wise et al., 2011). At Fz, power difference was generally inversely proportional to frequency, with a modest peak in the alpha range. As predicted, AA was unaffected and, while there was a significant effect on HFD at lateral channels, this was in the opposite direction to the non-significant trends in the ketamine data.

Comparison With Ketamine Study

Theta Reduction at F4

Our primary predicted finding was that control theta power decreased at F4 relative to the patients. Both here, and in Shadli et al. (2018), theta reduced at several frontal channels with reduced anxiety. However, only F4 theta reduction predicted anxiety symptom improvements with ketamine as measured by the Fear Questionnaire. Our F4 result, therefore, supports the notion that the anxiolytic action of ketamine might be mediated through reduced theta power in the F4 channel.

We also found stronger theta at Fz in patients relative to healthy controls and no differences at the lateral channels (F7 and F8)—consistent with a recent review concluding that midline theta is an important index of psychiatric illness (McLoughlin et al., 2022). Frontal midline theta is a distinct rhythm recorded at Fz above the midcingulate cortex (Mitchell et al., 2008). It lasts a few seconds during arithmetic mental tasks, such as addition in the N-back working memory task; and has since been associated with anxiety-like behavior. However, there are several forms of such theta rhythmicity. Administration of anxiolytic drugs, including benzodiazepines and buspirone, *increase* frontal-midline theta power in the Uchida-Kraepelin task with associated decreases in STAI (anxiety) scores (for review see Mitchell et al., 2008).

The apparent specificity of the involvement of F4 is unexpected. The changes linked to psychiatric disorder in right frontal theta (Shadli et al., 2018) and in the distinct midfrontal theta (Mitchell et al., 2008; McLoughlin et al., 2022) appear more widespread—consistent with our present results. However, source separation has demonstrated multiple midfrontal thetas (Zuure et al., 2020) and these appear involved a range of types of cognitive control (Cavanagh and Frank, 2014). It is likely, then, that ketamine's wide-ranging effects (both across brain sites and across frequency bands) are the result of impact on multiple mechanisms, the bulk of which reflect longer-term consequences

of anxiety (e.g., changes in theta) or immediate side-effects (e.g., changes in gamma, see below). The F4 effect, then, would be related to a specific mechanism that, rather than being a consequence, is causally related to the generation or maintenance of anxiety. Much further work would be needed to determine if this is the case.

The mechanisms of action of ketamine on psychiatric disorders in general and anxiety and F4 theta in particular are unclear. As noted in the introduction, its therapeutic effect is not *via* its known NMDA receptor effects (Zarate et al., 2006; Aan Het Rot et al., 2012; Murrough et al., 2015; Zarate and Machado-Vieira, 2017; Duman, 2018) nor linked to its metabolites (Glue et al., 2019). Given its wide-ranging effects on brain activity, most of which appear causally unrelated to anxiety it will be hard to uncover its primary therapeutic mechanisms. Its effects on theta rhythmicity (Engin et al., 2009) in a well-validated rat electrophysiology model of anxiolytic action (McNaughton et al., 2007) could provide a guide to its anxiolytic action. Whether its antidepressant actions are related to theta (or F4) remains to be determined but, given the nature of the drugs detected by the rat model, is unlikely.

Gamma Band Changes

With ketamine (Shadli et al., 2018), gamma power across frontal channels (including F4) increased. In contrast, gamma power at F4 in control participants relative to anxiety disorder patients decreased. This implies that the increase in gamma power after ketamine administration is unrelated to its anxiolytic action. At the doses used in our previous studies of anxiety reduction, ketamine produces strong dissociative effects (Glue et al., 2019), which include euphoria and hallucinations. Since these are not symptoms of anxiety it suggests that an increase in gamma power is associated with the hallucinatory effects of ketamine. Gamma frequency has previously been linked to NMDA antagonism. Blockade of the NMDA receptors in rat neocortex *in vivo* has led to dose-dependent increase in gamma power (Pinault, 2008). Administration of NMDA receptor antagonists, such as ketamine, have also induced hallucinations in healthy participants (Krystal et al., 1994; Lahti et al., 1995). These studies imply that the dissociative effects of ketamine result from its NMDA antagonist properties, causing an increase in gamma band power.

Higuchi's Fractal Dimension Changes

Shadli et al. (2018) found no significant HFD differences between pre- and post-ketamine administration at any dosage. In contrary, we found significant differences in HFD at the lateral channels (F7 and F8) between anxiety patients and controls, consistent with our earlier findings (Kawe et al., 2019). These results suggest that a shift from an anxious to a non-anxious state is related to a reduction in HFD at the lateral channels, corresponding to left and right prefrontal sites. Note that the direction of change here is the opposite of the non-significant trend differences with ketamine. The HFD differences, here, are also at lateral sites whereas the theta power differences are not.

Alpha Asymmetry Differences

No significant difference was observed in FAA between anxiety disorder patients and controls—consistent with our hypothesis that no difference in FAA would be observed between anxiety patients and controls. Shadli et al. (2018) found no significant difference between pre-ketamine and post-ketamine treatment on FAA at any dose.

Overview of Findings and Limitations

There is an urgent need to uncover the causes of anxiety disorders to reduce the global crisis, which is being worsened by the COVID-19 pandemic. Ketamine and similar fast acting drugs could be a game changer in the treatment of anxiety disorders. However, ketamine is currently an off-label drug because of its abuse potential, and strong dissociative and hallucination effects, limiting its use out of the clinic. Continuous efforts are needed to better understand its mechanism of action, which will provide for development of similar drugs with reduced side effects. Given our low sample size, our findings need to be approached with considerable caution. Future studies should have larger sample sizes of both anxious and healthy volunteers and more direct comparison of ketamine affects with natural anxiety differences. Further our method is comparative and while consistent with our hypothesis and strengthening our previous conclusions about ketamine, cannot be taken as proof. That said, our *right frontal theta (F4)* or the quite distinct frontal-central (Fz) theta should provide guidance toward better understanding of the mechanism of action of ketamine in anxiety disorders.

DATA AVAILABILITY STATEMENT

The raw data supporting the conclusions of this article will be made available by the authors, on reasonable request, without undue reservation.

ETHICS STATEMENT

The studies involving human participants were reviewed and approved by the University of Otago Human Ethics Committee. The patients/participants provided their written informed consent to participate in this study.

AUTHOR CONTRIBUTIONS

SS and NM developed the research idea. SS and RD collected and processed the data. PG screened and consented patient volunteers. SS wrote up the initial draft. NM and PG revised the manuscript. All authors contributed to the article and approved the submitted version.

FUNDING

This work was supported by the Health Research Council of New Zealand (grant nos. 14/129, 19/027, and 20/112), who had no involvement in the study design, data collection, analysis, interpretation, or writing that went toward this report.

REFERENCES

Aan Het Rot, M., Zarate, C. A. Jr., Charney, D. S., and Mathew, S. J. (2012). Ketamine for depression: where do we go from here? *Biol. Psychiatry* 72, 537–547. doi: 10.1016/j.biopsych.2012.05.003

Akar, A. S., Kara, S., Agambayev, S., and Bilgic, V. (2015). Nonlinear analysis of EEGs of patients with major depression during different emotional states. *Comput. Biol. Med.* 67, 49–60. doi: 10.1016/j.compbiomed.2015.09.019

Allen, J. J., Urry, H. L., Hitt, S. K., and Coan, J. A. (2004). The stability of resting frontal electroencephalographic asymmetry in depression. *Psychophysiology* 41, 269–280. doi: 10.1111/j.1469-8986.2003.00149.x

Anderson, J. L., Sellbom, M., Bagby, R. M., Quilty, L. C., Veltri, C. O., Markon, K. E., et al. (2013). On the convergence between PSY-5 domains and PID-5 domains and facets: implications for assessment of DSM-5 personality traits. *Assessment* 20, 286–294. doi: 10.1177/1073191112471141

Bachmann, M., Lass, J., Suhhova, A., and Hinrikus, H. (2013). Spectral asymmetry and Higuchi's fractal dimension measures of depression electroencephalogram. *Comput. Math. Methods Med.* 2013:251638. doi: 10.1155/2013/251638

Bandelow, B., and Michaelis, S. (2015). Epidemiology of anxiety disorders in the 21st century. *Dialogues Clin. Neurosci.* 17, 327–335.

Bandelow, B., Zohar, J., Hollander, E., Kasper, S., Moller, H. J., Post-Traumatic Stress, et al. (2008). World Federation of Societies of Biological Psychiatry (WFSBP) guidelines for the pharmacological treatment of anxiety, obsessive-compulsive and post-traumatic stress disorders – first revision. *World J. Biol. Psychiatry* 9, 248–312. doi: 10.1080/15622970802465807

Baxter, A. J., Vos, T., Scott, K. M., Ferrari, A. J., and Whiteford, H. A. (2014). The global burden of anxiety disorders in 2010. *Psychol. Med.* 44, 2363–2374. doi: 10.1017/S0033291713003243

Bigdely-Shamlo, N., Mullen, T., Kothe, C., Su, K.-M., and Robbins, K. A. (2015). The PREP pipeline: standardized preprocessing for large-scale EEG analysis. *Front. Neuroinform.* 9:16. doi: 10.3389/fninf.2015.00016

Bokma, W. A., Wetzer, G., Gehrels, J. B., Penninx, B., Batelaan, N. M., and van Balkom, A. (2019). Aligning the many definitions of treatment resistance in anxiety disorders: a systematic review. *Depress. Anxiety* 36, 801–812. doi: 10.1002/da.22895

Bystritsky, A. (2006). Treatment-resistant anxiety disorders. *Mol. Psychiatry* 11, 805–814. doi: 10.1038/sj.mp.4001852

Carver, C. S., and White, T. L. (1994). Behavioral inhibition, behavioral activation, and affective responses to impending reward and punishment: the BIS/BAS scales. *J. Pers. Soc. Psychol.* 67, 319–333.

Cavanagh, J. F., and Frank, M. J. (2014). Frontal theta as a mechanism for cognitive control. *Trends Cogn. Sci.* 18, 414–421. doi: 10.1016/j.tics.2014.04.012

Chisholm, D., Sweeny, K., Sheehan, P., Rasmussen, B., Smit, F., Cuijpers, P., et al. (2016). Scaling-up treatment of depression and anxiety: a global return on investment analysis. *Lancet Psychiatry* 3, 415–424. doi: 10.1016/s2215-0366(16)30024-4

Cryan, J. F., and Sweeney, F. F. (2011). The age of anxiety: role of animal models of anxiolytic action in drug discovery. *Br. J. Pharmacol.* 164, 1129–1161. doi: 10.1111/bph.2011.164.issue-4

de la Salle, S., Choueiry, J., Shah, D., Bowers, H., McIntosh, J., Ilivitsky, V., et al. (2016). Effects of ketamine on resting-state EEG activity and their relationship to perceptual/dissociative symptoms in healthy humans. *Front. Pharmacol.* 7:348. doi: 10.3389/fphar.2016.00348

DiazGranados, N., Ibrahim, L. A., Brutsche, N. E., Ameli, R., Henter, I. D., Luckenbaugh, D. A., et al. (2010). Rapid resolution of suicidal ideation after a single infusion of an N-methyl-D-aspartate antagonist in patients with treatment-resistant major depressive disorder. *J. Clin. Psychiatry* 71, 1605–1611. doi: 10.4088/JCP.09m05327blu

Domino, E. F., Chodoff, P., and Corssen, G. (1965). Pharmacologic effects of CI-581, a new dissociative anesthetic, in man. *Clin. Pharmacol. Ther.* 6, 279–291. doi: 10.1002/cpt196563279

Duman, R. S. (2018). Ketamine and rapid-acting antidepressants: a new era in the battle against depression and suicide. *F1000 Res.* 7:e659. doi: 10.12688/f1000research.14344.1

Duncan, W. C. Jr., and Zarate, C. A. Jr. (2013). Ketamine, sleep, and depression: current status and new questions. *Curr. Psychiatry Rep.* 15:394. doi: 10.1007/s11920-013-0394-z

DuPont, R. L., Rice, D. P., Miller, L. S., Shiraki, S. S., Rowland, C. R., and Hanvood, H. J. (1996). Economic cost of anxiety disorder. *Anxiety* 2, 167–172.

Eysenck, H. J., and Eysenck, S. B. G. (1991). *ADULT EPQ-R.* London: Hodder Education.

Engin, E., Treit, D., and Dickson, C. T. (2009). Anxiolytic- and antidepressant-like properties of ketamine in behavioral and neurophysiological animal models. *Neuroscience* 161, 359–369. doi: 10.1016/j.neuroscience.2009.03.038

Feder, A., Parides, M. K., Murrough, J. W., Perez, A. M., Morgan, J. E., Saxena, S., et al. (2014). Efficacy of intravenous ketamine for treatment of chronic posttraumatic stress disorder: a randomized clinical trial. *JAMA Psychiatry* 71, 681–688. doi: 10.1001/jamapsychiatry.2014.62

Glue, P., Medlicott, N. J., Harland, S., Neehoff, S., Anderson-Fahey, B., Le Nedelec, M., et al. (2017). Ketamine's dose-related effects on anxiety symptoms in patients with treatment refractory anxiety disorders. *J. Psychopharmacol.* 31, 1302–1305. doi: 10.1177/0269881117705089

Glue, P., Neehoff, S., Sabadel, A., Broughton, L., Le Nedelec, M., Shadli, S., et al. (2019). Effects of ketamine in patients with treatment-refractory generalized anxiety and social anxiety disorders: exploratory double-blind psychoactive-controlled replication study. *J. Psychopharmacol.* 34, 267–272. doi: 10.1177/0269881119874457

Higuchi, T. (1988). Approach to an irregular time series on the basis of the fractal theory. *Phys. D* 31, 277–283.

Hong, L. E., Summerfelt, A., Buchanan, R. W., O'Donnell, P., Thaker, G. K., Weiler, M. A., et al. (2010). Gamma and delta neural oscillations and association with clinical symptoms under subanesthetic ketamine. *Neuropsychopharmacology* 35, 632–640. doi: 10.1038/npp.2009.168

Kalisch, R., Baker, D. G., Basten, U., Boks, M. P., Bonanno, G. A., Brummelman, E., et al. (2017). The resilience framework as a strategy to combat stress-related disorders. *Nat. Hum. Behav.* 1, 784–790. doi: 10.1038/s41562-017-0200-8

Kawe, T. N. J., Shadli, S. M., and McNaughton, N. (2019). Higuchi's fractal dimension, but not frontal or posterior alpha asymmetry, predicts PID-5 anxiousness more than depressivity. *Sci. Rep.* 9:19666. doi: 10.1038/s41598-019-56229-w

Kessler, R. C. (2007). The global burden of anxiety and mood disorders: putting ESEMeD findings into perspective. *J. Clin. Psychiatry* 68, 10–19.

Kessler, R. C., and Greenberg, P. E. (2002). "The economic burden of anxiety and stress disorders," in *Neuropsychopharmacology: The Fifth Generation of Progress*, eds D. C. Kenneth, L. Davis, J. T. Coyle, and C. Nemeroff (Baltimore, MD: American College of Neuropsychopharmacology).

Kessler, R. C., Chiu, W. T., Demler, O., Merikangas, K. R., and Walters, E. E. (2005). Prevalence, severity, and comorbidity of 12-month DSM-IV disorders in the National Comorbidity Survey Replication. *Arch. Gen. Psychiatry* 62, 617–627. doi: 10.1001/archpsyc.62.6.617

Kessler, R. C., Petukhova, M., Sampson, N. A., Zaslavsky, A. M., and Wittchen, H. U. (2012). Twelve-month and lifetime prevalence and lifetime morbid risk of anxiety and mood disorders in the United States. *Int. J. Methods Psychiatr. Res.* 21, 169–184. doi: 10.1002/mpr.1359

Kochs, E., Scharein, E., Möllenberg, O., Bromm, B., and Schulte am Esch, J. (1996). Analgesic efficacy of low-dose ketamine. *Anesthesiology* 85, 304–314.

Kowalczyk, M., Kowalczyk, E., Kwiatkowski, P., Lopusiewicz, L., Sienkiewicz, M., and Talarowska, M. (2021). Ketamine-new possibilities in the treatment of depression: a narrative review. *Life* 11:1186. doi: 10.3390/life11111186

Krystal, J. H., Karper, L. P., Seibyl, J. P., Freeman, G. K., Delaney, R., Bremner, J. D., et al. (1994). Subanesthetic effects of the noncompetitive NMDA antagonist, ketamine, in humans: psychotomimetic, perceptual, cognitive, and neuroendocrine responses. *Arch. Gen. Psychiatry* 51, 199–214. doi: 10.1001/archpsyc.1994.03950030035004

Lahti, A. C., Koffel, B., LaPorte, D., and Tamminga, C. A. (1995). Subanesthetic doses of ketamine stimulate psychosis in schizophrenia. *Neuropsychopharmacology* 13, 9–19.

Lai, R., Katalinic, N., Glue, P., Somogyi, A. A., Mitchell, P. B., Leyden, J., et al. (2014). Pilot dose-response trial of i.v. ketamine in treatment-resistant depression. *World J. Biol. Psychiatry* 15, 579–584. doi: 10.3109/15622975.2014.922697

Maron, E., and Nutt, D. (2017). Biological markers of generalized anxiety disorder. *Dialogues Clin. Neurosci.* 19, 147–157.

McLoughlin, G., Gyurkovics, M., Palmer, J., and Makeig, S. (2022). Midfrontal theta activity in psychiatric illness: an index of cognitive vulnerabilities across disorders. *Biol. Psychiatry* 91, 173–182. doi: 10.1016/j.biopsych.2021.08.020

McNaughton, N., and Glue, P. (2020). Ketamine and neuroticism: a double-hit hypothesis of internalizing disorders. *Pers. Neurosci.* 3:e2. doi: 10.1017/pen.2020.2

McNaughton, N., Kocsis, B., and Hajós, M. (2007). Elicited hippocampal theta rhythm: a screen for anxiolytic and procognitive drugs through changes in hippocampal function? *Behav. Pharmacol.* 18, 329–346. doi: 10.1097/FBP.0b013e3282ee82e3

Mennella, R., Patron, E., and Palomba, D. (2017). Frontal alpha asymmetry neurofeedback for the reduction of negative affect and anxiety. *Behav. Res. Ther.* 92, 32–40. doi: 10.1016/j.brat.2017.02.002

Meyer, A. (2017). A biomarker of anxiety in children and adolescents: a review focusing on the error-related negativity (ERN) and anxiety across development. *Dev. Cogn. Neurosci.* 27, 58–68. doi: 10.1016/j.dcn.2017.08.001

Mitchell, D. J., McNaughton, N., Flanagan, D., and Kirk, I. J. (2008). Frontal-midline theta from the perspective of hippocampal "theta". *Prog. Neurobiol.* 86, 156–185. doi: 10.1016/j.pneurobio.2008.09.005

Mognon, A., Jovicich, J., Bruzzone, L., and Buiatti, M. (2011). ADJUST: an automatic EEG artifact detector based on the joint use of spatial and temporal features. *Psychophysiology* 48, 229–240.

Muller, J., Pentyala, S., Dilger, J., and Pentyala, S. (2016). Ketamine enantiomers in the rapid and sustained antidepressant effects. *Ther. Adv. Psychopharmacol.* 6, 185–192. doi: 10.1177/2045125316631267

Murrough, J. W., Yaqubi, S., Sayed, S., and Charney, D. S. (2015). Emerging drugs for the treatment of anxiety. *Expert Opin. Emerg. Drugs* 20, 393–406. doi: 10.1517/14728214.2015.1049996

Muthukumaraswamy, S. D., Shaw, A. D., Jackson, L. E., Hall, J., Moran, R., and Saxena, N. (2015). Evidence that subanesthetic doses of ketamine cause sustained disruptions of NMDA and AMPA-mediated frontoparietal connectivity in humans. *J. Neurosci.* 35, 11694–11706. doi: 10.1523/JNEUROSCI.0903-15.2015

Nemeroff, C. B. (2007). Prevalence and management of treatment-resistant depression. *J. Clin. Psychiatry* 68, 17–25.

Olesen, J., Gustavsson, A., Svensson, M., Wittchen, H. U., Jonsson, B., CDBE2010 Study Group, et al. (2012). The economic cost of brain disorders in Europe. *Eur. J. Neurol.* 19, 155–162. doi: 10.1111/j.1468-1331.2011.03590.x

Pinault, D. (2008). N-methyl d-aspartate receptor antagonists ketamine and MK-801 induce wake-related aberrant γ oscillations in the rat neocortex. *Biol. Psychiatry* 63, 730–735. doi: 10.1016/j.biopsych.2007.10.006

Rivolta, D., Heidegger, T., Scheller, B., Sauer, A., Schaum, M., Birkner, K., et al. (2015). Ketamine dysregulates the amplitude and connectivity of high-frequency oscillations in cortical–subcortical networks in humans: evidence from resting-state magnetoencephalography-recordings. *Schizophr. Bull.* 41, 1105–1114. doi: 10.1093/schbul/sbv051

Rodriguez, C. I., Kegeles, L. S., Levinson, A., Feng, T., Marcus, S. M., Vermes, D., et al. (2013). Randomized controlled crossover trial of ketamine in obsessive-compulsive disorder: proof-of-concept. *Neuropsychopharmacology* 38, 2475–2483. doi: 10.1038/npp.2013.150

Roy-Byrne, P. (2015). Treatment-refractory anxiety: definition, risk factors, and treatment challenges. *Dialogues Clin. Neurosci.* 17, 191–206.

Schűttler, J., Stanski, D. R., White, P. F., Trevor, A. J., Horai, Y., Verotta, D., et al. (1987). Pharmacodynamic modelling of the EEG effects of ketamine and its enantiomers in man. *J. Pharmacokinet. Biopharm.* 15, 241–253. doi: 10.1007/BF01066320

Shadli, S. M., Ando, L. C., McIntosh, J., Lodhia, V., Russell, B. R., Kirk, I. J., et al. (2021). Right frontal anxiolytic-sensitive EEG 'theta' rhythm in the stop-signal task is a theory-based anxiety disorder biomarker. *Sci. Rep.* 11:19746. doi: 10.1038/s41598-021-99374-x

Shadli, S. M., Glue, P., McIntosh, J., and McNaughton, N. (2015). An improved human anxiety process biomarker: characterization of frequency band, personality and pharmacology. *Transl. Psychiatry* 5:e699. doi: 10.1038/tp.2015.188

Shadli, S. M., Kawe, T., Martin, D., McNaughton, N., Neehoff, S., and Glue, P. (2018). Ketamine effects on EEG during therapy of treatment-resistant generalized anxiety and social anxiety. *Int. J. Neuropsychopharmacol.* 21, 717–724. doi: 10.1093/ijnp/pyy032

Spielberger, C. D., Gorsuch, R. L., Lushene, R., Vagg, P., and Jacobs, G. (1983). *Manual for the State-Trait Anxiety Inventory*. Palo Alto, CA: Consulting Psychologists Press.

Stewart, J. L., Coan, J. A., Towers, D. N., and Allen, J. J. (2014). Resting and task-elicited prefrontal EEG alpha asymmetry in depression: support for the capability model. *Psychophysiology* 51, 446–455. doi: 10.1111/psyp.12191

Van Ameringen, M., Patterson, B., Turna, J., Pipe, A., and Nakua, H. (2017). The treatment of refractory generalized anxiety disorder. *Curr. Treat. Options Psychiatry* 4, 404–417. doi: 10.1007/s40501-017-0129-6

Wise, V., McFarlane, A. C., Clark, C. R., and Battersby, M. (2011). An integrative assessment of brain and body function 'at rest' in panic disorder: a combined quantitative EEG/autonomic function study. *Int. J. Psychophysiol.* 79, 155–165. doi: 10.1016/j.ijpsycho.2010.10.002

Zarate, C. A. Jr., and Machado-Vieira, R. (2017). Ketamine: translating mechanistic discoveries into the next generation of glutamate modulators for mood disorders. *Mol. Psychiatry* 22, 324–327. doi: 10.1038/mp.2016.249

Zarate, C. A. Jr., Mathews, D., Ibrahim, L., Chaves, J. F., Marquardt, C., Ukoh, I., et al. (2013). A randomized trial of a low-trapping nonselective N-methyl-D-aspartate channel blocker in major depression. *Biol. Psychiatry* 74, 257–264. doi: 10.1016/j.biopsych.2012.10.019

Zarate, C. A., Singh, J. B., Carlson, P. J., Brutsche, N. E., Ameli, R., Luckenbaugh, D. A., et al. (2006). A randomized trial of an n-methyl-d-aspartate antagonist in treatment-resistant major depression. *Arch. Gen. Psychiatry* 63, 856–864. doi: 10.1001/archpsyc.63.8.856

Zuure, M. B., Hinkley, L. B., Tiesinga, P. H. E., Nagarajan, S. S., and Cohen, M. X. (2020). Multiple midfrontal thetas revealed by source separation of simultaneous MEG and EEG. *J. Neurosci.* 40, 7702–7713. doi: 10.1523/JNEUROSCI.0321-20.2020

Conflict of Interest: PG has a contract with Douglas Pharmaceuticals to develop novel ketamine formulations.

The remaining authors declare that the research was conducted in the absence of any commercial or financial relationships that could be construed as a potential conflict of interest.

Publisher's Note: All claims expressed in this article are solely those of the authors and do not necessarily represent those of their affiliated organizations, or those of the publisher, the editors and the reviewers. Any product that may be evaluated in this article, or claim that may be made by its manufacturer, is not guaranteed or endorsed by the publisher.

frontiers | Frontiers in Neuroscience

ORIGINAL RESEARCH
published: 05 July 2022
doi: 10.3389/fnins.2022.949230

Early Development and the Functional Correlation of Brain Structural Connectivity in Preterm-Born Infants

Tingting Liu[1†], Zhiyong Zhao[1†], Yuqing You[2], Fusheng Gao[2], Ying Lv[3], Mingyan Li[3], Chai Ji[3], Can Lai[2], Hongxi Zhang[2] and Dan Wu[1]*

[1] Key Laboratory for Biomedical Engineering of Ministry of Education, Department of Biomedical Engineering, College of Biomedical Engineering and Instrument Science, Zhejiang University, Hangzhou, China, [2] Department of Radiology, Children's Hospital, Zhejiang University School of Medicine, Hangzhou, China, [3] Department of Child Health, The Children's Hospital, Zhejiang University School of Medicine, Hangzhou, China

Exuberant axon growth and competitive pruning lead to dramatic and comprehensive changes in white matter pathways of the infant brain during the first few postnatal months, yet the development of structural configuration in early infancy has not been fully characterized. This study aimed to investigate the developmental trajectory of structural connectivity reflecting relative fiber density in 43 preterm-born infants aged 0–3 months of corrected age without any complications utilizing probabilistic tractography based on fiber orientation distribution and to explore the potential function correlation associated with the network properties based on the Chinese Communication Development of Infant at 10 months of corrected age. The findings revealed significant increases in global efficiency, local efficiency, normalized clustering coefficient, and small-worldness ($p_{adj} < 0.001$ for each), while the normalized characteristic path length showed a non-significant decrease with age ($p_{adj} = 0.118$). Furthermore, those findings were validated by another parcelation strategy. In addition, the early local efficiency was found to be significantly correlated with words understood at 10 months of corrected age. A unique developmental pattern of structural networks with enhancing efficiency and the small-world property was found in early infancy, which was different from those of neonates or toddlers. In addition, this study revealed a significant correlation between local efficiency and late language comprehension, which indicated that enhanced structural connectivity may lay the structural foundation for language specialization.

Keywords: structural network, diffusion MRI, tractography, infant brain development, language outcome

OPEN ACCESS

Edited by:
Peng Wang,
Chinese Academy of Medical Sciences and Peking Union Medical College, China

Reviewed by:
Yu Zhao,
Vanderbilt University Medical Center, United States
Su-Zhen Dong,
Shanghai Jiao Tong University, China

***Correspondence:**
Dan Wu
danwu.bme@zju.edu.cn

† These authors have contributed equally to this work

Specialty section:
This article was submitted to Brain Imaging Methods, a section of the journal Frontiers in Neuroscience

Received: *20 May 2022*
Accepted: *13 June 2022*
Published: *05 July 2022*

Citation:
Liu T, Zhao Z, You Y, Gao F, Lv Y, Li M, Ji C, Lai C, Zhang H and Wu D (2022) Early Development and the Functional Correlation of Brain Structural Connectivity in Preterm-Born Infants. Front. Neurosci. 16:949230. doi: 10.3389/fnins.2022.949230

INTRODUCTION

Exuberant axon growth and competitive pruning lead to dramatic and comprehensive changes in white matter pathways of the infant brain during the first few postnatal months (Innocenti and Price, 2005; Vanderhaeghen and Cheng, 2010), which may induce a profound alteration in the topology of white matter. Infancy is regarded to be the fastest stage of global and local reconfiguration (Cao et al., 2017), but is not yet fully characterized.

Structural network with diffusion MRI-based tractography provides a powerful approach to investigate the brain connectivity, which has been used to study the network dynamics during

the perinatal period and childhood (Hagmann et al., 2010; Brown et al., 2014; van den Heuvel et al., 2015; Baum et al., 2017), and reveals that neonates, children, and adults exhibit a distinct development pattern of brain structural connectivity. Previous studies revealed that the clustering coefficient and small-worldness increased during the perinatal period (Brown et al., 2014; van den Heuvel et al., 2015; Batalle et al., 2017) and then decreased from toddler to adult (Hagmann et al., 2010; Dennis et al., 2013). Combined with the results of another study, which revealed a significant decrease in clustering coefficients and small-worldness from neonates to childhood (Huang et al., 2015), it is reasonable to speculate that there is an inflection point in network properties during infancy.

However, the developmental pattern of brain structural networks in infancy remains less understood, possibly due to the lack of data and difficulty of acquisition in this period. Yap et al. (2011) conducted a longitudinal study to investigate the developmental trends of white matter connectivity in 39 participants at 2 weeks, 1 year, and 2 years and found that all brains exhibited small-world properties with increasing local efficiency. Tymofiyeva et al. (2013) performed deterministic tractography in 8 preterm-born neonates, 8 term-born neonates, 10 six-month-old infants, and 7 adults and found that the clustering coefficient decreased from preterm-born neonates to 6-month-old infants and then increased until adult; while the small-worldness increased from preterm-born neonates to term-born neonates, kept steady until 6 months old, and then decreased until adult. These two studies with small sample sizes did not reach consistent conclusions, and the discrete scan timepoints (neonate, 6 months, and 1 year) hindered the continuous characterization of development. In addition, tensor-based tractography used in the previous studies was not ideal for immature infant brain due to difficulties in distinguishing whether the signal reduction was due to immature tissue or crossed fibers within voxels (Descoteaux, 1999), which can be addressed by the probabilistic tractography method based on fiber orientation distribution (FOD; Tournier et al., 2010).

Moreover, structural brain networks at an early stage may indicate the functional outcome at a later stage. Baum et al. (2017) revealed the mediation effect of modular segregation of structural networks on the development of executive function in youth. However, the functional correlates of early white matter networks were still unknown. This study aimed to investigate the development of structural brain networks in 0–3 months old preterm-born infants utilizing high angular resolution diffusion imaging (HARDI) and the potential function under network measures by correlating with 10 months old Chinese Communication Development of Infant (CDI).

MATERIALS AND METHODS

Subjects

In total, sixty-seven preterm-born infants were enrolled for MRI scans from 0 to 3 months of corrected age at the Children's Hospital of Zhejiang University School of Medicine. The parents of all participants provided written informed consent, and the ethical approval was granted by the institutional review board of the local hospital. Exclusion criteria included (1) extremely preterm birth (less than 28 weeks); (2) any acquired lesions on MRI (assessed by a radiologist T.L.); (3) visible artifacts on MRI; (4) congenital malformation or syndrome; (5) encephalopathy caused by various factors; (6) intrauterine growth restriction; (7) intracranial infection; (8) alcohol or an illicit drug during pregnancy; and (9) neurological or psychiatric family history. Among the 67 infants recruited, the following infants were excluded: 16 participants who failed the CDI follow-up, 3 extremely preterm-born infants (GA at birth less than 28 weeks), 1 participant with visual brain parenchymal lesion, 2 participants with intrauterine infection, and 2 participants with poor image quality.

Image Acquisition

A certified nurse gave all infants 50 mg/kg oral or enema chloral hydrate 30 min before the scan. Ear protectors were applied for hearing protection, and a vacuum immobilization mat was applied to reduce motion. The scanner's physiological monitoring system was used to continuously monitor the heart and respiratory rates by a neonatologist in the scanner room. MRI was carried out on a 3T Philips Achieva system with an 8-channel head coil. A single-shot echo-planar imaging sequence was used for acquiring multi-shell HARDI data, and 32 non-collinear diffusion-encoding directions were acquired with b-values of 800 and 1,500 s/mm^2. An additional b0 image with the opposite phase-encoding direction was acquired for eddy correction. The particularized parameters were as follows: TR/TE = 9,652/115 ms, voxel size = 1.5 mm × 1.5 mm × 2 mm, FOV = 180 mm × 180 mm × 120 mm, and SENSE acceleration factor of 2.

Data Preprocessing

First, the HARDI data were preprocessed using MRtrix3,[1] including denoising (Veraart et al., 2016), Gibb's ring artifact removal (Kellner et al., 2016), eddy correction (Andersson and Sotiropoulos, 2016), slice-to-volume correction (Andersson et al., 2017), and bias correction (Tustison et al., 2010). The weighted linear least squares method (Basser et al., 1994) was used for obtaining fraction anisotropy (FA) and mean diffusivity (MD).

Cortical Parcelation

The Edinburgh Neonatal Atlas 50 (ENA50) (Blesa et al., 2020) with multiple templates (e.g., DTI metrics) and parcelation schemes was transformed to the individual subject space utilizing a multi-channel registration method based on MD, FA, and the mean DWI contrasts (Djamanakova et al., 2013). Two sets of parcelation schemes including the University of North Carolina (UNC; Shi et al., 2011) and Melbourne Children's Regional Infant Brain (M-CRIB; Alexander et al., 2017) parcellations were obtained for each participant. The transformation matrix between ENA alignment to individual data was used to transform the ENA gray matter probability map to individual space, and the voxels with gray matter probability less than 0.4, as well

[1] https://www.mrtrix.org/

as subcortical and cerebellar regions, were excluded, and 78 cortical regions of UNC were defined as structural network nodes to study network dynamics. In addition, for assessing whether findings were biased by the parcelation schemes, 68 cortical nodes from the M-CRIB atlas were used for validating the reproducibility of the results.

Whole-Brain Tractography

The individual FOD was generated from the preprocessed HARDI data according to the MRtrix3 multi-shell multi-tissue constrained spherical deconvolution (MSMT-CSD) pipeline (Jeurissen et al., 2014), and all individual data were up-sampled to an isotropic voxel of 1 mm. Then, the whole-brain tractography was performed based on individual FOD images utilizing the second-order integration over the FOD method (Tournier et al., 2010), and the tractography profile was as follows: step size = 0.5 mm, minimum/maximum length = 10/250 mm, maximum angle = 90°, and cutoff = 0.05. Afterward, 10 million streamlines were filtered to 1 million utilizing the spherical-deconvolution informed filtering of tractograms (SIFT) method (Smith et al., 2013), which selectively removed streamlines such that the streamline density was as close as possible to fiber density.

Network Construction

The number of fiber tracts connecting two cortical nodes was first normalized to node volumes (sum of two nodes) and then normalized to the total number of tracts across the brain. The tract density between each pair of the 78 cortical nodes forms a 78 × 78 symmetric connectivity matrix. Concerning false-negative connections due to spurious streamlines in probabilistic tractography, we set the network density (the proportion of actual connections among potential connections) to range from 0.2 to 0.3 with an interval of 0.01 (11 thresholds) to calculate network measures, where 0.2 is the minimal network density with full connectivity, and then averaged the measures at all densities (**Figure 1**). In addition, the procedure was repeated based on the M-CRIB parcelation to evaluate the reproducibility of the findings from UNC parcelation.

Network Measures

Five global network measures were calculated for each infant: local efficiency, global efficiency, normalized clustering coefficient, normalized characteristic path length, and small-worldness.

The global efficiency (E_{glob}) is the average of the inverse shortest path length in a structural network (Latora and Marchiori, 2001), which quantifies the exchange of information across the whole network where information is concurrently exchanged, and can be calculated as follows:

$$E_{glob} = \frac{1}{n}\sum_{i\in N}\frac{\sum_{j\in N, j\neq i}\left(d_{ij}^{w}\right)^{-1}}{n-1} \tag{1}$$

where d_{ij}^{w} is the shortest weighted path length between i and j.

The local efficiency (E_{loc}) is the global efficiency computed on the neighborhood of the node (Latora and Marchiori, 2001), which quantifies a network's resistance to failure on a small scale, and can be calculated as follows:

$$E_{loc} = \frac{1}{2}\sum_{i\in N}\frac{\sum_{j,h\in N, j\neq i}\left(w_{ij}w_{ih}\left[d_{jh}^{w}\left(N_i\right)\right]^{-1}\right)^{1/3}}{k_i\left(k_i-1\right)} \tag{2}$$

where w_{ij} is the connection weight between node i and j; $d_{jh}^{w}(N_i)$ is the shortest path length between j and h (node i is the only neighbor of j and h along this shortest path); and k_i is the number of links connected to node i.

The weighted clustering coefficient (CC) is the proportion of triangles around a single node, and thus, the average CC of the network reflects the prevalence of clustered connections (Watts and Strogatz, 1998). In this study, a variant CC was calculated, which is free from the disproportionate influence of low-degree nodes (Newman, 2003):

$$\mathrm{CC} = \frac{\sum_{i\in N} 2t_i^{w}}{\sum_{i\in N} k_i\left(k_i-1\right)} \tag{3}$$

where t_i^{w} is weighted geometric mean of triangles around node i and can be calculated as follows:

$$t_i^{w} = \frac{1}{2}\sum_{j,h\in N}\left(w_{ij}w_{ih}w_{jh}\right)^{1/3} \tag{4}$$

The characteristic path length (CPL) is the average shortest path length among all node pairs in the network and measures the network integration (Watts and Strogatz, 1998), and it can be calculated as follows:

$$d_{ij}^{w} = \sum_{a_{uv}\in g_{i\leftrightarrow j}^{w}} f\left(w_{uv}\right) \tag{5}$$

where f is a mapping from weight to length and $g_{i\leftrightarrow j}^{w}$ is the shortest weighted path between node i and j.

Small-worldness characterizes a network that is remarkably more clustered than a random network, but has roughly the same CPL as a random network, and can be calculated as follows:

$$\mathrm{S} = \frac{CC/CC_{\mathrm{rand}}}{CPL/CPL_{\mathrm{rand}}} \tag{6}$$

where CC/CC_{rand} is the normalized CC of a random network and CPL/CPL_{rand} is the normalized CPL of a random network.

Statistical Analysis

All statistical tests were performed utilizing the R-Project 4.1.2.[2] Factors that were potentially associated with network measures were first screened using univariate analysis, and the significant ones were taken as covariates into the multiple regression to analyze the correlations between network measures and gestational age (GA) at birth, and postmenstrual age (PMA) at scan. Pearson's correlation analysis was conducted between

[2]https://www.r-project.org/

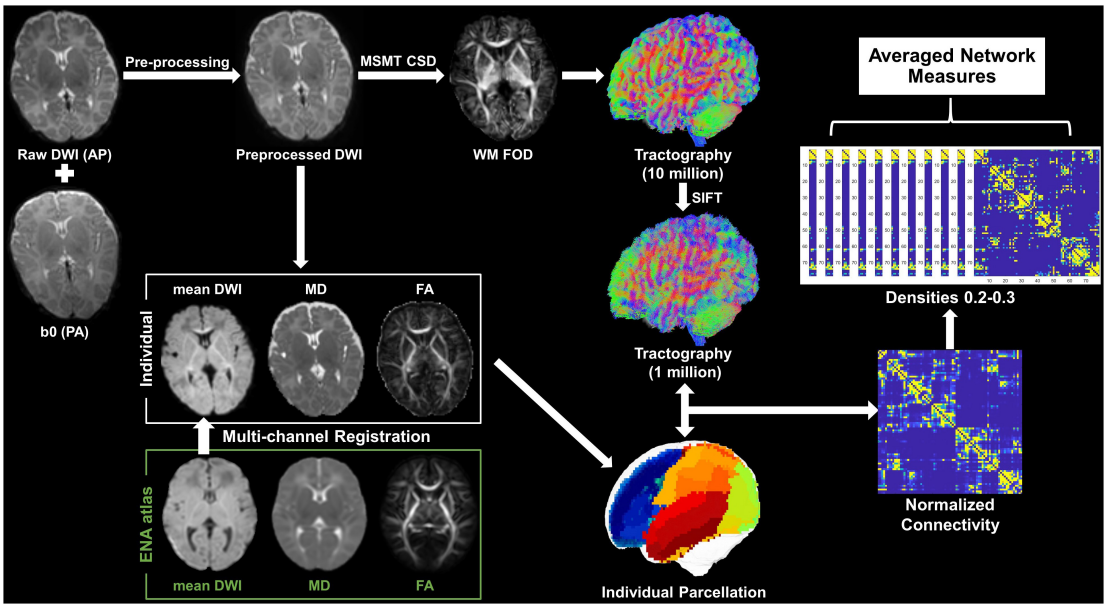

FIGURE 1 | Pipeline of data analysis. Mean DWI, MD, and FA were generated from the preprocessed dMRI and were then co-registered with the ENA atlas to obtain individual parcelation. The WM FOD was calculated according to the MSMT-CSD pipeline in MRtrix3, based on which whole-brain tractography was obtained followed by a SIFT operation. The individual parcelation and filtered tractography were used to generate a 78 × 78 symmetric connectivity matrix. Network measures were calculated at a series of network densities, and then, they were averaged for statistical analysis.

network measures obtained from UNC and M-CRIB parcelation to evaluate the effect of the parcelation scheme.

For assessing the correlation between network properties and language outcomes, univariate analysis was used to identify potential factors that were significantly associated with the Chinese CDI scores, which were included as covariates for subsequent multiple analysis. It was noted that the observed network measures were first regressed against PMA at scan and bodyweight at scan, and then, the residuals were used as PMA-corrected indicators of network for subsequent language correlation analysis. The *p*-values were adjusted by the false discovery rate method. The significance level for all analyses was set at 0.05.

RESULTS

Demographic Information of Participants

After exclusion, 43 preterm-born infants aged 39.9–50.9 postmenstrual weeks (0–3 months of corrected age) without any complications were included in the final analysis, with GA at birth ranging from 28.1 to 35.6 postmenstrual weeks (detailed information was demonstrated in **Figure 2** and **Table 1**). In addition, the mean head motion was 0.65 mm, which showed no significant effect on the network measures based on an ANCOVA.

No Significant Effect of Gestational Age Was Found on Network Measures

In this study, PMA at scan, bodyweight at scan, and delivery were found to be significantly correlated with network measures and were treated as covariates in the multiple regression analysis between network properties and GA at birth. However, no significant correlation was found, indicating that the network measures were not affected by preterm birth in this study.

Developmental Trajectory of Structural Brain Network in 0–3-Month-Old Infants

The averaged structural connectivity matrices of infants aged 0–1, 1–2, and 2–3 months (**Figure 3**) demonstrated an enhancing fiber density with age. All brain network measures except the normalized CPL exhibited significant age-dependent alterations in infants aged 0–3 months (**Figure 4A**). These findings

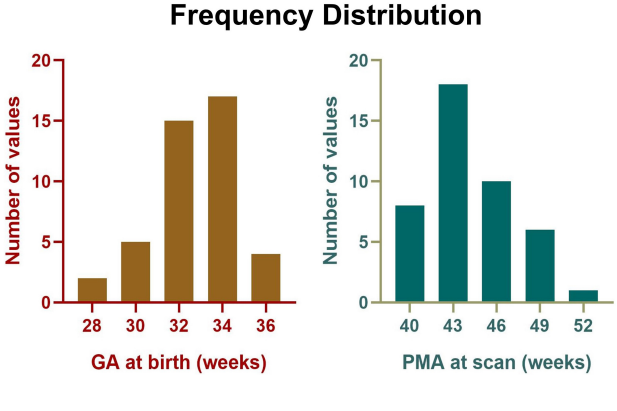

FIGURE 2 | Frequency distribution of GA at birth and PMA at scan for all participants.

TABLE 1 | Demographic information of the infants and their communication development of infant (CDI) sub-scores at 10 months.

Demographic information	
Gender (male/female)	25/18
Gestational age at birth (weeks)	32.7 ± 1.9
Postmenstrual age at scan (weeks)	44.4 ± 2.7
Multiple-birth/singleton	1.83 ± 0.4
Head motion (mm)	0.64 ± 0.3
Body weight at birth (kg)	42.3 ± 4.2
Body length at birth (cm)	11/32
Delivery (vaginal/cesarean)	4.50 ± 0.9
Body weight at scan (kg)	30.9 ± 3.6
Maternal age at delivery (years)	6.1 ± 1.5
Maternal education	25/18
Chinese CDI (10 months of corrected age)	
Words understood	38.4 ± 24.3
Words production	1.1 ± 1.6
Phrases understood	2.0 ± 1.6
Actions and gestures	4.3 ± 2.4

revealed that both integration (E_{glob}) and segregation (E_{loc} and normalized CC) increased significantly with age, and the developmental rates (β) of E_{glob}, E_{loc}, and normalized CC were 0.005, 0.002, and 0.039 per week, respectively ($p_{adj} < 0.001$ for each). The normalized CPL showed a gradual decline with age, although the statistic was not significant (β = −0.007 per week, $p_{adj} = 0.552$). Furthermore, the increased clustering and decreased CPL together resulted in the fast growth of small-worldness (β = 0.047 per week, $p_{adj} = 0.024$) (**Figure 4A**).

In addition, the network properties obtained from M-CRIB parcelation revealed a similar developmental trajectory to that of UNC parcelation (**Figure 4B**), and the developmental trajectories of the two parcellations were significantly correlated (**Figure 4** and **Table 2**).

Local Efficiency Was Significantly Correlated With Words Understood at 10 Months

The PMA at scan, body weight at scan, delivery, and maternal education were found significantly correlated with communication outcome at 10 months of corrected age and were used as covariates in multiple regression between the network measure and CDI scores. However, only the local efficiency was found significantly correlated with words understood (correlation coefficient = 0.339, $p_{adj} = 0.047$) (**Figure 5**), while no other network measures were found to be significantly correlated with communication outcomes (**Table 3**).

DISCUSSION

This study investigated the developmental trends of structural brain networks in infants aged 0–3 months, which was not presented before. The structural networks were generated utilizing a probabilistic tractography based on FOD followed by a

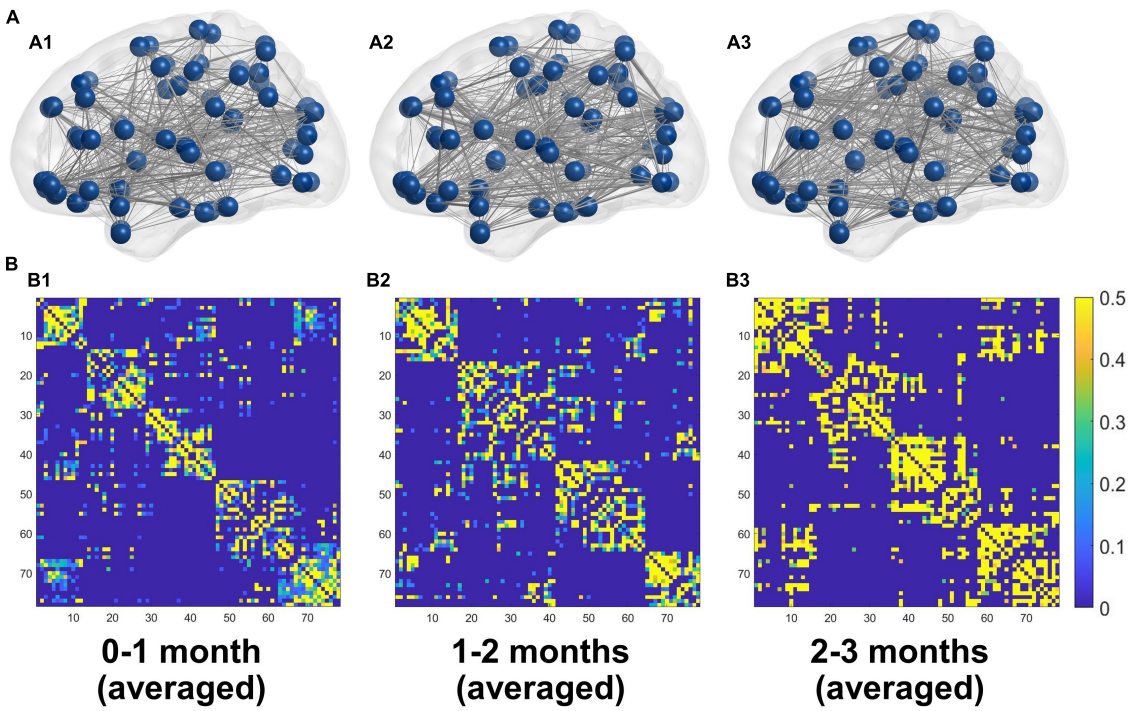

FIGURE 3 | (A) 3D representations of the mean structural networks of 0–1 (A1), 1–2 (A2), and 2–3 (A3) months groups. **(B)** The averaged structural connectivity matrices of 0–1 (B1), 1–2 (B2), and 2–3 (B3) months groups.

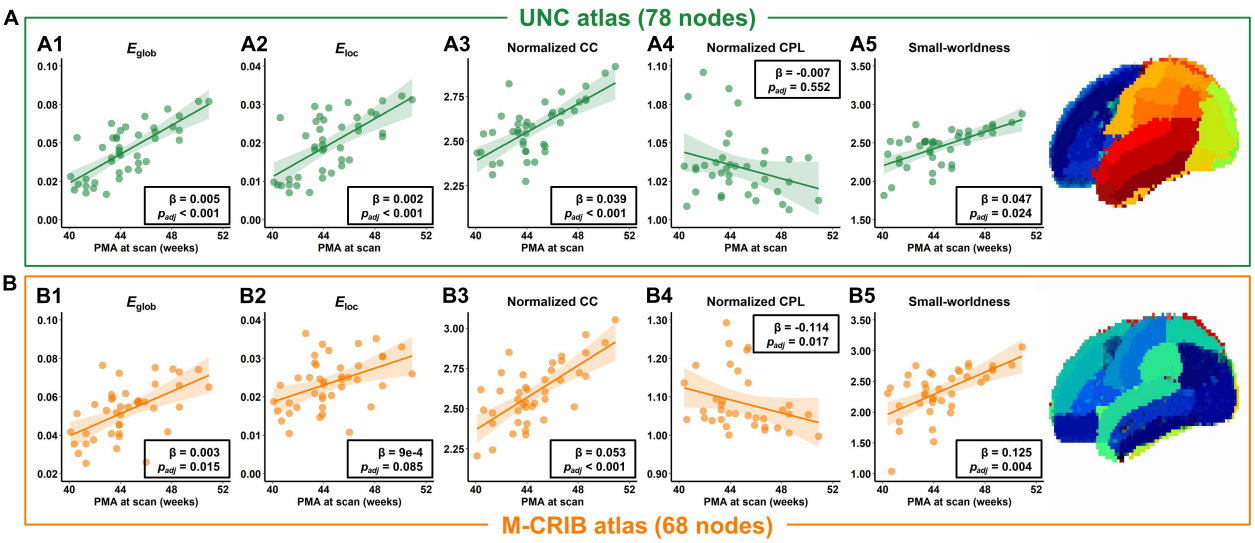

FIGURE 4 | Developmental trajectories of network measures in infants aged 0–3 months, in terms of the global efficiency (E_{glob}), local efficiency (E_{loc}), normalized clustering coefficient (CC), normalized characteristic path length (CPL), and small-worldness, based on the UNC atlas **(A)** or M-CRIB atlas **(B)**.

SIFT, and the findings were validated by another parcelation. The results also indicated that higher local efficiency in early infancy may be associated with language comprehension at a later stage.

Enhanced Information Transfer Efficiency Within the Infant Brain

This study revealed a significant and monotonic increase in global and local efficiency in infants aged 0–3 months, which indicated an enhanced information transfer efficiency and greater fault tolerance within the infant brain. Few studies have discussed the evolution of network efficiency in infants and have not reached consistent conclusions. Batalle et al. (2017) investigated the development of structural brain networks in neonates aged 25–45 postmenstrual weeks and revealed an increase in global efficiency but a decrease in local efficiency with age. However, all studies in infancy used selected scan times and found inconsistent findings. For example, Huang et al. (2015) revealed that neonates had significantly lower structural brain network efficiency than toddlers, while Yap et al. (2011) reported a significant increase in local efficiency in 1-year-old toddlers compared with neonates, but global efficiency remained constant.

TABLE 2 | Correlation between the network measures from University of North Carolina (UNC) and Melbourne children's regional infant brain (M-CRIB) atlases.

Network measures	Correlation coefficient	*P*-value
E_{glob}	0.582	**<0.001**
E_{loc}	0.600	**<0.001**
Normalized CC	0.807	**<0.001**
Normalized CPL	0.556	**<0.001**
Small-worldness	0.831	**<0.001**

Bold value represents adjusted p-value < 0.05.

The results of this study were consistent with Huang et al. and provided a continuous developmental profile of network efficiency during early infancy.

Linear Rising Clustering Coefficients and Small-World Properties

This study found significantly higher normalized CC and small-world properties of structural brain network in infants aged 0–3 months and a slight decrease in normalized CPL. This finding was consistent with the results of network development in perinatal studies utilizing DTI (Brown et al., 2014; van den Heuvel et al., 2015; Batalle et al., 2017), but in contrast to those studies comparing newborns and toddlers (Huang et al., 2015). This implied that the small-world property of the brain structural network may not monotonically decrease during infancy, and

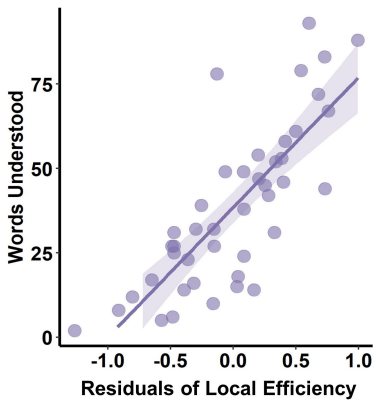

FIGURE 5 | Correlation between PMA-corrected local efficiency and words understood at 10 months.

TABLE 3 | Correlation of postmenstrual age (PMA)-corrected network measures and communication outcomes, and the correlation coefficients were demonstrated.

Residuals of network measures	Words understood	Phrase understood	Words production	Actions and gestures
E_{glob}	0.008	−0.185	0.103	−0.191
E_{loc}	**0.339**	0.161	0.063	0.136
Normalized CC	0.137	−0.077	0.062	−0.138
Normalized CPL	0.136	0.190	0.028	0.193
Small-worldness	0.086	0.004	0.011	−0.270

Bold value represents adjusted p-value < 0.05.

there is likely a turning point of small-world properties between 3 and 12 months, which remains to be confirmed by a wider age range of infant studies.

Higher Local Efficiency Was Associated With Better Words Understood

After controlling for age, we found that higher local efficiency of structural connectivity at birth was associated with better word comprehension at 10 months, and this is the first report on the relationship between structural connectivity and cognition development to the best of our knowledge. Local efficiency measures the capability of a network to information transmission locally, indicating how well each cluster exchanges information when the index node is eliminated (Latora and Marchiori, 2001). In addition, the local functional connectivity of the network is thought to be the foundation for functional segregation and specialization (Sporns, 2013), which may be associated with cognitive functions. For example, Chan et al. (2014) studied the functional network organization across the lifespan (20–89 years) utilizing functional MRI and revealed that segregation was predictable for long-term memory function. Given that functional network organization is determined by the underlying structural network (Cao et al., 2017), we speculate that enhanced structural connectivity in local regions related to language may lay the structural foundation for language specialization.

Limitation

Several limitations of this study should be noted. First, this study lack term-born infants as healthy control. We excluded infants whose brain development might be compromised by certain factors, e.g., extreme preterm birth and encephalopathy, to ensure that relatively healthy participants were enrolled. In addition, the fact that there was no correlation between GA at birth and the structural network measurements supported that our study population was not affected by preterm-born. Nevertheless, future validation of the current findings from healthy term-born infants would be ideal. Second, participants were sedated with chloral hydrate. However, chloral hydrate is recognized as safe and is often applied to infants for minimizing head motion (Finnemore et al., 2014). Despite that sedation may reduce brain activity (Williams et al., 2015), there is no evidence that it might affect infant brain structure. Finally, due to the narrow age range of participants in this study, the potential inflection point of the small-world property was not revealed, and future studies with a larger age range were needed.

CONCLUSION

This study investigated the developmental trajectories of structural connectivity reflecting relative fiber connections in infants aged 0–3 months, and the findings were validated by another parcelation scheme. A unique developmental pattern of structural networks with enhancing efficiency and small-world property was found in early infancy. In addition, this study revealed a significant correlation between local efficiency and late language comprehension, which indicated that enhanced structural connectivity in local regions related to language may lay the structural foundation for language specialization.

DATA AVAILABILITY STATEMENT

The raw data supporting the conclusions of this article will be made available by the authors, without undue reservation.

ETHICS STATEMENT

The studies involving human participants were reviewed and approved by the Children's Hospital of Zhejiang University School of Medicine. Written informed consent to participate in this study was provided by the participants' legal guardian/next of kin.

AUTHOR CONTRIBUTIONS

TL contributed to the data processing and manuscript writing. ZZ contributed to the conception of the study. YY, FG, HZ, and CL contributed to MRI scanning. YL, ML, and CJ contributed to the participants recruitment. DW contributed to the conception and design of the study and major revision of manuscript. All authors contributed to the article and approved the submitted version.

FUNDING

This study was supported by the Ministry of Science and Technology of the People's Republic of China (2018YFE0114600), the National Natural Science Foundation of China (61801424, 81971606, and 82122032), and the Science and Technology Department of Zhejiang Province (202006140 and 2022C03057).

REFERENCES

Alexander, B., Murray, A. L., Loh, W. Y., Marthews, L. G., Adamson, C., Beare, R., et al. (2017). A new neonatal cortical and subcortical brain atlas: the Melbourne Children's Regional Infant Brain (M-CRIB) atlas. *Neuroimage* 147, 841–851. doi: 10.1016/j.neuroimage.2016.09.068

Andersson, J. L. R., Graham, M. S., Drobnjak, I., Zhang, H., Filippini, N., and Bastiani, M. (2017). Towards a comprehensive framework for movement and distortion correction of diffusion MR images: within volume movement. *Neuroimage* 152, 450–466. doi: 10.1016/j.neuroimage.2017.02.085

Andersson, J. L. R., and Sotiropoulos, S. N. (2016). An integrated approach to correction for off-resonance effects and subject movement in diffusion MR imaging. *Neuroimage* 125, 1063–1078. doi: 10.1016/j.neuroimage.2015.10.019

Basser, P. J., Mattiello, J., and LeBihan, D. (1994). MR diffusion tensor spectroscopy and imaging. *Biophys. J.* 66, 259–267.

Batalle, D., Hughes, E. J., Zhang, H., Tournier, J. D., Tusor, N., Aljabar, P., et al. (2017). Early development of structural networks and the impact of prematurity on brain connectivity. *Neuroimage* 149, 379–392. doi: 10.1016/S0006-3495(94)80775-1

Baum, G. L., Ciric, R., Roalf, D. R., Betzel, R. F., Moore, T. M., and Shinohara, R. T. (2017). Modular Segregation of Structural Brain Networks Supports the Development of Executive Function in Youth. *Curr. Biol.* 27, 1561–1572.e8.doi: 10.1016/j.cub.2017.04.051

Blesa, M., Galdi, P., Sullivan, G., Wheater, E. N., Stoye, D. Q., Lamb, G. J., et al. (2020). Peak Width of Skeletonized Water Diffusion MRI in the Neonatal Brain. *Front. Neurol.* 11:235 doi: 10.3389/fneur.2020.00235

Brown, C. J., Miller, S. P., Booth, B. G., Andrews, S., Chau, V., Poskitt, K. J., et al. (2014). Structural network analysis of brain development in young preterm neonates. *Neuroimage* 101, 667–680. doi: 10.1016/j.neuroimage.2014.07.030

Cao, M., Huang, H., and He, Y. (2017). Developmental Connectomics from Infancy through Early Childhood. *Trends Neurosci.* 40, 494–506. doi: 10.1016/j.tins.2017.06.003

Chan, M. Y., Park, D. C., Savalia, N. K., Petersen, S. E., and Wig, G. S. (2014). Decreased segregation of brain systems across the healthy adult lifespan. *Proc. Natl. Acad. Sci. U.S.A.* 111, E4997–E5006.

Dennis, E. L., Jahanshad, N., McMahon, K. L., de Zubicaray, G. I., Martin, N. G., Hickie, I. B., et al. (2013). Development of brain structural connectivity between ages 12 and 30: a 4-Tesla diffusion imaging study in 439 adolescents and adults. *Neuroimage* 64, 671–684. doi: 10.1016/j.neuroimage.2012.09.004

Descoteaux, M. (1999). *High Angular Resolution Diffusion imaging (HARDI). Wiley Encyclopedia of Electrical and Electronics Engineering*. Hoboken: Wiley.

Djamanakova, A., Faria, A. V., Hsu, J., Ceritoglu, C., Oishi, K., Miller, M. I., et al. (2013). Diffeomorphic brain mapping based on T1-weighted images: improvement of registration accuracy by multichannel mapping. *J. Magn. Reson. Imaging* 37, 76–84. doi: 10.1002/jmri.23790

Finnemore, A., Toulmin, H., Merchant, N., Arichi, T., Tusor, N., Cox, D., et al. (2014). Chloral hydrate sedation for magnetic resonance imaging in newborn infants. *Pediatr. Anesth.* 24, 190–195. doi: 10.1111/pan.12264

Hagmann, P., Sporns, O., Madan, N., Cammoun, L., Pienaar, R., Wedeen, V. J., et al. (2010). White matter maturation reshapes structural connectivity in the late developing human brain. *Proc. Natl. Acad. Sci. U.S.A.* 107, 19067–19072. doi: 10.1073/pnas.1009073107

Huang, H., Shu, N., Mishra, V., Jeon, T., Chalak, L., Wang, Z. Y. J., et al. (2015). Development of Human Brain Structural Networks Through Infancy and Childhood. *Cerebral Cortex* 25, 1389–1404. doi: 10.1093/cercor/bht335

Innocenti, G. M., and Price, D. J. (2005). Exuberance in the development of cortical networks. *Nat. Rev. Neurosci.* 6, 955–965. doi: 10.1038/nrn1790

Jeurissen, B., Tournier, J. D., Dhollander, T., Connelly, A., and Sijbers, J. (2014). Multi-tissue constrained spherical deconvolution for improved analysis of multi-shell diffusion MRI data. *Neuroimage* 103, 411–426. doi: 10.1016/j.neuroimage.2014.07.061

Kellner, E., Dhital, B., Kiselev, V. G., and Reisert, M. (2016). Gibbs-ringing artifact removal based on local subvoxel-shifts. *Magn. Reson. Med.* 76, 1574–1581. doi: 10.1002/mrm.26054

Latora, V., and Marchiori, M. (2001). Efficient behavior of small-world networks. *Phys. Rev. Lett.* 87:198701. doi: 10.1103/PhysRevLett.87.198701

Newman, M. E. J. (2003). The structure and function of complex networks. *Siam Rev.* 45, 167–256. doi: 10.1137/S003614450342480

Shi, F., Yap, P. T., Wu, G. R., Jia, H. J., Gilmore, J. H., Lin, W. L., et al. (2011). Infant Brain Atlases from Neonates to 1-and 2-Year-Olds. *PLoS One* 6:e18746. doi: 10.1371/journal.pone.0018746

Smith, R. E., Tournier, J. D., Calamante, F., and Connelly, A. (2013). SIFT: spherical-deconvolution informed filtering of tractograms. *Neuroimage* 67, 298–312. doi: 10.1016/j.neuroimage.2012.11.049

Sporns, O. (2013). Network attributes for segregation and integration in the human brain. *Curr. Opin. Neurobiol.* 23, 162–171.

Tournier, J. D., Calamante, F., and Connelly, A. (2010). Improved probabilistic streamlines tractography by 2nd order integration over fibre orientation distributions. *Proc. Intl. Soc. Mag. Reson. Med.* 1670.

Tustison, N. J., Avants, B. B., Cook, P. A., Zheng, Y., Egan, A., Yushkevich, P. A., et al. (2010). N4ITK: improved N3 bias correction. *IEEE Trans. Med. Imaging* 29, 1310–1320. doi: 10.1109/TMI.2010.2046908

Tymofiyeva, O., Hess, C. P., Ziv, E., Lee, P. N., Glass, H. C., Ferriero, D. M., et al. (2013). A DTI-Based Template-Free Cortical Connectome Study of Brain Maturation. *PLoS One* 8:e63310. doi: 10.1371/journal.pone.0063310

van den Heuvel, M. P., Kersbergen, K. J., de Reus, M. A., Keunen, K., Kahn, R. S., Groenendaal, F., et al. (2015). The Neonatal Connectome During Preterm Brain Development. *Cerebral Cortex* 25, 3000–3013. doi: 10.1093/cercor/bhu095

Vanderhaeghen, P., and Cheng, H. J. (2010). Guidance Molecules in Axon Pruning and Cell Death. *Cold Spring Harb. Perspect. Biol.* 2:a001859. doi: 10.1101/cshperspect.a001859

Veraart, J., Novikov, D. S., Christiaens, D., Ades-Aron, B., Sijbers, J., and Fieremans, E. (2016). Denoising of diffusion MRI using random matrix theory. *Neuroimage* 142, 394–406. doi: 10.1016/j.neuroimage.2016.08.016

Watts, D. J., and Strogatz, S. H. (1998). Collective dynamics of 'small-world' networks. *Nature* 393, 440–442. doi: 10.1038/30918

Williams, G., Fabrizi, L., Meek, J., Jackson, D., Tracey, I., Robertson, N., et al. (2015). Functional magnetic resonance imaging can be used to explore tactile and nociceptive processing in the infant brain. *Acta Paediatr.* 104, 158–166. doi: 10.1111/apa.12848

Yap, P. T., Fan, Y., Chen, Y., Gilmore, J. H., Lin, W., and Shen, D. (2011). Development trends of white matter connectivity in the first years of life. *PLoS One* 6:e24678. doi: 10.1371/journal.pone.0024678

Conflict of Interest: The authors declare that the research was conducted in the absence of any commercial or financial relationships that could be construed as a potential conflict of interest.

frontiers | Frontiers in Neuroscience

TYPE Original Research
PUBLISHED 05 August 2022
DOI 10.3389/fnins.2022.974940

OPEN ACCESS

EDITED BY
Jinglei Lv,
The University of Sydney, Australia

REVIEWED BY
Xu-Yun Hua,
Shanghai University of Traditional Chinese Medicine, China
Ruiping Hu,
Fudan University, China

*CORRESPONDENCE
Tong Wang
wangtong60621@163.com
Ying Shen
shenying_1981@hotmail.com

†These authors have contributed equally to this work and share first authorship

SPECIALTY SECTION
This article was submitted to Brain Imaging Methods, a section of the journal Frontiers in Neuroscience

RECEIVED 21 June 2022
ACCEPTED 19 July 2022
PUBLISHED 05 August 2022

CITATION
Wu Q, Xu X, Zhai C, Zhao Z, Dai W, Wang T and Shen Y (2022) High-frequency repetitive transcranial magnetic stimulation improves spatial episodic learning and memory performance by regulating brain plasticity in healthy rats. *Front. Neurosci.* 16:974940. doi: 10.3389/fnins.2022.974940

High-frequency repetitive transcranial magnetic stimulation improves spatial episodic learning and memory performance by regulating brain plasticity in healthy rats

Qi Wu[1,2†], Xingjun Xu[1†], Chenyuan Zhai[1], Zhiyong Zhao[3], Wenjun Dai[1], Tong Wang[1*] and Ying Shen[1*]

[1]Rehabilitation Medicine Center, The First Affiliated Hospital of Nanjing Medical University, Nanjing, China, [2]Department of Rehabilitation, Hengyang Medical School, The First Affiliated Hospital, University of South China, Hengyang, China, [3]College of Biomedical Engineering & Instrument Science, Zhejiang University, Hangzhou, China

Background: Repetitive transcranial magnetic stimulation (rTMS) is an effective way to stimulate changes in structural and functional plasticity, which is a part of learning and memory. However, to our knowledge, rTMS-induced specific activity and neural plasticity in different brain regions that affect cognition are not fully understood; nor are its mechanisms. Therefore, we aimed to investigate rTMS-induced cognition-related neural plasticity changes and their mechanisms in different brain regions.

Methods: A total of 30 healthy adult rats were randomly divided into the control group and the rTMS group (n = 15 rats per group). The rats in the control and the rTMS group received either 4 weeks of sham or high-frequency rTMS (HF-rTMS) over the prefrontal cortex (PFC). Cognitive function was detected by Morris water maze. Functional imaging was acquired by resting-state functional magnetic resonance imaging (rs-fMRI) before and after rTMS. The protein expressions of BDNF, TrkB, p-Akt, Akt, NR1, NR2A, and NR2B in the PFC, hippocampus, and primary motor cortex (M1) were detected by Western blot following rTMS.

Results: After 4 weeks of rTMS, the cognitive ability of healthy rats who underwent rTMS showed a small but significant behavioral improvement in spatial episodic learning and memory performance. Compared with the pre-rTMS or the control group, rats in the rTMS group showed increased regional homogeneity (ReHo) in multiple brain regions in the interoceptive/default mode network (DMN) and cortico-striatal-thalamic network, specifically the bilateral PFC, bilateral hippocampus, and the left M1. Western blot analyses showed that rTMS led to a significant increase in the expressions of *N*-methyl-D-aspartic acid (NMDA) receptors, including NR1, NR2A, and NR2B in the PFC, hippocampus, and M1, as well as an upregulation of BDNF, TrkB, and p-Akt

in these three brain regions. In addition, the expression of NR1 in these three brain regions correlated with rTMS-induced cognitive improvement.

Conclusion: Overall, these data suggested that HF-rTMS can enhance cognitive performance through modulation of NMDA receptor-dependent brain plasticity.

KEYWORDS

repetitive transcranial magnetic stimulation, resting-state functional magnetic resonance imaging, cognitive improvement, neural plasticity, *N*-methyl-D-aspartic acid receptors, healthy rat

Introduction

Alzheimer's disease is the main cause of dementia and is quickly becoming one of the most expensive, lethal, and burdensome diseases of this century. In 2018, Alzheimer's Disease International estimated the prevalence of dementia at about 50 million people worldwide, a number projected to triple by 2050, with two-thirds of those with the disease living in low-income and middle-income countries (Scheltens et al., 2021). Although there is no consensus yet on the origin of AD, one of the dominant working hypotheses is involved in the progressive deficits in neural plasticity resulting from the amyloid-β (Aβ) cascade (Battaglia et al., 2007; Li et al., 2021). A healthy nervous system is endowed with synaptic plasticity and other neural plasticity, which are believed to be key physiological mechanisms for learning and memory. There has been much anatomical and functional evidence pointing toward AD as a kind of disconnection syndrome, which is manifested as a decline in the linkages between different brain areas in the cognitive network, and neural plasticity dysfunction (Brier et al., 2014). However, few available medications have successfully reversed or affected the disease course of AD. Because it affects neural plasticity both at the site of stimulation and in remote brain regions and acts through functional anatomical connections, rTMS has been regarded as a potentially safe and cost-effective treatment for AD (Li et al., 2021). Understanding the potential mechanisms of rTMS for cognitive improvement of brain plasticity has been meaningful for preventing and treating AD.

Abbreviations: AD, Alzheimer's disease; MCI, mild cognitive impairment; rTMS, repetitive transcranial magnetic stimulation; PFC, prefrontal lobe; HF-rTMS, high-frequency repetitive transcranial magnetic stimulation; rs-fMRI, resting-state functional magnetic resonance imaging; FC, functional connectivity; OPFC, orbital medial prefrontal cortex; DMN, default mode network; FPN, fronto-parietal network; CEN, central executive network; BDNF, brain-derived neurotrophic factor; NMDA, *N*-methyl-D-aspartic acid; S1, primary somatosensory cortex; Cg, cingulate cortex; M1, primary motor cortex; M2, secondary motor cortex; Ent, medial entorhinal cortex; RSG, retrosplenial granular cortex; RSD, retrosplenial dysgranular cortex; V2, secondary visual cortex; DG, dentate gyrus; CA2, cornus ammonis 2; Au, auditory cortex; TeA, temporal association cortex; S2, secondary somatosensory cortex.

Resting-state functional magnetic resonance imaging has been shown to disrupt a distributed network, especially the linkages between the hippocampus, the prefrontal cortex (PFC), and other brain areas, pathologically involved in preclinical AD (Zarei et al., 2013). Ample evidence has demonstrated that overall brain plasticity declines in AD patients (Battaglia et al., 2007; Cai et al., 2017; Noguchi-Shinohara et al., 2021). Plasticity in the PFC, hippocampus, and several other brain regions was impaired in both patients with AD and APP/PS1 mice (Battaglia et al., 2007). Plasticity in the number and strength of neural connections is the physical basis of learning and memory (Todd et al., 2019). Therefore, the enhancement of brain activity and the triggering of specific structural and functional changes promoted by neural plasticity effects could be expected to improve cognitive abilities (Li et al., 2014). The use of rTMS could induce temporary excitation/inhibition and long-term effects in specific cortical areas as well as in deep sites via the magnetic field, the effects of which can last for a considerable time. Over recent years, rTMS was broadly applied when investigating the changes across cortical networks (Stagg et al., 2010; Kohl et al., 2019). Previous evidence has demonstrated that the dorsolateral prefrontal cortex (DLPFC), the core part of PFC, plays crucial roles in various cognitive tasks such as working memory, episodic memory, attention, problem-solving, etc. (Giglia et al., 2021; Jones and Graff-Radford, 2021). Abnormal activities of the DLPFC as well as functional disconnection involving DLPFC have been observed in MCI and AD (Cai et al., 2017). Considering its local dysfunction and roles in various neural circuits relevant to the physiological mechanisms of cognitive impairment, the function of the DLPFC and its relationship with the other brain regions in AD or MCI should be especially emphasized. HF-rTMS over the DLPFC can improve cognitive function in patients with MCI and AD (Chou et al., 2020). Previous studies have shown that rTMS over the DLPFC modified cognitive performances via modulating brain functional connectivity of DLPFC and other brain regions in MCI or AD patients (Guo et al., 2021; Esposito et al., 2022). Thus, rTMS-induced activity and neural plasticity underlie cognitive improvement. However, to our knowledge, the specific activity and neural plasticity in different brain regions that

affect cognition by rTMS over the PFC or DLPFC are not fully understood.

High-frequency rTMS can induce long-lasting PFC-hippocampus neural plasticity and improve cognitive function (Ma et al., 2014; Li et al., 2019). However, it is not clear how rTMS impacts neural plasticity in different brain regions. The NMDA receptors play a central role in synaptic plasticity, which is closely related to learning and memory abilities (Gribkova and Gillette, 2021). Functional NMDA receptors are tetramers composed of different subunits (NR1, NR2A-D, NR3A-B). The NR1, NR2A, and NR2B subunits have been demonstrated to be essential for the regulation of synaptic plasticity in the adult hippocampus (Tsien et al., 1996). NMDA receptor dysfunction has been reported to play a role in the pathophysiology of AD (Lin et al., 2014). A 10-Hz rTMS produced a long-term potentiation-like excitatory effect through NMDA receptor-dependent glutamatergic activity (Brown et al., 2021). Zhang et al. (2015) reported that rTMS facilitated spatial cognition and synaptic plasticity associated with increasing levels of BDNF and NMDA receptors. To date, researchers have mainly focused on synaptic plasticity of the hippocampus, and few studies have examined synaptic plasticity-related intracellular signaling pathways in different brain regions responding to rTMS. The mechanism of rTMS on NMDA receptors of distant sites in the brain is still unclear.

It has been shown that rTMS can improve various cognitive domains in several disease models. However, although its exploration in healthy animals is essential to attribute its pure effect in learning and memory processes, there have been few studies in this regard. Addressing healthy animals contributes to a better understanding of the basic mechanisms by which rTMS improves cognitive function and its modulation (Zorzo et al., 2021). The understanding of how rTMS promotes cognitive effects in healthy animals is crucial for directing the power of rTMS to reduce the burden of cognitive decline. Also, it is important to know how rTMS and its mechanisms affect neural plasticity in different brain regions in healthy rats. In the present study, we explored the cognitive improvement effect of rTMS on healthy rats, focusing on cognitive-related neural plasticity changes and their underlying mechanisms in different brain regions. We believe it would be noteworthy for preventing and treating neural plasticity impairment-related diseases.

Materials and methods

Ethics statement

All experimental procedures and protocols were approved by the Ethics Committee of Nanjing Medical University (Animal Ethics Number: 2007005-2) and were designed to minimize the suffering and number of animals used. All the procedures were conducted with strict attention to safe animal care and use following National Institutes of Health guidelines for humane animal care.

Animals and study design

A total of 30 male adult Sprague Dawley rats (250–300 g) were included in the study. All the rats were provided by the Experimental Animal Center of Nanjing Medical University (Medical Experimental Animal Number: SYXK2018-20020). The rats were randomly divided into a control group and an rTMS group (n = 15 rats per group). For each group of experiments, the animals were matched by age and body weight. All the rats were housed in animal facilities under controlled conditions (55 ± 5% relative humidity, 24 ± 2°C, and a 12/12 h light/dark cycle). Animals were allowed to acclimate to these conditions for at least 7 days before inclusion in the experiments. Rats in the rTMS group received 4 weeks of HF-rTMS intervention, and rats in the control group received sham rTMS intervention. Each group had six animals for behavioral testing, six for Western blot analysis, and three for rs-fMRI. After 4 weeks of intervention, rats for molecular testing in each group were sacrificed with pentobarbital (50 mg/kg, intraperitoneal) and the brain tissues, including the PFC, hippocampus, and M1, were harvested (**Figure 1A**).

Repetitive transcranial magnetic stimulation protocol

Rats in the rTMS group engaged in corresponding real rTMS intervention 5 days per week for four consecutive weeks in the awake state. The coil was turned by 90° and placed 5 cm away from the skull for the sham rTMS in the control group to ensure auditory conditions were similar but did not receive brain stimulation. The CCY-IA rTMS apparatus was supplied by Wuhan Yiruide Medical Equipment Co., LTD (Wuhan, Hubei, China). Repetitive TMS was implemented with a parallel-wound solenoidal circular coil stimulator (Y064, height = 20.4 mm, 50-mm outer diameter, 25-mm inner diameter, number of turns = 6 layers × 5 turns/layer = 30 turns) with 3.5-T peak magnetic welds, specifically designed for rodents. Rats were hand-restrained in a suitable cloth when treated with rTMS. The coil center was placed over the middle of the interocular line with the handle pointing forward (Gersner et al., 2011). One rTMS session consisted of 10 burst trains, with each train containing 10 pulses at 10 Hz with 10-s intertrain intervals, totaling 1,000 pulses, lasting 10 min. The motor threshold (MT) intensities when using rats were measured preliminarily (Gersner et al., 2011). The stimulation intensity was set at 80% of the average MT of rats.

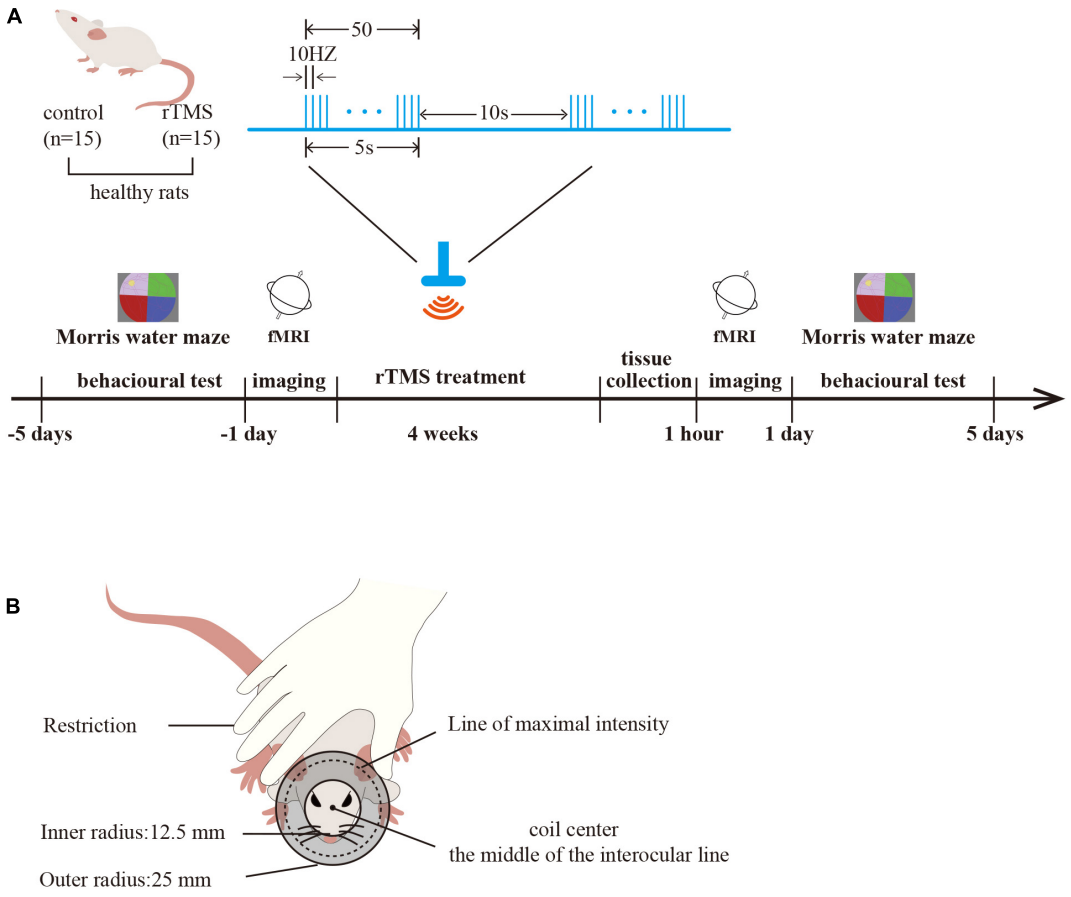

FIGURE 1
Study protocol. **(A)** Experimental timeline and parameters of one rTMS session. Timeline showing a time series event of rat treatment. Healthy rats received rTMS intervention (rTMS: real, rTMS group; sham, control group) for 4 weeks. The brain tissues were harvested 1 h after rTMS intervention (n = 6 rats per group), and the spatial cognition function was tested in the Morris water maze (MWM) before and after rTMS intervention (n = 6 rats per group). rs-fMRI was used to detect the activation of the brain before and after rTMS intervention (n = 3 rats per group). One rTMS session consisted of 10 burst trains, with each train containing 10 pulses at 10 Hz with 10-s intertrain intervals. **(B)** A schematic diagram of rat stimulation. The circular coil was positioned over the rat's head and the coil center was placed over the middle of the interocular line with the handle pointing forward.

In our study, the mean of MT intensities (n = 6 per group) of rats was 42.60 ± 9.10% of the maximum stimulator output (Figures 1A,B).

Functional magnetic resonance imaging acquisition

Data on fMRI were acquired on a 7.0-T MRI scanner (Biospec 7T/20 USR, Bruker Biospin, Ettlingen, Germany). A quadrature volume resonator (inner diameter of 72 mm) was used for radiofrequency transmission, and a four-element surface coil array was used for signal reception. The rats (n = 3 rats per group) were anesthetized with 2% isoflurane and NO_2/O_2 mixed gas anesthesia in a chamber. During the MRI scan, the rat was prostrated on a custom-made holder to minimize head motion. An echo-planar imaging (EPI) sequence was used with the following scanning parameters: matrix size = 256 × 256, flip angle = 70°, resolution = 0.5 mm × 0.5 mm, slice thickness = 1 mm, slice gap = 0, repetition time (TR) = 330 ms, echo time (TE) = 10 ms, slice number = 25.

Functional magnetic resonance imaging data analysis

Image preprocessing of the rs-fMRI data was performed for all individuals using the SPM12[1] toolkit, which included the following steps: (1) Slice time correction: correcting the time information of each layer of each volume of each

1 http://www.fil.ion.ucl.ac.uk/spm/

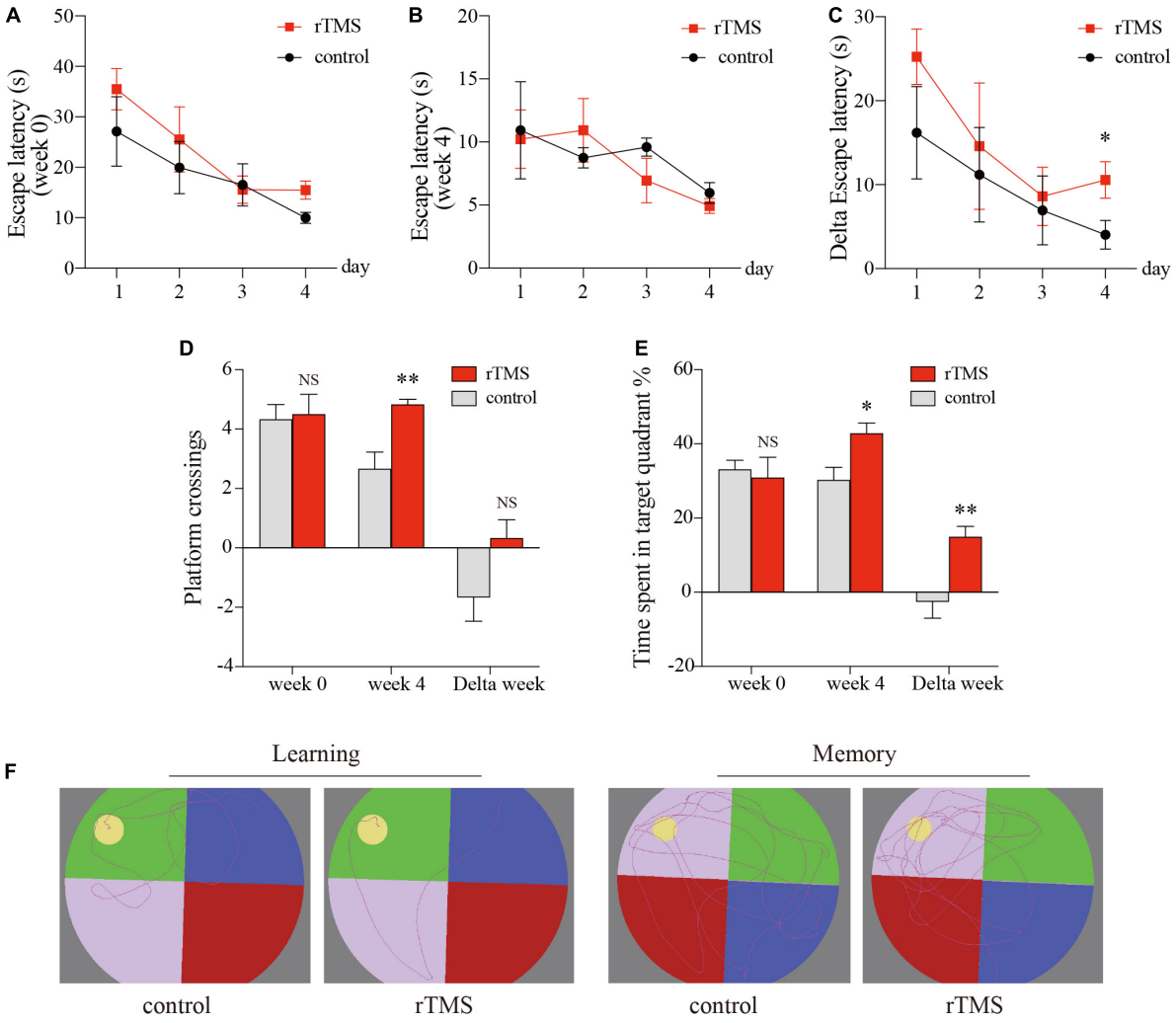

FIGURE 2
rTMS over the PFC improved spatial episodic learning and memory ability in healthy rats. At 4 weeks post rTMS, rats in indicated groups were applied for Morris water maze (MWM) tests. Latencies of pre- and post-rTMS (**A,B**, respectively), delta latencies of pre- and post-rTMS **(C)**. **(D)** The frequency of swimming across the platform location in the probe trial. **(E)** Percentage of time spent in the platform quadrant in the probe trial. **(F)** Representative track plots of rats in hidden platform test (left plots, "learning") and probe trial stage (right plots, "memory"). Data are shown as mean ± SEM; $n = 6$ per group; $^{*}P < 0.05$ and $^{**}P < 0.01$ vs. control group.

rat to eliminate the phase difference of the time series between layers; (2) Head motion correction: the first volume of each rat was used as a reference standard, and the remaining volumes were spatially registered to the referred image using a 6-parameter rigid-body transformation to eliminate head movements. At the same time, the averaged image after head motion correction was generated; (3) Spatial normalization: a template was used as a reference standard, and the averaged image after head motion correction was used as the source image to estimate the registration parameters (12-parameter affine transformation and non-linear deformation), and then applied to normalize the brain images of all the tested rats to the template space to eliminate the differences among the rats. (4) Nuisance signals regression: 13 parameters (six head movement + six head movement first derivative + whole-brain signal) were regressed; (5) Detrend: removing device linear signal drift; (6) Filtering: the filter is 0.01–0.1 Hz. After that, regional homogeneity (ReHo) was used to measure the "coherence" of local brain activity. The principle is to calculate the Kendall harmony coefficient between each pixel and its surrounding 12 pixels. Then, Gaussian smoothing and Z-transformation were performed for ReHo maps. For each state of all rats before and after treatment, the calculated ReHo index was subjected to a single-sample test (the threshold was $p < 0.001$) and FDR correction, and then the statistics of each brain function index were generated under the threshold of cluster size > 50 to analyze the results. The paired *t*-test was

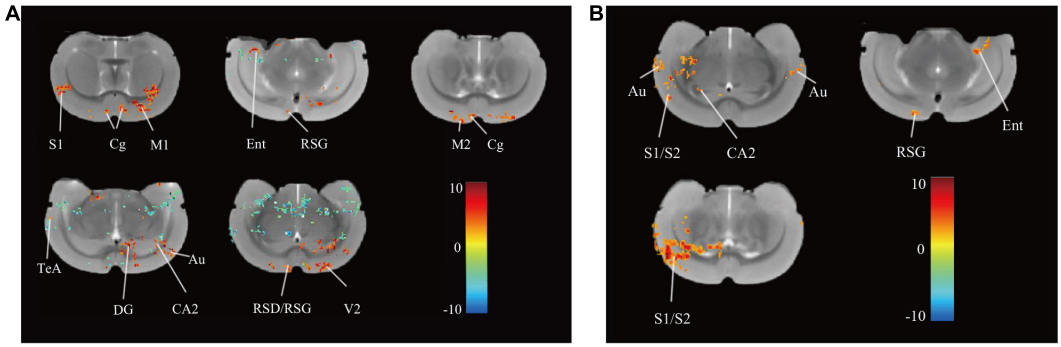

FIGURE 3
Differences in ReHo before and after rTMS and between group. **(A)** Brain regions with significant differences in ReHo between pre- and post-rTMS in the rTMS group ($P < 0.05$, uncorrected, cluster size = 50). The hot color represents the higher ReHo in post-rTMS. The cold color represents the higher ReHo in pre-rTMS. **(B)** Brain regions with significant differences in ReHo between the rTMS and the control group after rTMS ($P < 0.05$, uncorrected, cluster size = 50). The hot color represents the higher ReHo in the rTMS group. S1, primary somatosensory cortex; Cg, cingulate cortex; M1, primary motor cortex; Ent, medial entorhinal cortex; RSG, retrosplenial granular cortex; M2, secondary motor cortex; RSD, retrosplenial dysgranular cortex; TeA, temporal association cortex; V2, secondary visual cortex; DG, dentate gyrus; CA2, cornus ammonis 2; Au, auditory cortex; S2, secondary somatosensory cortex.

performed for each brain function index before and after treatment in all rats; the threshold was uncorrected $p < 0.05$, cluster size = 50.

Spatial episodic learning and memory test by using Morris water maze

Morris water maze (MWM) tests were used to evaluate the spatial learning and memory 1 day before and 1 day after rTMS treatment in rats from each group ($n = 6$ rats/group), as previously described (Hong et al., 2020). Morris water labyrinth equipment (JLBehv-MWMG, Shanghai Jiliang Technology Co., Ltd., Shanghai, China) included a circular pool and a video photography tracking system. The pool (1.5-m diameter and 0.5-m in height) was filled with 22–24°C black water. A hidden platform (9 cm in diameter) that served as the escape platform was submerged 2.0 cm below the water surface. The rat faced the wall of the pool and was gently placed in the water. The first four consecutive days constituted the latency trial when the rats were trained to find the escape platform once a day. The average time required to complete the task was called "full average escape latency." Rats were considered to have achieved it if they remained on the platform for 2 s. If rats failed to reach the platform within 60 s, they would be manually guided to the platform and held there for 15 s to familiarize themselves with the environment and the platform position before being placed back into the cage. At this time, the escape latency was recorded as 60 s. The latency and swimming path for reaching the platform were recorded for each rat, and its decline over days of training reflected learning and memory. On the fifth day, the platform was removed to perform a probe trial, and each rat was allowed to search the maze for 60 s. The rats were placed into the quadrant opposite the first quadrant and the number of platform crossings within the 60 s was recorded. This exploratory test was used to assess the memory level and spatial cognitive ability. The escape latency to find the platform, the time spent in the target quadrant, and platform crossings were tracked and analyzed by the ANY-maze video tracking software (Stoelting, Keele, WI, United States).

Western blot analyses

Tissue samples of the PFC, hippocampus, and M1 were dissected and homogenized in RIPA lysis buffer (Beyotime, Shanghai, China). Total protein was quantified by a BCA assay (Beyotime, Shanghai, China), separated by SDS-PAGE, and transferred to PVDF membranes (Millipore, Boston, MA, United States). The primary antibodies were as follows: rabbit anti-BDNF (ab108319, Abcam, Cambridge, Cambridgeshire, Umnited States), rabbit anti-TrkB (ab179515, Abcam, Cambridge, Cambridgeshire, UK), rabbit anti-Akt (T55972, Abmart, Shanghai, China), rabbit anti-p-Akt (4060S, Cell signal technology, Boston, MA, United States), rabbit anti-NR1 (5704S, Cell signal technology, Boston, MA, United States), rabbit anti-NR2A (ab124913, Abcam, Cambridge, Cambridgeshire, United States), rabbit anti-NR2B (4207S, Cell signal technology, Boston, MA, United States), and rabbit anti-β-actin (wx488142, ABclonal, Wuhan, Hubei, China). After rinsing, the membranes were incubated with HRP-conjugated secondary antibodies. The densities of the bands on the membranes were visualized by enhanced chemiluminescence (ChemiScope6100, Qinxiang, Shanghai, China), followed by exposure to X-ray film

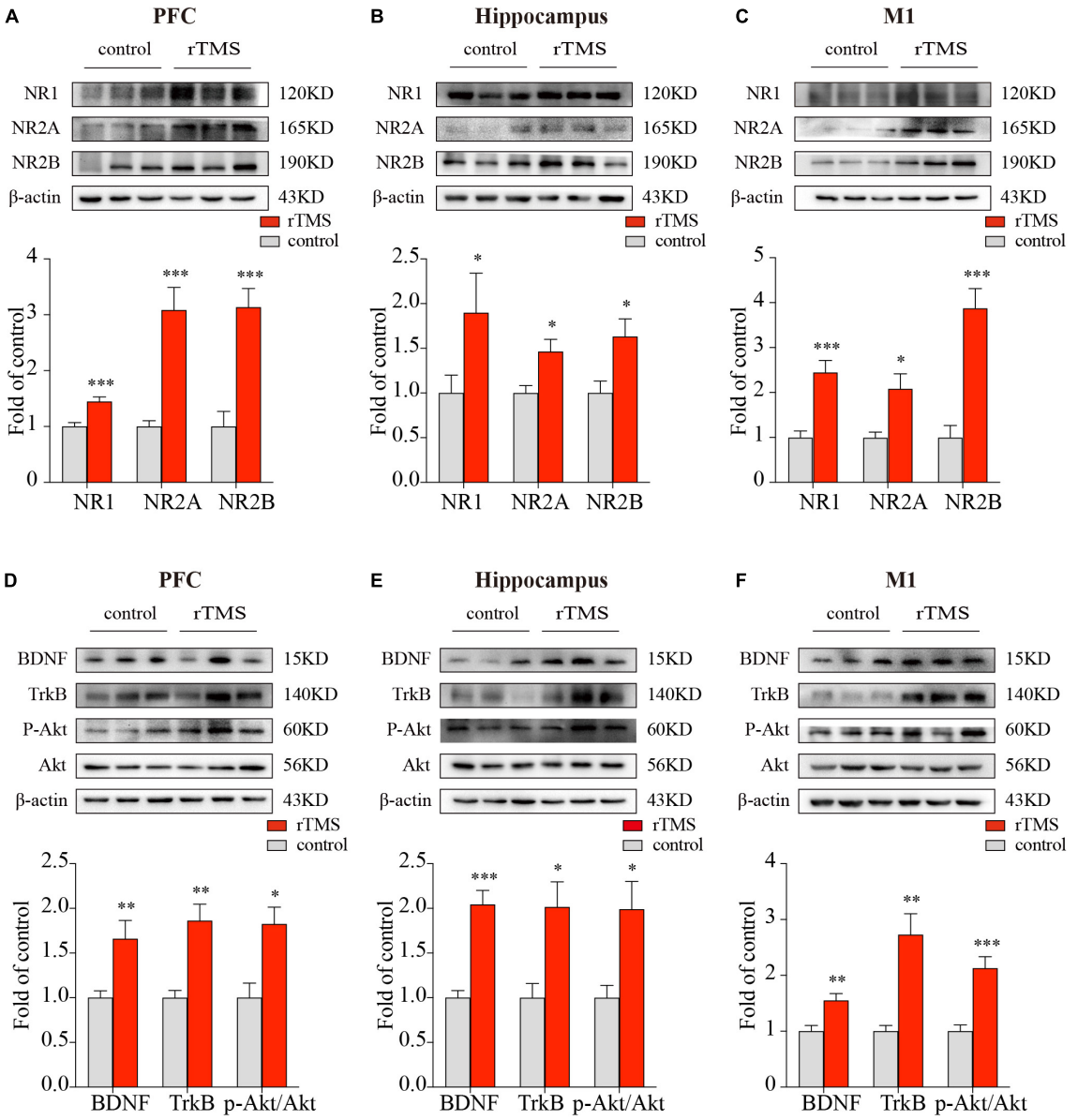

FIGURE 4
Western blot analysis of synaptic plasticity-related proteins in the PFC, hippocampus, and M1. The representative blots depict NMDA receptors compositions in brain tissues from PFC **(A)**, hippocampus **(B)**, as well as M1 **(C)**. The representative blots depict the BDNF/TrkB/Akt pathway compositions in brain tissues from PFC **(D)**, hippocampus **(E)**, as well as M1 **(F)**. Data are shown as mean ± SEM; $n = 6$ per group; $^{*}P < 0.05$, $^{**}P < 0.01$, and $^{***}P < 0.001$ vs. control group.

(RX-U, Fujifilm, Tokyo, Japan). Finally, the results were quantified by using NIH Image J software (Bethesda, MD, United States) and expressed as a ratio to the β-actin protein.

Statistical analyses

Statistical analyses were performed using GraphPad Prism software (version 9.0 c, GraphPad Software, Inc., La Jolla, CA, United States) and SPSS (version 21, SPSS Inc., IBM, Armonk, NY, United States). A Kolmogorov–Smirnov test showed that all data were normally distributed. Data with normal distributions are expressed as the mean ± SEM. Two-way ANOVA with Tukey's test for multiple comparisons was used to determine differences among individual groups. The unpaired *t*-test was used when comparing two separate groups. Spearman's correlation was used to analyze the correlation between the relative band intensity of NR1 with the performance in the MWM

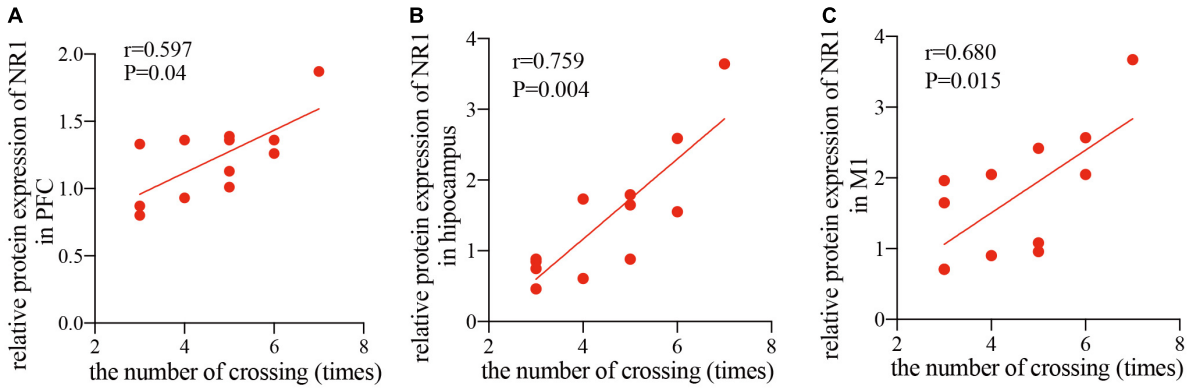

FIGURE 5
Correlation scatters plot of the number of times crossing and the relative protein expression of NR1 in healthy rats after rTMS. Correlation between the number of crossings in the MWM task and the relative protein expression of NR1 in the PFC **(A)** (r = 0.597, $P < 0.05$), hippocampus **(B)** (r = 0.759, $P < 0.01$), and M1 **(C)** (r = 0.659, $P < 0.05$).

task. For all statistical significance, the levels were set at $P < 0.05$.

Results

Use of repetitive transcranial magnetic stimulation over the prefrontal cortex improved spatial episodic learning and memory abilities in healthy rats

We used the MWM test to evaluate the effect of rTMS on spatial episodic learning and memory in healthy rats. In the spatial learning stage, all rats from different groups benefited from the 4-day training and exhibited gradually decreased latency to the platform (Figures 2A–C). In the latency trial, there were no significant differences in the escape latencies between the control group and the rTMS group in week 0 (Figure 2A) and week 4 (Figure 2B), while the delta latency of pre- and post-rTMS showed that the escape latencies of rTMS group decreased more significantly after 4 weeks of rTMS than the control group (rTMS vs. control, two-way ANOVA, F = 4.405, $P < 0.05$ for time, F = 39.097, $P < 0.0001$ for group, F = 0.035, $P > 0.05$ for day × group Figure 2C). In the spatial probe trial, cognitive performance was represented by the frequency of swimming across the platform and the percentage of time spent in the platform quadrant (Figures 2D,E). The frequency of swimming across the platform in week 4 in the rTMS rats was small but significantly higher than in the control rats ($P < 0.05$, Figure 2D). The change in percentage of time spent in the target quadrant in week 4 and the delta time spent in the target quadrant was significantly higher in the rTMS group than in the control group ($P < 0.05$ and $P < 0.01$, respectively, Figure 2E). These results proved that rTMS treatment could enhance spatial episodic learning and memory ability in healthy rats.

Use of repetitive transcranial magnetic stimulation over the prefrontal cortex increased regional homogeneity in the prefrontal cortex, hippocampus, primary motor cortex, and other brain regions in healthy rats

After rTMS intervention, 13 regions in the rTMS group, namely, the right primary somatosensory cortex (S1), left and right cingulate cortex (Cg), left primary motor cortex (M1), right medial entorhinal cortex (Ent), right retrosplenial granular cortex (RSG), right secondary motor cortex (M2), right retrosplenial dysgranular cortex (RSD), right temporal association cortex (TeA), left dentate gyrus (DG), left cornus ammonis 2 (CA2), left auditory cortex (Au), and left secondary visual cortex (V2) showed increased ReHo ($P < 0.05$, uncorrected, cluster size = 50, Figure 3A) over pre-rTMS. The rTMS group also showed increased ReHo in the left and right Au, right primary/secondary somatosensory cortex (S1/S2), right CA2, right RSG, and left Ent as compared to the control group ($P < 0.05$, uncorrected, cluster size = 50, Figure 3B). Previous studies reported that structures in the frontal module (orbital cortex, prelimbic cortex, cingulate cortex 1, and cingulate cortex 2) belong to the architectonic subdivision of the "orbital medial prefrontal cortex" (OPFC) (Hsu et al., 2016; Carlén, 2017), and DG and CA 2 belong to the hippocampus. In addition, PFC (Cg), hippocampus (DG and CA2), M1/M2, and TeA are the

brain regions important for the interoceptive/default mode network (DMN), whereas the Ent, RSD, and S1/S2 belong to the cortico-striatal-thalamic network. Hippocampus, RSG, and Au are important brain regions of both the interoceptive/DMN and cortico-striatal-thalamic network. Therefore, use of rTMS over the PFC could activate the interoceptive/DMN and cortico-striatal-thalamic network in healthy rats.

Use of repetitive transcranial magnetic stimulation over the prefrontal cortex increased the protein expressions of *N*-methyl-D-aspartic acid receptors and activated the brain-derived neurotrophic factor/TrkB/Akt pathway in the prefrontal cortex, primary motor cortex, and hippocampus in healthy rats

Since NMDA receptors play a central role in synaptic plasticity, the promotion of synaptic plasticity depends on the synthesis of new plasticity-related proteins. To further evaluate the effect and mechanisms of rTMS on brain plasticity, we examined the synaptic plasticity-related proteins NMDA receptors and their interaction with the BDNF/TrkB/Akt pathway through the use of Western blot. We detected the protein expressions of NR1, NR2A, and NR2B in the PFC, hippocampus, and M1. In the PFC, hippocampus, and M1, rTMS over the PFC significantly increased NR1($P < 0.001$, **Figure 4A**; $P < 0.001$, **Figure 4B**; $P < 0.001$, **Figure 4C**, respectively), NR2A ($P < 0.001$, **Figure 4A**; $P < 0.01$, **Figure 4B**; $P < 0.001$, **Figure 4C**, respectively), and NR2B ($P < 0.001$, **Figure 4A**; $P < 0.05$, **Figure 4B**; $P < 0.001$, **Figure 4C**, respectively). To explore the mechanism by which rTMS upregulates NMDA receptors, we focused on BDNF, which stands out for its high level of expression in the brain and its potent effects on synapses. We found rTMS increased the protein expressions of BDNF in the PFC, hippocampus, and M1 ($P < 0.01$, **Figure 4D**; $P < 0.001$, **Figure 4E**; $P < 0.01$, **Figure 4F**, respectively). Moreover, we examined TrkB, the receptor of BDNF, and its downstream p-Akt and Akt in these three brain regions. Western blot showed rTMS increased TrkB ($P < 0.01$, **Figure 4D**; $P < 0.05$, **Figure 4E**; $P < 0.01$, **Figure 4F**, respectively) and p-Akt/Akt ($P < 0.05$, **Figure 4D**; $P < 0.05$, **Figure 4E**; $P < 0.001$, **Figure 4F**, respectively) in the PFC, hippocampus, and M1. All these results indicated that in the PFC, hippocampus, and M1, rTMS-induced neural plasticity was, at least partly, NMDA receptor-dependent synaptic plasticity, and rTMS-induced increase of NMDA receptors might depend on activation of the BDNF/TrkB/Akt pathway in the PFC, hippocampus, and M1.

The synaptic plasticity-related protein NR1 changes in the prefrontal cortex, hippocampus, and primary motor cortex correlated to a cognition improvement in the repetitive transcranial magnetic stimulation-treated healthy rats

Since the NR1 subunit is considered indispensable for functional NMDA receptor assemblies, whereas, NR2A and NR2B subunits are not present at all synaptic NMDA receptors (Papouin et al., 2012), therefore, to study the relationship between the improved cognitive function by rTMS and the NMDA receptor-dependent neural plasticity, we conducted a correlation analysis between the relative band intensity of NR1 and performance in the MWM task (number of crossings) in the PFC, hippocampus, and M1. The analysis showed that after 4 weeks of rTMS, the number of times crossing the platform, reported in the water maze exploration experiment, was positively correlated with the relative protein expression of NR1 in healthy rats in the PFC ($r = 0.597$, $P < 0.05$, **Figure 5A**), hippocampus ($r = 0.759$, $P < 0.01$, **Figure 5B**), and M1 ($r = 0.659$, $P < 0.05$, **Figure 5C**). Taken together, rTMS-induced improvement of cognitive function was significantly correlated with the expression of NMDA receptors in the PFC, hippocampus, and M1.

Discussion

Although a huge number of studies has drawn upon patients or animals with cognitive impairment to study the effects of rTMS on neural plasticity, especially in the PFC and hippocampus, relatively few cognitive impairment studies have focused on the effects of rTMS on the neural plasticity of brain regions other than the PFC and hippocampus, especially the M1 region. Moreover, the potential mechanisms of the enhanced plasticity benefits of rTMS in the PFC for cognitive improvement remain unclear. In this study, we evaluated the ReHo values of the brain using rs-fMRI and detected synaptic plasticity-related proteins to reflect neural plasticity. This study demonstrated that 4 weeks of rTMS over the PFC improved spatial episodic learning and memory ability and promoted brain plasticity via activating the interoceptive/DMN and cortico-striatal-thalamic network in healthy rats, and in the PFC, hippocampus, and M1, rTMS-induced NMDA

receptor-dependent synaptic plasticity correlated to the cognitive improvement. Furthermore, we found rTMS-induced synaptic plasticity in these brain regions was accompanied by activation of the BDNF/TrkB/Akt/NMDAR pathway. We first provide evidence that rTMS-induced cognitive enhancement-related neural plasticity in both the delivered site and the distant sites are, at least partly, a result of NMDA receptor-dependent synaptic plasticity, and the mechanism of the neural plasticity in these activated brain regions might be the activation of the BDNF/TrkB/Akt pathway.

Use of repetitive transcranial magnetic stimulation over the prefrontal cortex improves spatial episodic learning and memory

Repetitive TMS has been shown to improve cognitive impairment in AD patients (Chou et al., 2020; Li et al., 2021). We further investigated the effect of rTMS on cognitive function in healthy rats. The MWM test was conducted after 4 weeks of real/sham rTMS on healthy rats to evaluate their cognitive behaviors. Previous studies suggest that there are many options for intervention sites for rTMS. The PFC, especially the DLPFC, is a core region involved in cognitive functioning, such as working memory and executive functions, and DLPFC plasticity is correlated with cognitive ability in AD (Balderston et al., 2020; Chou et al., 2020; Jones and Graff-Radford, 2021). Therefore, the PFC was chosen as the intervention site in this study. Solé-Padullés et al. (2006) first represented the evidence that rTMS over the left DLPFC is capable of transitorily and positively influencing brain function and cognition among the elderly with memory complaints. A recent systematic review and meta-analysis showed that high-frequency rTMS over the left DLPFC and low-frequency rTMS on the right DLPFC improved memory functions in MCI and AD (Chou et al., 2020). Moreover, several meta-analyses comparing the TMS-induced effect of the different region's stimulation protocols (i.e., left DLPFC) in AD or MCI, showed that the benefits induced by rTMS are most likely due to the stimulation of the left DLPFC (Begemann et al., 2020; Chou et al., 2020). These findings support our use of HF-rTMS over the PFC to investigate cognitive enhancement in healthy rats. Our results showed that rTMS over the PFC could improve spatial learning and memory in healthy rats (**Figure 2**). Consistent with our study, Zhang et al. (2015) and Shang et al. (2019) found HF-rTMS can enhance spatial episodic learning and memory in cognitively impaired animal models, which may be related to the improvement of neural plasticity in the brain.

Use of repetitive transcranial magnetic stimulation over the prefrontal cortex increases regional homogeneity in brain regions in interoceptive/default mode network and the cortico-striatal-thalamic network

Neural plasticity has been defined in terms of the capacity to acquire cognitive skills (Carlén, 2017). It is therefore not surprising that neural plasticity abnormalities are present in patients with cognitive impairment (Burke and Barnes, 2006). The blood-oxygenation-level dependent (BOLD)-fMRI approach has long been used to assess brain plasticity. In this study, brain activity was measured synchronically by using ReHo during rs-fMRI, which showed that rTMS over the PFC increased PFC activity, manifested by the increased ReHo in the PFC, including the left and right cingulate cortex (**Figure 3A**), which was consistent with Yin et al. (2020).

Functional imaging studies indicate that rTMS can affect the physiological functions of not only the brain area below its coil but also relatively distant brain areas. Increasing evidence shows that spatial learning and memory loss are a severe consequence of neural plasticity disturbance in the hippocampus. The two main areas that form the hippocampus – the cornus ammonis 1, 2, and 3 (CA1, CA2, and CA3) and the dentate gyrus (DG) – contribute separately to spatial learning and memory processes. Converging evidence has suggested that DLPFC-hippocampus network connectivity is pathologically involved in preclinical AD (Goveas et al., 2011). In parallel, dialog between the hippocampus and the PFC allows the memory to reemerge into consciousness, which promotes the consolidation and storage of episodic memories (Preston and Eichenbaum, 2013). In this study, although the delivered target of rTMS was the PFC, after rTMS, the ReHo in the rTMS group also increased in CA2, DG, and other brain regions as compared to the pre-rTMS or control group (**Figures 3A,B**). These results suggested that rTMS over the PFC directly induced the neural plasticity in the PFC, and representations in the hippocampus were boosted by indirect manipulation. Consistent with our study, Wang et al. (2014, 2018) found that the targeted enhancement of PFC-hippocampal brain networks improved associative semantic and episodic memory performance, which involved localized long-term plasticity. The roles of the hippocampus and PFC in memory processing, individually or in concert, are a major topic of interest in memory research, and PFC and hippocampus are strongly connected by direct and indirect pathways (Eichenbaum, 2017). Therefore, rTMS over the PFC improves spatial episodic learning and memory via promoting neural plasticity in the PFC-hippocampus.

In recent years, AD was regarded as a disease associated with the deterioration of neural plasticity in the whole

brain. Altered functional connectivity between the DLPFC, posterior hippocampus, and other brain regions with advanced age may contribute to age-related differences in episodic memory (Ankudowich et al., 2019). Therefore, targeting rTMS at the DLPFC may promote interconnected network activity and integration, which may be directly related to the multi-domain cognitive improvements observed (Alcalá-Lozano et al., 2018). Previous studies demonstrated that the DLPFC is considered a key region contributing to several large-scale brain networks, such as the interoceptive/DMN, FPN, and CEN (Liston et al., 2014; Sarpal et al., 2020; Zheng et al., 2020). In this study, compared with both the pre-intervention (**Figure 3A**) and the control groups (**Figure 3B**), the brain regions activated after rTMS were parts of the interoceptive/DMN or cortico-striatal-thalamic network. We also found some reports that were consistent with our results. Dunlop et al. (2016) reported that rTMS over the dorsomedial PFC successfully modulated cortico-striatal connectivity in obsessive-compulsive disorder. By using [^{18}F]-FDG microPET, Parthoens et al. (2014) found that rTMS over the PFC of rats increased neural activity in the medial entorhinal cortex, which is involved in spatial learning and memory (Ga et al., 2013). Hippocampal-targeted theta-burst stimulation enhanced associative memory formation via modulating parahippocampal and retrosplenial cortices (Tambini et al., 2018), which are involved in episodic-like and spatial memory (Sato, 2021). Koch et al. (2018) reported that rTMS enhanced memory and neural activity in AD patients by manipulating DMN. These all support the fact that rTMS over the PFC could improve spatial learning and memory and promote neural plasticity by activating interoceptive/DMN and the cortico-striatal-thalamic network, which is consistent with our findings.

Repetitive transcranial magnetic stimulation-induced neural plasticity is, at least partly, *N*-methyl-D-aspartic acid receptor-dependent synaptic plasticity

Resting state-fMRI in this study provided indirect evidence that HF-rTMS over the PFC increased neural plasticity in the PFC, hippocampus, M1, and other brain regions, which belong to the interoceptive/DMN and the cortico-striatal-thalamic network. A previous study showed that stimulating this region directly excited neurons, and consequently reduced the synaptic conduction threshold, thereby making the synapse become relatively active and increasing the synaptic connections (Gribkova and Gillette, 2021). Several basic studies reported that HF-rTMS improved cognitive function by regulating synaptic plasticity in rodents with cognitive impairment (Zhang et al., 2015; Shang et al., 2019). Therefore, as a form of neural plasticity, synaptic plasticity needs concern in this study.

N-Methyl-D-aspartic acid receptors, the major mediator of postsynaptic response during synaptic neurotransmission, are thought to be able to generate a persistent increase in synaptic strength and participate in the regulation of synaptic plasticity, memory, and cognition. Activation of NMDA receptors allows a calcium flux into dendritic spines that serve as the proximal trigger for synaptic plasticity. Impaired NMDA receptors' function is regarded as the most likely cause of the NMDA receptor-dependent cortical plasticity deficit in aging and AD (Battaglia et al., 2007). Using GLYX-13, an NMDA receptor glycine site functional partial agonist, could enhance cognition (Moskal et al., 2014). Whereas, the NMDA receptor antagonist memantine was regarded as a symptomatological and neuroprotective treatment for AD (Danysz and Parsons, 2003). Therefore, we detected the protein expression of NR1, NR2A, and NR2B in several brain regions. Consistent with the result of the rs-fMRI, we also found rTMS significantly increased synaptic plasticity in the PFC, hippocampus, and M1, as manifested by the increased protein expression of synaptic plasticity-related proteins NR1, NR2A, and NR2B in these brain regions, indicating rTMS-induced neural plasticity might be synaptic plasticity (**Figures 4A–C**). Consistent with our results, Zhang et al. (2015) and Shang et al. (2016), respectively, found that rTMS facilitated spatial cognition and synaptic plasticity associated with up-regulation of NR1, NR2A, and NR2B in the hippocampus. Based on the above, the rTMS-induced NMDA receptor-dependent synaptic plasticity occurred not just locally in the targeted delivered site but also in the non-stimulated brain regions at distant sites, and it is reasonable to believe that NMDA receptor-dependent synaptic plasticity is, at least partly, the underlying mechanism of rTMS-induced neural plasticity.

Use of repetitive transcranial magnetic stimulation over the prefrontal cortex induces upregulation of *N*-methyl-D-aspartic acid receptors by activating the brain-derived neurotrophic factor/TrkB/Akt pathway

Another concern is how rTMS upregulates NMDA receptors in different brain regions. It is now widely accepted that the main function of BDNF in the adult brain is to regulate synapses, with structural and functional effects ranging from short-term to long-lasting, on excitatory or inhibitory synapses, in many brain regions. Previous studies showed that rTMS improved cognition, increased BDNF-NMDAR pathway level and synaptic plasticity, and enhanced cognitive behavior in cognitively impaired patients or animal models

(Zhang et al., 2015; Velioglu et al., 2021). The effects of BDNF in rTMS-induced synaptic plasticity are mediated by its specific membrane-bound receptor TrkB (tropomyosin-related kinase B) receptors (Shang et al., 2019). A previous study showed that increasing the phosphorylation of Akt in hippocampal neurons by activation of BDNF/TrkB signaling would upregulate NMDA receptors and promote synaptic plasticity (Nakai et al., 2014), and cognitive decline in different models accompanied by decreasing the level of BDNF/TrkB signaling (Mercerón-Martínez et al., 2021). In addition, Li et al. (2022) reported that activation of Akt promoted the interaction of cAMP-response element-binding protein (CREB) and the promoter of NR2B to increase NR2B. Kay et al. (2013) and Hu et al. (2015), respectively, reported that activation of Akt/CREB also increased NR1 and NR2A, and that the inhibition of BDNF-PI3K/Akt or Akt/CREB pathways led to chronic nervous system impairment. Thus, we speculated that rTMS increased NMDA receptors via activating BDNF/TrkB/Akt pathway. The increase of NMDA receptors accompanied by increasing in BDNF, TrkB, and p-Akt/Akt in the PFC, hippocampus, and M1 verified the speculation (**Figures 4D–F**). Therefore, rTMS promotes NMDA receptor-dependent synaptic plasticity by activating BDNF/TrkB/Akt pathways in the PFC, hippocampus, and M1.

Repetitive transcranial magnetic stimulation-induced upregulation of NR1 in the prefrontal cortex, hippocampus, and primary motor cortex correlates with cognitive enhancement

A number of studies have shown that rTMS-induced neural plasticity in the PFC or hippocampus correlated with cognition enhancement (Wang et al., 2014, 2018). Recently, Li et al. (2019) reported that 6 weeks of HF-rTMS treatment over the left DLPFC improved long-term potentiation-like plasticity in M1 in AD patients, and the long-term potentiation-like plasticity improvement in M1 correlated to the observed cognition change. Considering that no other studies to date have reported cognition-related plasticity was shown in the M1 after rTMS over the PFC, therefore, based on Li's study, in addition to the PFC and hippocampus, we also found that rTMS over the PFC led to an increase in ReHo in the M1 by rs-fMRI and an upregulation of synaptic plasticity-related proteins by Western blot in M1, indicating rTMS-induced NMDA receptor-dependent synaptic plasticity in the PFC, hippocampus, and M1. The NR1 subunit is often considered indispensable for functional NMDA receptor assemblies, thus we detected the correlation between protein expressions of NR1 and rTMS-induced cognitive changes. More specifically, we found protein expressions of NR1 in the PFC, hippocampus, and M1 correlated with rTMS-induced cognitive changes (**Figures 5A–C**). In clinical practice, M1 plasticity is relatively easy to acquire. Therefore, in the future, detection of the neural plasticity in the M1, and perhaps in other brain regions, might be a potential assessment tool reflecting cognition and the therapeutic effect of rTMS. Collectively, enhancement of the cognitive abilities by rTMS over the PFC is associated with modulation of the neural plasticity of interoceptive/DMN and cortico-striatal-thalamic network in the brain.

Limitations

Several limitations are inherent in the present study. First, we only demonstrated that the PFC rTMS can improve cognition in healthy rats, but we have not verified it in disease models. Whether the effects of rTMS observed in the healthy rats could also be replicated in cognitively impaired rats should be investigated further. Second, our sample size, especially in terms of the number of rats who underwent rs-fMRI, was small, thus the functional connectivity analysis-related study could not be performed in this study. Finally, stimulation from the coil could not be accurately localized to a specific brain area because of the small size of the rat brain compared with the size of the coil. Therefore, we could not ensure that each stimulation was applied to the exact same area. Further study will be required to rigorously evaluate whether effects are truly inverted and if the same inversion is present for other stimulation targets.

Conclusion

The present results demonstrated that HF-rTMS over the PFC improved spatial episodic learning and memory and promoted brain plasticity via activating interoceptive/DMN and cortico-striatal-thalamic network in healthy rats. In addition, rTMS-induced brain plasticity, locally in the targeted delivered site and in the non-stimulated regions at distant sites, was NMDA receptor-dependent synaptic plasticity, which was achieved through activating the BDNF/TrkB/Akt pathway. In conclusion, we demonstrated that HF-rTMS can enhance cognitive performance through the modulation of NMDA receptor-dependent brain plasticity.

Data availability statement

The original contributions presented in this study are included in the article/supplementary material, further inquiries can be directed to the corresponding authors.

Ethics statement

The animal study was reviewed and approved by the Ethics Committee of Nanjing Medical University.

Author contributions

YS, QW, and XX contributed to the conception and design of the study. XX and QW performed the experiments. QW, ZZ, and CZ conducted the statistical analyses. TW and ZZ provided expert interpretation of the data. QW and YS drafted the manuscript. WD, QW, and YS edited and confirmed the final manuscript. YS and TW were the principal investigators of the study and were responsible for the study conception and interpretation of the data, and had final responsibility for the decision to submit the manuscript for publication. All authors listed have made a substantial, direct, and intellectual contribution to the work, and approved it for publication.

Funding

The National Key R&D Program of China (Grant Numbers: 2018YFC2001600 and 2018YFC2001603) and the Nanjing Municipal Science and Technology Bureau (Grant Number: 2019060002).

Acknowledgments

We thank Dr. Liu Wentao in Jiangsu Key Laboratory of Neurodegeneration of Nanjing Medical University in experimental conduction.

Conflict of interest

The authors declare that the research was conducted in the absence of any commercial or financial relationships that could be construed as a potential conflict of interest.

Publisher's note

All claims expressed in this article are solely those of the authors and do not necessarily represent those of their affiliated organizations, or those of the publisher, the editors and the reviewers. Any product that may be evaluated in this article, or claim that may be made by its manufacturer, is not guaranteed or endorsed by the publisher.

References

Alcalá-Lozano, R., Morelos-Santana, E., Cortés-Sotres, J. F., Garza-Villarreal, E. A., Sosa-Ortiz, A. L., and González-Olvera, J. J. (2018). Similar clinical improvement and maintenance after rTMS at 5 Hz using a simple vs. complex protocol in Alzheimer's disease. *Brain Stimul.* 11, 625–627. doi: 10.1016/j.brs.2017.12.011

Ankudowich, E., Pasvanis, S., and Rajah, M. N. (2019). Age-related differences in prefrontal-hippocampal connectivity are associated with reduced spatial context memory. *Psychol. Aging* 34, 251–261. doi: 10.1037/pag0000310

Balderston, N. L., Flook, E., Hsiung, A., Liu, J., Thongarong, A., Stahl, S., et al. (2020). Patients with anxiety disorders rely on bilateral dlPFC activation during verbal working memory. *Soc. Cogn. Affect. Neurosci.* 15, 1288–1298. doi: 10.1093/scan/nsaa146

Battaglia, F., Wang, H.-Y., Ghilardi, M. F., Gashi, E., Quartarone, A., Friedman, E., et al. (2007). Cortical plasticity in Alzheimer's Disease in humans and rodents. *Biol. Psychiat.* 62, 1405–1412. doi: 10.1016/j.biopsych.2007.02.027

Begemann, M. J., Brand, B. A., Ćurčić-Blake, B., Aleman, A., and Sommer, I. E. (2020). Efficacy of non-invasive brain stimulation on cognitive functioning in brain disorders: a meta-analysis. *Psychol. Med.* 50, 2465–2486. doi: 10.1017/S0033291720003670

Brier, M. R., Thomas, J. B., and Ances, B. M. (2014). Network dysfunction in Alzheimer's Disease: Refining the disconnection hypothesis. *Brain Connect* 4, 299–311. doi: 10.1089/brain.2014.0236

Brown, J. C., Yuan, S., DeVries, W. H., Armstrong, N. M., Korte, J. E., Sahlem, G. L., et al. (2021). NMDA-receptor agonist reveals LTP-like properties of 10-Hz rTMS in the human motor cortex. *Brain Stimulat.* 14, 619–621.

Burke, S. N., and Barnes, C. A. (2006). Neural plasticity in the ageing brain. *Nat. Rev. Neurosci.* 7, 30–40. doi: 10.1038/nrn1809

Cai, S., Peng, Y., Chong, T., Zhang, Y., von Deneen, K. M., and Huang, L. (2017). Differentiated effective connectivity patterns of the executive control network in progressive MCI: A potential biomarker for predicting AD. *Curr. Alzheimer Res.* 14, 937–950. doi: 10.2174/1567205014666170309120200

Carlén, M. (2017). What constitutes the prefrontal cortex? *Science* 358, 478–482. doi: 10.1126/science.aan8868

Chou, Y., Ton That, V., and Sundman, M. (2020). A systematic review and meta-analysis of rTMS effects on cognitive enhancement in mild cognitive impairment and Alzheimer's disease. *Neurobiol. Aging* 86, 1–10. doi: 10.1016/j.neurobiolaging.2019.08.020

Danysz, W., and Parsons, C. G. (2003). The NMDA receptor antagonist memantine as a symptomatological and neuroprotective treatment for Alzheimer's disease: preclinical evidence. *Int. J. Geriatr. Psychiat.* 18, S23–S32. doi: 10.1002/gps.938

Dunlop, K., Woodside, B., Olmsted, M., Colton, P., Giacobbe, P., and Downar, J. (2016). Reductions in Cortico-Striatal Hyperconnectivity Accompany Successful Treatment of Obsessive-Compulsive Disorder with Dorsomedial Prefrontal rTMS. *Neuropsychopharmacology* 41, 1395–1403. doi: 10.1038/npp.2015.292

Eichenbaum, H. (2017). Prefrontal-hippocampal interactions in episodic memory. *Nat. Rev. Neurosci.* 18, 547–558. doi: 10.1038/nrn.2017.74

Esposito, S., Trojsi, F., Cirillo, G., de Stefano, M., Di Nardo, F., Siciliano, M., et al. (2022). Repetitive Transcranial Magnetic Stimulation (rTMS) of dorsolateral prefrontal cortex may influence semantic fluency and functional connectivity in fronto-parietal network in mild cognitive impairment (MCI). *Biomedicines* 10:994. doi: 10.3390/biomedicines10050994

Ga, R., Mp, B., Ej, W., and Gw, R. (2013). Young APOE4 targeted replacement mice exhibit poor spatial learning and memory, with reduced dendritic spine density in the medial entorhinal cortex. *Learn. Memory* 20, 256–266. doi: 10.1101/lm.030031.112

Gersner, R., Kravetz, E., Feil, J., Pell, G., and Zangen, A. (2011). Long-Term effects of repetitive transcranial magnetic stimulation on markers for

neuroplasticity: Differential outcomes in anesthetized and awake animals. *J. Neurosci.* 31, 7521–7526. doi: 10.1523/JNEUROSCI.6751-10.2011

Giglia, G., Gambino, G., Cuffaro, L., Aleo, F., Sardo, P., Ferraro, G., et al. (2021). Modulating long term memory at late-encoding phase: An rTMS study. *Brain Topogr.* 34, 834–839. doi: 10.1007/s10548-021-00872-y

Goveas, J. S., Xie, C., Ward, B. D., Wu, Z., Li, W., Franczak, M., et al. (2011). Recovery of hippocampal network connectivity correlates with cognitive improvement in mild Alzheimer's disease patients treated with donepezil assessed by resting-state fMRI. *J. Magn. Reson. Imaging* 34, 764–773. doi: 10.1002/jmri.22662

Gribkova, E. D., and Gillette, R. (2021). Role of NMDAR plasticity in a computational model of synaptic memory. *Sci. Rep.* 11:21182.

Guo, Y., Dang, G., Hordacre, B., Su, X., Yan, N., Chen, S., et al. (2021). Repetitive transcranial magnetic stimulation of the dorsolateral prefrontal cortex modulates electroencephalographic functional connectivity in Alzheimer's Disease. *Front. Aging Neurosci.* 13:679585. doi: 10.3389/fnagi.2021.679585

Hong, Y., Liu, Q., Peng, M., Bai, M., Li, J., Sun, R., et al. (2020). High-frequency repetitive transcranial magnetic stimulation improves functional recovery by inhibiting neurotoxic polarization of astrocytes in ischemic rats. *J. Neuroinflam.* 17:150. doi: 10.1186/s12974-020-01747-y

Hsu, L.-M., Liang, X., Gu, H., Brynildsen, J. K., Stark, J. A., Ash, J. A., et al. (2016). Constituents and functional implications of the rat default mode network. *Proc. Natl. Acad. Sci. U. S. A.* 113, E4541–E4547. doi: 10.1073/pnas.1601485113

Hu, X.-L., Gao, L.-Y., Niu, Y.-X., Tian, X., Wang, J., Meng, W.-H., et al. (2015). Neuroprotection by Kukoamine a against oxidative stress may involve N-methyl-D-aspartate receptors. *Biochim. Biophys. Acta* 1850, 287–298. doi: 10.1016/j.bbagen.2014.11.006

Jones, D. T., and Graff-Radford, J. (2021). Executive dysfunction and the prefrontal cortex. *Continuum* 27, 1586–1601. doi: 10.1212/CON.0000000000001009

Kay, J. C., Xia, C.-M., Liu, M., Shen, S., Yu, S. J., Chung, C., et al. (2013). Endogenous PI3K/Akt and NMDAR act independently in the regulation of CREB activity in lumbosacral spinal cord in cystitis. *Exp. Neurol.* 250, 366–375. doi: 10.1016/j.expneurol.2013.10.015

Koch, G., Bonnì, S., Pellicciari, M. C., Casula, E. P., Mancini, M., Esposito, R., et al. (2018). Transcranial magnetic stimulation of the precuneus enhances memory and neural activity in prodromal Alzheimer's disease. *Neuroimage* 169, 302–311. doi: 10.1016/j.neuroimage.2017.12.048

Kohl, S., Hannah, R., Rocchi, L., Nord, C. L., Rothwell, J., and Voon, V. (2019). Cortical paired associative stimulation influences response inhibition: cortico-cortical and cortico-subcortical networks. *Biol. Psychiat.* 85, 355–363. doi: 10.1016/j.biopsych.2018.03.009

Li, M.-L., Peng, Y., An, Y., Li, G.-Y., and Lan, Y. (2022). LY395756 promotes NR2B expression via activation of AKT/CREB signaling in the juvenile methylazoxymethanol mice model of schizophrenia. *Brain Behav.* 12:e2466. doi: 10.1002/brb3.2466

Li, P., Legault, J., and Litcofsky, K. A. (2014). Neuroplasticity as a function of second language learning: Anatomical changes in the human brain. *Cortex* 58, 301–324. doi: 10.1016/j.cortex.2014.05.001

Li, X., Qi, G., Yu, C., Lian, G., Zheng, H., Wu, S., et al. (2021). Cortical plasticity is correlated with cognitive improvement in Alzheimer's disease patients after rTMS treatment. *Brain Stimulat.* 14, 503–510. doi: 10.1016/j.brs.2021.01.012

Li, Y., Li, L., and Pan, W. (2019). Repetitive transcranial magnetic stimulation (rTMS) Modulates hippocampal structural synaptic plasticity in rats. *Physiol. Res.* 68, 99–105. doi: 10.33549/physiolres.933772

Lin, C.-H., Huang, Y.-J., Lin, C.-J., Lane, H.-Y., and Tsai, G. (2014). NMDA neurotransmission dysfunction in mild cognitive impairment and Alzheimer's Disease. *Curr. Pharm. Des.* 20, 5169–5179. doi: 10.2174/1381612819666140110115603

Liston, C., Chen, A. C., Zebley, B. D., Drysdale, A. T., Gordon, R., Leuchter, B., et al. (2014). Default mode network mechanisms of transcranial magnetic stimulation in depression. *Biol. Psychiat.* 76, 517–526. doi: 10.1016/j.biopsych.2014.01.023

Ma, J., Zhang, Z., Kang, L., Geng, D., Wang, Y., Wang, M., et al. (2014). Repetitive transcranial magnetic stimulation (rTMS) influences spatial cognition and modulates hippocampal structural synaptic plasticity in aging mice. *Exp. Gerontol.* 58, 256–268. doi: 10.1016/j.exger.2014.08.011

Mercerón-Martínez, D., Ibaceta-González, C., Salazar, C., Almaguer-Melian, W., Bergado-Rosado, J. A., and Palacios, A. G. (2021). Alzheimer's Disease, Neural Plasticity, and Functional Recovery. *J. Alzheimers Dis.* 82, S37–S50. doi: 10.3233/JAD-201178

Moskal, J. R., Burch, R., Burgdorf, J. S., Kroes, R. A., Stanton, P. K., Disterhoft, J. F., et al. (2014). GLYX-13, an NMDA receptor glycine site functional partial agonist enhances cognition and produces antidepressant effects without the psychotomimetic side effects of NMDA receptor antagonists. *Exp. Opin. Investig. Drugs* 23, 243–254. doi: 10.1517/13543784.2014.852536

Nakai, T., Nagai, T., Tanaka, M., Itoh, N., Asai, N., Enomoto, A., et al. (2014). Girdin phosphorylation is crucial for synaptic plasticity and memory: A potential role in the interaction of BDNF/TrkB/Akt signaling with NMDA receptor. *J. Neurosci.* 34, 14995–15008. doi: 10.1523/JNEUROSCI.2228-14.2014

Noguchi-Shinohara, M., Koike, M., Morise, H., Kudo, K., Tsuchimine, S., Komatsu, J., et al. (2021). MEG activity of the dorsolateral prefrontal cortex during optic flow stimulations detects mild cognitive impairment due to Alzheimer's disease. *PLoS One* 16:e0259677. doi: 10.1371/journal.pone.0259677

Papouin, T., Ladépêche, L., Ruel, J., Sacchi, S., Labasque, M., Hanini, M., et al. (2012). Synaptic and extrasynaptic NMDA receptors are gated by different endogenous coagonists. *Cell* 150, 633–646. doi: 10.1016/j.cell.2012.06.029

Parthoens, J., Verhaeghe, J., Wyckhuys, T., Stroobants, S., and Staelens, S. (2014). Small-animal repetitive transcranial magnetic stimulation combined with [^{18}F]-FDG microPET to quantify the neuromodulation effect in the rat brain. *Neuroscience* 275, 436–443. doi: 10.1016/j.neuroscience.2014.06.042

Preston, A. R., and Eichenbaum, H. (2013). Interplay of hippocampus and prefrontal cortex in memory. *Curr. Biol.* 23, R764–R773. doi: 10.1016/j.cub.2013.05.041

Sarpal, D. K., Tarcijonas, G., Calabro, F. J., Foran, W., Haas, G. L., Luna, B., et al. (2020). Context-specific abnormalities of the central executive network in first-episode psychosis: relationship with cognition. *Psychol. Med.* 1–10. [Epub ahead of print]. doi: 10.1017/S0033291720004201

Sato, N. (2021). Episodic-like memory of rats as retrospective retrieval of incidentally encoded locations and involvement of the retrosplenial cortex. *Sci. Rep.* 11:2217. doi: 10.1038/s41598-021-81943-9

Scheltens, P., De Strooper, B., Kivipelto, M., Holstege, H., Chételat, G., Teunissen, C. E., et al. (2021). Alzheimer's disease. *Lancet* 397, 1577–1590. doi: 10.1016/S0140-6736(20)32205-4

Shang, Y., Wang, X., Li, F., Yin, T., Zhang, J., and Zhang, T. (2019). rTMS Ameliorates Prenatal Stress–Induced Cognitive Deficits in Male-Offspring Rats Associated With BDNF/TrkB Signaling Pathway. *Neurorehabil. Neural Repair* 33, 271–283. doi: 10.1177/1545968319834898

Shang, Y., Wang, X., Shang, X., Zhang, H., Liu, Z., Yin, T., et al. (2016). Repetitive transcranial magnetic stimulation effectively facilitates spatial cognition and synaptic plasticity associated with increasing the levels of BDNF and synaptic proteins in Wistar rats. *Neurobiol. Learn. Mem.* 134, 369–378. doi: 10.1016/j.nlm.2016.08.016

Solé-Padullés, C., Bartrés-Faz, D., Junqué, C., Clemente, I. C., Molinuevo, J. L., Bargalló, N., et al. (2006). Repetitive transcranial magnetic stimulation effects on brain function and cognition among elders with memory dysfunction. a randomized sham-controlled study. *Cereb. Cortex* 16, 1487–1493. doi: 10.1093/cercor/bhj083

Stagg, C. J., O'Shea, J., and Johansen-Berg, H. (2010). Imaging the effects of rTMS-induced cortical plasticity. *Restor. Neurol. Neurosci.* 28, 425–436. doi: 10.3233/RNN-2010-0553

Tambini, A., Nee, D. E., and D'Esposito, M. (2018). Hippocampal-targeted Theta-burst Stimulation Enhances Associative Memory Formation. *J. Cogn. Neurosci.* 30, 1452–1472. doi: 10.1162/jocn_a_01300

Todd, T. P., Fournier, D. I., and Bucci, D. J. (2019). Retrosplenial cortex and its role in cue-specific learning and memory. *Neurosci. Biobehav. Rev.* 107, 713–728. doi: 10.1016/j.neubiorev.2019.04.016

Tsien, J. Z., Huerta, P. T., and Tonegawa, S. (1996). The essential role of hippocampal CA1 NMDA receptor–dependent synaptic plasticity in spatial memory. *Cell* 87, 1327–1338. doi: 10.1016/S0092-8674(00)81827-9

Velioglu, H. A., Hanoglu, L., Bayraktaroglu, Z., Toprak, G., Guler, E. M., Bektay, M. Y., et al. (2021). Left lateral parietal rTMS improves cognition and modulates resting brain connectivity in patients with Alzheimer's disease: Possible role of BDNF and oxidative stress. *Neurobiol. Learn Mem.* 180:107410. doi: 10.1016/j.nlm.2021.107410

Wang, J. X., Rogers, L. M., Gross, E. Z., Ryals, A. J., Dokucu, M. E., Brandstatt, K. L., et al. (2014). Targeted enhancement of cortical-hippocampal brain networks and associative memory. *Science* 345, 1054–1057. doi: 10.1126/science.1252900

Wang, W. C., Wing, E. A., Murphy, D. L. K., Luber, B. M., Lisanby, S. H., Cabeza, R., et al. (2018). Excitatory TMS modulates memory representations. *Cogn. Neurosci.* 9, 151–166. doi: 10.1080/17588928.2018.1512482

Yin, M., Liu, Y., Zhang, L., Zheng, H., Peng, L., Ai, Y., et al. (2020). Effects of rTMS treatment on cognitive impairment and resting-state brain activity in

stroke patients: A randomized clinical trial. *Front. Neural. Circ.* 14:563777. doi: 10.3389/fncir.2020.563777

Zarei, M., Beckmann, C. F., Binnewijzend, M. A. A., Schoonheim, M. M., Oghabian, M. A., Sanz-Arigita, E. J., et al. (2013). Functional segmentation of the hippocampus in the healthy human brain and in Alzheimer's disease. *NeuroImage* 66, 28–35. doi: 10.1016/j.neuroimage.2012.10.071

Zhang, N., Xing, M., Wang, Y., Tao, H., and Cheng, Y. (2015). Repetitive transcranial magnetic stimulation enhances spatial learning and synaptic plasticity via the VEGF and BDNF–NMDAR pathways in a rat model of vascular dementia. *Neuroscience* 311, 284–291. doi: 10.1016/j.neuroscience.2015.10.038

Zheng, A., Yu, R., Du, W., Liu, H., Zhang, Z., Xu, Z., et al. (2020). Two-week rTMS-induced neuroimaging changes measured with fMRI in depression. *J. Affect Disord.* 270, 15–21. doi: 10.1016/j.jad.2020.03.038

Zorzo, C., Méndez, M., Pernía, A. M., and Arias, J. L. (2021). Repetitive transcranial magnetic stimulation during a spatial memory task leads to a decrease in brain metabolic activity. *Brain Res.* 1769:147610. doi: 10.1016/j.brainres.2021.147610

frontiers | Frontiers in Neuroscience

TYPE Original Research
PUBLISHED 25 August 2022
DOI 10.3389/fnins.2022.949698

OPEN ACCESS

EDITED BY
Xiang Li,
Massachusetts General Hospital and Harvard Medical School, United States

REVIEWED BY
Caihong Wang,
The First Affiliated Hospital of Zhengzhou University, China
Enze Shi,
Northwestern Polytechnical University, China

*CORRESPONDENCE
Jiliang Fang
fangmgh@163.com
Yong Liu
1909768139@qq.com

†These authors have contributed equally to this work and share first authorship

SPECIALTY SECTION
This article was submitted to Brain Imaging Methods, a section of the journal Frontiers in Neuroscience

RECEIVED 21 May 2022
ACCEPTED 08 August 2022
PUBLISHED 25 August 2022

CITATION
Sun J, Guo C, Ma Y, Du Z, Wang Z, Luo Y, Chen L, Gao D, Li X, Xu K, Hong Y, Yu X, Xiao X, Fang J and Liu Y (2022) A comparative study of amplitude of low-frequence fluctuation of resting-state fMRI between the younger and older treatment-resistant depression in adults.
Front. Neurosci. 16:949698.
doi: 10.3389/fnins.2022.949698

A comparative study of amplitude of low-frequence fluctuation of resting-state fMRI between the younger and older treatment-resistant depression in adults

Jifei Sun[1†], Chunlei Guo[1†], Yue Ma[1], Zhongming Du[2], Zhi Wang[1], Yi Luo[1], Limei Chen[1], Deqiang Gao[1], Xiaojiao Li[1], Ke Xu[1], Yang Hong[1], Xue Yu[3], Xue Xiao[3], Jiliang Fang[1*] and Yong Liu[4*]

[1]Guang'anmen Hospital, China Academy of Chinese Medical Sciences, Beijing, China, [2]Dongzhimen Hospital, Beijing University of Chinese Medicine, Beijing, China, [3]Beijing First Hospital of Integrated Chinese and Western Medicine, Beijing, China, [4]Affiliated Hospital of Traditional Chinese Medicine, Southwest Medical University, Luzhou, China

Background: Treatment-resistant depression (TRD) may have different physiopathological neuromechanism in different age groups. This study used the amplitude of low frequency fluctuations (ALFF) to initially compare abnormalities in local functional brain activity in younger and older patients with TRD.

Materials and methods: A total of 21 older TRD patients, 19 younger TRD, 19 older healthy controls (HCs), and 19 younger HCs underwent resting-state functional MRI scans, and the images were analyzed using the ALFF and further analyzed for correlation between abnormal brain regions and clinical symptoms in TRD patients of different age groups.

Results: Compared with the older TRD, the younger TRD group had increased ALFF in the left middle frontal gyrus and decreased ALFF in the left caudate nucleus. Compared with the matched HC group, ALFF was increased in the right middle temporal gyrus and left pallidum in the older TRD group, whereas no significant differences were found in the younger TRD group. In addition, ALFF values in the left middle frontal gyrus in the younger TRD group and in the right middle temporal gyrus in the older TRD were both positively correlated with the 17-item Hamilton Rating Scale for Depression score.

Conclusion: Different neuropathological mechanisms may exist in TRD patients of different ages, especially in the left middle frontal gyrus and left caudate nucleus. This study is beneficial in providing potential key targets for the clinical management of TRD patients of different ages.

KEYWORDS

treatment-resistant depression (TRD), amplitude of low-frequency fluctuation, MRI, major depressive disorder (MDD), age

Introduction

Major depressive disorder (MDD) is a common clinical psychiatric disorder with depressed mood, decreased cognitive function and somatic disorders as the main clinical features (Lawson et al., 2017). Epidemiological surveys show that MDD is expected to be the number one disease burden globally by 2030 (Ho et al., 2018). In addition, MDD is the leading cause of disability worldwide, with approximately 800,000 deaths by suicide each year (Fabbri et al., 2021). However, despite numerous studies, 30–40% of MDD patients still do not respond significantly antidepressants (Bergfeld et al., 2018). This type of MDD that does not respond significantly to two adequate doses and courses of antidepressant medication can be called treatment-resistant depression (TRD) (Gaynes et al., 2020). TRD is a complex subtype of MDD with lower quality of life, higher costs and more severe activity impairment than non-TRD (Qiao et al., 2017; Jaffe et al., 2019). Therefore, understanding the pathogenesis of TRD and exploring potential biomarkers are of great importance to guide clinical treatment.

Patients with TRD may have differences in clinical symptoms at different ages. Previous studies have shown that younger TRD have more severe depressive symptoms than older TRD (Conelea et al., 2017). In addition, older TRD tend to have more severe cognitive and somatic dysfunction (Mulsant and Pollock, 1998; Knöchel et al., 2015). It has also been shown that age has been shown to be a moderator of response to treatment with numerous antidepressants (Ochs-Ross et al., 2020). Therefore, these different clinical symptoms suggest that different neuropathological mechanisms may exist in TRD patients of different ages.

However, there are fewer studies on the age classification of younger and older TRD patients, and there is no uniform consensus. A study defined the age of younger TRD patients as under 60 years (<60 years), while older TRD patients were defined as over 60 years (≥60 years), suggest that the younger group was more likely to have a history of psychiatric hospitalization and higher depression severity scores (Conelea et al., 2017). Another study defined the age range of TRD in adolescents as 14–17 years (Ghaziuddin et al., 2011). In addition, some studies have defined the age range of older TRD as 55–72 years (Lijffijt et al., 2022) and 65–84 years (Gronemann et al., 2020), but these studies were single-age studies and lacked the effect of different age boundaries on the primary outcome. Therefore, the neurobiological evidence for the age boundary between younger and older TRD is unclear and further clinical studies are necessary to elucidate it.

In recent years, resting state-functional functional magnetic resonance (rs-fMRI) has been gradually applied in the field of psychiatric disorders, including MDD (Wang et al., 2020; Liu P. et al., 2021), autism (Guo et al., 2017), and bipolar disorder (Zhang et al., 2021a). Amplitude of low-frequency fluctuation (ALFF) is a commonly studied metric in rs-fMRI and is able to describe the intensity of spontaneous brain activity in the resting state from an energy perspective (Zang et al., 2007). In addition, ALFF has been recently applied to clinical studies of MDD subtypes of disease (Guo et al., 2012; Liu et al., 2015). Only one study of ALFF at different ages in MDD with a first episode and without medication, and the abnormal brain regions in both groups were concentrated in the frontal, temporal, parietal, and occipital lobes (Guo et al., 2013). Up to date, little is known about the neuroimaging differences between younger and older TRD.

However, the use of an earlier age of onset to differentiate between different age groups of MDD patients is susceptible to severe psychopathology and risk factors (Klein et al., 1999; Zisook et al., 2007). Previous studies have found that age-related changes in affective, cognitive, and reasoning functions stabilize between the ages of 20 and 60 (Hedden and Gabrieli, 2004). In addition, another clinical study with a large sample observed different clinical symptoms of MDD in early onset depression (EOD) and late onset depression (LOD), using a cut-off age of 40 years (Korten et al., 2012). Therefore, we focused on younger TRD (21–40 years) and older TRD (41–60 years) as the age division range. This study was based on ALFF and focused on the differences in local functional brain activity between younger TRD and older TRD patients. In addition, to explore whether there is a correlation between abnormal brain area alters and clinical symptoms in the TRD group. This study will provide some insight into understanding the neuropathological mechanisms of TRD at different ages.

Materials and methods

Participants

A total of 40 outpatients with TRD from Guang'anmen Hospital, China Academy of Chinese Medical Sciences, Beijing First Hospital of Integrated Chinese and Western Medicine, and Xuanwu Hospital of the Capital Medical University, were recruited for this study. All patients with TRD showed the initial diagnosis of MDD in the fifth edition of the American Diagnostic and Statistical Manual of Mental Disorders (DSM-V). The inclusion criteria were as follows: (1) age, 21–60 years; (2) 17-item Hamilton depression rating scale (HAMD-17) score $>$ 17; (3) right-handedness; (4) no response to two or more adequate doses and courses of antidepressant therapy. Thirty-eight gender- and age-matched healthy controls (HCs) (16 men and 22 women) were included in the HC group, which reflected the following: (1) age, 21–60 years; (2) HAMD-17 score $<$ 7; (3) right-handedness; (4) no history of any mental illness in first-degree relatives.

The exclusion criteria for patients and HCs were as follows: (1) serious mental illness and other diseases such as cardiovascular and cerebrovascular disorders; (2) history of drug and alcohol abuse; (3) any contraindications to MRI, such as presence of a heart pacemaker, metal fixed false teeth, or severe claustrophobia; (4) pregnant or lactating status; (5) bipolar disorder or suicidal ideation.

All patients were required to sign an informed consent form before enrollment. This study was approved by the ethics committee of Guang'anmen Hospital, China Academy of Chinese Medical Sciences.

Clinical materials and subgroups

In this study, we collected clinical information on all participants, including gender, age, years of education, and duration of illness. Patients in the TRD group were diagnosed by experienced psychiatrists and assessed for depression severity using the HAMD-17 scale. According to previous studies (Korten et al., 2012), all patients were divided into younger TRD group (21–40 years) and older TRD group (41–60 years). The HC group was also divided into two subgroups: younger HC group (21–40 years) and older HC group (41–60 years).

Scan acquisition

All subjects in this study underwent MRI using a Magnetom Skyra 3.0 T scanner (Siemens, Erlangen, Germany), and the scans were performed at Guang'anmen Hospital, China Academy of Chinese Medical Sciences, and the scan parameters were the same. Before the scanning procedure, the subjects were instructed to remain awake and avoid active thinking. During the scanning process, the subjects were required to wear earplugs and noise-canceling headphones, to use a hood to immobilize the head, and to lie flat on the examination bed. The scanning procedure involved a localizer scan, high-resolution three-dimensional T1-weighted imaging, and BOLD-fMRI.

The scanning parameters were as follows: for three-dimensional T1-weighted imaging, time repetition/time echo = 2500/2.98 ms, flip angle = 7°, matrix = 64 × 64, field of view = 256 mm × 256 mm, slice thickness = 1 mm, slice number = 48, slices = 192, scanning time = 6 min 3 s; for BOLD-fMRI, time repetition/time echo = 2000/30 ms, flip angle = 90°, matrix = 64 × 64, field of view = 240 mm × 240 mm, slice number = 43, slice thickness/spacing = 3.0/1.0 mm, number of obtained volumes = 200, and scanning time = 6 min 40 s.

Image processing

fMRI data preprocessing

The acquired rs-fMRI data were preprocessed using MATLAB-based DPARSF 5.1 software (DPARSF 5.1[1]) (Chao-Gan and Yu-Feng, 2010), as follows: (1) conversion of DICOM raw data to NIFTI format; (2) removal of the first 10 time points to stabilize the data; (3) slice timing; (4) realignment of head motion (removal of patients with head movements greater than 2 mm in any direction and motor rotation greater than 2°); (5) the resulting aligned image time series for each subject were each co-registered with the corresponding 3D T1-weighted image and the Diffeomorphic Anatomical Registration Through Exponentiated Lie Algebra (DARTEL) tool was used to normalize the data for all subjects to Montreal Neurological Institute (MNI) space, which was performed using the MNI coordinate space with 3mm × 3mm × 3mm; (6) linear detrending in order to reduce the influence of MRI equipment; (7) regression of covariates, including brain white matter signal, cerebrospinal fluid signal, and head movement parameters; (8) smoothening (a 6-mm full-width at half-maximum Gaussian kernel).

Amplitude of low frequency fluctuations analysis

Data were spatially normalized and smoothed, and a fast Fourier transform was performed to switch the time series to the frequency domain to obtain the power spectrum.

1 http://www.rfmri.org/DPARSF

The square root of the power spectrum at each frequency was calculated to obtain the average square root of the ALFF measurement for each voxel in the range of 0.01–0.08 Hz. Finally, time bandpass filtering (0.01–0.08 Hz) was performed. To reduce the inter-individual variability, ALFF was transformed to zALFF using Fisher's z transformation before statistical analysis.

Statistical analyses

Clinical data analysis

Clinical data were analyzed using the SPSS 23.0 statistical software (IBM Corporation, Somers, NY, United States). One-way analysis of variance was used to compare age and educational level among the four groups, and the chi-square test was used to compare gender differences. A two-sample t-test was used to compare the duration of disease and HAMD-17 scores between the two patient groups, with a threshold of $P < 0.05$ (two-tailed) set as statistically significant.

fMRI data analysis

Within-group patterns

Imaging data were analyzed using the DPARSF toolbox, and a voxel-based one-way analysis of variance was performed to compare the whole-brain ALFF map among the four groups. Gender, age, years of education, and framewise displacement (a metric derived from Jenkinson's formula < 0.2) were used as covariates, and brain areas with ALFF differences among the four groups were corrected for Gaussian random fields (GRF). The corrected cluster level was set at $P < 0.05$ (two-tailed), and threshold voxel levels of $P < 0.005$ were defined as statistically different. The threshold was set to clusters > 20 voxels.

Between-group differences

We extracted the mean ALFF values of abnormal brain regions in each of the four groups and performed *post hoc* between-group 2-sample t-test analysis in SPSS 23.0 software to show the difference between each two groups (younger TRD group vs. older TRD group, younger TRD group vs. younger HC group, older TRD group vs. older HC group, younger HC group vs. older HC group). And using Bonferroni correction, the threshold was statistically significant at $P < 0.0125$ (0.05/4).

Correlations with symptoms

To verify the relationship between clinical symptoms and abnormal brain areas in the younger TRD group and the older TRD group, we performed Pearson correlation analysis between ALFF values and HAMD-17 scores for abnormal brain areas extracted from the two groups separately. Significance was set at a statistical threshold of $P < 0.05$ (two-tailed).

Results

Characteristics of research datasets

Two older TRD patients were excluded because of excessive head movement displacement. Therefore, a total of 19 younger TRD patients, 19 older TRD patients, 19 younger HCs, and 19 older HCs met the inclusion criteria. There were no significant differences between the younger TRD group and the older TRD group in terms of gender, years of education, duration of illness, and HAMD-17 scores. There were no statistical differences between the younger TRD group and the older TRD group in terms of gender, age, and years of education when compared to matched controls in each age group (**Table 1**).

Abnormal amplitude of low frequency fluctuations among four groups

Age, gender, years of education, and frame displacement were used as covariates. One-way ANOVA revealed statistically significant differences in ALFF among the four groups in the left middle frontal gyrus, right middle temporal gyrus, right postcentral gyrus, left pallidum, and left caudate nucleus (**Table 2** and **Figure 1**).

Abnormal amplitude of low frequency fluctuations in younger treatment-resistant depression group vs. older treatment-resistant depression group

Compared to the older TRD group, the younger TRD group had increased ALFF in the left middle frontal gyrus and decreased ALFF in the left caudate nucleus (**Figure 2**).

Abnormal amplitude of low frequency fluctuations in younger treatment-resistant depression group vs. younger healthy control group

Compared with the younger HC group, the younger TRD group had increased ALFF in the left middle frontal gyrus and left pallidum, and decreased ALFF in the right postcentral gyrus (**Figure 2**).

TABLE 1 Demographic and clinical characteristics of the study participants.

Variable	Younger TRD (n = 19)	Older TRD (n = 19)	Younger HCs (n = 19)	Older HCs (n = 19)	$t(F)/\chi 2$	P-value
Gender (M/F)	9/10	7/12	9/10	7/12	0.864	0.834[a]
Age (years)	33.10 ± 5.38	50.42 ± 5.98	31.36 ± 4.24	50.63 ± 6.26	69.738	<0.001[b]*
Education (years)	14.94 ± 2.69	12.89 ± 3.84	15.15 ± 1.95	12.84 ± 3.54	3.169	0.029[c]*
Duration of illness (months)	41.36 ± 15.67	47.05 ± 23.09	NA	NA	−0.888	0.381[d]
HAMD-17 score	22.57 ± 3.09	23.10 ± 3.60	NA	NA	−0.483	0.632[d]

[a]The P-values of gender distribution among the three groups were obtained using the chi-square test. *Post hoc* t-test: P = 1 (Younger TRD vs. Younger HCs), P = 1 (Older TRD vs. Older HCs).
[b]P-value from one-way analysis of variance tests. *Post hoc* t-test: P = 0.336 (Younger TRD vs. Younger HCs), P = 0.907 (Older TRD vs. Older HCs).
[c]P-value from one-way analysis of variance tests. *Post hoc* t-test: P = 0.835 (Younger TRD vs. Younger HCs), P = 0.958 (Older TRD vs. Older HCs).
[d]P-value from a two-sample t-test.
*Significant difference.

TABLE 2 Brain areas with different ALFF signals for four groups.

Clusters	Brain regions	Peak coordinates (MNI)			Cluster size	F-values
		X	Y	Z		
1	Left middle frontal gyrus	−24	49	14	31	8.415
2	Right middle temporal gyrus	48	−57	21	22	9.761
3	Right postcentral gyrus	24	−45	54	25	14.442
4	Left pallidum	−13	−1	−1	55	10.340
5	Left caudate nucleus	−18	−9	24	23	10.413

One-way ANOVA, $P < 0.005$, GRF corrected, cluster size > 20.

Abnormal amplitude of low frequency fluctuations in older treatment-resistant depression group vs. older healthy control group

Compared with the older HC group, the older TRD group had increased ALFF in the left middle frontal gyrus, right middle temporal gyrus, left pallidum, and left caudate nucleus, and decreased ALFF in the right postcentral gyrus (Figure 2).

Abnormal amplitude of low frequency fluctuations in younger healthy control group vs. older healthy control group

There was no significant difference in the comparison of ALFF between the younger HC group and the older HC group (Figure 2).

Correlation between amplitude of low frequency fluctuations and clinical symptoms

To test whether there was a correlation between clinical characteristics and abnormal brain regions ALFF in the younger TRD group and the older TRD group, we further performed a Pearson correlation analysis. We found that the left middle frontal gyrus ALFF values in the younger TRD group were positively correlated with HAMD-17 scores (r = 0.499, P = 0.029). In addition, the right middle temporal gyrus ALFF values in the older TRD group were positively correlated with HAMD-17 scores (r = 0.507, P = 0.026) (Figure 3).

Discussion

To our knowledge, this is the first study using the ALFF method to analyze abnormalities in the physiopathological mechanisms of the brain between younger TRD and older TRD. The present study found no significant differences in clinical symptoms between younger and older TRD, but abnormal neuronal functional activity in some brain regions, with abnormalities associated with cognitive control networks (CCN) and reward networks. Compared to the matched HC group, TRD also exhibited abnormalities in some brain regions at different ages. The older TRD showed more extensive ALFF abnormalities than younger TRD. This study provides new insights into the differences in physiopathological mechanisms in patients with TRD at different ages.

This study found that the younger TRD group had increased ALFF in the left middle frontal gyrus than the

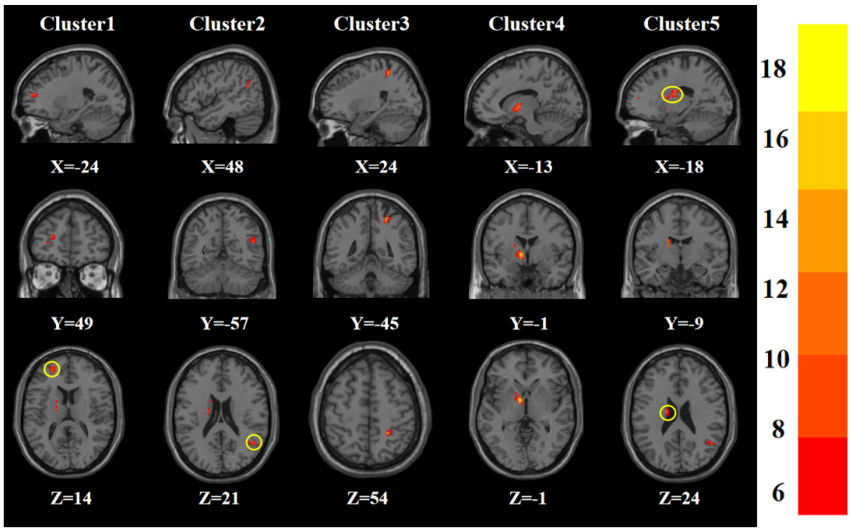

FIGURE 1
Statistical maps showing ANOVA result of ALFF abnormalities among patients with younger TRD, older TRD group, younger HC group, and older HC group (GRF corrected). The color bars indicate the *F*-value.

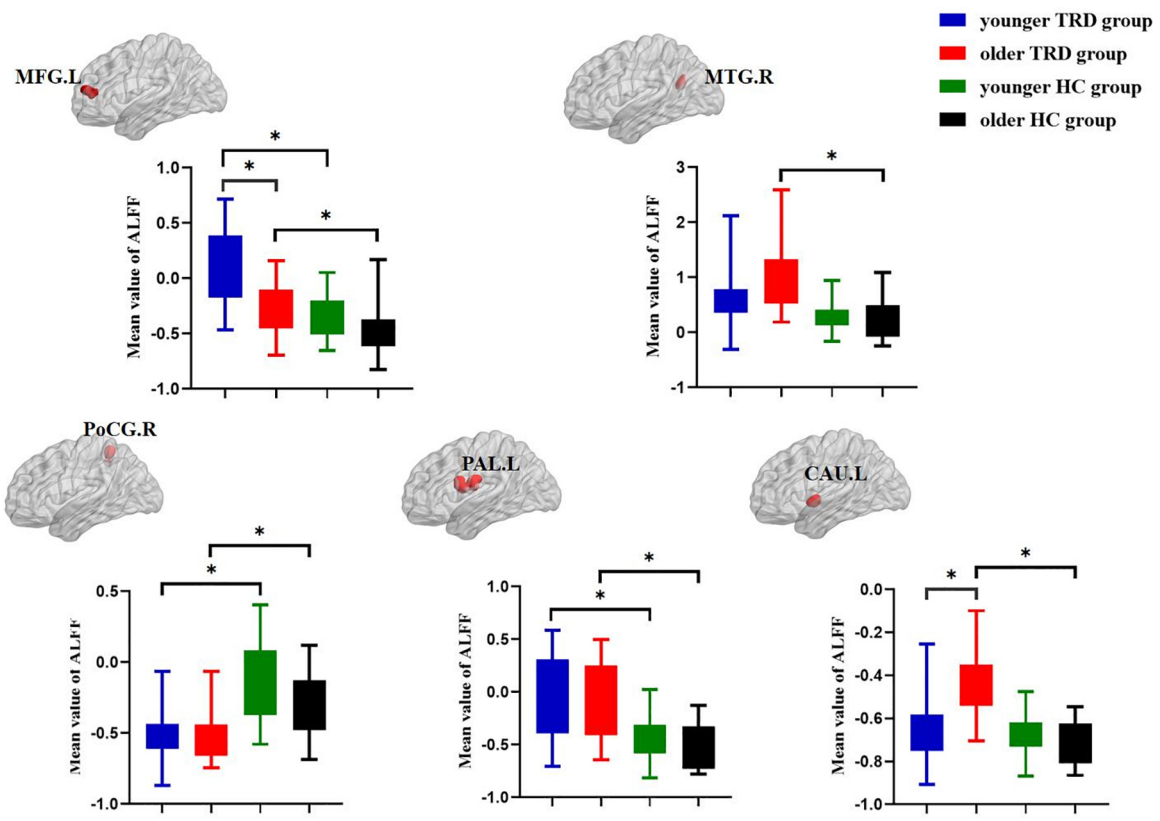

FIGURE 2
Post hoc two-sample *t*-tests (Bonferroni corrected) comparison showing ALFF values differences at peak voxel between each pair group (younger TRD group vs. older TRD group, younger TRD group vs. younger HC group, older TRD group vs. older HC group, younger HC group vs. older HC group). MFG.L, Left middle frontal gyrus; MTG.R, Right middle temporal gyrus; PoCG.R, Right postcentral gyrus; PAL.L, Left pallidum; CAU.L, Left caudate nucleus. *$P < 0.0125$.

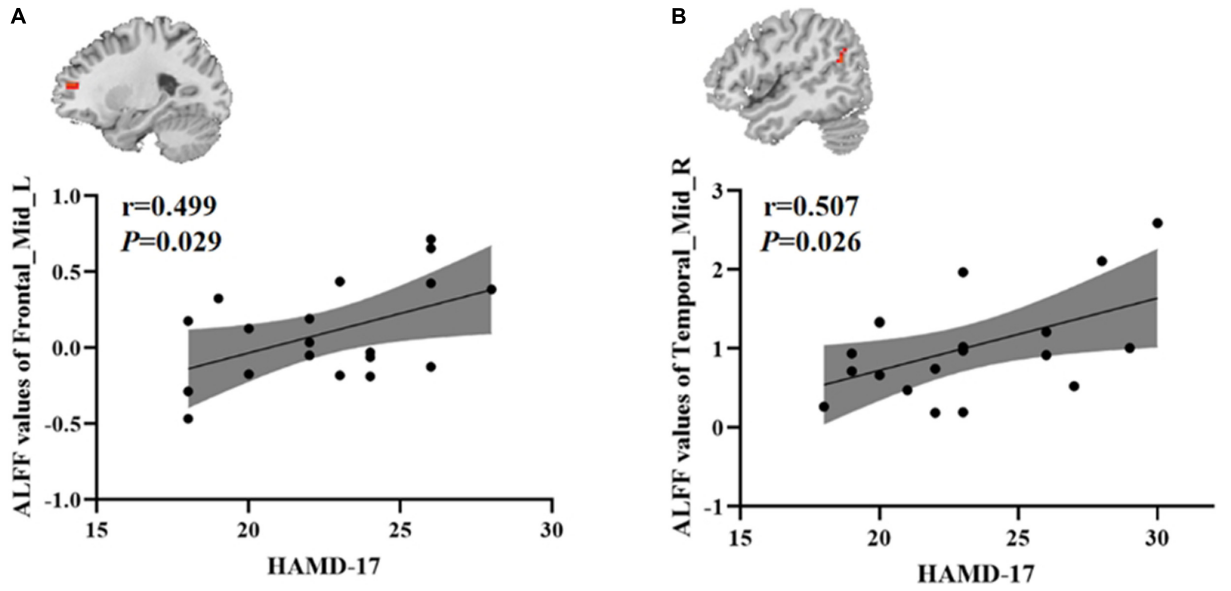

FIGURE 3
Positive correlation between the ALFF values of abnormal brain regions and the HAMD-17 scores: **(A)** ALFF values in the younger TRD group; **(B)** ALFF values in the older TRD group; Frontal_Mid_L, Left middle frontal gyrus; Temporal_Mid_R, Right middle temporal gyrus; ALFF, amplitude of low-frequency fluctuations; HAMD-17, 17-item Hamilton Rating Scale for Depression.

older. The middle frontal gyrus is an important component of the dorsolateral prefrontal cortex (DLPFC) and an important component of the CCN, which is closely associated with negative emotions, top-down attention, and working memory (Fales et al., 2009; Wang et al., 2016; Egorova et al., 2018). Patients with MDD with DLPFC damage tend to show low interest in things, memory loss, and lack of motivation (Hamilton et al., 2012; Kang et al., 2012; Martin et al., 2017). Previous studies have found that EOD has increased ALFF in the superior frontal gyrus than LOD, suggesting that hyperactivity of the superior frontal gyrus in the resting state may provoke strong negative affect for the individual (Guo et al., 2012). Another study also showed that regional homogeneity (ReHo) was increased in the right inferior frontal triangular gyrus of the EOD than in the LOD, suggesting that abnormal functional activity in the prefrontal lobe helps to distinguish the EOD from the LOD (Zhang et al., 2021b). Therefore, the results of the present study suggest that the hyperactivity of the left middle frontal gyrus in the resting state in younger TRD may be related to the high level of stress caused by the life and work environment of young people. In addition, we further found that ALFF in the left middle frontal gyrus of the younger TRD group was positively correlated with HAMD-17 scores, whereas this was not found in the older TRD. This suggests that the left middle frontal gyrus may be a neuroimaging marker for young TRD and is an important brain region for distinguishing younger TRD from older TRD.

We found that ALFF was decreased in the left caudate nucleus in the younger TRD group compared to the older TRD group. The caudate nucleus is an important component of the striatum and is one of the central nodes of emotional processing (Pizzagalli et al., 2009; Stoy et al., 2012). The caudate nucleus is involved in the cortico-striato-pallidum-thalamus emotion regulation loop, which regulates the body's response to external stimuli and maintains the balance of emotion regulation (Alexander et al., 1990; Haber and Calzavara, 2009; Peters et al., 2016). Meanwhile, the caudate nucleus is also an important component of the reward network and is involved in pleasure deficit and motivated reward processing in humans (Macpherson and Hikida, 2019; Cao et al., 2021). Previous studies found that ALFF in the right caudate nucleus was significantly increased in the MDD group than in the HC group, suggesting that abnormal spontaneous brain activity in the caudate nucleus may be associated with MDD (Liu et al., 2014; Chen et al., 2022). Another study also found that ketamine improved patients' emotional perception through its modulatory effect on the caudate nucleus in TRD patients (Murrough et al., 2015). Therefore, the results of this study suggest that the degree of functional impairment of the left caudate nucleus is more severe in older TRD patients than in younger TRD. This further suggests that different physiopathological mechanisms may exist in patients with TRD at different ages of onset.

We found increased ALFF in the right middle temporal gyrus and left caudate nucleus in the older TRD group compared

to the older HC group, which was not found in the younger TRD group compared to the younger HC group. Middle temporal gyrus is involved in emotional perception, audiovisual processing, memory and social cognitive functions, and is also an important component of the default mode network (DMN) (Raichle et al., 2001; Raichle and Snyder, 2007; Xu et al., 2019; Liu M. et al., 2021). Several previous studies have shown abnormalities in the functional activity of the DMN in patients with TRD, and the DMN varies by disease stage and age (de Kwaasteniet et al., 2015; Huang et al., 2020; Woody et al., 2021). A work showed that early-onset recurrent depression was increased ReHo in the right middle temporal gyrus than in the younger HC group, suggesting that this partially compensatory elevation of DMN may be one of the causes of abnormal brain function in early-onset recurrent depression (Sun et al., 2022). Therefore, the results of this study suggest that dysfunction and abnormalities of the right middle temporal gyrus and left caudate nucleus in older patients with TRD may be an important pathogenetic mechanism in younger patients with TRD. In addition, we found that ALFF values in the right middle temporal gyrus of the older TRD group were positively correlated with HAMD-17 scores, suggesting that this region may be an important neuroimaging marker and potential therapeutic target for older TRD patients. However, whether ALFF in this brain region associated with clinical symptoms can be a valid marker of TRD progression needs to be further elucidated.

Interestingly, compared with the two matched HC groups, the two subtype TRD groups had increased ALFF in the left middle frontal gyrus, left pallidum, and decreased ALFF in the right postcentral gyrus. The pallidum is not only a component of the striatum, but also a transmission node connecting the prefrontal cortex to the amygdala, which is closely associated with motivation and reward circuits in MDD patients (Smith et al., 2009; Knowland et al., 2017). Previous studies have found that the functional connectivity (FC) of median cingulate and paracingulate gyri and left pallidum was decreased in MDD patients compared to the HC group (Huang et al., 2021). In addition, a review also showed that vagus nerve stimulation and deep brain stimulation can reverse striatal abnormalities and thus alleviate TRD symptoms (Mohr et al., 2011). The postcentral gyrus belongs to the somatosensory-motor area, which is a higher-level center for the regulation of somatosensory and motor functions in the human body and an important part of the frontoparietal network, and is closely related to executive control and emotion management functions (Zhang et al., 2019; Liu M. et al., 2021). The postcentral gyrus plays an important role in the physiopathological mechanisms of TRD, and abnormalities of the postcentral gyrus predispose therefore TRD patients to somatic disorders (Klok et al., 2019). Previous studies have also found that electroconvulsive therapy can alleviate residual dysfunction in depression by reversing abnormal FC in the middle occipital gyrus and postcentral gyrus. Therefore, the results of this study suggest that cognitive control, reward motivation, and somatosensory-motor function were impaired in patients with TRD at different ages, independent of age of onset.

Some limitations need to be noted. First, for ethical reasons, TRD patients were not discontinued from antidepressants prior to enrollment. Therefore, we do not exclude the potential effects of antidepressants on brain function. Second, we only compared the differences in brain function between the TRD and HC groups, but the nTRD group was not included in this study. Therefore, the results of brain regions with abnormal ALFF (TRD group vs. HC group) only suggest an association with major depression and lack the specificity of TRD pathophysiology, which needs further study in the future. Third, only one clustering method was used to analyze the images in this study, and we will use different clustering methods to compare the results in future studies to improve the scientific significance of the results of this study. Finally, the small sample size of the present study limited the age classification range of the subjects. Therefore, we will further expand the sample size in future studies to improve the scientific value of this study.

Conclusion

To summarize, we found that different neuropathological mechanisms may exist in TRD patients of different ages, especially in the left middle frontal gyrus and left caudate nucleus. This study is beneficial to provide potential key targets for clinical treatment of TRD patients in different age groups.

Data availability statement

The raw data supporting the conclusions of this article will be made available by the authors, without undue reservation.

Ethics statement

The experimental protocol was approved by the Ethics Committee of Guang'anmen Hospital, China Academy of Chinese Medical Science (NO. 2017-021-SQ), Trial registration, China Clinical Trials Registry, chiCTR1800014277. All patients signed an informed consent form before enrollment. The patients/participants provided their written informed consent to participate in this study. Written informed consent was obtained

from the individual(s) for the publication of any potentially identifiable images or data included in this article.

Author contributions

JF conceived and designed the experiments and revised the manuscript. JS collected cases, analyzed data, and wrote manuscript. CG analyzed data and revised manuscript. YM, ZD, ZW, YiL, LC, DG, XL, and KX collected cases and analyzed data. YH scanned the subjects. XY and XX evaluated patients and collected cases. YoL revised the manuscript. All authors contributed to the article and approved the submitted version.

Funding

This research was supported by the National Natural Science Foundation of China (82174282 and 81774433), China Academy of Chinese Medical Sciences Innovation Fund (CI2021A03301), and National Key Research and Development Program of China (2018YFC1705802).

Conflict of interest

The authors declare that the research was conducted in the absence of any commercial or financial relationships that could be construed as a potential conflict of interest.

Publisher's note

All claims expressed in this article are solely those of the authors and do not necessarily represent those of their affiliated organizations, or those of the publisher, the editors and the reviewers. Any product that may be evaluated in this article, or claim that may be made by its manufacturer, is not guaranteed or endorsed by the publisher.

References

Alexander, G. E., Crutcher, M. D., and DeLong, M. R. (1990). Basal ganglia-thalamocortical circuits: Parallel substrates for motor, oculomotor, "prefrontal" and "limbic" functions. *Prog. Brain Res.* 85, 119–146.

Bergfeld, I. O., Mantione, M., Figee, M., Schuurman, P. R., Lok, A., and Denys, D. (2018). Treatment-resistant depression and suicidality. *J. Affect. Disord.* 235, 362–367. doi: 10.1016/j.jad.2018.04.016

Cao, Z., Ottino-Gonzalez, J., Cupertino, R. B., Juliano, A., Chaarani, B., and Banaschewski, T. (2021). Characterizing reward system neural trajectories from adolescence to young adulthood. *Dev. Cogn. Neurosci.* 52:101042. doi: 10.1016/j.dcn.2021.101042

Chao-Gan, Y., and Yu-Feng, Z. (2010). DPARSF: A MATLAB toolbox for "pipeline" data analysis of resting-state fmri. *Front. Syst. Neurosci.* 4:13. doi: 10.3389/fnsys.2010.00013

Chen, Q., Bi, Y., Zhao, X., Lai, Y., Yan, W., Xie, L., et al. (2022). Regional amplitude abnormities in the major depressive disorder: A resting-state fMRI study and support vector machine analysis. *J. Affect. Disord.* 308, 1–9. doi: 10.1016/j.jad.2022.03.079

Conelea, C. A., Philip, N. S., Yip, A. G., Barnes, J. L., Niedzwiecki, M. J., Greenberg, B. D., et al. (2017). Transcranial magnetic stimulation for treatment-resistant depression: Naturalistic treatment outcomes for younger versus older patients. *J. Affect. Disord.* 217, 42–47. doi: 10.1016/j.jad.2017.03.063

de Kwaasteniet, B. P., Rive, M. M., Ruhé, H. G., Schene, A. H., Veltman, D. J., Fellinger, L., et al. (2015). Decreased Resting-State Connectivity between Neurocognitive Networks in Treatment Resistant Depression. *Front. Psychiatry* 6:28. doi: 10.3389/fpsyt.2015.00028

Egorova, N., Cumming, T., Shirbin, C., Veldsman, M., Werden, E., and Brodtmann, A. (2018). Lower cognitive control network connectivity in stroke participants with depressive features. *Transl. Psychiatry* 7:4. doi: 10.1038/s41398-017-0038-x

Fabbri, C., Pain, O., Hagenaars, S. P., Lewis, C. M., and Serretti, A. (2021). Transcriptome-wide association study of treatment-resistant depression and depression subtypes for drug repurposing. *Neuropsychopharmacology* 46, 1821–1829. doi: 10.1038/s41386-021-01059-6

Fales, C. L., Barch, D. M., Rundle, M. M., Mintun, M. A., Mathews, J., Snyder, A. Z., et al. (2009). Antidepressant treatment normalizes hypoactivity in dorsolateral prefrontal cortex during emotional interference processing in major depression. *J. Affect. Disord.* 112, 206–211. doi: 10.1016/j.jad.2008.04.027

Gaynes, B. N., Lux, L., Gartlehner, G., Asher, G., Forman-Hoffman, V., Green, J., et al. (2020). Defining treatment-resistant depression. *Depress. Anxiety* 37, 134–145. doi: 10.1002/da.22968

Ghaziuddin, N., Dumas, S., and Hodges, E. (2011). Use of continuation or maintenance electroconvulsive therapy in adolescents with severe treatment-resistant depression. *J. ECT* 27, 168–174. doi: 10.1097/YCT.0b013e3181f665e4

Gronemann, F. H., Jorgensen, M. B., Nordentoft, M., Andersen, P. K., and Osler, M. (2020). Socio-demographic and clinical risk factors of treatment-resistant depression: A Danish population-based cohort study. *J. Affect. Disord.* 261, 221–229. doi: 10.1016/j.jad.2019.10.005

Guo, W. B., Liu, F., Xue, Z. M., Xu, X. J., Wu, R. R., and Ma, C. Q. (2012). Alterations of the amplitude of low-frequency fluctuations in treatment-resistant and treatment-response depression: A resting-state fMRI study. *Prog. Neuro Psychopharmacol. Biol. Psychiatry* 37, 153–160. doi: 10.1016/j.pnpbp.2012.01.011

Guo, W. B., Liu, F., Xun, G. L., Hu, M. R., Guo, X. F., Xiao, C. Q., et al. (2013). Reversal alterations of amplitude of low-frequency fluctuations in early and late onset, first-episode, drug-naive depression. *Prog. Neuro Psychopharmacol. Biol. Psychiatry* 40, 153–159. doi: 10.1016/j.pnpbp.2012.08.014

Guo, X., Chen, H., Long, Z., Duan, X., Zhang, Y., and Chen, H. (2017). Atypical developmental trajectory of local spontaneous brain activity in autism spectrum disorder. *Sci. Rep.* 7:39822. doi: 10.1038/srep39822

Haber, S. N., and Calzavara, R. (2009). The cortico-basal ganglia integrative network: The role of the thalamus. *Brain Res. Bull.* 78, 69–74. doi: 10.1016/j.brainresbull.2008.09.013

Hamilton, J. P., Etkin, A., Furman, D. J., Lemus, M. G., Johnson, R. F., and Gotlib, I. H. (2012). Functional neuroimaging of major depressive disorder: A meta-analysis and new integration of base line activation and neural response data. *Am. J. Psychiatry* 169, 693–703. doi: 10.1176/appi.ajp.2012.11071105

Hedden, T., and Gabrieli, J. D. (2004). Insights into the ageing mind: A view from cognitive neuroscience. *Nat. Rev. Neurosci.* 5, 87–96. doi: 10.1038/nrn1323

Ho, M. C., Hsu, Y. C., Lu, M. L., Gossop, M., and Chen, V. C. (2018). 'Cool' and 'Hot' executive functions in suicide attempters with major depressive disorder. *J. Affect. Disord.* 235, 332–340. doi: 10.1016/j.jad.2018.04.057

Huang, H., Botao, Z., Jiang, Y., Tang, Y., Zhang, T., Tang, X., et al. (2020). Aberrant resting-state functional connectivity of salience network in first-episode schizophrenia. *Brain Imaging Behav.* 14, 1350–1360. doi: 10.1007/s11682-019-00040-8

Huang, Q., Xiao, M., Ai, M., Chen, J., Wang, W., Hu, L., et al. (2021). Disruption of Neural Activity and Functional Connectivity in Adolescents With Major Depressive Disorder Who Engage in Non-suicidal Self-Injury: A Resting-State fMRI Study. *Front. Psychiatry* 12:571532. doi: 10.3389/fpsyt.2021.571532

Jaffe, D. H., Rive, B., and Denee, T. R. (2019). The humanistic and economic burden of treatment-resistant depression in Europe: A cross-sectional study. *BMC Psychiatry* 19:247. doi: 10.1186/s12888-019-2222-4

Kang, H. J., Voleti, B., Hajszan, T., Rajkowska, G., Stockmeier, C. A., Licznerski, P., et al. (2012). Decreased expression of synapse-related genes and loss of synapses in major depressive disorder. *Nat. Med.* 18, 1413–1417. doi: 10.1038/nm.2886

Klein, D. N., Schatzberg, A. F., McCullough, J. P., Dowling, F., Goodman, D., Howland, R. H., et al. (1999). Age of onset in chronic major depression: Relation to demographic and clinical variables, family history, and treatment response. *J. Affect. Disord.* 55, 149–157. doi: 10.1016/s0165-0327(99)00020-8

Klok, M., van Eijndhoven, P. F., Argyelan, M., Schene, A. H., and Tendolkar, I. (2019). Structural brain characteristics in treatment-resistant depression: Review of magnetic resonance imaging studies. *BJPsych Open* 5:e76. doi: 10.1192/bjo.2019.58

Knöchel, C., Alves, G., Friedrichs, B., Schneider, B., Schmidt-Rechau, A., Wenzler, S., et al. (2015). Treatment-resistant Late-life Depression: Challenges and Perspectives. *Curr. Neuropharmacol.* 13, 577–591. doi: 10.2174/1570159x1305151013200032

Knowland, D., Lilascharoen, V., Pacia, C. P., Shin, S., Wang, E. H., and Lim, B. K. (2017). Distinct Ventral Pallidal Neural Populations Mediate Separate Symptoms of Depression. *Cell* 170, 284–297.e18. doi: 10.1016/j.cell.2017.06.015

Korten, N. C., Comijs, H. C., Lamers, F., and Penninx, B. W. (2012). Early and late onset depression in young and middle aged adults: Differential symptomatology, characteristics and risk factors? *J. Affect. Disord.* 138, 259–267. doi: 10.1016/j.jad.2012.01.042

Lawson, R. P., Nord, C. L., Seymour, B., Thomas, D. L., Dayan, P., Pilling, S., et al. (2017). Disrupted habenula function in major depression. *Mol. Psychiatry* 22, 202–208. doi: 10.1038/mp.2016.81

Lijffijt, M., Murphy, N., Iqbal, S., Green, C. E., Iqbal, T., Chang, L. C., et al. (2022). Identification of an optimal dose of intravenous ketamine for late-life treatment-resistant depression: A Bayesian adaptive randomization trial. *Neuropsychopharmacology* 47, 1088–1095. doi: 10.1038/s41386-021-01242-9

Liu, C. H., Ma, X., Song, L. P., Tang, L. R., Jing, B., Zhang, Y., et al. (2015). Alteration of spontaneous neuronal activity within the salience network in partially remitted depression. *Brain Res.* 1599, 93–102. doi: 10.1016/j.brainres.2014.12.040

Liu, J., Ren, L., Womer, F. Y., Wang, J., Fan, G., Jiang, W., et al. (2014). Alterations in amplitude of low frequency fluctuation in treatment-naïve major depressive disorder measured with resting-state fMRI. *Hum. Brain Mapp.* 35, 4979–4988. doi: 10.1002/hbm.22526

Liu, P., Tu, H., Zhang, A., Yang, C., Liu, Z., Lei, L., et al. (2021). Brain functional alterations in MDD patients with somatic symptoms: A resting-state fMRI study. *J. Affect. Disord.* 295, 788–796. doi: 10.1016/j.jad.2021.08.143

Liu, M., Wang, Y., Zhang, A., Yang, C., Liu, P., Wang, J., et al. (2021). Altered dynamic functional connectivity across mood states in bipolar disorder. *Brain Res.* 1750:147143. doi: 10.1016/j.brainres.2020.147143

Macpherson, T., and Hikida, T. (2019). Role of basal ganglia neurocircuitry in the pathology of psychiatric disorders. *Psychiatry Clin. Neurosci.* 73, 289–301. doi: 10.1111/pcn.12830

Martin, D. M., McClintock, S. M., Forster, J. J., Lo, T. Y., and Loo, C. K. (2017). Cognitive enhancing effects of rTMS administered to the prefrontal cortex in patients with depression: A systematic review and meta-analysis of individual task effects. *Depress. Anxiety* 34, 1029–1039. doi: 10.1002/da.22658

Mohr, P., Rodriguez, M., Slavíčková, A., and Hanka, J. (2011). The application of vagus nerve stimulation and deep brain stimulation in depression. *Neuropsychobiology* 64, 170–181. doi: 10.1159/000325225

Mulsant, B. H., and Pollock, B. G. (1998). Treatment-resistant depression in late life. *J. Geriatr. Psychiatry Neurol.* 11, 186–193. doi: 10.1177/089198879901100404

Murrough, J. W., Collins, K. A., Fields, J., DeWilde, K. E., Phillips, M. L., Mathew, S. J., et al. (2015). Regulation of neural responses to emotion perception by ketamine in individuals with treatment-resistant major depressive disorder. *Transl. Psychiatry* 5:e509. doi: 10.1038/tp.2015.10

Ochs-Ross, R., Daly, E. J., Zhang, Y., Lane, R., Lim, P., Morrison, R. L., et al. (2020). Efficacy and safety of esketamine nasal spray plus an oral antidepressant in elderly patients with treatment-resistant depression-TRANSFORM-3. *Am. J. Geriatr. Psychiatry* 28, 121–141. doi: 10.1016/j.jagp.2019.10.008

Peters, S. K., Dunlop, K., and Downar, J. (2016). Cortico-striatal-thalamic loop circuits of the salience network: a central pathway in psychiatric disease and treatment. *Front. Syst. Neurosci.* 10:104. doi: 10.3389/fnsys.2016.00104

Pizzagalli, D. A., Holmes, A. J., Dillon, D. G., Goetz, E. L., Birk, J. L., Bogdan, R., et al. (2009). Reduced caudate and nucleus accumbens response to rewards in unmedicated individuals with major depressive disorder. *Am. J. Psychiatry* 166, 702–710. doi: 10.1176/appi.ajp.2008.08081201

Qiao, J., Qian, L. J., Zhao, H. F., Gong, G. H., and Geng, D. Q. (2017). The relationship between quality of life and clinical phenotype in patients with treatment resistant and non-treatment resistant depression. *Eur. Rev. Med. Pharmacol. Sci.* 21, 2432–2436.

Raichle, M. E., MacLeod, A. M., Snyder, A. Z., Powers, W. J., Gusnard, D. A., and Shulman, G. L. (2001). A default mode of brain function. *Proc. Natl. Acad. Sci. U.S.A.* 98, 676–682. doi: 10.1073/pnas.98.2.676

Raichle, M. E., and Snyder, A. Z. (2007). A default mode of brain function: A brief history of an evolving idea. *NeuroImage* 37, 1083–1099. doi: 10.1016/j.neuroimage.2007.02.041

Smith, K. S., Tindell, A. J., Aldridge, J. W., and Berridge, K. C. (2009). Ventral pallidum roles in reward and motivation. *Behav. Brain Res.* 196, 155–167. doi: 10.1016/j.bbr.2008.09.038

Stoy, M., Schlagenhauf, F., Sterzer, P., Bermpohl, F., Hägele, C., Suchotzki, K., et al. (2012). Hyporeactivity of ventral striatum towards incentive stimuli in unmedicated depressed patients normalizes after treatment with escitalopram. *J. Psychopharmacol.* 26, 677–688. doi: 10.1177/0269881111416686

Sun, J. F., Chen, L. M., He, J. K., Wang, Z., Guo, C. L., Ma, Y., et al. (2022). A Comparative Study of Regional Homogeneity of Resting-State fMRI Between the Early-Onset and Late-Onset Recurrent Depression in Adults. *Front. Psychology* 13:849847. doi: 10.3389/fpsyg.2022.849847

Wang, M., Ju, Y., Lu, X., Sun, J., Dong, Q., Liu, J., et al. (2020). Longitudinal changes of amplitude of low-frequency fluctuations in MDD patients: A 6-month follow-up resting-state functional magnetic resonance imaging study. *J. Affect. Disord.* 276, 411–417. doi: 10.1016/j.jad.2020.07.067

Wang, Y. L., Yang, S. Z., Sun, W. L., Shi, Y. Z., and Duan, H. F. (2016). Altered functional interaction hub between affective network and cognitive control network in patients with major depressive disorder. *Behav. Brain Res.* 298, 301–309. doi: 10.1016/j.bbr.2015.10.040

Woody, M. L., Panny, B., Degutis, M., Griffo, A., and Price, R. B. (2021). Resting state functional connectivity subtypes predict discrete patterns of cognitive-affective functioning across levels of analysis among patients with treatment-resistant depression. *Behav. Res. Ther.* 146:103960. doi: 10.1016/j.brat.2021.103960

Xu, J., Lyu, H., Li, T., Xu, Z., Fu, X., Jia, F., et al. (2019). Delineating functional segregations of the human middle temporal gyrus with resting-state functional connectivity and coactivation patterns. *Hum. Brain Mapp.* 40, 5159–5171. doi: 10.1002/hbm.24763

Zang, Y. F., He, Y., Zhu, C. Z., Cao, Q. J., Sui, M. Q., Liang, M., et al. (2007). Altered baseline brain activity in children with ADHD revealed by resting-state functional MRI. *Brain Dev.* 29, 83–91. doi: 10.1016/j.braindev.2006.07.002

Zhang, H., Qiu, M., Ding, L., Mellor, D., Li, G., Shen, T., et al. (2019). Intrinsic gray-matter connectivity of the brain in major depressive disorder. *J. Affect. Disord.* 251, 78–85. doi: 10.1016/j.jad.2019.01.048

Zhang, Z., Bo, Q., Li, F., Zhao, L., Wang, Y., Liu, R., et al. (2021a). Increased ALFF and functional connectivity of the right striatum in bipolar disorder patients. *Prog. Neuropsychopharmacol. Biol. Psychiatry* 111:110140. doi: 10.1016/j.pnpbp.2020.110140

Zhang, Z., Chen, Y., Wei, W., Yang, X., Meng, Y., Yu, H., et al. (2021b). Changes in Regional Homogeneity of Medication-Free Major Depressive Disorder Patients With Different Onset Ages. *Front. Psychiatry* 12:713614. doi: 10.3389/fpsyt.2021.713614

Zisook, S., Rush, A. J., Lesser, I., Wisniewski, S. R., Trivedi, M., Husain, M. M., et al. (2007). Preadult onset vs. adult onset of major depressive disorder: A replication study. *Acta Psychiatr. Scand.* 115, 196–205. doi: 10.1111/j.1600-0447.2006.00868.x

Frontiers in Neuroscience

Provides a holistic understanding of brain function from genes to behavior

Part of the most cited neuroscience journal series which explores the brain - from the new eras of causation and anatomical neurosciences to neuroeconomics and neuroenergetics.

Discover the latest Research Topics

See more →

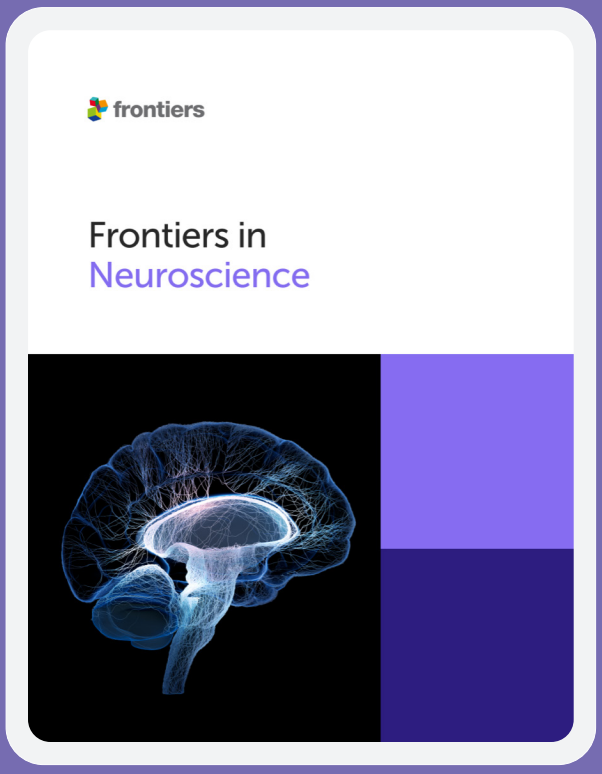

Frontiers

Avenue du Tribunal-Fédéral 34
1005 Lausanne, Switzerland
frontiersin.org

Contact us

+41 (0)21 510 17 00
frontiersin.org/about/contact